School of Chemistry
Trinity College Dublin

# Synthesis and Characterisation of Transition Metal Dichalcogenides & their Heterostructures

L.M.J.J. Peters
16341639

June 2021

A dissertation submitted for the degree of
Doctor of Philosophy in Chemistry.
Based on research under the supervision of
Dr.Niall McEvoy.

# Declaration

I declare that this thesis has not been submitted as an exercise for a degree at this or any other university and it is entirely my own work.

I agree to deposit this thesis in the University's open access institutional repository or allow the library to do so on my behalf, subject to Irish Copyright Legislation and Trinity College Library conditions of use and acknowledgement

Signed: _____ Date: _____

# Abstract

Since the first isolation of graphene in 2004 the interest in 2D materials has exponentially grown. Two-dimensional layered materials demonstrate profoundly different properties when isolated in their mono- or few layer form compared to their bulk equivalents. While graphene lacks a band gap, and is thus not applicable for many logic devices, various other 2D materials, which do have a band gap, have been discovered and isolated. An important class of layered materials is the transition metal dichalcogenides (TMDs). This extended class of materials has generated generated a lot of attention due to their electronic properties, which range from metallic to semiconducting, as well as their layer-dependent properties and strong light-matter interactions. TMDs consists of a transition metal e.g. molybdenum, tungsten or platinum, sandwiched between two chalcogen atoms; sulfur, selenium or tellurium.

Many of the TMDs have band gaps in a useful optical range of 1 - 2 eV. Furthermore, it is possible to open the band gap from an indirect to direct upon thinning the material from bulk to monolayer. Along with this, TMDs have also shown other interesting properties such as strong light-matter interaction and high charge-carrier mobilities. Further optimisation of the material properties can be realised by creating heterostructures of different TMDs. Heterostructures of two dissimilar TMDs result in devices with atomically sharp and clean interfaces in which the band gap can be aligned.

In this work TMDs are synthesised using a microreactor chemical vapour deposition (CVD) method in which the metal precursor is brought in close proximity to the growth substrate. This method increases the reactivity on the surface and minimises the amount of metal precursor required for the synthesis. The quality and properties of the synthesised materials in this work were intensively studied by various characterisation techniques such as Raman spectroscopy, photoluminence (PL) spectroscopy, X-ray photo-electron spectroscopy and atomic force microscopy.

In the first results chapter of this thesis the chemical vapour deposition synthesis of $WSe_2$ was optimised through parametric investigation. These parameters include metal precursors, reaction time, temperature, pressure and gas flow. The parameters influence the formation of $WSe_2$ on the growth substrate as well as the growth mechanism, nucleation density and lateral size of the flakes. Electrical FET devices with $WSe_2$ as channel material, made from the optimised synthesis method, demonstrated p-type charge carrier transport and reasonable mobility. Collaborative work investigated the influence of environmental effects on the properties of the $WSe_2$ FETs and the synthesised flakes were further used to demonstrate the first vertical field emission transistor.

Not only the growth parameters but also the morphology of the growth substrate influences the growth mechanism of the synthesised TMD. An in-depth study on the effects of different sapphire planes and annealing of sapphire substrates on the growth of CVD $MoS_2$ flakes showed a wide variation in alignment, growth mechanisms, flake size and flake thickness on the different sapphire planes. The size and shape of the terraces on the sapphire planes can hinder or promote the growth of $MoS_2$ and can

result in the growth of aligned $MoS_2$. The step height between the terraces of the surface can influence the lateral growth or promote vertical, multi layer growth. Depending on the application of the $MoS_2$, different properties are required and a particular substrate can be selected to promote $MoS_2$ growth with these properties.

Finally a direct growth CVD growth method was developed in which a micro-reactor is used to synthesise TMD heterostructures. This growth method allows the formation of both lateral and vertical heterostructures as well as sulfide and selenide heterostructures, offering a large range of possible device architectures. Both double-step and single-step synthesis of TMD heterostructures were attempted. Double-step offers more variety in possible combinations of formed heterostructures, however the crystalline quality of the TMDs and the interface is better when using a single-step approach. On top of this, single-step synthesis allowed the formation of both lateral and vertical heterostructures offering a large range of possible device architectures. The growth of of lateral and vertical heterostructures can be controlled by the concentration of the initially grown TMD. The synthesised materials were intensively studied by Raman and PL spectroscopy, XPS and TOF-SIMS as well as various AFM modes including peak force tunneling AFM. FET Devices produced from the synthesised heterostructures show interesting properties such as photoconductivity.

# Acknowledgements

First of all I would like to sincerely thank my supervisor Dr. Niall McEvoy for the opportunity to do a PhD as part of the ASIN group and for his constant support, enthusiasm, encouragement, brilliant suggestions and endless patience.

I also have to thank Prof. Georg Duesberg for being my co-supervisor for the past 4.5 years. and I would also like to acknowledge the financial support from Science Foundation Ireland via grant nr. 15/SIRG/3329.

I owe a debt of gratitude to Dr Cormac Ó Coileáin, without whose excellent knowledge of about everything this thesis would not have been possible. Thank you for teaching me about very useful and completely useless stuff.

Of course I have to thank everyone else in the ASIN Group over the years for their help, support and lots of craic. Dr. John McManus, Dr. Conor Cullen and Dr. Maria O'Brien, thank you for training me up on all the equipment and help with everything. Katie O'Neill, for her amazing knowledge about AFM. Dr. Graeme Cunningham and Dr. Daniela Angione, thank you for helping me out with measuring and understanding electrical devices! And finally the internship and project students Alan, Loris, Patryk for carrying out such amazing work!

I have to thank Mike Finneran for his help in fixing up the IMP and keeping me optimistic. Thank you for all the hours you put into that tool. To Dr. Peter Gleeson, thank you for sharing your knowledge on EBL and your motivating chats. And of course thanks to all the technical and admin staff in CRANN.

Many thanks to all the collaborators in Munich, Salerno and Trinity for the help with measurements and all the interesting work you were able to create from my humble samples. Thank you Dr. Kangho Lee, Rita Tilmann, Dr. Francesca Urban, Prof. Antonio Di Bartolomeo, Julia Lawless and Dr. Stephen O'Brien.

I would not have been able to finish this thesis without the help from my friends. The past few years I made some amazing friends here in Dublin. I especially want to thank Matej, Jessica and Siobán for their encouragement, tea and karaoke parties and sarcastic remarks. You guys really pulled me through when I really needed it. There are too many people in Dublin that I would like to thank including Aisling, Rob, Amol, Lili, Seppe and Lara. To everyone else that I forgot in here, you know who you are!

Of course I have to include my brilliant friends from back in college as well who are always available for some interesting discussions and letting me crash on their couch. Dieter, Lisa, Elise, Pieter, Robin, Teresa and Nathan, thank you for keeping up with me during all those years.

Robin Jacobs, my beloved weirdo, thank you for being there for me and believing in me, especially when I did not and putting up with my thesis writing depressions. You are my favourite person to be stuck with in a lockdown! (Outside a lockdown as well FYI.)

Finally, I have to thank everyone in my family. I am grateful that all of you are always there for me even if I do not always show you how much I appreciate you. Thanks mum and dad for always trying to be on my side and putting up with me

my whole life and thanks to Matthijs, my sweet and bloody annoying baby brother. I also must acknowledge my granny who first showed me the wonderful world of science and who has been one of the most important role models in my life.

# Contents

# List of Figures

# List of Tables

# Abbreviations

| | |
|---|---|
| **2D** | Two dimensional |
| **AFM** | Atomic Force Microscopy |
| **ALD** | Atomic layer deposition |
| **BP** | Black phosphorus |
| **c-AFM** | conductive AFM |
| **CB** | Conduction band |
| **CFT** | Crystal Field Theory |
| **CVD** | Chemical vapour deposition |
| **CZ** | Czochralski process |
| $\mathbf{\Delta H}_{mix}$ | Mix enthalpy |
| $\mathbf{\Delta H}_{s}$ | Formation enthalpy |
| **DMD** | Digital micro mirror device |
| **DMF** | Di-methyl formamide |
| **E** | Electric field |
| $\mathbf{E}_{C}$ | Conduction band energy |
| $\mathbf{E}_{F}$ | Fermi level |
| $\mathbf{E}_{V}$ | Valence band energy |
| **EtOH** | Ethanol |
| **FET** | Field effect transistors |
| **FWHM** | Full width half maximum |
| **h-BN** | Hexagonal boron nitride |
| **HF** | Hydrogen fluoride |
| **HOPG** | Highly oriented pyrolytic carbon |
| **HPLC** | High purity liquid chromatography |
| **IMP** | Intelligent micro patterning |
| **IPA** | Isopropanol |

| | |
|---|---|
| **IR** | Infrared |
| **JFET** | Juction field effect transistor |
| **LBM** | Layer breathing mode |
| **LED** | Light emitting diodes |
| **LF** | Low frequency |
| **LPE** | Liquid phase exfoliation |
| $\mu$ | carrier mobility |
| $\mu_e$ | electron mobility |
| $\mu_h$ | hole mobility |
| **MESFET** | Metal semiconductor field effect transistor |
| **MIBK** | Methyl isobutyl ketone |
| **MOS** | Metal oxide semiconductor |
| **MOSFET** | Metal oxide semiconductor field effect transistor |
| **NIR** | Near infrared |
| **NMP** | N-methyl-2-pyrrolidine |
| **PDMS** | Poly dimethylsiloxane |
| **PECS** | Precision etching and coating system |
| **PF-TUNA** | Peak force tunneling AFM |
| **PL** | Photoluminescence |
| **PMMA** | Poly methyl metacrylate |
| **PVD** | Physical vapour deposition |
| **QCM** | Quartz crystal microbalance |
| $\mathbf{R}_{tot}$ | Total resistance |
| **RTO** | Rapid thermal oxidation |
| **SB** | Schottky barrier |
| **SM** | Shearing mode |
| **SS** | Subthreshold swing |
| **STM** | Scanning tunneling microscopy |
| **T** | Temperature |
| $\mathbf{T}_m$ | Melting temperature |
| $\mathbf{T}_R$ | Room temperature |

| | |
|---|---|
| **TAC** | Thermally assisted conversion |
| **TFET** | Tunneling field effect transistor |
| **THF** | Tetrahydrofuran |
| **TLM** | Transfer length measurement |
| **TMD** | Transition metal dichalcogenide |
| **TOF-SIMS** | Time of flight secondary ion mass spectrometry |
| **UV** | Ultra violet |
| $\mathbf{v}_d$ | Drift velocity |
| **VB** | Valence band |
| **XPS** | X-ray photoelectron spectroscopy |

# Part I

# Introduction

# 1 Introduction

In 1965 Gordon Moore predicted that the number of components on an integrated circuit would double every 2 years.[1] This prediction, better known as Moore's law, has been correct so far. For years silicon based semiconductor technology has flourished, not only did the number of components on a chip increase, the prices of the chips went down as well. The problem is that the current silicon based technology is reaching its limits as the down scaling of devices reaches atomic dimensions. This makes it incredibly challenging to make components smaller still as dimensions reach the limit where individual atoms count when downscaling. Thermal issues also become problematic when channel dimensions decrease and there are also issues with quantum tunneling. In quantum tunneling electrons cross an energy barrier with a higher energy level than the electrons have, resulting in increasing leaking currents. For these reasons novel semiconductor materials and architectures are being investigated.

Already back in 1959 Richard Feynman effectively introduced the concept and importance of nanotechnology in his lecture "Plenty of Room at the Bottom".[2] In this lecture Feynman explained not just the need to scale down materials laterally but also to top down materials to decrease the thickness. This lecture motivated scientists to face the challenges of the nanometer domain and how to overcome these domains, eventually leading to the formation of materials that were only a single molecule layer thick, making them the thinnest materials possible. These materials are referred to as 2 dimensional (2D) materials.

Beyond the pursuit of smaller computer chips there are various applications which could use novel materials, where the properties are optimised for the application. These properties range from the physical properties, such as the mechanical strength, flexibility or thermal conductivity, to electronic properties, such as the band gap, mobility and light-matter interaction. All these properties can be obtained by 2D materials and combinations of 2D materials.

The isolation of graphene in 2005 by Novoselov *et al*, brought 2D materials back in the spotlight.[3] Before, 2D materials were expected to be unstable at single layer level. This research showed otherwise and therefore heralded a new era of research into 2D materials. A large variety of different 2D materials are available with a wide range of properties. Transition metal dichalcogenides (TMDs) are a group of 2D materials with versatile properties. To obtain TMDs suitable for electronic applications, highly crystalline materials are preferred. Chemical vapour deposition

is a synthesis method which can deliver this, though this requires optimisation of the process, precursors and substrates. Properties of TMDs can be enriched by combining different TMDs, to form TMD heterojunctions, which are also a perfect fit for electric junctions due to the small lattice mismatch between TMDs.

In this work the growth of highly qualitative TMDs is performed, to obtain TMD heterostructures. The synthesised materials are characterised by different spectroscopic methods, including Raman spectroscopy and photoluminescence spectroscopy as well as other characterisation techniques such as atomic force microscopy and time-of-flight secondary ion mass spectroscopy.

In **Part I Introduction**, the motivation for the research is first set out followed by an overview of the dissertation. This is followed by **Part II Theoretical Background**. In this part a review of the literature, pertaining to 2D TMDs, is given. In this review the properties and applications of TMDs are discussed as well as those of TMD heterostructures. The theoretical background discusses semiconductors and device structures as well and finally an overview of synthesis methods for TMDs and their heterostructures is presented.

Following the theoretical background, the experimental details for the CVD synthesis as well as the characterisation methods used in this work are discussed in **Part III Experimental Details**. The growth parameters used in the CVD process are explained in detail and a theoretical and practical description of the characterisation techniques and tools is presented.

The results and discussion chapters can be found in **Part IV Results & Discussion**. This part is divided in 3 different chapters. The first results chapter: **Parametric Study on the CVD growth of $WSe_2$** examines the effect of different reaction parameters on the CVD growth and crystalline quality of $WSe_2$. These parameters include: the reaction time, temperature and pressure in the furnace setup.

Besides reaction other parameters such as the growth substrate can be of influence on the synthesis reaction. The chapter on **Substrate effects on the growth of $MoS_2$** examines the influence of the substrate and the morphology of the substrate on the growth mechanism of CVD grown $MoS_2$. This is studied with a comparative study of $MoS_2$ growth on $SiO_2$/Si and contrasting sapphire substrates. The annealing of the substrates thermodynamically relaxes the surface and improves the ordering of the surface atoms.

The chapter on **Direct synthesis of TMD Heterostructures** discusses the formation of TMD heterostructures by using double and single step synthesis of TMD heterostructures. The advantages and disadvantages of these methods are examined. These methods can lead to the formation of both lateral and vertical heterostructures and shows the electrical properties of the formed materials. Devices of both individual flakes of varying thicknesses as well as heterostructures have been produced and tested to better understand the properties and possible applications of TMD devices.

Finally the dissertation ends with **Part V Conclusions & Outlook**. In this part an overview of the obtained knowledge and conclusions will be given as well as possible lines of investigation which could follow as future work on the topic.

# Part II

# Theoretical background

# 2 2D Materials

Two dimensional materials or layered materials have been known for centuries, as these materials naturally occur as minerals. There are many 2D materials, though the best known 2D material is undoubtedly single layer graphite, better known as graphene. Graphene is a structure made up of single atomic layers of carbon ordered in a hexagonal lattice. The material was first theoretically described in 1947 by P. Wallace, who described the structure of a single hexagonal graphite layer and defined graphene and its conductive properties by use of the band theory of solids. [4]

For almost 60 years 2D layers were considered to be thermodynamically unstable and therefore layers of one or few atoms thick film would not be able to exist under ambient conditions. This was generally assumed until A. Geim and K. Novoselov isolated few layer graphene in 2004 [5] and narrowed it down to a single layer in 2005. [3] The isolation of graphene unleashed an exponential increase in the interest and research on 2D materials. This research lead to the expansion of the number of 2D layered materials and the isolation and growth of these materials.

## 2.1 Graphene

Graphene is the most commonly known and popular 2D material as it has extremely interesting properties. The single layer of graphite is a two-dimensional carbon allotrope, which has a hexagonal honeycomb lattice structure as shown in Figure 2.1(a). [6]

The material is flexible because of elongation of the covalent carbon-carbon bonds. These covalent bonds are also the cause of the strength of the graphene as the Young's modulus goes up to 1 TPa and the tensile strength is about 130 GPa. [7,8] Graphene is a unique example of an extremely thin thermal conductor in the range of 5000 $cm^2(Vs)^{-1}$. [9] The mobility can reach values up to 350.000 $cm^2(Vs)^{-1}$ and it has an optical transparency of 97.7%. [10,11]

However, as a material graphene has major drawbacks due to the absence of a band gap. Graphene must first be modified by means of doping before it can be used in transistor applications. Therefore other 2D materials, such as transition metal dichalcogenides and hexagonal boron nitride, with their diverse properties, are gaining more interest.

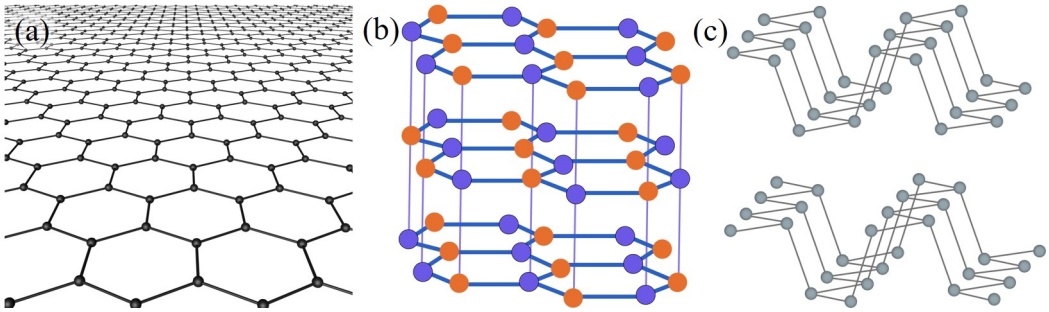


Figure 2.1: Ball stick models of (a) graphene, (b) stacking of 3 h-BN layers and (c) Stacking of 2 black phosphorus layers.

## 2.2 Hexagonal boron nitride

Boron nitride is found in different crystallographic forms such as amorphous, hexagonal and cubic. The most stable crystalline form is the hexagonal boron nitride (h-BN). Hexagonal boron nitride has a layered structure where the crystal lattice is similar to that of graphite, as shown in Figure 2.1(b). Also similar to graphite, h-BN can be thinned down to a monolayer. h-BN is an insulator in its monolayer form, where it is a semiconductor in bulk. In each h-BN monolayer, or basal plane, the atoms are bound by covalent bonds, whereas the layers are held together in the edge plane by weak Van der Waals forces. Similar to graphene the stacking modes of the sheets can be different, though usually the atoms lay eclipsed from each other on the layers with boron atoms placed on top of nitrogen atoms and vice versa.

## 2.3 Black phosphorus

Black phosphorus (BP) or phosphorene consists of a hexagonal lattice of phosphorus atoms, forming a quadrangular pyramid structure.[12] The single layer of black phosphorus, the most stable allotrope of phosphorus, has a corrugated or accordion-like structure as shown in Figure 2.1(c). BP shows a thickness-dependent bandgap energy from 0.3 eV for bulk BP to 2.0 eV for monolayer BP.[13] This large spread in the bandgap indicates that BP holds a wide light absorption ranged from ultraviolet (UV) light to near-infrared (NIR) light, making BP a potential candidate for the optoelectronic applications.[14] Other 2D compounds which are similar in structure to BP are arsenene, antimonene and bismuthene.[15]

## 2.4 Transition Metal Dichalcogenides

### 2.4.1 Physical properties

Transition metal dichalcogenides are a large and varied group of materials, which all abide to the same formula: $MX_2$. In this formula M is a transition metal from the 4-7 or 9-10 group, as metals from these groups can lead to layered $MX_2$-materials,

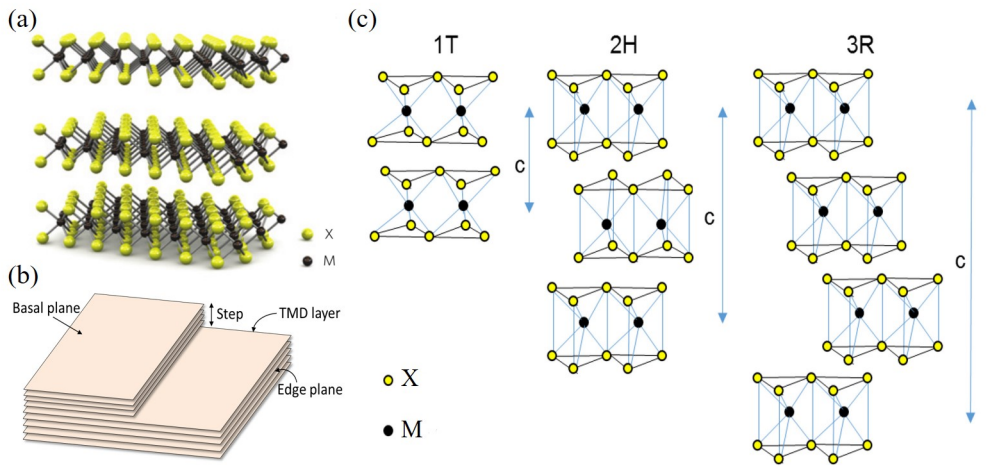


Figure 2.2: (a) Ball stick model of the stacking of 3 individual TMD layers.[18] (b) Illustration of the basal plane and edge plane of a layered TMD material. (c) The 3 different stacking types 1T, 2H and 3R of TMDs.[22]

and X is a chalcogen (sulfur, selenium or tellurium). For this reason, TMDs are also often referred to as $MX_2$-materials. At present over 40 different TMDs are known.[16]

In the monolayer the metal atom is sandwiched with covalent bonds between two chalcogen layers. The different monolayers are kept together by weak Van der Waals forces.[17,18] (See Figure 2.2(a)) A multilayer TMD crystal can be divided in 2 planes: The basal plane and the edge plane. (As shown in Figure 2.2(b)) The basal plane can in theory be an infinitely large sheet, as the edge plane is only a single layer thick. The basal plane has a low chemical reactivity towards atoms attaching perpendicular to the plane due to a lack of reactive sites. In contrast to graphene, where the edge plane is reactive due to the presence of dangling bonds,[19] the properties of the edge plane are dependent on structure of these edges. The edges can have a zigzag or armchair structure.[20] Zigzag edges in 2H $MoS_2$ are calculated to be metallic and ferromagnetic, whereas armchair edges are semiconducting and non-magnetic. The metallic zigzag edges find applications in catalysis, such as hydrogen evolution reaction.[21]

$MX_2$ materials crystallise mainly into thin layered sheets. The materials can crystallise in three different packing structures: the 1T phase with an octahedral symmetry, the hexagonal close-packed 2H phase and the 3R phase which has rhombohedral symmetry. The most common crystal structure in TMDs is the 2H phase, which results in an AbA trigonal prismatic structure. The crystal phase determines the properties of the material, for example the 1T phase of $MoS_2$ is metallic,[17] while the 2H phase of the same material is semiconducting.[22–24] (See Figure 2.2(c).)

Another advantage of TMDs is that they have a relatively low thermal conductivity due to the presence of two different atomic species. The two different species reduce the phonon free path length and thereby reduce the thermal conductivity.[25] This leads to theoretical values of an in-plane thermal conductivity of up to $18\pm2$ $Wm^{-1}K^{-1}$ and an out-of-plane thermal conductivity of $4.2\pm0.4$ $Wm^{-1}K^{-1}$

for $MoS_2$.[25]

The mechanical strength of TMDs is extraordinary in terms of Young's modulus and tensile strength. The theoretical prediction of the value for the Young's modulus of $MoS_2$ is 0.27 TPa[23] which is in good agreement with the experimental value for suspended $MoS_2$ nanosheets, namely 0.33±0.07 TPa.[26]

### 2.4.2 Electronic structure

TMDs have either (semi-)metallic or semiconducting properties depending on their composition and structure.[27] (See Table 2.1) The different intrinsic properties can be explained when the symmetry point group and the filling of d-orbitals in the transition metal are taken into account as a function of the group number.[16] Crystal field theory (CFT) explains the splitting of the d-orbitals in a high- or low-spin splitting.

To demonstrate the crystal field splitting $WSe_2$ is used as an example. Tungsten is a group 6 element and therefore has 4 d-electrons ([Xe] $4f^{14}$ $5d^4$ $6s^2$) and is surrounded by a $D_{3h}$ coordination environment.[16] (See Figure 2.3(a) and (b)) In $WSe_2$ tungsten has a $d^2$ conformation as 2 d-electrons of tungsten react to form $\sigma$-bonds with 2 selenium atoms.

Another interesting electronic property of TMDs is the tuneable band gap. During the thinning of the number of layers from bulk to monolayer, the bandgap increases and transitions from indirect to direct in some TMDs such as $MoS_2$ and $WS_2$. This shift originates from quantum confinement effects, effects due the spatial confinement of electron–hole pairs, present in mono- and few layers of TMDs and the loss of crystal symmetry.[31,32] The change in the band structure is depicted in Figure 2.3(c).

The direct bandgap in monolayer material allows for applications such as transistors, photodetectors and electroluminescent devices. As the direct band gap increases the quantum efficiency, thereby converting more electrons which can be harvested for use in solar cells.[33] The direct band gap in TMD monolayers provides a major advantage over graphene as these monolayers can be implemented in

| Material | Type | Band gap monolayer | Band gap bulk | Mobility (theoretical) |
|---|---|---|---|---|
| Graphene | semi-metallic | N/A. | N/A. | 200,000 $cm^2(Vs)^{-1}$ |
| $MoS_2$ | semi-conducting | 1.8 eV | 1.2 eV | 340 $cm^2(Vs)^{-1}$ |
| $WS_2$ | semi-conducting | 2.1 eV | 1.4 eV | 1103 $cm^2(Vs)^{-1}$ |
| $MoSe_2$ | semi-conducting | 1.5 eV | 1.1 eV | 240 $cm^2(Vs)^{-1}$ |
| $WSe_2$ | semi-conducting | 1.7 eV | 1.4 eV | 705 $cm^2(Vs)^{-1}$ |
| $PtSe_2$ | semi-conducting | 1.2 eV | 0.21 eV | 4000 $cm^2(Vs)^{-1}$ |
| BP | semi-conducting | 2.0 eV | 0.3 eV | 10,000 $cm^2(Vs)^{-1}$. |
| h-BN | insulating | 5.4-6.0 eV | 5.6-6.0 eV | N.A. |

Table 2.1: Overview of different 2D materials and their properties. Adapted from Das *et al*,[28] Wang *et al*,[29] and Ling *et al.*[30]

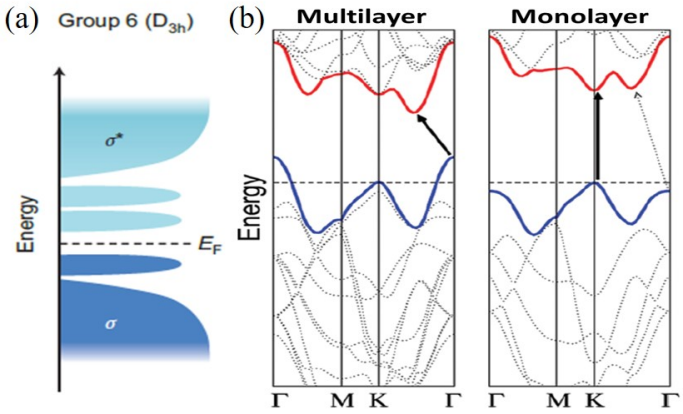


Figure 2.3: (a) Filling of d-orbitals located within the bandgap of bonding ($\sigma$) and anti-bonding states ($\sigma^*$) in group 6 TMDs.[16] (b) Shift in electronic band structure of $MoS_2$ from bulk to monolayer.[31]

transistor devices without the need for doping.

### 2.4.3 Applications

TMDs are of interest due to their anisotropic electronic and mechanical properties, bond-free interfaces, layer dependent properties and exceptionally large surface-area-to-volume ratios. 2D TMDs have also a large variety in different material properties and potential applications, depending on the choice of metal and chalcogen.[17,34–36]

#### Field effect transistors

Most monolayer TMDs are semiconductors, with bandgaps similar to that of silicon. The band gaps of the TMDs can often be tuned by changing their layer number, making them strong candidates for applications in nanoelectronics.[37] The monolayer nature of TMDs allows superior gate control of the channel. This property can be used to reduce the power consumption of current integrated circuits and potentially in architectures such as tunnelling field-effect transistors (TFETs). In 2011 top-gated $MoS_2$ FETs with moderate mobilities ~60-70 $cm^2$ $(Vs)^{-1}$, large on/off ratios (~$10^8$), and low sub-threshold swings were shown at room temperature.[18]. The addition of a top gate dielectric to a TMD device allows superior gate control, thus enabling small off-currents and large switching ratios.[38,39].

TMDs are also very attractive for use in flexible electronics due to their stability. A number of works have demonstrated high performance $MoS_2$ field-effect transistors (FETs) on flexible substrates.[40,41]

#### (Opto-)electronics

TMDs have also shown promise in the field of opto-electronics. Due to their tunable bandgap, strong light matter interaction and viability for use in atomic heterostructures. TMDs have found applications in photodetectors, photovoltaics, and

light-emitting devices. They have been implemented in photodetectors with low dark currents, high responsivity and fast switching speeds over a wide spectral range.[42–44] As many TMDs are direct bandgap semiconductors in their monolayer form, with high photoluminescence efficiency, they are well suited for use in LEDs.[45] In photovoltaics TMDs show promising results under both laser radiation as well as visible light, there have also been applications of TMDs in flexible photovoltaic devices.[46,47]

Modifying TMDs, through chemical functionalisation, doping or plasma treatments, further broadens their range of potential applications. These treatments have been investigated in the context of (opto-)electronic devices though it is important to note that any modification to the TMD device can have a large impact on the electrical properties of the device.

### Other applications

Other possible applications of TMDs are resistive switching,[48] energy storage, sensing[49] and catalysis.[50] Resistive switching has been observed in various TMDs and other 2D materials and these memristors are among others of interest for potential use in memory technology and neuromorphic computing.[51–53] The atomically layered structure, large specific surface area and electrochemical properties are features which make 2D TMDs attractive for energy storage.[54,55]

TMDs have also been successfully implemented as sensors for bio-molecules.[56,57] As gas sensors, TMDs have been shown to be competitive with the state of the art for certain analytes.[58,59] These materials have also shown promising catalytic behaviour for water splitting and $CO_2$ photoreduction.[60,61] For applications such as sensing and catalysis chemical functionalisation is especially relevant. 2D materials are particularly suited to functionalisation due to their exceptionally large surface-area-to-volume ratio.

# 3 Semiconductors

## 3.1 Band structures

In solids, orbitals of individual atoms overlap creating energy bands with different energies and electron fillings. Three different types of materials can be distinguished by their band structures: conductors, semiconductors and insulators. In a conductor, or metal, there is a free flow between the valence band (VB), the last band filled with electrons, and the conduction band (CB), the first empty band, as these bands overlap. The overlapping bands mean that the Fermi level ($E_F$), the top energy level electrons can reach at 0 K, falls within an energy band. The opposite is valid for insulators. Insulators have no available energy states as there is a large band gap between the VB and CB which cannot be overcome by electrons and is therefore referred to as a forbidden gap. The last type of material is the semiconductor. In a semiconductor a band gap is present, though this gap is small enough that electrons can bridge this gap when excited, creating available energy states. For an overview of the band structures of the different materials see Figure 3.1.

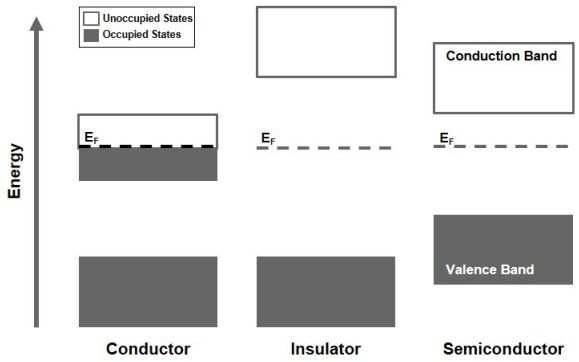


Figure 3.1: Band structure of solids. Band structures of a metal, insulator and semiconductor respectively

## 3.2 Mobility

A very important characteristic of a semiconducting material is its carrier mobility ($\mu$). The carrier mobility refers to the electron mobility or the hole mobility, in the absence of electrons. Mobility can be viewed as the ease with which a carrier can move through the material under an applied field. $\mu$ is a material constant

which relates directly to the movement of carriers to the applied field. When an electric field (E) is applied across a material, electrons (or holes) are accelerated to an average velocity, called the drift velocity ($v_d$). These charge carrier concentrations are influenced by intrinsic properties as well as doping. In a vacuum, an applied field will accelerate the electron in the electric field. However, scattering from ions, crystal defects or phonons or other impurities slows down the carrier. The mobility is given by Equation 3.1:

$$v_d = \mu E \tag{3.1}$$

In ambipolar materials both electrons and holes contribute to the conductivity of the material, therefore both the electron mobility ($\mu_e$) and hole mobility ($\mu_h$) should be taken into account. This leads to the total conductivity given by:

$$\sigma = e(n\mu_e + p\mu_h) \tag{3.2}$$

In this equation $e$ is the elementary charge, $n$ is the number density of electrons, and $p$ is the number density of holes. As $\mu$ is directly related to $v_d$, which in its turn is heavily dependent on scattering events, controlling the different types of scattering is a possible way of investigating $\mu$ in a material. Many measurements use a cryostat to measure $\mu$ as a function of the temperature.

## 3.3 Doping

Doping is the process of introducing a minuscule amount of foreign atoms in the crystal lattice of a semiconductor to produce a p- or n-type semiconductor, which influences the conductivity of the semiconductor.

In p-type doping an impurity, which has an electron deficiency in comparison to the intrinsic semiconductor, is introduced. This deficiency causes additional holes in the band gap, creating an acceptor level, which allows excitation of valence band electrons, thereby lowering the Fermi-level. These excitations leave mobile holes in the valence band.

In an n-type doped semiconductor an impurity which has an additional valence electron compared to the intrinsic semiconductor is introduced. This additive creates an extra electron energy band, or donor level, just below the CB, which decreases the band gap and improves the conductivity of the semiconductor. In Figure 3.2 both the band structures of n-type and p-type semiconductors are shown.

## 3.4 pn-Junctions

A pn-junction is an interface between a region with electrons as carrier, a n-type semiconductor, and a region filled with holes as carrier, a p-type semiconductor. In Figure 3.3 the band diagram for a typical pn-junction is shown. When no voltage is applied to the system the Fermi-level must be equal throughout the system. This

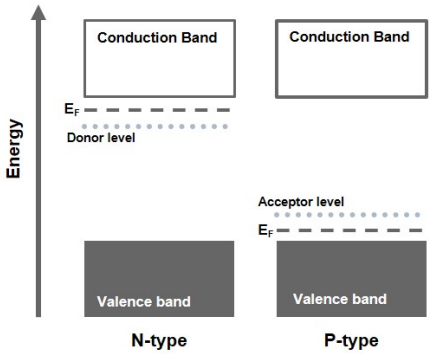


Figure 3.2: Band structures of n- and p-type doped semiconductors

results in a depletion region of the charge carriers at the interface between the different regions of the p-n junction.

When a forward bias is applied to the system, the p-type material is biased positively with respect to the n-type. This reduces the built-in potential at the junction and thereby lowers the barrier to the charge carrier conduction. As the barrier is lowered, an increased amount of charge carriers on both sides gain enough energy to cross, causing an exponential increase in the current. If the junction is reverse biased, the built-in potential increases, meaning very little current flows through the system, only a low level of drift current. This current is present until the break-down voltage of the junction is reached, where the material does not conduct any more.

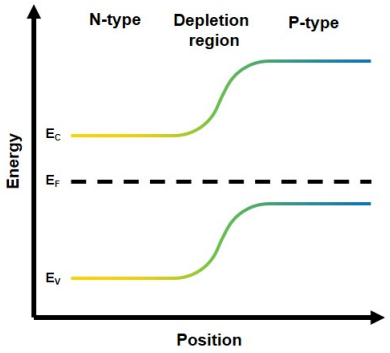


Figure 3.3: Energy band diagram of a pn-junction. The energy of the valence band maximum ($E_V$) and conduction band minimum ($E_C$) and the Fermi level ($E_F$) are plotted as a function of the position.

## 3.5 FET

A field effect transistor (FET) is a type of transistor where the flow of the current is modulated through the transistor. A FET consists of a channel of n- or p-doped semiconductor material through which the current can flow and the gate allows or blocks the flow of electrons between the source and the drain.[62] The devices have

three terminals: source, gate, and drain and are unipolar transistors as they are a single-carrier-type device.

FET is a collection of different types of transistor devices such as junction field-effect transistor (JFET), metal oxide semiconductor field effect transistor (MOSFET), metal semiconductor field effect transistor (MESFET) and a tunneling field effect transistor (TFET).

### 3.5.1 MOSFET

A metal oxide semiconductor field-effect transistor is based on the modulation of charge concentrations generated by a metal oxide semiconductor (MOS) capacitance.[63] This includes two terminals, a source and drain, which are each connected to separate highly doped regions. These regions are typically denoted by 'N+' or 'P+' depending on the type of doping. The two regions are separated by a slightly doped region of the opposite type, referred to as the body. The body is denoted, 'N' of 'P', for the type of doping. The active region constitutes a MOS capacitance with a third electrode, the gate, which is located above the body and insulated from all other regions by an oxide layer.

There are broadly speaking 2 kinds of MOSFETs: nMOSFET and pMOSFET depending on the doping of the device. In a nMOSFET the source and drain are 'N+' regions, while the body of the device is a 'P' region. When a positive gate-source voltage is applied an n-channel is formed at the surface of the 'P' region, just below the oxide layer, by depleting the body region of holes. The channel extends between the source and drain, but the current is only conducted through the channel when the gate voltage is high enough to attract electrons from the source and the drain. When zero or negative current is applied between the gate and source the channel disappears and the current cannot flow between the source and drain.

In contrast to the nMOSFET in the pMOSFET the source and drain are 'P+' regions and the body is a 'N' region. When a negative gate-source voltage, a positive source-gate, is applied it creates a p-channel at the surface of the 'N' region, just below the oxide layer, by depleting the body region of electrons. The current is only conducted through the channel when the gate voltage is low enough to attract holes from the source region into the channel. When a near-zero or positive voltage is applied between the gate and body, the channel disappears and there is no current flow between the source and drain.

## 3.6 Heterostructures

A heterojunction or heterostructure is the interface between two regions, or layers, of dissimilar crystalline materials. This can mean a lateral interface, where the regions are in the same basal plane or horizontally stacked, or a vertical interface, in which case the regions are stacked in a vertical manner. A last possible interface is an alloy, in which the different materials have blended. The different interfaces or

heterostructures can be seen in Figure 3.4)

In semiconductor devices heterostructures are widely used to create p-n junctions from different materials or to create quantum wells by stacking materials with different bandgaps.[64] Heterostructures provide higher band-to-band tunnelling current as the distance from the conduction band to the valence band is smaller than in a homogeneous structure, reducing the field strength required for high currents and are therefore fundamental building blocks for electronic devices.[65] Currently group III-V semiconductors such as GaSb/InAs[66], InAs/InSb[67] and InP/InGaAs[68] are used for heterojunctions.

2D materials are also applicable for the formation of heterostructures. In 2010 the first 2D heterojunctions of graphene and h-BN were reported.[69] Heterojunctions of 2D materials have an advantage over bulk materials as 2D materials do not have dangling bonds on the basal plane and are kept together with weak Van der Waals forces. Therefore overcoming limitations due to lattice match mismatch in vertically stacked heterostructures, as is often the problem in 3D heterostructures. 2D heterostructures also create clean atomically sharp interfaces. These structures are fundamentally different and more flexible than traditional III-V heterostructures. Due to the high photon excited carrier generation and collection efficiency, TMD heterojunction based photodetectors exhibit high photoresponsivity and increased response speed.[42]

### 3.6.1 Heterojunction types

Heterojunctions can be classified into 3 different types. type I, a straddling gap junction, type II, a staggered gap junction, and type III, a broken gap junction. The different types are shown in Figure 3.5. Due to the variation in the gaps between the different types, these all have different applications. Type I has applications in opto-electronic devices such as light emitting diodes (LEDs), where type II is used for photovoltaic devices and type III finds applications in field effect transistors.

In a type I, straddling gap, junction the bandgap of the smaller gap material is completely contained in the bandgap of larger gap material. Resulting in $E_{V_1} < E_{V_2}$ while $E_{C_1} > E_{C_2}$. Type I heterojunctions result in ultrafast recombination between electrons and holes, making the junction suitable for opto-electronic applications. Examples of 2D material heterojunctions where type-I alignments can be formed are

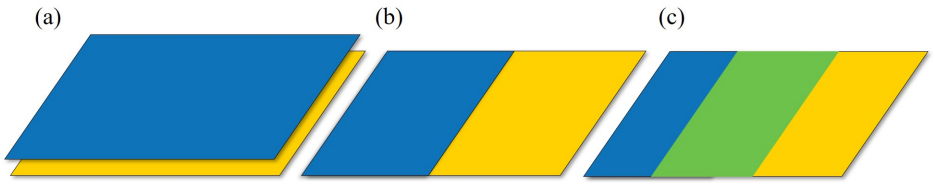


Figure 3.4: The three different types of heterostructure interfaces. (a) A vertical interface or vertical stack, (b) A horizontal or lateral stacking of the materials and (c) Alloying of the materials at the interface shown in green.

$WSe_2$/BP and MoSeTe-Te/$Ca(OH)_2$.[70–72]

In a type II band gap alignment, the conduction band and valence band of the second semiconductor are both lower than the conduction and valence bands of the first semiconductor. In this staggered gap, the band gap of the second semiconductor is not restricted to being smaller than the first semiconductor as is the case for the type I alignment. So $E_{V_1} > E_{V_2}$ while $E_{C_1} > E_{C_2}$. The type II aligned heterojunctions can easily promote electron and hole-carrier transfer and separation at the interface, which enhance the efficiency of photovoltaic solar cells.[73] Combinations of the most commonly synthesized TMDs ($MoS_2$, $WS_2$, $MoSe_2$ and $WSe_2$) form type II heterojunctions.

Finally in a type III, broken gap, alignment the band gaps partially overlap between the valence band of the first semiconductor and the conduction band of the second semiconductor. $E_{V_1} > E_{V_2}$ while $E_{C_1} > E_{C_2}$ and $E_{V_1} < E_{C_2}$. The conduction band electron states on the n-type material are more or less aligned with valence band hole states on the p-type material. Due to this overlap the junction has a negative resistance and facilitates a high electron tunneling efficiency. For 2D heterojunctions this has been shown for various stacks such as BP/$SnSe_2$, $WTe_2$/$MoS_2$ and $SnSe_2$/$MoTe_2$.[74–76]

### 3.6.2 Vertical heterostructures

Previously the different kinds of heterostructures were introduced. A vertical heterostructure has a Van der Waals stacking, as the different TMD layers are kept together by the Van der Waals forces between the individual layers. This stacking should result in a straightforward combination of the different TMDs. Emergent properties can arise in vertical heterostructures depending on the stacking order of the 2D materials.[77,78]

An example of this is the stacking of $MoS_2$ and $WS_2$ when the TMDs are stacked with $MoS_2$ on the bottom and $WS_2$ on top, a $MoS_2$/$WS_2$ stack, the stack shows a higher level of catalytic activity, compared to the reversed $WS_2$/$MoS_2$ stacks.[79] The formed heterostack is a type II junction, in this junction the spatial separation of photogenerated electron–hole pairs is enhanced. The stacking of the materials

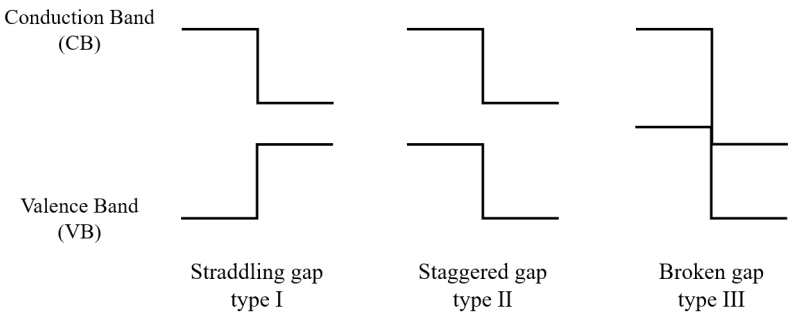


Figure 3.5: The three different types of heterojunctions, Type I, a straddling gap, type II, a staggered gap and type III, a broken gap junction.

is possible due to the small lattice mismatch and the weak Van der Waals forces between the layers diminishes the effect of any mismatch, also aiding the stacking.

### 3.6.3 Lateral heterostructures

TMDs are perfect building blocks for heterostructures as the interlayer Van der Waals forces should result in an easy combination of the different TMDs. This combined with the small lattice mismatches between different TMDs results in a perfect material to make both lateral and vertical heterostructures. Lateral $MoS_2/WS_2$ structures can result into localized photoluminescence enhancement as well as the formation of intrinsic p–n junctions,[80] though $MoS_2/WS_2$ lateral structures more often find applications in photonics.[81–83] Where lateral structures containing both p- and n-type TMDs, such as $MoSe_2/WSe_2$, find more applications in pn-junctions.[84]

# 4 Synthesis of TMDs

## 4.1 Synthesis

Several methods for the synthesis of TMD materials are known. The different methods all yield materials with different quality specifications, therefore the synthesis method defines the applications of the material. In this section the most commonly used synthesis methods will be discussed. In general these methods can be subdivided into two categories: top-down and bottom-up methods. Top-down methods start from bulk (or multilayer) material and attempt to isolate mono-layer (or few layer) material by application of external energy. In contrast, bottom-up methods can be defined as methods which start from (atomically) small building blocks and attempt to synthesize the 2D material from these blocks.

### 4.1.1 Mechanical exfoliation

Mechanical exfoliation, or the Scotch tape method, is the oldest and best known method to produce 2D materials and has so far produced the best quality 2D materials. This method is a top-down method and was first described for the isolation of 2D materials by Novoselov and Geim for the isolation of graphene monolayers but the method can also be applied for the isolation of monolayer TMDs.[5] The TMD layers, which are held together by weak Van der Waals forces, are exfoliated using adhesive tape. The weak Van der Waals forces are broken by the mechanical force, creating a thinning of the number of layers. Repetition of this process results in a reduced number of layers until a monolayer is isolated.

A large drawback of this method is the limited flake size. The size of monolayer flakes that are obtained by this technique are in the order of 1–50 $\mu$m on $SiO_2$/Si.[28,85] Larger flakes have been exfoliated on metal substrates, though the applications of TMDs on metal substrates is limited.[86] Another disadvantage of mechanical exfoliation is the inability to control the size and location of the material on the surface. These drawbacks cause the method to be unsuitable for use in electronic applications. Nevertheless, the quality of mechanically-exfoliated material is outstanding and is often used in research as a benchmark for other production methods.

### 4.1.2 Liquid phase exfoliation

As the name would suggest liquid phase exfoliation (LPE) is an exfoliation method in which the exfoliation occurs with the bulk material dispersed in a liquid. This method is more scalable and has a higher yield than mechanical exfoliation. Liquid-exfoliation methods are especially suited for applications where individual flakes are not required and few layer TMDs suffice. For example in energy storage, catalysis or solar cells. This method is also suitable for mass production of thin TMDs.

The most commonly used solvents for liquid phase exfoliation are N-methyl-2-pyrrolidone (NMP), dimethyl formamide (DMF) and tetrahydrofuran (THF).[87–89] Different techniques for liquid exfoliation of 2D materials are available. Most LPE techniques are based on sonication of the multilayer material but other techniques (especially for graphene[90]) are based on thermal shock detachment of the monolayers.[91]

Direct sonication techniques rely on the solvent or surfactant to overcome the cohesive energy between the adjacent layers; therefore the surface energies of the solvents must be similar to those of the material as to minimise the enthalpy of mixing ($\Delta H_{mix}$).[88,92] A large issue with this method is that sonication can lead to tearing of the individual layers and results in a large variation in layer thickness. Therefore control of the sonication parameters and centrifugation parameters is essential to yield large and thin TMD layers.[92]

In thermal shock techniques the exfoliation mechanisms are based on vaporization of ions intercalated in between the monolayers. When the ions vaporize, the monolayers are forced apart. An example of ion intercalation is lithium-intercalation.[93,94]

### 4.1.3 Atomic layer deposition

Atomic layer deposition (ALD) is a vapour deposition method where a minimum of two vapour phase precursors sequentially react at the surface in a self-limiting manner. The ALD principle was first demonstrated in 1989 by Tuomo Suntola.[95] who used ALD for the synthesis of zinc sulfide (ZnS). Currently ALD is generally used for the synthesis of thin layer insulators such as $Al_2O_3$ and $HfO_2$.[96–98]

A basic ALD cycle consists of a saturating pulse of precursor A, an evacuation by purging of the reactor, a saturating pulse of precursor B and subsequent evacuation of the reactor. This cycling is repeated until the desired amount of material is deposited. ALD has been successfully applied in the deposition of many materials including $MoS_2$ and $WS_2$.[99–101]

A large advantage of ALD is that the reactions occur at relatively low temperatures, compared to other vapour deposition methods, and leads to atomically thin layers. Unfortunately achieving self-limiting ALD deposition sequences is very difficult due to the wide range of parameters which must be optimised, often leading to rough surfaces with small grain sizes.

### 4.1.4 Thermally assisted conversion

In thermally assisted conversion (TAC), or thermally assisted chalcogenisation, a layer of transition metal is deposited on the surface by a physical vapour deposition (PVD) method, such as sputtering or evaporation. The metal layer is subsequently converted to a TMD by heating it in a furnace under a chalcogen-containing vapour flow.

The TAC process can result in the production of large-scale polycrystalline TMD that has a few- to multilayer thickness with grain sizes in the order of 10-100 nm.[102] The TAC growth method is a straightforward technique to prepare large-area films.[103] TAC growth is mainly used for the synthesis of sulfur-based TMDs, which has as a general formula for the reaction:

$$M(s) + 2S(g) \rightarrow MoS_2(s) \tag{4.1}$$

This reaction can already occur at 550 °C and has been demonstrated to result in large-area $MoS_2$ .[103–105] Instead of using the metal, the metal oxide can also be used as a precursor (e.g. $MoO_3$ for $MoS_2$). When the metal oxide is used the sulfurization of the substrate already occurs at 650 °C.[106] The reaction mechanism differs from the sulfurization of the metal film as the sulfur vapour first reacts with the oxide to form a sulfoxide and a metal sub-oxide, see Equation 4.2. After which the sub-oxide reacts with the sulfur to form the TMD, shown in Equation 4.3.[106]

$$MoO_3(s) + S(g) \rightarrow MoO_{3-x}(s) + SO_x(g) \tag{4.2}$$

$$MoO_{3-x}(s) + 3S(g) \rightarrow MoS_2(s) + SO_{3-x}(g) \tag{4.3}$$

For the formation of selenium TMDs the process is slightly more difficult as the chemical reactivity of selenium (Se) is much lower compared to that of most sulfide TMDs as the oxidation state needs to be reduced to +IV. However, the formation of $WS_2$ also requires a reducing agent for surface activation, as there is insufficient reduction of $WO_3$ during growth. Therefore a reducing agent is necessary for the sub-oxide formation of selenide TMDs and $WS_2$.[107,108] Hydrogen ($H_2$) gas is most commonly used as a reducing agent for this purpose, which leads to the following total reaction[109]:

$$WO_3(s) + 3Se(g) + H_2(g) \rightarrow WSe_2(s) + H_2O(g) + SeO_2(g) \tag{4.4}$$

A further decrease of the reaction temperature is possible through the use of chalcogen plasma or the use of halides to decrease the energy barrier.[110] Synthesis of (single crystalline) monolayers is very difficult using the TAC approach. The resulting film also has a very high polycrystallinity due to the granularity of the starting material, which makes the material interesting for applications in which a large surface area is required such a catalysis.[58,111]

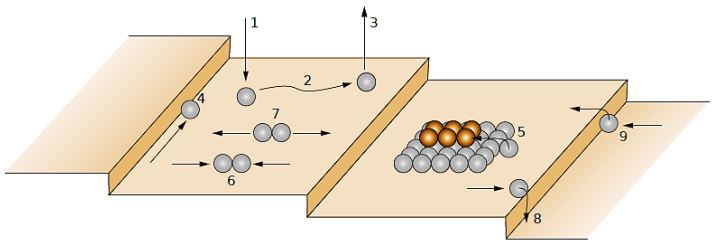


Figure 4.1: Representation of the different processes which can take place on a surface during CVD deposition: 1) Adsorption, 2) Surface diffusion, 3) Desorption, 4) Edge diffusion, 5) Transformation from mono- to bi-layer island, 6) Dimer formation, 7) Dimer decay, 8) Step-down hopping, 9) Step-up jump. Adapted from Dhanaraj *et al.*[114]

### 4.1.5 Chemical vapor deposition

Chemical vapour deposition (CVD) is a process whereby a thin solid film is deposited onto a substrate through chemical reactions of the gaseous species in the reaction chamber.[112] The technique combines reactions in the vapour phase of the chamber with surface reactions at the substrate.[113] For the synthesis reagent gases are simultaneously introduced into the chamber. CVD can be incorporated in a industrial production flow, though high growth temperatures offer a challenge for integration with current silicon technologies as only processes below 450 °C are compatible with Si technology. Still the high throughput and material quality obtained by CVD make it a promising method for production of large-area 2D materials.

Many processes are involved in CVD such as: Transport of precursor molecules to the surface where they adsorb, diffuse and react and the incorporation of reacted precursor molecules into the crystal lattice and removal of by-products.[114] These processes are depicted in Figure 4.1. We cannot directly influence these processes. Therefore, controllable parameters must be defined and adjusted. CVD processes can be classified based on these adjustable parameters. For instance: Temperature, pressure, energy source and deposition time.[112] Usually only one of the parameters is used for the abbreviation of the specific CVD method, e.g. PECVD for plasma enhanced CVD, but unfortunately a CVD process is defined by every change in each parameter. In practice the choice of parameters is often based on practical considerations and defining one parameter will decide and influence other parameters.

The different CVD methods lead to different materials with different purposes. There is the synthesis of flat single crystal monolayers,[115] to full multi crystalline coverage synthesis of $MoS_2$ across sapphire[116,117] or electrically compatible substrates like $SiO_2$/Si.[118]

#### CVD processes for TMDs

As mentioned above depending on the reaction parameters different CVD processes can be identified. Optimisation of these parameters will result to the growth of TMDs. The surface processes are dependent on the CVD precursors and reaction

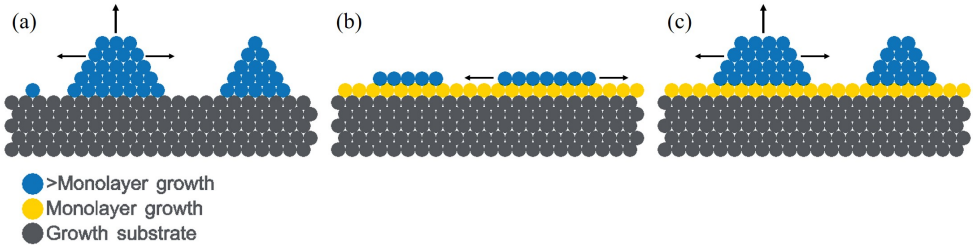


Figure 4.2: Depiction of the different growth modes. (a) Volmer-Weber island formation growth, (b) Frank-Van der Merwe layer-by-layer growth and (c) Stranski-Krastanov monolayer with island growth.

parameters and can be tuned to enable targeted synthesis for desired applications. Ranging from extended uniform thickness films over a sample, large few layer crystalline material with varying thickness or very high quality isolated single crystals for fundamental studies.[119]

### Growth modes

In chemical vapour deposition three primary growth modes can be distinguished for the growth of thin film layers: Volmer-Weber growth,[120] Frank-Van der Merwe growth[121] and Stranski-Krastanov growth.[122] (See Figure 4.2) The optimal growth regime is the Frank-Van der Merwe growth mode as this growth mode results in a layer-by-layer growth, though Volmer-Weber and Stranski-Krastanov growth are more common.

In Stranski-Krastanov growth mode a monolayer is grown until full coverage of the monolayer is achieved after which the growth continues as island growth on top of the monolayer, while the Volmer-Weber growth mode is a full island growth mode where different multilayer islands are formed. In this mode layered individual islands with different thicknesses are formed. The different islands can stitch together and form a large layer if they come into contact. The growth of islands of CVD TMDs is limited by surface diffusion of adatoms or the diffusion of atoms in the vapour phase.[123]

When different island domains interconnect the fusion of the domains is dependent on the orientation of the different islands. If the domains have the same rotational alignment the domains will coalesce into a single crystal, though more often there is a mismatch in the orientation of the different domains resulting in the formation of grain boundaries.[115]

### Nucleation

In general the reaction of a gaseous reagent will lead to precipitation of the reagent on the surface. On this surface the molecules adsorb to the substrate, migrate on the surface and aggregate, forming a crystal nucleus. This process is defined by the surface mobility of the adsorbed species/atoms (adatoms) and competitive processes, like desorption.[114]

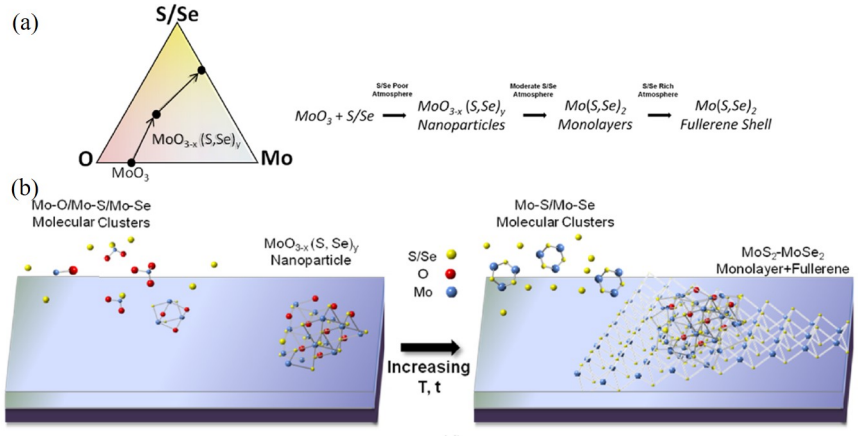


Figure 4.3: Possible reaction mechanism of TMD growth. (a) Phase diagram and reaction taking place during CVD process. (b) Illustration of the metal nucleus cluster formation followed by TMD growth.Adapted with permission from Cain *et al.* Copyright 2016 American Chemical Society[127]

Nucleation can be influenced by different processes. Pre-treatment of surfaces is a process that can facilitate nucleation. When enhancing the wettability by use of surface treatment the free energy required for nucleation is diminished. A possible way to improve the wettability is to increase the hydrophilicity of the surface. $SiO_2$ can be made more hydrophilic by an oxygen plasma treatment.[124] Another surface treatment that enhances the wettability of the surface is the deposition of graphene-like aromatic molecules such as perylenes.[106,125]

In contrast to improving the growth by use of the cleaned oxygen treated substrates, nucleation of TMDs can be improved by adding step edges. Nucleation is preferred at step edges due to the reduced energy barrier at the edges according to Najmaei et al.[126] By creating step edges, for example by use of lithographic processes, growth could be controlled and optimised to obtain large-area coverage.

For the CVD growth of TMDs the knowledge of the nucleation is very limited and therefore mainly based on speculation. STEM images taken by Cain et al.[127] indicate that the nucleation centre of CVD flakes is formed by a 10-30 nm core/shell structure consisting of a partially sulfurised or selenised molybdenum trioxide core ($MoO_{3-x}$(S,Se)$y$) which is wrapped in a fullerene like shell of the corresponding TMD. Based on this observation a nucleation and growth mechanism was proposed (See Figure 4.3). According to this mechanism evaporation of molybdenum oxide in a chalcogen poor environment leads to the formation of condensed $MoO_{3-x}(S,Se)_y$ clusters on the surface which react further to monolayer $Mo(S,Se)_2$ in a moderate chalcogen atmosphere to $MoO_{3-x}(S,Se)_y$ monolayers. When the temperature, and chalcogen concentration further increases the transformation of the TMD will be completed, resulting in a fullerene core/shell structure nucleation centre.[127]

#### Defects

Defects are common features in CVD grown TMDs, especially in monolayers. One of the most common defect in TMDs are chalcogen vacancies. $MoS_2$ often have a substantial amount of sulfur vacancies giving them a S:Mo ratio of <2.10.[128] Other defects are grain boundaries formed between flakes, when the flakes merge to form a larger domain while having a different orientation. Controlling the growth parameters can reduce the presence of grain boundaries by aligned growth of flakes by use of a crystalline substrate, such as sapphire, or by lowering the nucleation, thereby ensuring the growth of less individual domains.[116,129] To date large uniform CVD films of TMDs are still polycrystalline, consisting of many different domains with grain boundaries. Chalcogen vacancies in TMD materials have effect on the scattering, the stability and charge traps in the material, where grain boundaries are detrimental to properties such as carrier mobility.[126]

## 4.2 CVD Growth of Heterostructures

TMD heterostructures are constructed by vertical stacking or lateral stitching of TMDs. This synthesis can be done by methods such as mechanical exfoliation, TAC and CVD. For the scope of this thesis only CVD synthesis methods will be discussed.

To synthesise these 2D heterostructures by CVD two synthesis approaches can be distinguished: direct and indirect synthesis. In direct growth the heterostructure is directly synthesized during the fabrication of the materials, while indirect fabrication requires an extra step after the synthesis of the materials. This extra step is usually transfer of one of the materials on the other to form a stack.

The main challenge in heterostructure synthesis is to achieve controllable growth of the heterostructures. The formation of alloy regions as well as unwanted nucleation influence the properties of the heterostructure. Another important factor for vertical TMD stacks is interlayer coupling, which indicates the interaction between the layers.

### 4.2.1 Indirect synthesis

Indirect synthesis is a straightforward way to create heterostructures. TMDs are individually synthesised by CVD after which the TMDs are transferred on top of each other to create a heterostructure. This transfer process is similar to mechanical exfoliation. The first TMD heterostructures were created via this approach by exfoliating and stacking of various TMDs. Often this method is still used to form heterostacks by stacking mechanically exfoliated TMDs materials[34,130,131], though stacks from LPE TMDs have been shown in literature as well.[132] CVD grown TMDs can also be stacked with this approach.[133]

This method allows for the combination a large variation of different TMDs and other 2D materials.[131] Individual materials can be selected and stacked on top of each other to form vertical heterostructures. This in contrast to other methods

where the possibility to form heterostructures also depends on material properties and tool limitations. Heterostructures formed by means of transfer are likely to introduce impurities or strain at the interface between layers, leading to reductions in the interactions between the layers.[134] Another large disadvantage of this method is that, similar to mechanical exfoliation, the stacking is a labor and time intensive process and is therefore mainly suitable for proof of concept purposes.

### 4.2.2 Direct synthesis

Direct synthesis of heterostructures does not require a transfer of the TMDs, which minimises the chance of foreign contamination originating from the transfer such as polymer and solvent residues. In direct synthesis a difference between two approaches can be made: single or double step approach. The double step approach requires two (or more) subsequent furnace runs to be performed to form the different TMDs, where the single step approach only requires a single furnace run to form the heterostructures. In the double step approach the sample is taken out of the vacuum atmosphere in between the different synthesis steps, therefore exposing it to oxidants and other contaminants, where there is no disruption of the vacuum in the single step synthesis. The double step synthesis does offer advantages do to better control over individual growth parameters and larger possible combinations of TMDs.

### 4.2.3 Double step synthesis

In double step synthesis multiple synthesis process steps are required to form the different TMDs, as each TMD is formed by an individual synthesis process. Different combinations of TMDs can be synthesized as heterostructures with few limitations from the precursors or from tool constraints, therefore this method can lead to a large variation of different heterostructures since different furnace set ups can be used for the distinct synthesis runs. Parameters are adjusted for the growth of each individual TMD and are not influenced by conflicting growth parameters for the other TMD.

Both vertical and lateral $MoS_2/WS_2$ heterostructures can be synthesised by this method as demonstrated by Yoo *et al* who controlled the in-plane and out-plane growth by controlling the purity of the initially grown TMD layer.[135] The growth of $NbS_2/WS_2$ is both lateral and vertical direction has also been shown to be dependent on the reaction parameters.[136]

This growth approach allows for patterning of the initially grown material, therefore allowing directed growth of the second material. The double step growth method is a more flexible process, compared to the single step approach, though this is often achieved at the expense of interface quality.

### 4.2.4 Single step synthesis

In the single step synthesis a single furnace run is performed to create the heterostructure. This requires the reaction parameters to be optimised for both TMDs and more process control is needed to form the preferred heterostructures. Often the choice of TMDs is limited by the tool, as cross contamination of the furnace is possible. The advantage of the single-step synthesis is the minimization of oxidation and the formation of defects at the interface as the system vacuum remains intact during the whole process, though the control over the growth is limited. [80]

Single step formation of heterostructures can be achieved by mixing the different metal precursors, [137] individual introduction of the different precursors, [138] or changes in the temperature regime. [79] This methods can result in selective growth of materials to form heterostructures. The formation of both vertical and lateral heterostructures have been shown, possible reasons for the selective growth of this is due to the control of nucleation sites. [135] These can be controlled the temperature or due to the choice of carrier gases. [80,139]

# Part III

# Experimental details

# 5 Experimental details

## 5.1 Materials & Methods

### 5.1.1 Growth substrates

The CVD growth of 2D materials requires a growth substrate as the 2D films cannot exist freestanding. The growth substrate can influence the growth mechanism and the quality of the material. Epitaxial or directed growth of thin films is possible on highly crystalline substrates where there is only a small lattice mismatch between the substrate and the synthesized material.[140] Epitaxial growth has the advantage that it can lead to highly crystalline substrates with large grain sizes. Another important aspect of a growth substrate is the compatibility of the substrate with the desired application of the material.

In this work, the main interest is in the use of TMDs for electronic applications, therefore a semiconducting or insulating material would be optimal. As the TMDs are grown by a CVD process, the growth substrate should also have a high thermal stability. Finally, the substrate must be a commercially available material.

#### Silicon dioxide

Thermally grown silicon dioxide ($SiO_2$) on Si can be considered as a suitable test substrate. Silicon is a dielectric and therefore suitable for use in electronics. Due to the refractive index of 300 nm $SiO_2$, there is a phase shift of the interference color and material opacity of TMDs on the surface. This makes the materials easily identifiable on the $SiO_2$ surface and the layer thickness can be calculated by the difference in contrast between the layers.[141] Another advantage of $SiO_2$ is its wide availability. Silicon (Si) is grown by the standard Czochralski process (CZ)[142] and the top layer of the substrate is oxidised to $SiO_2$ after growth.

For the oxidation, two different processes are available: Wet oxidation and rapid thermal oxidation (RTO). Wet oxidation is a hydrothermal reaction. The Si wafer is oxidised in water with oxygen as oxidiser. An advantage of this oxidation method is the fast growth rate of the oxide layer due to the use of water. The wet oxide films exhibit a lower dielectric strength and higher porosity to impurity penetration (or doping) in comparison with RTO oxide layers.

In RTO, the wafer is heated in a furnace where the temperature is ramped up to 1000 °C in a few seconds. After oxidation the wafer is slowly cooled down to

prevent dislocations and wafer breakage due to thermal shock. The higher dielectric strength and lesser impurity penetration of $SiO_2$ prepared by RTO results in RTO being the preferred oxidation method for use in electrical applications.

The growth substrates used in this work are 500 $\mu$m thick Si samples with a top layer of 300 nm $SiO_2$ obtained by RTO. The sample size varies from $\sim$0.5x0.5cm $-$ $\sim$1x1 cm to ensure the sample fits in the furnace.

The Si substrates are cleaned before every CVD run by rinsing the substrates firstly in high-performance liquid chromatography (HPLC) acetone followed by HPLC isopropanol (IPA) after which the samples are dried with nitrogen gas ($N_2$). This procedure will remove most of the large contaminants on the surface. More thorough cleaning procedures for $SiO_2$ are the Radio Corporation of America (RCA) clean procedure, to remove all particles, organic contaminants and solvents on the surface or a hydrogen fluoride (HF) treatment, to etch away the $SiO_2$ on the surface resulting in Si with only a thin native $SiO_2$ layer.

**Sapphire**

A different growth substrate that can be used for the CVD growth of TMDs is alumina ($Al_2O_3$). In particular, sapphire, which is mono-crystalline $\alpha$-$Al_2O_3$, can result in an improved crystallinity and epitaxial growth on the surface.[143,144] Sapphire is a single crystalline material known for its chemical and thermal stability, and is used for the epitaxial growth of a wide range of materials especially on C- and R-plane sapphire.[145,146]

Besides being a suitable growth substrate, sapphire also has applications in optics[147] and chemical catalysis.[148] The stability of sapphire contrasts with commonly used $SiO_2$/Si substrates, which have a more limited thermal range and provide an amorphous surface for growth, resulting in randomly aligned material growth. According to Dumcenco et al.[116] CVD growth of $MoS_2$ on C-plane (0001) sapphire results in large area epitaxial growth of $MoS_2$ , a result of the coalescence of aligned $MoS_2$ flakes. Crystalline surfaces naturally feature steps, whose configurations depend on the planar orientation of the surface and can act to further order growth on.

Beyond the frequently used C-plane (0001) sapphire other common low-index sapphire planes are R-plane $(1\bar{1}02)$, A-plane $(11\bar{2}0)$ and M-plane $(10\bar{1}0)$. R-plane sapphire is used in high-speed integrated circuits and growth of III-V materials,[149,150] whereas A-plane is employed for the production of hybrid microcircuits.[145] All planes have different properties depending on their facets, resulting in different growth mechanisms occurring on the surface.

### 5.1.2 Precursors

#### Transition metals

In literature, different metal precursors are mentioned ranging from metal to metal oxides and metalorganic precursors.[151,152] The choice of the metal precursor depends on the required TMD, chalcogen precursor, preferred phase of the precursor (gaseous, solid) and contamination of the surface due to the precursor. In the processes detailed herein, the focus will be on W and Mo TMDs, therefore the metal precursors must contain W or Mo.

The precursors all need to be solid and contamination to the surface should be kept to a minimum. Certain precursors such as hexacarbonyl precursors ($M(CO)_6$) are known to result in TMD growth with CVD. The hexacarbonyls stabilise a zero oxidation state of the metal, are stable in air and decompose at low temperatures.[153] Unfortunately carbonyl groups cause large carbon contamination of the surface.[154]

To ensure good control over the amount of transition metal released during the CVD process the metal precursor was deposited on a $SiO_2$/Si seed substrate by sputtering or drop casting, depending on the used precursor. For an overview of the precursors see Table 5.1.

To sputter the different metal on the seed substrate, a Gatan 682 Precision Etching and Coating System (PECS) was used. During sputtering, the surface of a metal target is bombarded with argon (Ar) ions, leading to the ejection of target material and onto the substrate. The film deposition rate and thickness were monitored with a quartz crystal microbalance (QCM).

For the metal sputtering of the seed substrates, the substrate was first cleaned (for cleaning procedure see subsection 5.1.1) after which the seed substrate was placed in the sputtering tool and the metal was deposited. The layer thickness of the seed layer was 20 nm on average and additional patterning to the seed layer was done by the use of hard masks.

Oxidation following metal deposition can be beneficial for the precursor as oxidation lowers the energy barrier for the metal to react with the chalcogen. To oxidize the obtained metal layers, the sputtered metal film was placed upon a hotplate at 500 °C. The temperature was first ramped up to 500 °C in 10 min. followed

| Metal | Precursor | Deposition mode |
|---|---|---|
| Tungsten | Tungsten oxide ($WO_x$) | Sputtering+oxidation |
| | Tungsten oxide dots | |
| | Tunsten hexachloride ($WCl_6$) | Drop casting |
| | Exfoliated $WO_3$ flakes | |
| Molybdenum | Molybdenum oxide ($MO_x$) | Sputtering+oxidation |
| | Exfoliated $MO_3$ flakes | Drop casting |
| Platinum | Platinum | Sputtering |
| | Platinum tetrachloride ($PtCl_4$) | Drop casting |

Table 5.1: Overview of the different metal TMD precursors and deposition method.

by annealing for 30 min. Finally the hotplate was cooled down overnight to room temperature ($T_R$).

Another deposition method for the metal precursors is drop casting. In drop casting a solid precursor, dispersed or dissolved in a solvent, is deposited on a heated substrate. After the solvent is evaporated a thin solid precursor layer remains on the surface. For the processes described here, a Si seed substrate is placed on a hotplate at 120-180 °C and after ∼5 min. an amount of 30-60 $\mu$L precursor dispersed in solvent (for example IPA, acetone or ethanol) is deposited on the surface.

#### Chalcogens

For the CVD synthesis of TMDs at least two precursors are necessary; one containing the metal, the other containing the chalcogen. The choice in chalcogen precursors is usually quite straightforward and in most cases, either $H_2S$/$H_2Se$ or the vaporized chalcogen is used.

For sulfur, there are studies reporting the use of more exotic (and more reactive) precursors like 1,2-ethanedithiol or 2-methylpropanethiol, to enable depositions at lower temperatures.[155] Sulfur is sometimes favoured over $H_2S$ as it is less toxic. However, sulfur is a solid at room temperature (melting point of 115 °C) and has to be vaporized in order to deliver it to the reactor. Gaseous precursors are more controllable compared to the evaporation of a solid and thus ensure a higher reproducibility of the results.

When using selenium as chalcogen, solid selenium is often preferred above gaseous $H_2Se$, as $H_2Se$ has a very high toxicity. There are some studies where $H_2Se$ is used as precursor despite its high toxicity.[151,156] Another selenium precursor that is used is dimethyl selenide ($(CH_3)_2Se$, DMSe).[154]

To minimise the health risk caused by the selenium for the selenium TMDS, a solid selenium precursor was chosen and for further protection a sealed ventilation box is placed over the furnace to prevent Se contamination from entering the lab atmosphere. The selenide precursor is selenide pellets, size <5 mm, ≥99.99% purity from Aldrich.

### 5.1.3 CVD process

Both furnaces used for the CVD growth of the TMDs are tube furnaces with 2 heating zones, a high-temperature zone downstream and a low-temperature zone upstream. In the furnace, the chalcogen precursor is placed upstream in the low temperature zone. Approximately 15–20 cm downstream from the chalcogen precursor in the high temperature zone the metal precursors are located, with the growth substrate placed face down on top of the metal precursor. For a schematic image of the furnace see Figure 5.1. The melting temperature of the chalcogens is well below the reaction temperature and using a lower-temperature for the evaporation of the chalcogen prevents excessive amounts of chalcogen in the furnace.

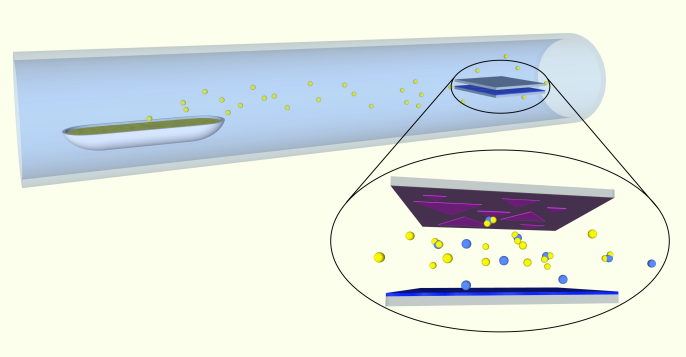

Figure 5.1: Schematic image of the furnace setup. On the left is the upstream low temperature zone of the furnace where the chalcogen precursor is evaporated, whereas on the right the downstream high temperature zone is shown. In the outline, the microreactor is shown in more detail. The bottom substrate is the seed layer, which contains the metal precursor whereas the top substrate is the growth substrate.

Separate furnaces were used for growing the sulfide and selenide TMDs to prevent cross-contamination. Both furnaces have a similar setup. The main difference between the different furnace setups is the chalcogen heating element. In the sulfur furnace this heater was an array of halogen lamps, see Figure 5.2(a), whereas a second furnace was in place for the selenium setup to heat up the selenium source as shown in Figure 5.2. More detailed information on the furnace setups can be found in Appendix B.

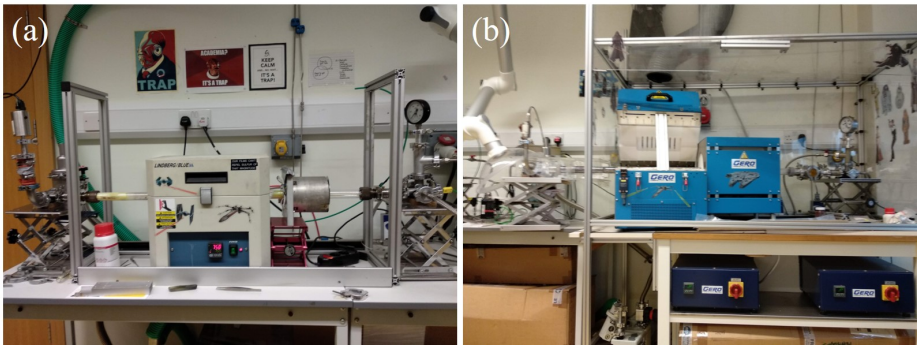


Figure 5.2: Pictures of the different TMD CVD furnaces. (a) the sulfur furnace and (b) the selenium furnace.

## 5.2 Characterisation methods

### 5.2.1 Optical microscopy

The simplest way to characterise transferred graphene or any other material is optical microscopy. Optical microscopy is simple, convenient and produces fast results. The technique was discovered back in the 17th century by Antoni van Leeuwenhoek[157] and is still one of the most commonly used characterisation methods to date. In this method, a sample is placed under a lens (or lenses) and illuminated. The

lenses magnify the image making inspection of the sample possible. When the TMD is placed on $SiO_2$, it results in a contrast making the TMD visible under the microscope, therefore optical microscopy can be used as a cheap and fast way to determine whether and whereabouts TMDs are present on the substrate. Optical microscopy can also be used as an indication for the number of layers present on the substrate.[141] The contrast increases with the number of layers. Defects in the material can also be visualised under the microscope when they are pronounced. A disadvantage of this characterisation method is that not every TMD gives a good visible contrast and it is difficult to discern grain boundaries. Optical microscopy is limited to the diffraction limit of light. To calculate the diffraction limit the following equation applies:

$$d = \frac{\lambda}{2n \sin(\theta)} \tag{5.1}$$

In the equation $d$ is the diffraction limit, $\lambda$ the wavelength of the incoming light, $n$ the refractive index and $\theta$ is the angle of incidence. This leads to a detection limit of about 0.5-0.2 $\mu$m.

### 5.2.2 Raman spectroscopy

Raman spectroscopy is a characterisation method used to observe vibrational, rotational and other modes in a system. These modes give information on the geometry of the molecule. Raman spectroscopy relies on inelastic scattering, or Raman scattering, of monochromatic light. When the light interacts with the surface, most light is reflected elastically, but for every $10^7$ photons there is one photon that scatters inelastically by interacting with the molecular or lattice vibrations in the sample. These vibrations will be visible in either Raman or infrared (IR) spectroscopy depending on the symmetry of the molecule/lattice. If the dipole moment of a molecule is changed by the vibration, it will be IR active, while a change in the polarisability of the molecule results in a Raman signal. The intensity of the Raman scattering is proportional to the change in polarisability change

If the light is scattered elastically, as is the case for Rayleigh scattering, the incident light comes in with the same oscillation frequency, $\omega_0$, as the scattered light. For Raman scattering, there is a shift in the frequency of the light, which corresponds to the vibrational frequency of the molecule, $\omega_q$, giving a total frequency of $\omega_0 \pm \omega_q$. The $\omega_0 - \omega_q$ shifts correspond to Stokes scattering, while $\omega_0 + \omega_q$ corresponds to Anti-Stokes scattering. In Stokes scattering, the photon excites the molecule to a virtual energy state, when the energy relaxes back thereby emitting a photon with a smaller energy than the incident photon.

Raman spectroscopy requires monochromatic light which is obtained from a laser. The wavelength of the light can range from the near infrared (IR) to the near ultraviolet (UV). The laser light will interact with the molecular vibrations, phonons and other excitations in the system of the molecule. These interactions result in an intensity shift of the energy of the laser photons, leading to a spectrum. The

change in energy due to the scattering is characteristic of the chemical bonds in the material.[158] Raman is a prominent method for TMD characterisation, owing to its ability to identify the structure and phase, detect defects and differentiate between mono-, bi- and multilayers as well as the fact that it is a non-destructive characterisation method.

### Classical Raman theory

Most Raman effects can be described by classical Raman theory. In classical Raman theory, molecules are described as a cluster of atoms performing only harmonic vibrations and the incident light is described as a wave and molecular rotations are neglected in this approximation. The incident light results in a oscillating electric field, $\vec{E}$, which induces a dipole moment in the system.[159] As defined by:

$$\vec{\mu} = \tilde{\alpha}\vec{E} \tag{5.2}$$

With $\vec{\mu}$ the molecular dipole moment and $\tilde{\alpha}$ the polarisability, which describes how much the electron density is perturbed by the electric field.
The electric field is characterised by its vector amplitude, ($\vec{E_0}$), and oscillation frequency:

$$\vec{E} = \vec{E_0}\cos(\omega_0 t) \tag{5.3}$$

The polarisability is influenced by nuclear motion, as the geometry of the nucleus always changes in order to minimise the energy of the system. The change in polarisability can be described using a Taylor series expansion:

$$\alpha = \alpha(Q) = \alpha_0 + \sum_{q=1}^{N}\left[\left(\frac{\partial\alpha}{\partial q}\right)_{q_0} q + \frac{1}{2}\left(\frac{\partial^2\alpha}{\partial q\partial q'}\right)_{q_0 q_0'} - q - q' + Q\left(q^3\right)\right] \tag{5.4}$$

In this formula where the polarisation has expanded around the equilibrium nuclear geometry, $Q_0$, and $Q$ represents the sum of all individual normal modes $q$. For each coordinate $q$, oscillations with frequency, $\omega_q$ can be excited. Given by the following formula:

$$q = q_0\cos(\omega_q t) \tag{5.5}$$

Combining Equation 5.4 and Equation 5.5 results in:

$$\mu(t) = \alpha(Q) * E = \alpha_(Q)E_0\cos(\omega_0 t) = \left[\alpha_0 + \left(\frac{\partial\alpha}{\partial q}\right)_{q_0} q_0\cos(\omega_q t)\right]E_0\cos(\omega_0 t) \tag{5.6}$$

Equation Equation 5.6 can be rewritten as:

$$\begin{aligned}\mu(t) = \alpha_0 E_0 \cos(\omega_0 t) + \frac{1}{2}\left(\frac{\partial\alpha}{\partial q}\right)_{q_0} q_0 E_0 \cos[(\omega_0 - \omega_q)t] \\ + \frac{1}{2}\left(\frac{\partial\alpha}{\partial q}\right)_{q_0} q_0 E_0 \cos[(\omega_0 + \omega_q)t]\end{aligned} \tag{5.7}$$

In Equation 5.7 the first term oscillates with the same frequency as the incident radiation and is therefore responsible for all elastic (Rayleigh) scattering. The second term describes the light which is red-shifted compared to the incident light. The source of this light is Stokes scattering which contains information about the system via its $\omega_q$ dependence. The last term is due to Anti-Stokes scattering, where the light is blue-shifted in respect to the incident radiation. This scattering is the mirror image of the Stokes scattering but has a strongly decreased intensity due to a lower population of thermally excited vibrational states as described by the Boltzmann factor.[160]

The different kinds of scattering are visualized in a schematic Raman spectrum in Figure 5.3. The frequency shift of the light depends on the bonds and symmetry in the material, displaying a characteristic peak for each Raman active vibration mode resulting in a unique fingerprint for a compound.

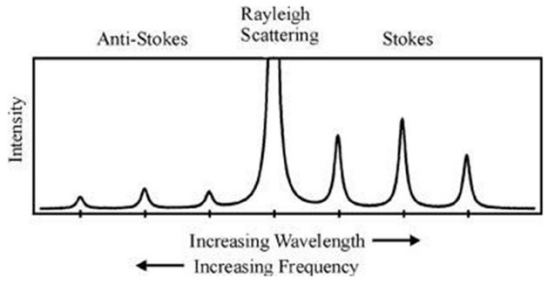


Figure 5.3: Overview of different kinds of scattering in the Raman spectrum.[158]

### Quantum mechanical Raman theory

Quantum mechanical Raman theory explains the resonant Raman scattering. According to quantum mechanical theory, radiation is emitted when a downwards transition between two discrete energy levels occur. In Raman spectroscopy, electrons are excited to a virtual excited state when the photon hits the system. To obtain a Raman effect, a change in energy level after relaxation of the electron is required. For Stokes scattering, the electron relaxes to an energy state higher than the initial state, emitting a photon with less energy than the incident photon. When the electron relaxes to a lower energy state, emitting a photon whose energy is higher than the initial photon, Anti-Stokes scattering occurs, as shown in Figure 5.4. To conserve the energy in the system a shift in the frequency of the photon occurs.

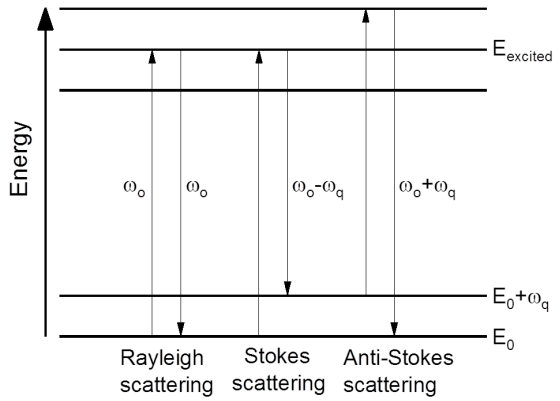


Figure 5.4: Graphic representation of the quantum energy transitions to a virtual energy state and relaxation of the electron for Rayleigh, Stokes and Anti-Stokes scattering.

### Selection rules

The different modes in a system can be determined by finding the symmetry group of the system. If the symmetry group is known, a character table can be determined, which gives the different symmetry modes in the system. For example the character table for $CO_2$, a triatomic linear molecule with symmetry group $D_{\infty h}$, is given in Table in Appendix C.

To ascertain whether a mode is Raman active, selection rules are used. The selection rules can be explained as follows: The equation for $\mu(t)$ shows that the inelastic scattered light depends on $(\partial\alpha/\partial q)_{q_0}$ term which describes the electronic polarisability at the equilibrium position along the normal coordinate of $q$. This means the polarisability must change along the coordinates of the molecule and the equilibrium position to have a Raman active mode. In a centrosymmetric molecule, a vibrational mode may be either Raman or IR active but not both according to the mutual exclusion principle. Raman and IR are therefore considered as complementary techniques.

To demonstrate the selection rules, different vibration modes for $CO_2$ are shown in Figure 5.5. In the first vibration mode, a symmetric stretch, the polarisability increases with the increase in internuclear distance, $(\partial\alpha/\partial q)_{q_0} \neq 0$, meaning that the mode is Raman active. The stretching of the bonds does not change the dipole moment as the dipole moment remains constant on the normal coordinate, $(\partial\mu/\partial q)_{q_0} = 0$, making the mode IR inactive. If the anti-symmetric stretching is considered, a change in dipole sign occurs when the system passes the equilibrium position, therefore $(\partial\mu/\partial q)_{q_0} \neq 0$ and the vibration mode is IR active. The polarisability changes during the stretching, however this change is symmetric around the equilibrium position and therefore $(\partial\alpha/\partial q)_{q_0} = 0$. As a result, this vibration mode is Raman inactive.

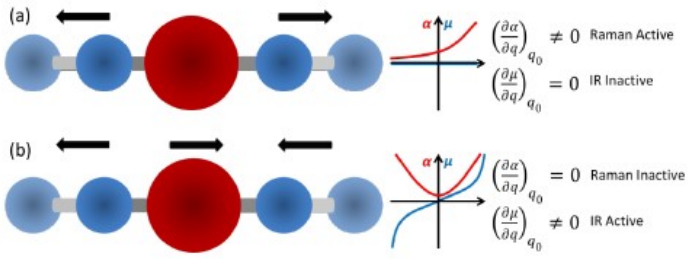


Figure 5.5: Schematic overview of vibrations in a triatomic linear molecule. (a) Symmetric stretching and (b) anti-symmetric stretching. Adapted from Dieing *et al.*[159]

### TMDs

The Raman spectroscopy of TMDs shows that individual trilayers typically have trigonal prismatic (H) or octahedral (T) structures, often in the following stacking orders: 1T, 2H and 3R, of which 2H is the most common stacking for $MoS_2$ and $WSe_2$ and will be used for the explanation of Raman characterisation of TMDs. In bulk the compounds have symmetry group $D_{6h}$, with space group P63/mmc, and a unit cell consisting of 2 layers of $MoS_2$, 6 atoms. The Raman active modes for this symmetry group are $A_{1g}$, $2E_{2g}$ and $E_{1g}$, where the $2E_{2g}$ are separated in $E^1_{2g}$ and $E^2_{2g}$. The symmetry group changes for few layers to $D_{3h}$ for odd layer numbers with Raman active modes $A_1^{'}$, $E^{''}$ and $2E^{'}$. Even layer numbers have the symmetry group $D_{3d}$, where the active Raman modes are $3A_{1g}$ and $3E_g$.[161,162] In Appendix C the character tables for the point symmetry groups are displayed from which the Raman modes of 2H $MoS_2$ can be derived.

In the Raman spectra of bulk 2H TMDs, two peaks are almost always clearly visible: the in-plane $E^1_{2g}$ mode, which arises from in-plane vibrations of both metal and chalcogen atoms, and the out-of-plane $A_{1g}$ mode, which occurs due to out-of-plane vibrations of chalcogen atoms. In Figure 5.6.[163] these modes as well as the other active and inactive Raman modes are shown. The $E^1_{2g}$ and $A_{1g}$ modes should be referred to as $E^{'}$ and $A_1^{'}$ in monolayer and odd-layers and $E_g$ and $A_{1g}$ in even layers. To avoid confusion the modes will from this point onwards be referred to as the bulk modes $E^1_{2g}$ and $A_{1g}$ regardless of layer thickness.

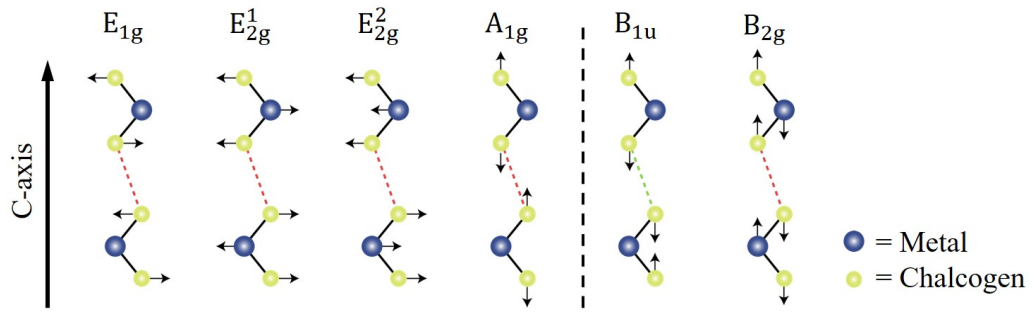


Figure 5.6: Overview of the active and inactive Raman modes in TMDs. Adapted from Tonndorf *et al.*[163]

The $E^1_{2g}$ and $A_{1g}$ peaks are generally used for the characterisation of TMDs. The peaks indicate the presence of the material, whereas intensity, position and width of the peaks give information on the quality and number of layers. For example in $MoS_2$, a shift in frequency is observed with increasing layer number due to suppressing atomic vibrations for increasing layer number. As a result, an increase in the number of layers of $MoS_2$ from monolayer to bulk results in the $E^1_{2g}$-peak red-shifting to lower wavenumbers, while the $A_{1g}$-peak blue-shifts to higher wavenumbers as shown in Figure 5.7. The $A_{1g}$ peak blue-shifts due to the higher restoring force on top, where the $E^1_{2g}$ peak stiffens with increasing layer number and therefore red-shifts.[164] The distance between the peaks can therefore be used to identify the layer thickness of $MoS_2$.

The peak width of both the $E^1_{2g}$ and $A_{1g}$ peak increases when increasing disorder, or the presence of defects on the surface.[165] This increase in width depends on the the degree of disorder, or defect density. The $A_{1g}$ mode shows a strong doping dependence; the phonon frequency decreases and line width broadens for electron doping, where there is less influence on the $E^1_{2g}$ mode.[166] This in contrast to strain, where the $E^1_{2g}$ mode shifts to lower wavelengths under the influence of strain and eventually splits up in two modes, though there is only a slight shift of the $A_{1g}$ mode to lower wavelengths.[167,168] Other factors which can influence the Raman spectrum include substrate, temperature, dopants, grain boundaries, dielectric environment, strain, and pressure.[166,169–174]

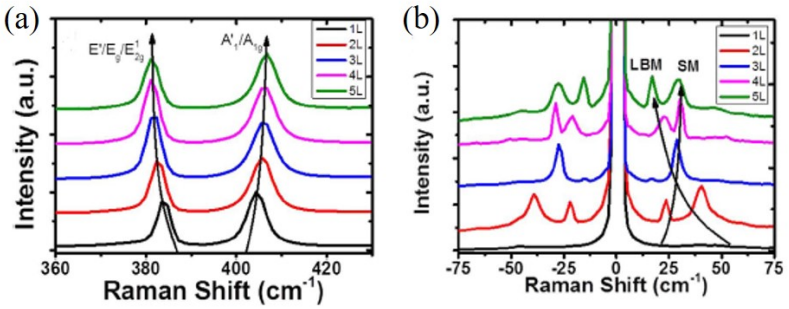


Figure 5.7: (a) Raman spectrum of 1-5-layer $MoS_2$. (b) Low-frequency $MoS_2$ Raman spectra of SMs and LBMs. Adapted from O'Brien *et al.*[175]

Apart from the $E^1_{2g}$-peak and the $A_{1g}$-peak, TMDs also have interlayer vibrations. The peaks of these vibrations are located in the low-frequency region of the Raman spectrum (<50 cm$^{-1}$) and contain useful information.[175,176] At low Raman shifts ∼<50 rel cm$^{-1}$ a narrowband filter set that is optimally aligned to detect Raman lines extremely close to the Rayleigh lineray at 0 cm$^{-1}$ as there is intense scattering in that area. As special equipment is needed for this, low frequency Raman modes are often absent in literature studies of $MoS_2$.

The modes corresponding to the low frequency Raman peaks are shear modes and layer-breathing modes which occur due to relative motion of the planes to the atomic layers. In monolayer $MoS_2$ these peaks are absent due to the lack of these

interactions. These low-frequency modes give information on the number of layers and the stacking of the material as demonstrated for $MoS_2$ in Figure 5.7.[175,176] The layer breathing and shear mode for $MoS_2$ are shown in Figure 5.8.

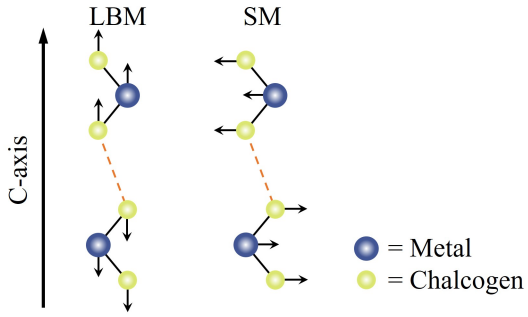


Figure 5.8: Overview of the layer breathing mode (LBM) and shearing mode (SM) of $MoS_2$ in low frequency Raman spectroscopy.

#### Tool specifications

The Raman spectroscope used is the Witec Alpha 300R spectrometer with an excitation wavelength of 532 nm. For the Raman spectra a spectral grating of 1800 lines/mm and a 100× microscope objective (0.95 N.A) with the spot size was ∼0.3 $\mu$m were used. Laser power was kept <100 $\mu$W to avoid laser damage on the surface. For low frequency Raman measurements the system was fitted with a Rayshield coupler. The system is capable of Raman mapping using piezo motors and can take several thousand spectra over an extended area. The majority of Raman maps collected were spectra over a 25x25 $\mu$m area with an integration time of 0.02 s. The acquired data was analysed using Witec Project 4.0 software.

### 5.2.3 Photoluminescence spectroscopy

Photoluminescence (PL) is a phenomenon in which energy provided by photons is absorbed by a material, followed by the emission of light. When the material is excited by a laser light with an energy higher than the (expected) band gap, electrons fill the conduction band and form holes in the valence band. The electrons and holes, generated by the excitation, will undergo energy and momentum relaxation, firstly there will be a non-radiative relaxation, wherein the excited state loses energy through phonons and Coulomb scattering, settling near the bottom of the conduction band, reaching the band gap minimum, after which they will recombine under the emission of photons. These photons can be measured and used to determine the size of the band gap. Therefore photoluminescence spectroscopy is a direct method for measuring the band gap in TMDs.

In TMDs a peak shift is associated with the decreasing layer number as the band structure changes with layer number. This is because in bulk material, electronic states near the Γ point of the Brillouin zone and the point of the indirect band gap

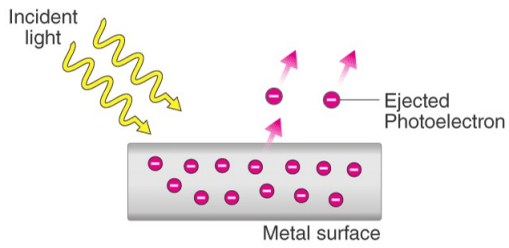


Figure 5.9: Schematic of the photoelectric effect.

come from a linear combination of d-orbitals on the transition metal atoms and anti-bonding $p_z$-orbitals on chalcogen atoms. These states are involved in the indirect transition therefore have a strong inter-layer coupling and depend significantly on the number of layers present. The conduction band states at the Brillouin zone K-point are a combination of localised d-orbitals on the metal atoms, which have an intrinsic absence of inter-layer coupling due to their location in the middle of the layer. The change in band structure also causes the PL intensity to increase exponentially at the monolayer, while it is practically absent for bulk TMDs.

The PL spectra of TMDs are very sensitive to changes in the structure and environment. The crystal quality of the surface has influenc on the intensity, peak position and the FWHM of the PL peak.[177] Similar to Raman, the PL is also sensitive to temperature,[178,179] strain,[172,180,181] defects,[182,183] substrate,[170] and dopants.[184]

The setup used for PL spectroscopy is the same setup as used for Raman spectroscopy, the Witec Alpha 300R system with a 532 nm excitation laser. The settings are similar to the Raman measurements, though the grating was set to 600 lines/mm.

### 5.2.4 X-ray photoelectron spectroscopy

XPS is a surface sensitive, spectroscopic technique which allows the identification of elements present in the sample, along with their chemical state. The principle of XPS is based on the photoelectric effect, which is the emission of electrons from a sample that has been illuminated by electromagnetic radiation with a photon energy above a specific threshold.[185] In an XPS system the sample is predominantly irradiated by monochromatic X-rays in a vacuum. The X-rays interact with the sample and cause emission of electrons by the photoelectric effect as shown in Figure 5.9. The kinetic energy of the emitted electrons is given by the following equation:[186]

$$E_b = \hbar\omega_i - (E_k + \phi) \tag{5.8}$$

In this equation $E_b$ is the binding energy of the atomic orbital from which the electron is emitted, $\hbar\omega_i$ is the energy of the incident photon, $E_k$ is the photoelectron's kinetic energy after emission and $\phi$ is the work function of the spectrometer. The work function of the spectrometer and the energy of the incident light are known and set at a fixed value, allowing the determination of the binding energy of the emitted electron by measuring the electron kinetic energy.

X-rays with an energy high enough to enable the emission of core-level electrons from the sample are used. The spectra obtained from these X-rays contain peaks of which intensities and positions are characteristic for an element. The position, or binding energy, of a peak is a result of the energy of a particular atomic orbital as well as the chemical environment of the atom. Depending on the bonding environment of an atom, the core-level electrons will be screened to a greater or lesser extent resulting in a change in $E_b$ when they are emitted. This enables determination of the exact bonding configuration and chemical state of an atom, giving complete chemical identification of the sample.

The inelastic mean free path of the emitted electrons is on the order of a few nanometres meaning that XPS is a very surface sensitive technique, making it ideally suited to the study of 2D and layered materials. In this work XPS was used to verify the chemical purity of grown materials and examine their stability and oxidation state.

XPS measurements were performed by mr.Conor Cullen. The XPS spectra were taken with a PHI VersaProbe III instrument equipped with a micro-focused, monochromatic Al K$\alpha$ source (1486.6 eV) and a dual beam charge neutralisation located in the Universität der Bundeswehr in Neubiberg, Germany. Core level spectra were recorded with a spot size of 100 $\mu$m and a pass energy of 26 eV using PHI SmartSoft VersaProbe software and processed with PHI MultiPak 9.8. Binding energies were referenced to the adventitious carbon signal at 284.8 eV. After subtraction of a Shirley type background, the spectra were fitted with Gaussian–Lorentzian peak shapes.

All analysis was performed using CasaXPS software. Spectral components were fitted using a Shirley background subtraction and appropriate line shapes. Relative atomic percentages were calculated using the relative sensitivity factors provided by the tool manufacturers.

### 5.2.5 Atomic force microscopy

The atomic force microscope (AFM) was developed in 1986 by Quate, Gerber and Binnig.[187] AFM is a very high resolution scanning probe method and one of the foremost tools for imaging and measuring, and materials at nanoscale. It is mainly used to image surfaces, such as the topography of the surface atomic layer and also to measure forces. This information is gathered by exploring the specimen surface with a sharp tip on the end of a cantilever. Piezoelectric elements facilitate precise movements enabling high resolution scanning. Electric potentials of samples can also be measured using conducting cantilevers.

In AFM the tip is brought close to or in contact with a surface after which it is rastered across the sample area. The interaction forces between it and the surface are measured through the deflection or change in oscillation of the cantilever on which the tip is mounted, as shown in Figure 5.10. When the tip comes near the surface, this results in attractive and repulsive forces on the tip as described by the Lennard

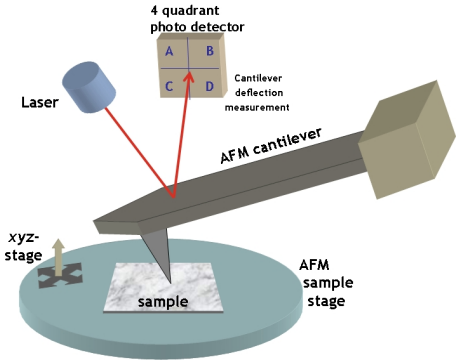


Figure 5.10: Schematic overview of the AFM setup.

Jones potential.[188] These forces lead to a net deflection of the cantilever which is measured by the reflection of a laser beam focused on the cantilever. This laser reflection is captured by 4 photodiodes. The intensities measured at the different photodiodes can be converted into a topographical surface map. The forces measured are from a combination of different sources, such as van der Waals interactions, electrostatic, short-range chemical forces and magnetic interactions. AFM is a very versatile technique which can be used in air, vacuum or liquid and in a static contact mode or tapping modes, it can be used to manipulate the surface and AFM can also be a non-destructive characterisation technique. Different information can be obtained from quantum nanomechanical AFM modes such as adhesion, deformation and dissipation. Through the use of special AFM tips it can also provide magnetic, adhesion and electrical information.

### Conductive AFM

Conductive atomic force microscopy (c-AFM) is an AFM mode where both the topology and conductivity of the material surface are measured simultaneously. It can be used to study the electrical properties of materials at the nanoscale. The method shares some similarities with scanning tunnelling microscopy (STM), though c-AFM has an advantage over STM as it uses a conductive cantilever instead of a sharp metallic wire and a tunneling gap does not need to be maintained. In addition to this the topography and current are measured independently. The conductivity is obtained by measuring the electric current between a metal coated conductive AFM tip and sample for an applied voltage bias. When the a voltage is applied, current typically flows through the tip and the conducting sample, as shown in Figure 5.11(a). Thereby producing producing constant voltage maps of current with nanometer spatial resolutions which can construct a conductive surface profile of the sample.

The conducting probe in c-AFM has a thin electrically conducting coating, common conducting coatings are platinum, gold, tungsten and conductive diamond. Standard c-AFM is in contact mode, though newer c-AFM techniques, such as Peak Force tunnelling AFM (PF-TUNA) allows for conductive tunnelling measurements

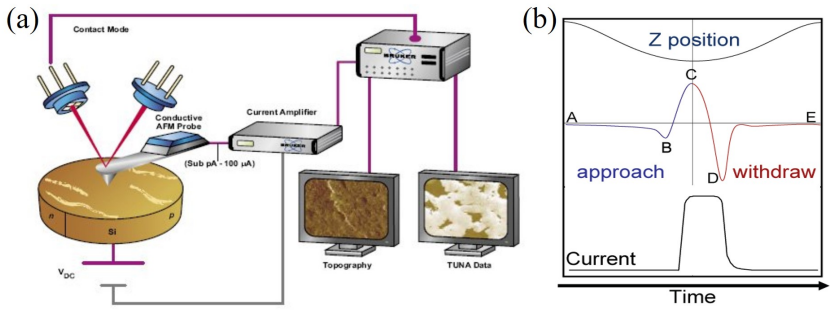


Figure 5.11: (a) Schematic image of a c-AFM setup. (b) graph showing the current, Z-position of the tip and applied force on the surface in function of the time during a single PF-TUNA tapping cycle. Images are adapted from Bruker.

in tapping mode. PF-TUNA is an off-resonance mode, in this mode the cantilever works at a frequency much lower than its resonant frequency. By controlling the peak force, the maximum interaction force, in each point on the sample, the tip surface interaction is optimized and the topography of the sample can be obtained. Due to the quasi-static process of the cantilever, the tip-sample interaction force can be measured and controlled precisely in each pixel at real time.[189]

A PF-TUNA tapping cycle is shown in Figure 5.11(b). During the cycle the tunnelling current is measured form A to E, the contact current is measured from point B to D and the Peak Force current is measured at C when the tip is in contact with the sample.

#### Tool specifications

The AFM measurements in this work was performed on a Bruker Multimode 8 with ScanAsyst Air AFM probes and NANOSENSORS Tapping Mode AFM Probes. The applied scan rate was typically 1 Hz. Peak force tapping mode was used to obtain the topography. PF-TUNA was performed (using PF-TUNA Pt/Ir tips from Bruker). Edge contact for the samples were made with conductive silver paint.

### 5.2.6 TOF-SIMS

Time of flight secondary ion mass spectrometry (TOF-SIMS) is a characterisation method used to obtain molecule-specific chemical information from surfaces with a molecular layer surface sensitivity. In this method, the surface is bombarded by high-energy ions from a primary ion beam. This bombardment causes the emission of secondary ions, both atomic and molecular ions, which are ejected from the sample. This produces a cloud of particles, part of which are ionized. Mass resolutions of ejected particles with atomic mass units >18,000 can be achieved. The ionized particles of one polarity are accelerated into a reflection type time-of-flight mass spectrometer. The particles move through a tube to arrive at an ion detection and counting system. As the ions all depart from the sample at the same time and are subject to the same accelerating voltage, the lighter ones arrive at the detection

system before the heavier ones, determining the mass/charge distribution ratios of the emitted ions.

The secondary ions are detected by the mass spectrometer. The fraction of ionized emitted particles is called secondary ion yield and ranges typically between $10^{-4}$ to $10^{-6}$. The following equation gives the secondary ion yield:

$$I_s^m = I_p y_m \alpha \pm \theta\eta \tag{5.9}$$

where $I_s^m$ is the secondary ion current of species $m$, $I_p$ is the primary particle flux which is adjusted to ensure analysis is kept within the static regime, $y_m$ is the sputter yield, $\alpha\pm$ is the probability of positive or negative ionisation, $\theta$ is the fractional concentration of the chemistry giving rise to species $m$ in the surface layer, and $\eta$ is the instrument transmission which is crucial to detect and analyze the generated ions.[190]

The next pulse of primary ions cannot start until the secondary ions of the first pulse have cleared the analyzer, thereby preventing mixing of slower heavy ions from the first pulse being overtaken by lighter, faster, ions from the second pulse. The interval between the pulses can be used for sputtering and charge neutralisation of the surface.

Ion images are produced by scanning the primary beam over the sample surface and recording the number of ions as a function of the position. The images of all the ions are detected in parallel. The bombarding ions also produce secondary electrons, which can be detected to obtain secondary electron images. The spatial resolution of the images depends largely upon the diameter of the pulse of primary ions. The secondary electron image resolution can be <40 nm.

Since the surface is bombarded with ions, this method is a destructive method. Therefore it is important to keep the dose of primary ions extremely low, below $10^{13}$ ions cm$^{-2}$, to ensure that during TOF-SIMS characterisation $< 1\%$ of the top surface layer receives an ion impact.[190]

#### Tool specifications

A liquid metal ion gun (LMIG) primary ion gun with $^{69}Ga^+$ at 30 keV, bunched mode (higher lateral resolution, low mass resolution) was applied for image acquisition in both positive and negative ion polarity (imaging 64x64, flyback) and unbunched mode (low lateral resolution, mass resolution >5000) for spectra acquisition in positive and negative ion polarity.

### 5.2.7 Contact angle

A contact angle is the angle where a liquid–vapor interface meets a solid surface. The angle quantifies the wettability of a solid surface by a liquid via Young's equation.[191]

$$\cos\theta = \frac{\gamma_{SV} - \gamma_{SL}}{\gamma_{LV}} + \frac{\kappa}{\gamma_{LV}}\frac{1}{\alpha} \tag{5.10}$$

In this equation $\theta$ is the contact angle, with $\gamma_{SV}$, $\gamma_{SL}$ and $\gamma_{LV}$ being the interfacial energy for respectively the solid-vapour, solid-liquid and liquid-vapour interface. $\kappa$ depicts the line tension, where $\alpha$ is the droplet radius.

A high contact angle indicates a low wettability with the surface, whereas the wettability increases as the contact angle decreases. When using water as solvent for the contact angle, the angle indicates the polarity of the material, with a small contact angle indicating a polar material while a large contact angle corresponds to an apolar material.

The contact angle of a material with a solvent can be obtained by dropping a drop of solvent, with a known volume, on the flat and clean surface of the solid material. When the solvent is dropped a picture of the droplet on the surface is taken. From this picture the contact angle is obtained by processing the image with the Contact Angle plugin for ImageJ.

To obtain information on the surface energy of the solid, the Van Oss-Chaudhury-Good method was used.[192] In this method the surface energy is divided the surface free energy is divided into a disperse part, the Lifshitz-Van der Waal component, along with a Lewis acid part and a Lewis base part for the acid-base interactions component.[193] Therefore contact angles of the surface are obtained with three different solvents, a neutral disperse liquid, a liquid with known acid parts and a liquid with known base parts with known surface energies. In this work, water, dichloromethane and glycerol are used as solvents. The surface energies for the material for the individual solvents are obtained first:

$$0.5\gamma_{solvent}(1+\cos\theta_{solvent}) = \sqrt{\gamma_S^d\gamma_{solvent}} + \sqrt{\gamma_S^-\gamma_{solvent}^+} + \sqrt{\gamma_S^+\gamma_{solvent}^-} \tag{5.11}$$

In this equation $\gamma_{solvent}$ is the surface energy of the solvent, $\theta_{solvent}$ is the contact angle of the solvent with the substrate, the $\gamma^d$, $\gamma^+$ and $\gamma^-$ are respectively the disperse, acidic and alkaline components of the energy of the solvent, $\gamma_S$, and the substrate, $\gamma_{solvent}$. In the dispersive solvent the equation is reduced to the following:

$$0.5\gamma_{solvent}(1+\cos\theta_{solvent_d}) = \sqrt{\gamma_S^d\gamma_{solvent}} \tag{5.12}$$

Therefore $\gamma_S^d$ can be obtained. When using the acidic and alkaline the formulas are reduced to the following:

$$0.5\gamma_{solvent}(1+\cos\theta_{solvent_a}) = \sqrt{\gamma_S^d\gamma_{solvent}} + \sqrt{\gamma_S^-\gamma_{solvent}^+} \tag{5.13}$$

and

$$0.5\gamma_{solvent}(1+\cos\theta_{solvent_b}) = \sqrt{\gamma_S^d\gamma_{solvent}} + \sqrt{\gamma_S^+\gamma_{solvent}^-} \tag{5.14}$$

With these formula $\gamma_S^-$ and $\gamma_S^+$ can be found, which leads to the surface energy, $\gamma_S$ given by the three different surface energy components:

$$\gamma_S = \gamma_S^d + 2\sqrt{\gamma_S^+\gamma_S^-} \tag{5.15}$$

### 5.2.8 Device fabrication

The TMD devices, made from the TMD flakes grown by CVD, were fabricated by defining contacts on samples by e-beam lithography (EBL) or Maskless UV lithography.

#### Electron beam lithography

For the EBL process the sample was first covered in a layer of electron-beam sensitive resist, PMMA A6, through spin coating. This resist is a positive resist, therefore the resist degrades when the resist is exposed to an appropriate dose of electrons, resulting in a patterning of the surface in the exposed areas. The degraded resist areas can be removed after exposure with a developer solution (IPA:MIBK 4:1), after which the contact metal is deposited using sputtering or e-beam evaporation. Following metal deposition, the polymer layer is removed by a lift-off step in acetone. Since the pattern for each sample is designed based on sample measurements, EBL offers the advantage of precise, small-scale and unique patterning of irregular samples. It does however become time-consuming and expensive for processing of large numbers of devices and is therefore not widely used in industrial processes.

When defining contacts with EBL, the contacts were defined using a Karl Zeiss Supra microscope. The Ti/Au (5nm / 100nm) metal contacts were then deposited using e-beam evaporation.

#### Maskless UV lithography

Maskless UV lithography is an optical lithography method that does not require the use of a physical lithography mask to define patterns on the substrate. The maskless litho setup used in this work is the SF-100 Intelligent Micro Patterning (IMP) tool. The IMP projects a monochrome image on the substrate using Smart Filter technology.[194]

This smart filter is a digital micro mirror device (DMD), which are 1024x768 mirrors, corresponding to the pixels in the mask design. These mirrors are individually controlled by the IMP software. The mirrors can each reflect or not reflect the light resulting in the monochromatic image on the surface. The pattern made by the filter can be aligned using the controllable stage of the IMP. When aligned the sample is exposed with UV-light at the white regions of the projected image. A schematic overview of this process is shown in Figure 5.12.

When a mask design is selected the smart filter projects this through a visible light filter, making it possible to align sample under the mask as required. Other than aligning the sample, other settings such as the exposure time, the size and angle of the designs and the dark vs. light field projection of the mask can be set. A screen shot of the software is shown in Figure 5.13.

Similar to EBL the sample is first covered in a resist. For UV lithography, this is a photoresist which reacts at the used UV wavelength. In this work the

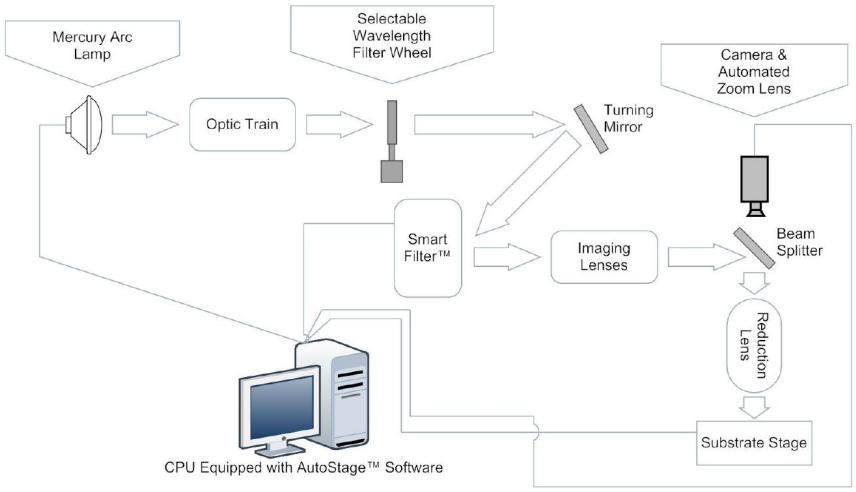


Figure 5.12: Block diagram of the IMP maskless lithography system. Detailing all the steps to produce and expose a mask via the smart filter. This image has been reproduced from the Intelligent Micro Patterning SF-100 Platform manual.[194]

used photoresist is a positive photoresist, MICROPOSIT S1813. After exposure the sample is developed in the developer solution, and afterwards rinsed in DI-water to remove the traces of developer and degraded resist. The metal deposition and resist removal was performed in the same manner as the metal deposition and resist removal for EBL.

Maskless lithography is a straightforward lithography method and has the ease that masks can be specifically designed for the grown material. The optical microscope allows for convenient alignment of the sample and the projected mask. This method has a lower resolution compared to EBL, though it is much faster for patterning of individual flakes. Maskless lithography does have limitations as only a small portion of the sample can be exposed at once, therefore standard UV lithography is better for larger areas and repeated patterns.

In this process samples were first pre-baked, 1 min at 120 °C, after which the photoresist was spin coated, 3000 rpm for 1 min. After spin coating the sample was placed at the hotplate for 2 min at 120 °C, to relax the resist coating and to evaporate the last of the solvent. The samples were exposed at the required positions to the litho pattern, projected by the smartfilter, for 0.8 s. The wavelength used for exposure was 434 nm. The samples were developed for 45 s in MICROPOSIT MF-319 developer. Finally contacts were deposited by e-beam evaporation and the resist was lifted off by overnight immersion in acetone, followed by an IPA rinse.

### 5.2.9 Electrical characterisation

In electrical measurements the electrical properties are measured by the use of different device structures, which lead to different measurements. Different measurement types include two-probe measurement, four-probe measurement, transfer

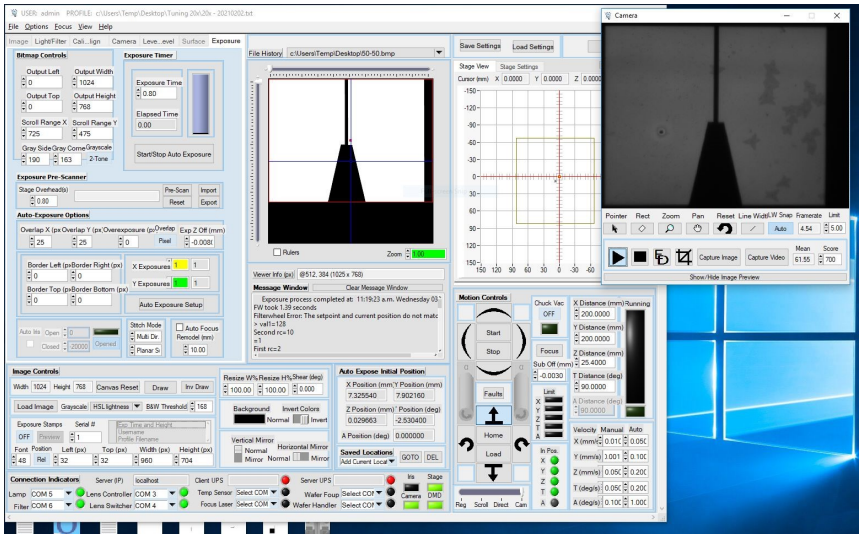

Figure 5.13: Screenshot of the IMP software. The design of the mask and the adjustable variables are shown on the left. The optical microscopy image of the projection is shown at the right top.[194]

length measurement (TLM), Hall bar measurement and Van der Pauw measurement. The characteristics that can be determined with these are output characteristics, resistance, on/off current ratio, subthreshold swing and mobility. In this report only 2- and 4-probe measurements are used and the description in this section is therefore limited to these methods.

In a two-probe measurement, the device consists out of 2 electrical contacts which are in contact with the semiconductor material which has a defined channel length/area. The current is measured in function of the source-drain voltage ($V_{ds}$), while the back-gate voltage ($V_{gs}$) is modulated. The four-probe measurement is similar but different contacts are used for the current and voltage, thereby ruling out the contact resistance in the device. Examples of both a two-probe and a four-probe device are shown in Figure 5.14. Important electrical properties are the mobility, on/off current ratio and the subthreshold swing ($SS$). The mobility characterises how fast an electron (or hole) can move through a metal or semiconductor when an electric field is applied, while the on/off ratio indicates the ability of the device to shut off and the subthreshold swing is the gate voltage required to change the drain current by one order of magnitude.

The electrical measurements were performed with 2-probe devices. Between two contacts the resistance is measured during a voltage sweep.[195,196] In this way the drain voltage and drain current are measured. This results in a $\frac{I_{ds}}{V_{ds}}$-plot from which the total resistance ($R_{tot}$ can be calculated. This plot also indicates whether the device shows Ohmic or non-Ohmic behaviour. A device has Ohmic behaviour if it follows Ohm's law:

$$R = \frac{V}{I} \tag{5.16}$$

According to Ohm's law the current flow through the resistor is proportional to the

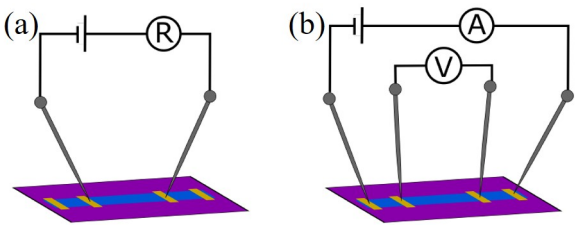


Figure 5.14: Illustration of a 2 probe and 4 probe device. (a) shows a 2 probe device where current is measured in function of the source-drain voltage, thereby giving the resistance of the device, while (b) shows a 4 probe device in which different contacts are used for the current and voltage, thereby ruling out the contact resistance in the device.

voltage, resulting in a linear $\frac{I_{ds}}{V_{ds}}$-plot. If the device shows non-Ohmic behaviour the plot is non-linear. An example of both Ohmic and non-Ohmic behaviour are shown in Figure 5.15.

When $V_{gs}$ is varied as well as $V_{ds}$ and the current is plotted on a logarithmic scale both the on/off current ratio and the subthreshold slope can be determined. (See Figure 5.16) The subthreshold slope is the slope of the linear region of the $\frac{I_{ds}}{V_{gs}}$-curve. To obtain the subthreshold swing the reciprocal of the subthreshold slope is taken as pictured in Figure 5.16(b). Therefore the formula for the subthreshold swing is:

$$SS = \frac{1}{\partial(\log I_{ds})/\partial(V_{gs} - V_{th})} \tag{5.17}$$

The on/off current ratio is the number of orders between the on and off state of the device. Indicating the ability of the device to shut off. If this ratio is small leakage current can cause undesired switching of the device, meaning that the device cannot switch off properly.

The field effect mobility ($\mu_{FE}$) can be derived with the following formula:

$$\mu_{FE} = \frac{1}{C_{ox}} \frac{\partial I_{ds}}{\partial V_{gs}} \frac{L}{W} \frac{1}{V_{ds}} \tag{5.18}$$

In which $C_{ox}$ the oxide capacitance for the area, $\frac{I_{ds}}{V_{gs}}$ the transconductance and $\frac{L}{W}$ is the length over width of the channel area. The channel area, transconductance and

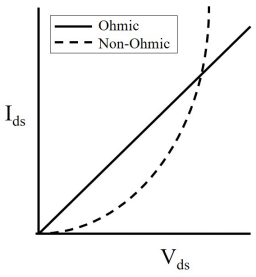


Figure 5.15: Schematic image of the electric transport characteristics of Ohmic behaviour (full line) and non-Ohmic behaviour (dashed line) in a device.

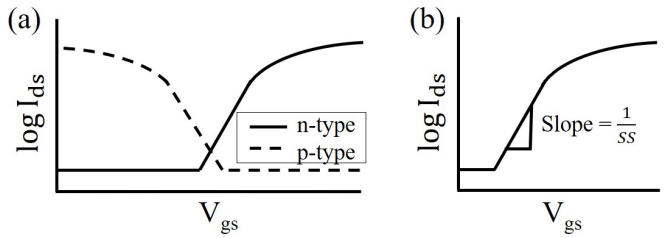


Figure 5.16: (a) A schematic $\frac{I_{ds}}{V_{gs}}$-graph for both n-type and p-type materials. (b) Graph showing how to determine the subthreshold swing of a device.

$\frac{1}{V_{ds}}$ are specific for the device while $C_{ox}$ depends on the substrate materials. The formula for $C_{ox}$ is:

$$C_{ox} = \varepsilon_o \varepsilon_r \frac{1}{d} \tag{5.19}$$

For this formula $\varepsilon_o$ is the permittivity of a vacuum ($8.854\times10^{-12}$ $\frac{F}{m}$), $\varepsilon_r$ the relative permittivity for a given dielectric material and d the thickness of the material. For 300 nm thick $SiO_2$ the $\varepsilon_r = 3.9$, which results in:

$$C_{ox} = \varepsilon_o \varepsilon_r \frac{1}{d} = 11.5 \frac{nF}{cm^2} \tag{5.20}$$

**Tool specifications**

The electrical characterisation of the TMD devices was carried out using two systems, one in vacuum ($\sim10^{-6}$ mbar) and the other in atmospheric conditions. The system at atmospheric pressure was a Karl Suss probe station connected to a Keithley 2612A source meter, where the vacuum system was a Janis probe station connected to another Keithley system. The voltage was applied through needle-probes, contacting gold electrodes deposited on the TMD films. The measured current was gathered and plotted automatically using Labview software to give current-voltage curves.

# Part IV

# Results & Discussion

# 6 Parametric Study on the CVD Growth of $WSe_2$

Tungsten diselenide ($WSe_2$) is a semiconducting material in both bulk and monolayer form. Bulk $WSe_2$ has an indirect band gap of 1.2 eV which transitions to a direct band gap of 1.65 eV in the monolayer material.[163] The material differs from other TMDs as it has relatively smaller effective electron and hole masses and is ambipolar.[197] Due to the ambipolar properties of $WSe_2$, the material can be used as both a n-type or a p-type charge carrier material, depending on the contact material.[198–201] The formation enthalpy for $WSe_2$ is negative ($\Delta H_S$ $\sim$-151.4 kJ $mol^{-1}$), indicating that the formation of $WSe_2$ is thermodynamically favorable.[202]

Different synthesis methods have proved to be successful for TMD production. All of these methods have associated drawbacks, such as a low throughput as is the case for mechanical exfoliation[3,85], small flake sizes, for liquid exfoliation[87], or result in poly-crystalline material, as in case of thermally assisted conversion.[102,103] Mechanical exfoliation can be used for test purposes, whereas LPE has applications in catalysis and TAC in gas sensing.[49] When large-area, crystalline monolayers are required, for example for the use of TMDs in some scalable (opto-) electronics applications, chemical vapor deposition (CVD) is considered the optimal growth method, due to the bottom-up approach, high crystallinity, flake size control and control over the number of layers.[203]

In CVD, both the nucleation rate and the material thickness can be controlled through the growth parameters. The fundamental growth parameters in CVD include: reaction precursors, temperature, reaction time, gas flow and pressure. In order to improve the growth of large crystalline monolayer $WSe_2$ these parameters need to be optimised. Some research has been done on the effects of reaction temperature,[204,205] precursors[154,205] and gas flow[206,207] on the CVD growth of $WSe_2$, where the effect of the reaction time and pressure has been less studied.

In this chapter, the CVD growth of $WSe_2$ in a microreactor is optimised by a parametric growth study. In the standard CVD process for TMD synthesis the metal precursor is a gas or a solid heated to the gas phase and is transported through the reactor to the growth substrate. This contrasts with the microreactor CVD where the metal precursor is brought in close proximity to the growth substrate, as previously described by O'Brien *et al* for $MoS_2$.[208] The microreactor CVD furnace setup is described in subsection 5.1.3

Due to the close proximity between the metal precursor and the substrate, the loss of source material during the reaction is minimal, therefore less metal precursor is needed for growth. As a minimal amount of precursor is required the furnace is less polluted. This is necessary as multiple selenide TMDs are synthesised in the furnace setup used in this chapter, and unintentional cross-contamination is to be avoided. A minimal amount of precursor is also advantagous from a resource efficiency point of view. The close proximity with the precursor also results in a better reaction rate as the narrow gap, or micro-cavity, between the metal precursor and growth substrate improves the reaction rate of the $WSe_2$ as well as resulting in better reaction control over the nucleation density. Finally the use of a microreactor allows for the possibility of placing features in defined locations on the growth substrate.[208]

Increasing the reaction time is expected to result in higher nucleation density and therefore more surface coverage. During the extended reaction time a greater quantity of the reactants will have evaporated, resulting in more nucleation on the surface. The increasing availability of precursors with time leads to a higher concentration of gaseous precursors and so an increased concentration of gaseous precursors leads to a higher reactivity.[209] A higher reactivity can also result in multilayer formation as the deposition rate increases, while the $SiO_2$ surface cannot adsorb all of the reaction products.

Precursors determine the reaction mechanism and the required energy needed for the reaction. Not only can precursors determine this, some precursors can promote nucleation on the surface, such as the use of halide precursors.[210] However, these precursors can also result in contamination of the surface, for example carbon contamination when using $(CH_3)_2Se$ as selenium precursor for the synthesis of TMDs.[154]

To overcome the energy barrier for reactions an activation energy is required to initiate the reaction. Often heat, high temperature, is used as energy source. Increasing the temperature therefore results in overcoming the energy barrier and a higher reaction rate. A strongly increased reaction rate can however result in a very high degree of nucleation, thereby limiting the lateral growth of the flakes. However, the use of a temperature below the activation temperature, besides when a plasma source is used, will not result in any TMD formation.

Changing the pressure in the furnace will have numerous effects. Firstly, due to the increased pressure more atoms/molecules will be present in the reaction tube, thus a high pressure will result in a higher flux of molecules on the surface and more collisions between the molecules present in the atmosphere. In theory, a higher pressure should result in more collisions between the different molecules and therefore result in a higher rate of reaction, but the higher collision rate could also damage the newly formed material. However, a vacuum environment for the CVD process is recommended as this removes additional molecules in the atmosphere which can contaminate the surface and hinder the reaction. The vacuum in the system results in a low-pressure regime. Secondly the increase in pressure will lead to a

higher evaporation temperature of the solid precursor materials. A higher evaporation temperature results in less evaporation and thereby a lower concentration of reagents in the furnace.

Another parameter is the gas flow in the furnace. A gas flow in the furnace is required to transport the precursors and possibly products through the tube. When the gas flow is limited it will not be able to transport the Se efficiently to the metal precursor as well as the growth substrate. In contrast, when the gas flow is too high metastable formed nuclei could break down due to the high gas flow or the impact of the fast precursor particles on the surface.

## 6.1 Precursors

In section subsection 5.1.2 an overview of different tungsten precursors for the synthesis of $WSe_2$ was given. In this section the results that the different precursors yielded are shown and discussed. For CVD of TMDs there are two categories of precursors: organic and inorganic precursors. An organic precursor, such as $M(CO)_6$, will typically need less activation energy i.e. the precursor requires a lower temperature in the CVD process due to a lower melting point. A major downside of organic precursors is carbon contamination. The metal-organic precursor can leave behind organic residues under certain conditions, which can remain on the substrate when using a low deposition temperature. This carbon contamination can be minimised by the use of a pure 100% $H_2$-flow.[154,211,212]

Inorganic precursors are generally more stable compared to metal-organic precursors. Thus, the resulting CVD process will have higher activation energy and require a higher deposition temperature. Examples of inorganic precursors are the pure metals and metaloxides ($MO_x$). Lowering of the melting temperature of these can be achieved by additives such as halides.[210,213]

The state of the precursor and the transport of the precursor to the substrate are important factors. The precursor can be transported through the furnace to the growth substrate[214] or it can be placed directly under the substrate, by placing metal powders in the reaction tube or boat, or by depositing the precursor on a seed substrate, thereby creating a microreactor.[208] Before the reaction the precursor can be in either solid or gaseous state. Due to instrumental limitations, the setup used in this work can only handle solid precursors, which limits the variety of precursors, but still results in a choice between powders, pellets and solid seed layers for the W precursor.[208]

O'Brien et al.[208] showed the successful use of a seed layer to grow TMD flakes. This growth method results in good transport of the metal source to the substrate and provides control over the amount of metal precursor used in the reaction. For these reasons, a solid seed layer was used in the CVD process described here.

Exfoliated $WO_3$ flakes have previously been shown to be a successful precursor for the creation of $WSe_2$ flakes,[208] the exfoliated $WO_3$ therefore appears to be a

reasonable option as a CVD precursor for CVD growth of $WSe_2$. To deposit the material on the seed substrate the dissolved solution was drop casted on the surface at 150 °C, leading to the formation of concentrated $WO_3$ circles on the surface. After drop casting the seeds were used as a metal precursor for the CVD process.

The use of exfoliated $WO_3$ as precursor resulted in the formation of small areas with tiny $WSe_2$ flakes, with lateral dimensions of ∼0.5-2 $\mu$m on the substrate according to optical microscopy image, See Figure 6.1(a). To confirm whether the formed flakes are $WSe_2$ and to inspect the quality of the $WSe_2$ Raman spectroscopy was performed.

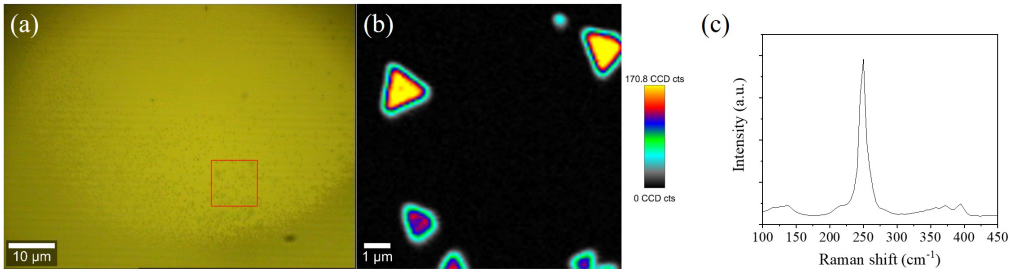


Figure 6.1: Results of CVD growth of $WSe_2$ flakes with exfoliated $WO_3$ as precursor. (a) Optical microscopy image of sample. Red inset shows area where Raman map. (b) Raman map of peak intensity at 250 $cm^{-1}$. (c) Raman spectrum of sample. Spectrum indicates the presence of $WSe_2$ due to the overlapping $E^1_{2g}/A_{1g}$ peak, the 2 LA(M) peak indicates multilayer $WSe_2$.

The Raman spectrum of $WSe_2$ should shows an overlap of the $E^1_{2g}$ peak and $A_{1g}$ peak at ∼250 $cm^{-1}$ for mono and few layer $WSe_2$, when probed with a 532 nm excitation laser as shown in Figure 6.2) The full width half max (FWHM) gives an indication of the quality of the material, a small FWHM indicates a low amount of scattering events and therefore a more crystalline surface. The overlapping Raman peaks can be instrumentally resolved by increasing the grating to 2400 lines/mm [163] but this peak overlap is not of significance for this work. Other than the $E^1_{2g}$+$A_{1g}$ peak there is the 2LA(M) peak, a second-order Raman mode due to LA phonons at the M point in the Brillouin zone, which shows up in the Raman spectrum as a shoulder of this peak at ∼260 $cm^{-1}$.

The Raman intensity map obtained for the $WSe_2$ flakes grown by using exfoliated $WO_3$ is shown in Figure 6.1(b). This map is the intensity map at 250 $cm^{-1}$, corresponding to the $E^1_{2g}$+$A_{1g}$ peak, and clearly shows the flakes, indicating that the flakes are $WSe_2$. The difference in intensity is due to layer thickness as the peak is more intense for monolayer $WSe_2$ compared to bi- and few layer $WSe_2$. The averaged Raman spectrum in Figure 6.1(c) confirms the observations from the Raman map, the spectrum clearly shows the main peak at 250 $cm^{-1}$, indicating the presence of $WSe_2$. The 2LA(M) peak is present as well as a shoulder of the $E^1_{2g}$+$A_{1g}$ peak.

In an attempt to improve the distribution of the $WO_3$-precursor during drop casting, and thereby the synthesis of $WSe_2$, the temperature at which the $WO_3$ was drop casted was varied. However, there did not appear to be any noticeable

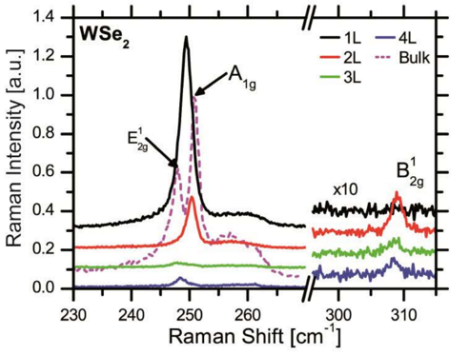


Figure 6.2: Raman spectra of monolayer, bilayer, few layer and bulk $WSe_2$. Adapted from Tonndorf *et al.*[163]

improvement in the distribution of $WO_3$ on the surface, or the growth of $WSe_2$. From this it can be concluded that though there are $WSe_2$ flakes formed during the synthesis with this process the coverage is low and the lateral dimensions of the flakes are relatively small.

A second possible metal precursor is tungsten hexachloride ($WCl_6$). $WCl_6$ has a reasonably low melting temperature ($T_m$) of 275 °C, and has previously been used for the CVD synthesis of both $WS_2$ and $WSe_2$.[205,210] Therefore it is a reasonable assumption that growth of $WSe_2$ with the micro-reactor CVD process should be possible. Following the sample preparation described by Thangaraja et al.,[210] $WCl_6$ powder was dissolved in ethanol (EtOH) as a 0.05 M solution and drop casted on the surface. Dissolution of $WCl_6$ in EtOH resulted in a change of colour of the solution over time (approximately 2-3 days) from yellow to a clear colourless solution. The colour change is caused by the reaction of $WCl_6$ with the EtOH. When $WCl_6$ comes in contact with EtOH the ethoxy groups from the EtOH replace the chloride groups in $WCl_6$.[215]

$$WCl_6 + nC_2H_5OH \rightarrow W(OC_2H_5)_nCl_{6-n} + nHCl \tag{6.1}$$

The use of the $WCl_6$ precursor in EtOH resulted in minuscule, sub micrometre sized crystalline shapes on the surface of the growth substrates. (See Figure 6.3(a)) It appeared as if these crystalline species had migrated from the seed layer to the growth substrate and afterwards partially reacted with the selenium as identical structures were apparent on the adjacent seed layer. The crystalline material appeared to be $WO_3$ by inspection with optical microscopy, due to the rectangular features. However the Raman spectra of $WSe_2$ in Figure 6.3 shows a small overlapping $A_{1g}/E^1_{2g}$ peak at ~250 $cm^{-1}$, but the spectrum obtained also contained peaks at wavelengths specific for $WS_2$, the $E^1_{2g}$ peak around ~350 $cm^{-1}$ and the $A_{1g}$ peak at ~417 $cm^{-1}$. The presence of $WS_2$ peaks in the spectrum is odd but could possibly be attributed to sulfur contamination from the lab environment. However, none of the Raman spectroscopy for the other precursors showed a peak at 350 $cm^{-1}$, therefore it could be possible that the peak originates from the formed $W(OC_2\ H_5)$,

due to the reaction of $WCl_6$ with the EtOH.

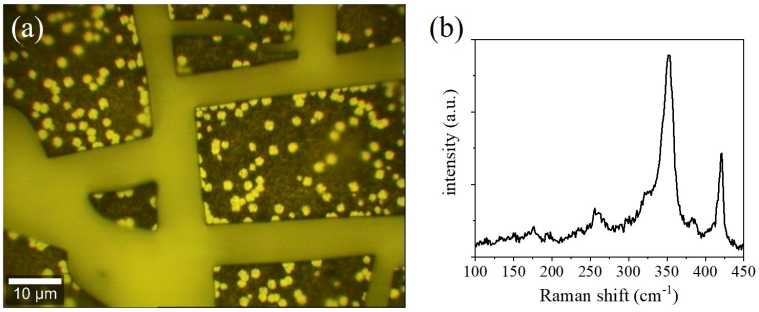


Figure 6.3: Results of CVD growth of $WSe_2$ flakes with $WCl_6$ dissolved in ethanol as precursor. (a) Optical microscopy image of sample. (b) Averaged Raman spectrum from point scans of the surface.

As it was not possible to determine whether the transfer of flakes from the seed layer to the substrate was due to the formed $W(OC_2H_5)_nCl_{6-n}$ as a result of dissolving the metal precursor in ethanol, $WCl_6$ was subsequently dissolved in chloroform instead of ethanol. In chloroform no side products are formed. Concentrations of 0.05 M and 5 mM $WCl_6$ dissolved in chloroform were used for the the CVD growth. The $WCl_6$ in chloroform was drop casted similar to the previous solution. Small areas of the surface were covered with barely resolvable crystalline features. The main part of these features did not show a discernible Raman signal, though a limited number of $WSe_2$ flakes, 5–10 per $cm^2$, were present on a few samples, as shown in Figure 6.4. These $WSe_2$ flakes were very limited in size, each being approximately 1 $\mu$m in length.

The use of dispersed tungsten precursors was relatively unsuccessful, probably in part due to the low solubility of $WO_3$ and $WCl_6$,[216] and thus the production of poorly dispersed metal precursors on the seed substrate. Due to the low solubility, and lack of exfoliation, of $WO_3$ a solid polycrystalline film as a precursor is expected to yield better results. The large film increases the concentration and homogeneity of the metal precursor, where a polycrystalline surface increases the available surface area. Layers of tungsten (10, 15 and 20 nm) were sputtered on $SiO_2$/Si seed substrates,

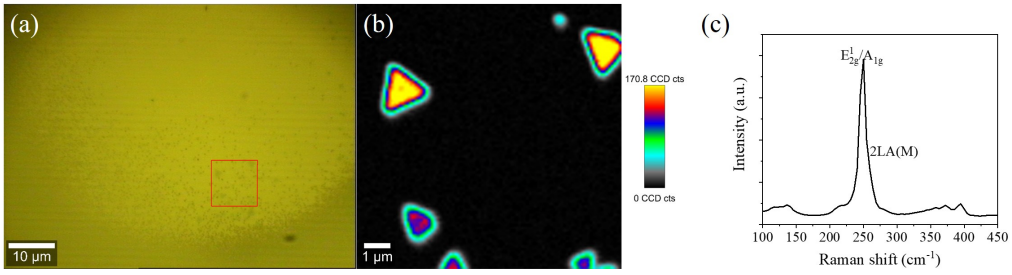


Figure 6.4: Results of CVD growth of $WSe_2$ flakes with $WCl_6$ dissolved in chloroform as precursor. (a) Optical microscopy image of sample. Red inset shows area where Raman map. (b) Raman map of peak intensity at 250 $cm^{-1}$. (c) Raman spectrum of sample. Spectrum indicates the presence of $WSe_2$ due to the overlapping $E^1_{2g}/A_{1g}$ peak, the 2 LA(M) peak indicates multilayer $WSe_2$.

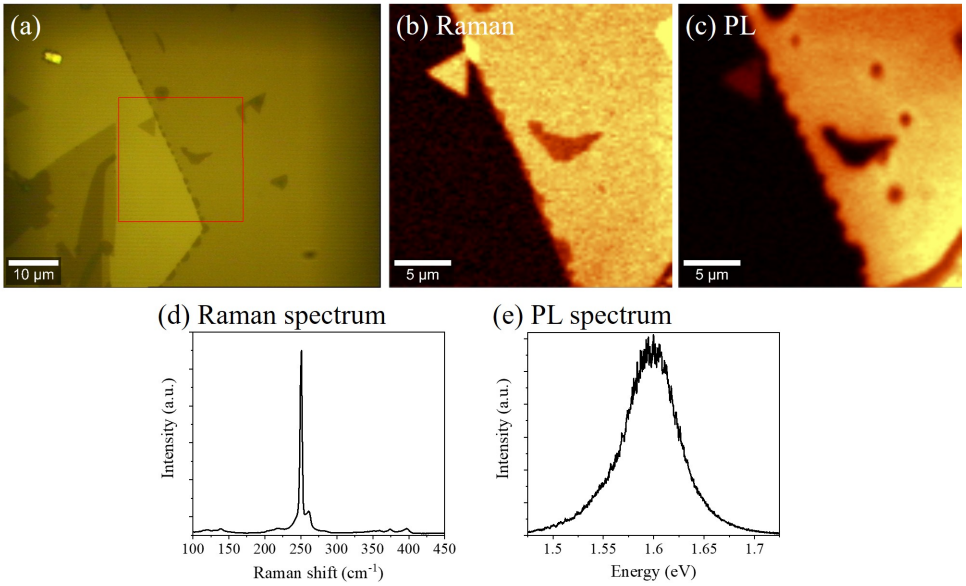


Figure 6.5: (a) Optical microscopy image of $WSe_2$ growth. (b) Raman intensity map of surface at ∼250 $cm^{-1}$ which shows flakes produced by $WO_x$ film seed layer, where (c) shows the PL intensity map at ∼1.6 eV and (d) and (e) show respectively the Raman spectrum and PL spectrum of the sample

followed by an oxidation step with a programmable hot plate, 60 min at 500 °C in atmospheric conditions, to create tungsten oxide ($WO_x$) layers. After this oxidation $WSe_2$ flakes are obtained after CVD on the growth substrates for the 15 and 20 nm $WO_x$ seed layers.

The samples from both 15 and 20 nm $WO_3$ films, resulted in $WSe_2$ flakes present on the surface, though an increase in the amount of W yielded better results. The $WSe_2$ grown with 20 nm W (ox) resulted in reasonably large flakes with sizes of 5-50 $\mu$m, see Figure 6.5(a). The Raman signal is uniform over the surface as shown in the Raman map in Figure 6.5(b) and the spectrum shows a clear $E^1_{2g}$+$A_{1g}$ peak of $WSe_2$ in Figure 6.5(d). The flakes were also mainly monolayer $WSe_2$, as indicated by the PL map at 1.6 eV and the PL spectrum, as shown in Figure 6.5(c) and (e). An issue with these growth parameters is that the flakes are mainly concentrated near the substrate edges. The size and number of flakes decreases exponentially from the edge towards the centre of the substrate. A possible theory is that due to the abundance of the $WO_x$ seed layer in the confined volume of the micro reactor migration of the Se vapour across the surface is restricted, thereby preventing the formation of $WSe_2$. The Se vapour can only be efficiently transported a few 100 $\mu$m into the sandwiched structure.

Controlling spacing between the seed and substrate layers could possibly allow greater Se flow within the micro reactors, thereby opening the possibility of improved surface coverage. Another approach is reducing the volume of seed material by masking during the initial sputtering of the 20 nm W, this was attempted by producing an array of dots with a diameter of 100 $\mu$m, on the seed layer. However, the use of the dotted array resulted in the formation of relatively few and small

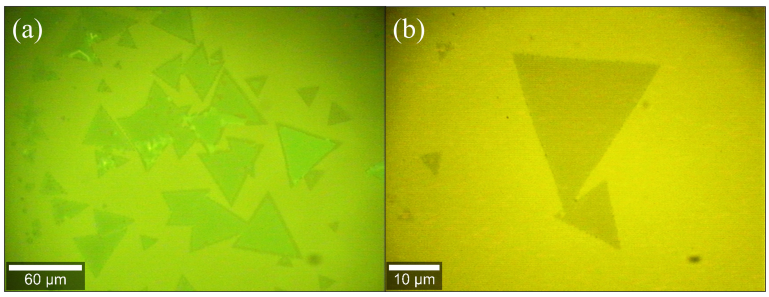


Figure 6.6: Optical microscopy images of $WSe_2$ growth. (a) Shows flakes produced by WOx film seed layer, where (b) shows the surface when using both a $WO_x$ layer and $WO_x$ dots.

$WSe_2$ flakes within the dots. Moreover, the number of flakes on the surface was limited to areas on the surface where the $WO_x$ dots came into contact with the growth substrate. In Figure 6.6 optical microscopy images of flakes contained in the dot area are shown. A slight increase in surface coverage, <5%, was shown within the deposited dots, most likely due the gasses being able to flow more freely between the seed layer and the growth substrate, resulting in a better diffusion of the precursors. This increase in coverage was not of sufficient benefit to warrant the additional effort required to pattern the seed layers for the focus of this study. However, this method could be useful when $WSe_2$ flakes in small localised areas are required.

It appears that the use of sputtered W followed by an oxidation step is the most successful precursor tested. While other precursors, such as $WCl_6$ in EtOH and exfoliated $WO_3$ flakes in IPA, also result in the growth of $WSe_2$ flakes and therefore may be considered as appropriate precursors for other setups or other growth methods such as ALD and will be used in the following sections. Additional refinements to the seed layer, such as creating spacing between the seed layer and substrate by adding $WO_3$ dots on the surface, have not as yet had a significant positive impact on the growth, but other approaches can be attempted, such as other deposited $WO_x$ structures on the seed layer to improve the diffusion of the gaseous precursors and thereby coverage in the centre of the growth substrate.

## 6.2 Reaction time

The effect of the duration of the reaction on the CVD growth of $WSe_2$ was investigated by varying the reaction time between 30 and 60 min. using 10 min. intervals. The sputtered and oxidised W films, as described in the previous section, were used as metal precursor. Other reaction parameters were kept constant with a forming gas flow of 150 sccm, a pressure of 1.5 Torr and a reaction temperature of 850 °C. In Figure 6.7 the optical microscopy images for the growth at the different reaction times is shown.

Increasing the reaction time results in more $WSe_2$ grow. Possibly due to a greater density of nuclei on the surface, or do to increased growth of nuclei due to the

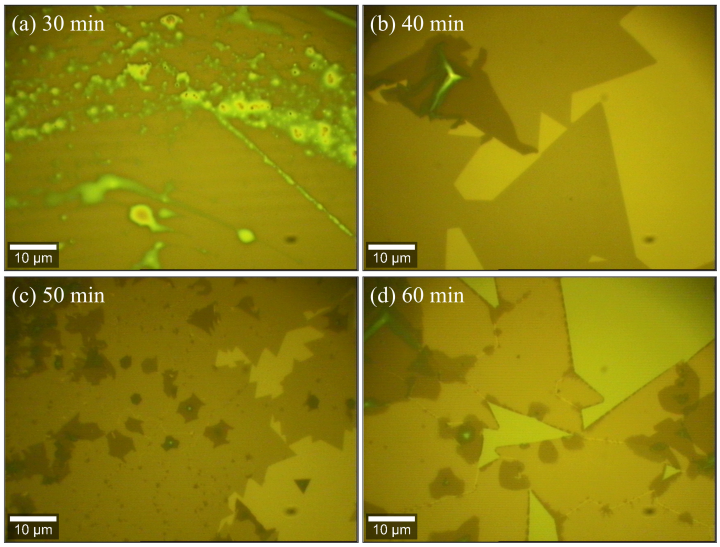


Figure 6.7: This figure shows the influence of the reaction time on the growth of $WSe_2$. (a-d) are optical microscopy images of the results obtained at different reaction times. (a) Shows the surface for a 30 min. reaction. (b) 40 min. (c) 50 min. and (d) 60 min.

increased dwell time. The most notable characteristic for the variation in reaction times is the lack of flakes for the 30 min. reaction samples as shown in Figure 6.7(a). Only slight traces of tungsten oxide, which have most likely evaporated from the seed layer, are present on the surface. For increasing reaction times, see Figure 6.7(b-d), the results show an increase in coverage, due to a higher degree of nucleation. The $WSe_2$ surface coverage, on a 1x1 cm $SiO_2$ growth substrate, increases from ∼23% for 40 min. to up to ∼40% for 60 min. reaction. (See Figure 6.8(a))

The flake size at 40, 50 and 60 min. also increases with reaction time as shown in Figure 6.8(b). The 40 min. reaction results in an average flake size of ∼19.1 $\mu$m, where the flake size further increases to ∼29.1 $\mu$m for 50 min. and to ∼40.6 $\mu$m for 60 min. reaction. The length of the bisected triangle was used to measure the size of the flakes. When investigating the shapes of the $WSe_2$ flakes for the 40 min. reaction samples, the flakes show clear triangular shapes on the surface, where longer reaction times result in overlapping flakes with more pronounced grain boundaries and multilayer growth.

The higher nucleation and growth rate associated with longer reaction time results in the formation of multilayers, which are present in large amounts on both the 50 and 60 min. growth samples. Multilayer formation can be useful for applications in for example photodetectors[43] and catalysis. Due to the increased nucleation density the formed flakes start to merge together when the flakes come into contact. The merging of flakes results in a continuous monolayer when the flakes have the same orientation, whereas grain boundaries are formed when the orientation of the flakes is different.

When characterizing the samples by AFM (See Figure 6.8(c) and (d)), it becomes apparent that both merging and formation of grain boundaries occurs for the

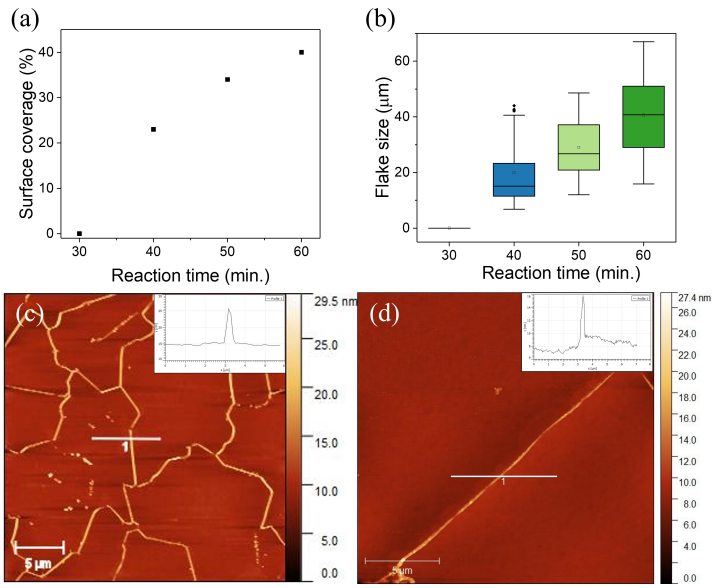


Figure 6.8: Statistical data on the $WSe_2$ growth as well as AFM height images of the surface. The graph in (a) shows the surface coverage. (b) shows a box plot of the different flake sizes, corresponding to the reaction times. For each reaction time 50-100 flakes were measured. In (c) and (d) are the AFM images. The grain boundaries are shown in (c) and flake edges in (d) with height profiles given in the right corner inset.

grown samples as grain boundaries are present on the surface. However, there are also continuous areas visible on the surface which do not have a triangular (or a hexagonal) shape, as is the case for individual $WSe_2$ flakes, where grain boundaries are absent, indicating the merging of different flakes. The grain boundaries on the surface can be clearly observed by AFM, due to the height difference of the grains, where grain boundaries are practically invisible when inspecting the sample with optical microscopy or Raman spectroscopy. From the AFM measurements the conclusion can also be drawn that the thickness of the flakes is ∼1 nm, which is thicker than the theoretical value of ∼0.7 nm on $SiO_2$/Si.[200], but which is consistent with other AFM measurements of monolayer $WSe_2$ flakes.[175]

Increasing the reaction time leads to larger flakes and higher surface coverage. The increase also results in multilayer growth of $WSe_2$. For a high coverage a higher reaction time, such as 50 or 60 min., is beneficial, when monolayer growth is preferred a reaction time of 40 min. can be considered optimal as this time results in reasonable sized flakes which are predominantly monolayer.

## 6.3 Temperature

Increasing the reaction temperature can stimulate the reactivity, the energy from the heat enables the formation of $WSe_2$ as it helps reaching the required activation energy. The melting point of $WO_3$ is 1473 °C at 1 atmosphere (atm), however the melting point is reduced with decreasing pressure as shown in Figure 6.9(a).[217] In

literature the reaction temperature for $WSe_2$ CVD growth is typically in the range of 850 - 1050 °C.[36,154]

Temperatures used in these experiments ranged from 750 – 900 °C. CVD growth of $WSe_2$ only successfully occurred when the reaction temperature was 850 °C or higher for the primary ramp of the temperature. Huang et al.[36] suggested that a higher temperature in the high-temperature heating zone followed by a sub-cooling step to the reaction temperature before the introduction of the selenium vapour in the furnace will cause a reduction of the $WO_3$ by the forming gas.

$$WO_3 + H_2 \rightarrow WO_{3-x} + H_2O \tag{6.2}$$

The reduced $WO_{3-x}$ is supposed to result in more nucleation which creates higher surface coverage and larger flake sizes. In theory this would suggest that having a lower intermediary temperature before ramping up to the reaction temperature or constant temperature would negatively influence the reaction, therefore a comparison between a constant reaction temperature of 850 °C, as shown in Figure 6.9(b) is compared to a reaction where the temperature is first ramped up to a higher temperature and then lowered down to the reaction temperature, which can be seen in Figure 6.9(c). The difference in the temperature stages does not lead to a difference in coverage, however the grain size increases when the temperature is initially ramped up. The grain size increases to about 3x the size when $T_1$=950 °C.


Figure 6.9: (a) Graph showing the melting temperature of $WO_3$ under different pressures,[217] (b) shows an optical microscopy image of a sample where the run temperature was kept constant at 850 °C. (c) Shows an optical microscopy image of a sample in a run with $T_1$ = 950 °C and then lowered to $T_2$ = 850 °C.

Both temperature ranges result in the formation of $WSe_2$ and result in a similar surface coverage. For FET applications a larger grainsize is better as this decreases electron scattering at grain boundaries, however for catalytic applications a higher density of grain boundaries is preferred. Therefore, both temperature ranges can be used for different applications. If the grain size does not make a large difference a reaction temperature of 850 °C would be preferable as this is more economical, however if large grain boundaries are required it would be better to initially ramp the temperature of the CVD process up to 950 °C.

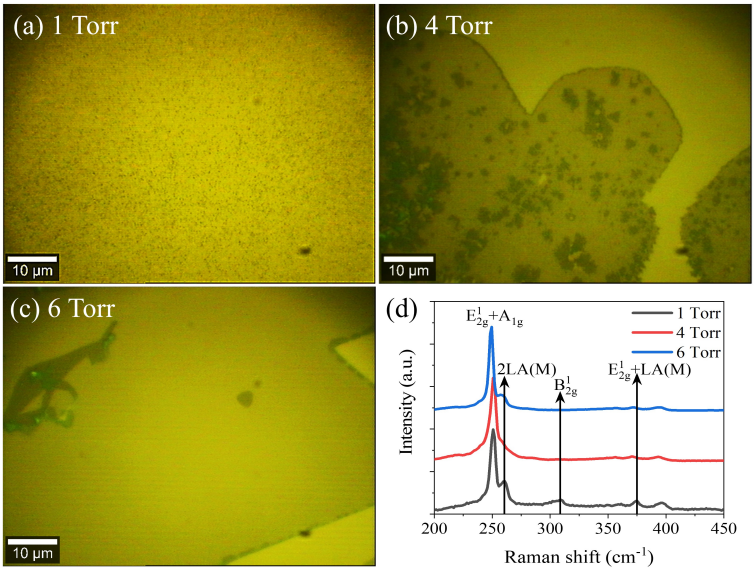


Figure 6.10: Influence of the pressure on the CVD growth of $WSe_2$. In (a), (b) and (c) optical microscopy images are shown for respective pressures of 1, 4 and 6 Torr. (d) Shows the Raman spectra for $WSe_2$ grown at those pressures.

## 6.4 Pressure

Under atmospheric pressure particles can move freely over the surface and particles other than the precursors will be present on the surface. A lower pressure, or vacuum, will remove the non-precursor particles which can influence the reaction or contaminate the surface. Decreasing the pressure however also leads to a more static environment in which the particles have a lower velocity, lesser movement over the surface, and are less reactive.

To obtain an optimised pressure for the growth of large area monolayer $WSe_2$ different pressures were tested ranging from 1 to 6 Torr ($\sim$1.3x10$^{-3}$ – 7.9x10$^{-3}$ atm). For this growth a reaction time of 40 min., obtained as the best value for monolayer growth in section 6.2, was used. Even though the tested pressure range is in the low vacuum range, the change in the pressure appears to have a significant influence on the $WSe_2$ growth as shown in Figure 6.10

In the 1 Torr pressure regime a high nucleation density is visible on the surface, as shown in Figure 6.10(a). However, the formed nuclei do not grow further out into flakes at this pressure. When increasing the pressure the nucleation on the surface decreases but the flake size increases, this agrees with several literature reports. [218,219]

The reduction in nucleation is possibly due to the diminished flow of the reagents and particles in the reaction tube. This decreased flow means that the particles have a reaction energy which is too low to create many nucleation sites, thereby causing less nucleation. The slower flow does result in a higher residence time, which means that a higher concentration of reactants is present in the tube. The higher concentration of reagents improves the ongoing growth of the flake, which requires a lower reactivity than nucleation, as this results in more collisions between the reagents.

This trend of increase in flake size with increasing pressure becomes apparent in the optical microscopy images in Figure 6.10(b) and (c) and the corresponding Raman spectra for the different pressures in Figure 6.10(d)

The optical microscopy images show that increasing the pressure results in larger flake sizes. For 1 Torr, the lowest pressure, only small $WSe_2$ nuclei are present on the surface, where the flakes expanded to ∼10–20 $\mu$m for 4 Torr and the nuclei grow further to form large flakes with flake sizes larger than 100 $\mu$m for 6 Torr. Not only the flake size does expand, the coverage of the growth substrate also increases. The lower pressure samples only had CVD flakes on the outer edges of the sample, covering about ∼15% of the surface, according to optical microscopy images, where the surface coverage is increased to ∼47% for 6 Torr. The increased pressure and the thereby higher rate of collisions is expected to have resulted in a deeper penetration of the selenium containing vapors (Se, $H_2Se$) between the sandwiched seed layer and growth substrate, as well as surface diffusion. This results in more reaction over the total surface.

As there does not seems to be any negative effect on the growth when increasing the pressure, it seems apparent that the change in pressure is too small to have a measurable effect on the evaporation temperature of the reagents. The increased collision rate does not appear to damage the newly-formed nuclei, only an increase in the size of the flakes is observed. Following this trend a further increase of the pressure would be expected to lead to even larger flake sizes.

The Raman spectra of the flakes grown at different pressures show a slight red shift for the overlapping $E^1_{2g}$ and $A_{1g}$-peaks of $WSe_2$ at ∼250 $cm^{-1}$ for the higher pressure, as shown in Figure 6.10(d).[163,175] The 1 Torr spectrum also shows peaks at ∼310 $cm^{-1}$ and ∼375 $cm^{-1}$ corresponding to the $B^1_{2g}$ and $E^1_{2g}$+LA(M) modes. These modes do not appear for monolayer $WSe_2$ but are only visible in few layer $WSe_2$ and support to the theory that there is no flake growth on the surface at this pressure but only the formation of small nuclei.[127,163,175]

Further characterization of the samples produced at 6 Torr was done by Raman spectroscopy and photoluminescence spectroscopy as shown in Figure 6.11. In the Raman spectra and maps, Figure 6.11(b) and (c), a decrease in peak intensity of the combined $E^1_{2g}/A_{1g}$ peak is visible for the increasing layer thickness. There is an increase in intensity for the 2LA(M) mode, a second order mode due to LA phonons at the M point in the Brillouin zone.[220] The intensity of the peak increases with the number of layers which is also the case for the $B^1_{2g}$ and $E^1_{2g}$+LA(M) modes. These observations are in agreement with previous reports.[221,222]

In the PL map and spectra, Figure 6.11(d) and (e), a large decrease in PL intensity is observed with increasing layer number as well as a shift in the peak going to lower energies going from 1.6 eV in the monolayer to 1.5 eV in the trilayer material. The photoluminescence peak is expected to shift from 1.6 eV in monolayer to 1.2 eV in bulk $WSe_2$[163] and intensity of the PL peak exponentially increases with decreasing layer number.[208] The decrease in intensity is expected due to elaborate

changes in the band structure as the material transitions from a direct to indirect band gap.[32,161] The shift to lower energies observed here for the few layer $WSe_2$ is not as pronounced as would be expected, though this shift can be influenced by many parameters such as defects and doping.

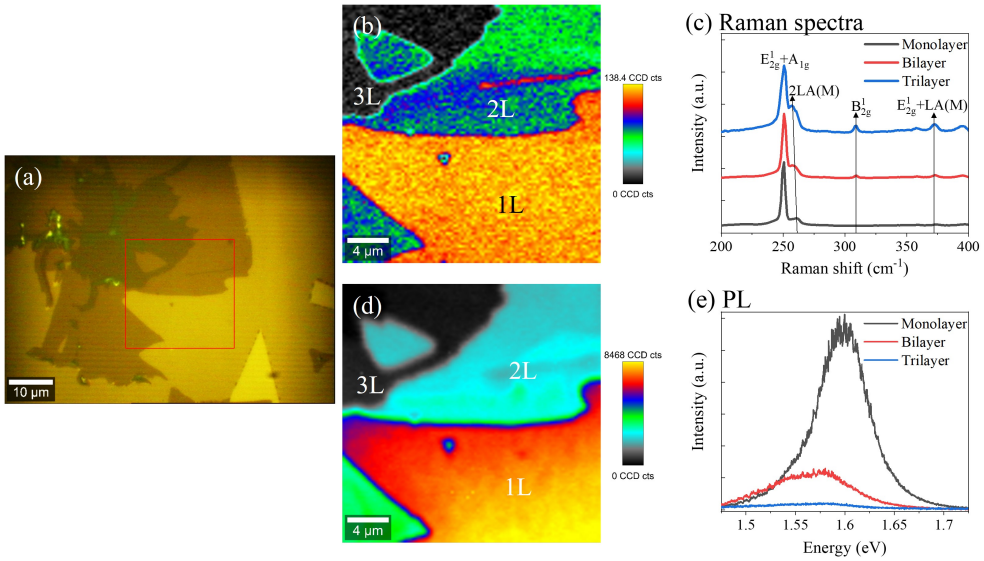


Figure 6.11: Optical microscopy, Raman spectroscopy and PL data for $WSe_2$ grown at 6 Torr. (a) Optical microscopy image, (b) Raman intensity map $E^1_{2g}+A_{1g}$ peak, (c) Raman spectra of 1L, 2L and multilayer $WSe_2$, (d) PL intensity map of A exciton and (e) PL spectra of 1L, 2L and multilayer $WSe_2$

## 6.5 Gas flow

Gas flow is of crucial importance in the reaction. When the gas flow is too low, Se will not be efficiently transported through the furnace to the sample. However, when the gas flow is too high, metastable formed nuclei might break down due to the gas flow or the impact of the fast and large Se particles on the surface. A higher gas flow is also more likely to result in a turbulent gas flow in the reaction tube when coming into contact with obstacles such as the tube walls and the sample boat.

In most literature a flow of argon (Ar) and forming gas ($Ar/H_2$ or $N_2/H_2$ gas mixtures) between 5 sccm and 200 sccm are reported for CVD processes for TMD growth. In the standard setup used in this work the gas flow of the forming gas ($Ar/H_2$ 9/1) was set to 150 sccm which is sufficient to transport the Se through the furnace to the growth substrate. To increase nucleation on the surface a low gas flow would appear to be a rational choice, while a higher gas flow could possibly increase the size of the flakes.

When the gas flow is reduced the pressure decreases automatically as well, due to the decrease in gas molecules. To obtain reliable results the pressure was kept constant at 4.0±0.1 Torr. The different gas flows examined were 50, 100, 150, 200 and 250 sccm, for which the results are shown in Figure 6.12. The flake size and coverage decreases with increasing gas flow from 100 sccm, however there is

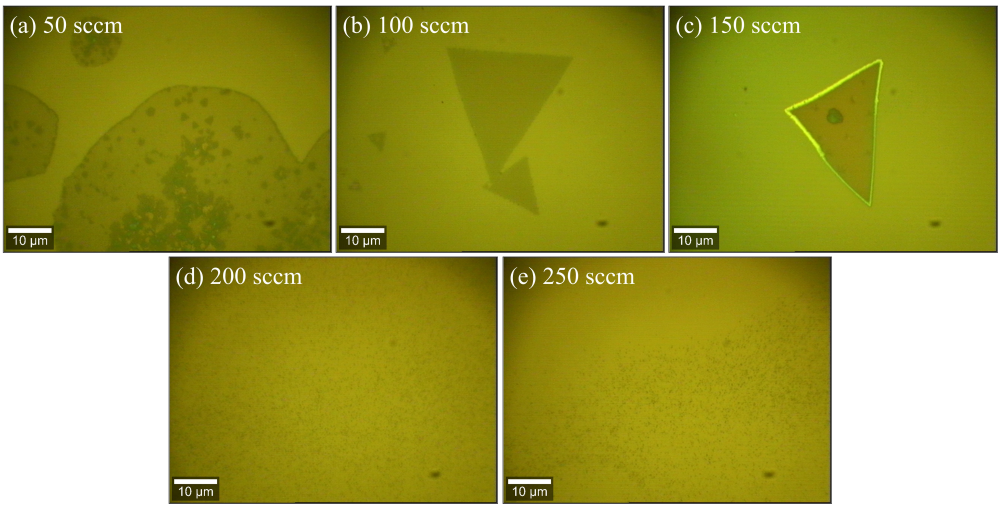


Figure 6.12: Influence of the gas flow on the CVD growth of $WSe_2$. Different optical microscopy images of $WSe_2$ grown using different gas flows are shown. With (a) 50 sccm, (b) 100 sccm, (c) 150 sccm, (d) 200 sccm and (e) 250 sccm.

$WSe_2$ present on the surface for all gas flows. For 200 and 250 sccm, shown in Figure 6.12(d) and (e), the flakes are very polycrystalline with lateral flake sizes below 0.5 $\mu$m. At the lower pressure the flakes are noticeably larger. The nucleation density on the surface decreases and gives way to lateral growth.

The gas flow regimes tested which yield the best results are 50 and 100 sccm. For 50 sccm, see Figure 6.12(a) the growth mode appears to be mainly a Stranski-Krastanov mode, layer plus island growth, where the 100 sccm growth, see Figure 6.12(b) is a Frank-Van der Merwe growth mode, layer by layer growth. Frank-Van der Merwe is preferable to Stranski-Krastanov when complete monolayer coverage is desired. With growth at 50 sccm a higher nucleation density as well as coverage is present on the surface, while 100 sccm results in a higher crystallinity of the surface. Depending on the needs of the application of $WSe_2$ either could be more beneficial.

## 6.6 Devices

$WSe_2$ is less studied as a FET material, compared to $MoS_2$, although it has many advantageous properties. Most TMDs exhibit natural n-type conduction, with p-type behaviour achieved through doping or coupling.[223,224] This is in contrast with $WSe_2$ which shows predominantly p-type conduction or ambipolar behaviour.[206,225–227] $WSe_2$ also has an indirect bandgap (1.0–1.2 eV) in the bulk form and shows a transition to a direct gap of 1.6 eV when it is thinned down to the monolayer form.[220,228]

Literature on $WSe_2$ FETs indicates a good field-effect mobility which is controllable by temperature and bias voltage,[229,230] a perfect subthreshold swing ~60 mV/dec[200] and an on/off ratio up to 8 orders of magnitude.[231] The ambipolar behaviour of $WSe_2$, can be controlled by selection of the contact metal and varying deposition method of the contacts.[198,232,233] Different contact metals will promote

hole or electron injection.[204,225] The interaction or bond which the contact metal forms with the $WSe_2$ also influences the properties of the FET.

A challenge for $WSe_2$ devices for integration in electronics is the formation of low-resistance ohmic contacts. ohmic contacts are often hindered due to the appearance of Schottky barriers, impeding the flow of current in both directions. The formation of Schottky barriers is due to Fermi level pinning, it creates an energy barrier for electrons and holes by bending the bands at the interface, radically degrading the performance of the devices.[234]

Here, the measurement of the electrical properties of monolayer $WSe_2$ flakes was performed on back-gated field effect transistors (FETs). The details for growth parameters for the growth are shown in subsection A.1.1. The patterning of the contacts on the flakes was performed by e-beam lithography, see the optical microscopy image in Figure 6.13(a). The contact metals used were Ni/Au 5/50 nm. Nickel was used as an adhesion layer as it has a better adhesion to the silicon dioxide substrate than the gold, which can easily be scratched away, and the electron affinity of nickel is close to that of $WSe_2$.

For a simple 2-probe device measured in-house the devices are shown in Figure 6.13. The output characteristics ($I_{ds}$ vs $V_{ds}$ curves, Figure 6.13(b)), are very linear which indicates ohmic behavior of the device. The slope of the curves decreases for increased gate voltage. The transfer characteristics ($I_{ds}$ vs $V_{gs}$ curves) are shown in Figure 6.13(c) which display the expected p-type behaviour of $WSe_2$, as p-type or ambipolar behaviour is predominant in $WSe_2$. The on/off ratio is $10^4$ which is in good agreement with values found in literature.[107,235] However, the value is most likely an underestimation as the on/off ratio is limited due to the substrate material and the contact materials. The contacts can result in a Schottky barrier decreasing the on/off ratio, where the substrate here is the growth substrate which is p-type doped $SiO_2$/Si that has been exposed to high (850 °C), which could cause the substrate to become leaky.

The field-effect mobility is derived from the linear slope of the transfer characteristics:

$$\mu = \frac{1}{C_{ox}} \frac{L}{W} \frac{\partial I_{ds}}{\partial V_{gs}} \frac{1}{V_{ds}} \tag{6.3}$$

where $L$ is the channel length, $W$ is the channel width, and $C_{ox}$ is oxide capacitance per unit area.

For a bias voltage of 20 to 100 mV, the field-effect mobility was estimated to be 25-27 $cm^2/(Vs)$, which is comparable to previously reported values for CVD $WSe_2$ devices in the absence of high-k dielectric encapsulation layers and room temperature configuration[205], though this is still low in comparison to exfoliated $WSe_2$ which has values of $\sim$200 $cm^2/(Vs)$.[201] This lower value is most probably due to defects which may be introduced during CVD processes, however CVD offers much better scope for scaling and semiconductor integration than mechanically exfoliated flakes. In these devices the sub-threshold swing is very low, which can partly be attributed to the $SiO_2$/Si growth substrate. The sub-threshold swing could be improved by

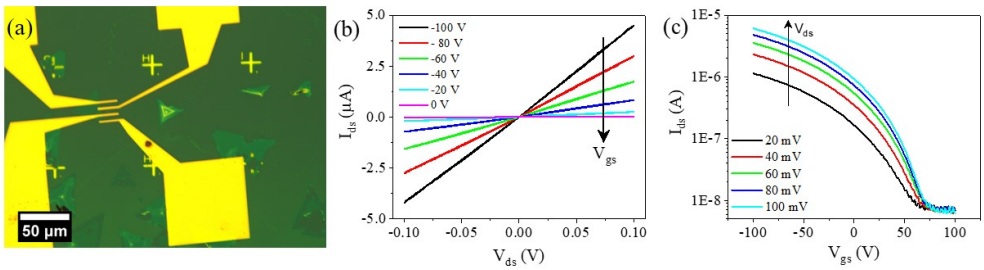


Figure 6.13: (a) Shows the optical microscopy image of the $WSe_2$ device. The electrical characteristics of monolayer $WSe_2$ flakes measured at room temperature are shown in (b) and (c). Figure (b) shows the output characteristics at various gate-to-source voltages ($V_{gs}$ from -100 - 0 V). where Figure (c) shows the on/off current for different source–drain voltages

transferring the $WSe_2$ flakes to a different substrate after growth or by as using a top gate and/or high-$\kappa$ dielectrics.

The electronic characteristics of the $WSe_2$ devices produced by the micro reactor method are comparable to those synthesised by other CVD methods. On top of this, further improvement of the samples and other contact materials, with higher, or better matching, work functions for the p-type material, could improve the performance of the device.

### 6.6.1 Environmental Effects

Different environmental parameters affect the properties of devices. For example this is used in TMD gas sensors or pressure sensors.[58,236] To study these effects on the CVD $WSe_2$ grown with the micro reactor method a collaborative study with Dr. Francesca Urban and Prof. Antonio Di Bartolomeo from CNR-SPIN Salerno was undertaken. This work led to the publication "Environmental Effects on the Electrical Characteristics of Back-Gated $WSe_2$ Field-Effect Transistors" by Urban *et al.*[237].

In this publication the effects of various environmental parameters on $WSe_2$ devices were studied. The material synthesis and device fabrication was performed in-house in the ASIN group lab, while the characterisation of the devices was executed at CNR-SPIN Salerno by Dr. Francesca Urban and Prof. Antonio Di Bartolomeo.

For this research $WSe_2$ flakes were grown by CVD. The growth substrate was P++ RTO $SiO_2$/Si and the growth parameters were similar to those described before. For a complete overview of the CVD growth parameters used to synthesize the samples see Appendix A.3.1. Device fabrication of a back-gated FET on monolayer $WSe_2$ was done by EBL. Using PMMA A3 as e-beam resist channels with a width of ~2 $\mu$m and a length of ~22 $\mu$m were created. A schematic and SEM image of the back-gated FET device are shown in Figure 6.14(a) and (b), respectively. Ni/Au with 5/50 nm thickness was used as the contact material. Further details on the EBL procedure are given in Appendix A.3.1.

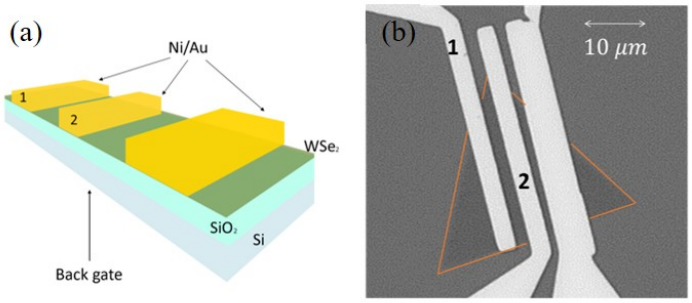


Figure 6.14: (a) Schematic representation of the back-gated FET $WSe_2$ device and (b) SEM image of the contacted device. Images are adapted from Urban *et al.*[237]

Polymer coating, pressure, temperature, and light are the different parameters investigated for their effect on the monolayer $WSe_2$ back-gated FET. Coating the device with a polymer layer, in this case PMMA, strongly influences the electrical transport. The polarity of the device changes from n-type to p-type conduction when the PMMA layer is added. The pressure on air-exposed $WSe_2$ FETs affects the device characteristics in a similar way to PMMA, turning the conduction from p- to n-type. When measuring the current-voltage (I-V) characteristics at different temperatures, a gate modulation of the Schottky barrier at the contacts is observed.

The carrier mobility and the subthreshold swing both undergo a change of behaviour with increasing temperature. The interface trap density, which is derived from the subthreshold swing, indicates the photoresponse of the device. The monolayer $WSe_2$ device, characterized at several laser wavelengths, achieved a responsivity as high as $\sim$0.5 $AW^{-1}$ at 700 nm, a photon energy close to the bandgap of few layer $WSe_2$.

### 6.6.2 Vertical field emission transistor

Also in collaboration with Prof. Antonio Di Bartolomeo from CNR-SPIN the first vertical field emission transistor on $WSe_2$ was established and characterised. The results from this publication were published as "A $WSe_2$ vertical field emission transistor" by Di Bartolomeo *et al.*[238]

In field emission electrons are extracted from the material by quantum tunnelling through the surface potential barrier upon the application of a strong electric field. Electric control of carrier concentration by a gate in this type of field-effect transistor structure is an effective way to tune the doping level and type in a device. Field emission is of great relevance for various applications, ranging from electron microscopy to display technology. In lateral field-emission devices, the traditional approach of placing a gate roughly in between the source and drain has been replaced by a gate behind the emitting tip, controlling its doping level and conductivity. This results in the modulation of a narrower gate voltage of the source–drain field-emission current by depleting or enhancing the carrier density available at the source for tunnelling. For a vertical field emission transistor the back gate voltage is modulated.

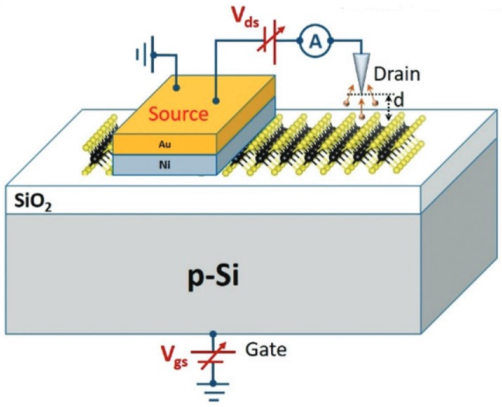


Figure 6.15: Schematic representation of the $WSe_2$ vertical field emission device in the SEM chamber. Image adapted from Di Bartolomeo *et al.*[238]

Similar monolayer $WSe_2$ devices as described in subsection 6.6.1 were fabricated for this work in TCD, where the measurements were performed in CNR-SPIN Salerno. In contrast to the method in subsection 6.6.1, the device was only physically probed with one tungsten tip contact, where the other contact was positioned at a given distance above the flake to measure the field emission current from the $WSe_2$ flake to the contact. In addition to this the SEM sample holder was electrically connected to the back-gate of the sample to observe a gate-modulated field emission current. The setup used for these measurements is shown in Figure 6.15

The n-type conduction of the device enables the field emission, or the extraction of electrons by quantum tunneling from the two dimensional $WSe_2$ monolayers. Electron emission occurs under an electric field $\sim$100 V $\mu m^{-1}$ and is stable over time. Most importantly, the field emission current can be modulated by the back-gate voltage.

## 6.7 Summary

In this chapter the growth of $WSe_2$ by a micro-reactor CVD aproach was optimised by a parametric study of various growth parameters. These parameters have a strong impact on the nucleation and growth mechanism of $WSe_2$. The metal precursor choice will determine whether there is formation of $WSe_2$ and if there is formation of flakes or polycrystalline surfaces. Increasing the reaction time leads to larger flakes and higher surface coverage. The increase also results in multilayer growth of $WSe_2$. When the pressure is increased this results in larger lateral flake sizes. Most likely this is due to a higher rate of collisions at increased pressure which results in a deeper penetration of the selenium vapour between the sandwiched seed layer and growth substrate, as well as surface diffusion, resulting in a higher nucleation density over the total surface.

The growth mode depends on the gas flow in the furnace. At lower gas flow the growth mode is mainly a Stranski-Krastanov mode, layer plus island growth, where increased gas flow results in a Frank-Van der Merwe growth mode, layer by

layer growth. When complete monolayer coverage is desired Frank-Van der Merwe is preferable to Stranski-Krastanov. The lower gas flow also yields a higher nucleation density as well as higher coverage on the surface, while increasing the flow brings on higher crystallinity of the surface.

Back-gated FET devices were fabricated using $WSe_2$ flakes grown using the micro reactor approach. These devices showed p-type behaviour and the mobility of the $WSe_2$ device is around 25-27 $cm^2/(Vs)$. The $WSe_2$ flakes were further used in collaborative studies. Environmental effects were studied and devices showed different behaviour depending on effects such as atmosphere, pressure and PMMA contamination. On top of this with these flakes the first ever vertical field emission transistor was produced.

# 7 Substrate effects on the growth of $MoS_2$

Growth substrates have a large influence on the growth mechanism of CVD grown TMDs which cannot be neglected. The best known example of crystal growth is epitaxial growth. The word epitaxial comes from the Greek words '*epi*' and '*taxis*' which mean "above" and "in an ordered manner" and the term epitaxial is used to indicate a growth mechanism where the formed material follows the lattice registry of the underlying growth substrate or underlying crystal growth in homoepitaxy. This means that the growth substrate functions as a template for the growth orientation.

In heteroepitaxy the new crystalline layers are formed in a well-defined orientation with respect to the growth substrate. Often epitaxial growth occurs when there is a lack of, or a minimal, lattice mismatch between the two materials, a good example of this is the growth of graphene on h-BN.[239] Both materials have a hexagonal lattice with a small lattice mismatch of ∼1.8%, making h-BN a perfect substrate for epitaxial growth.[240,241]

The advantages of epitaxial growth are aligned growth and the merging of grains, reducing the amount of grain boundaries, resulting in more crystalline products.[143,144] In the case of TMDs this can be observed for growth of TMDs on other TMDs. For example the lattice mismatch between $MoS_2$ and $WS_2$ is less than 0.01%.[242] Making them near optimal substrates for the epitaxial growth of crystallographically aligned heterostructures.

Besides the crystalline orientation of the substrate, epitaxial or ordered growth can also arise from substrate morphology. Ordered growth originating from the surface morphology can be expressed in many forms. This can be alignment of flakes, though it can also result in localised concentrated growth, or local aligned growth along the substrate terrace steps. Van der Waals forces between different materials or surface interactions can also lead to ordered growth. An example of oriented growth of gold particles on highly oriented pyrolytic graphite (HOPG) was reported by Dietzel *et al.*[243]. The ordered or epitaxial growth of III-V materials or metal oxides on sapphire has also been demonstrated.[149,244–246] According to Dumcenco *et al.*[116], CVD growth of $MoS_2$ on C-plane (0001) sapphire results in large-area epitaxial growth of $MoS_2$ as a result of the coalescence of aligned $MoS_2$ domains with a reduced density of grain boundaries.[247] Recently, Ma *et al.* showed seamless stitching of $MoS_2$ domains on A-plane sapphire as well.[248] This improved

growth should lead to better electrical and mechanical properties over a longer, $\mu$m scale

The effect of the substrate on the growth mechanism of a film cannot be neglected. Epitaxial or aligned growth can be beneficial to control the presence of grain boundaries, when the symmetries of the substrate and grown material overlap, and the ease of patterning the substrates when the presence and location of grain boundaries is known. While localised growth of smaller flakes with a larger surface area are beneficial for applications in catalysis.[61] It is evident that the growth of TMDs can be directed by substrate selection.

In this chapter the CVD growth of $MoS_2$ on a variety of substrates is investigated to improve the growth and crystalline quality of CVD grown $MoS_2$. The influence of the surface morphology, surface interaction and surface energy are hereby taken into consideration and are explored. In the following section the different substrates and possible surface treatments will be discussed. Part of these results were also published in the paper "Directing the Morphology of Chemical Vapor Deposition-Grown $MoS_2$ on Sapphire by Crystal Plane Selection.[117]

## 7.1 Substrates

A large variety of growth substrates have been used in literature to grow thin, mono to few layer, $MoS_2$. The most common substrates being: $SiO_2$/Si, sapphire and gold.[105,106,249–252] Other more exotic substrates for the CVD growth of $MoS_2$ include h-BN and silver.[252,253] This work will focus on $SiO_2$ and the different crystal planes of sapphire.

To date $SiO_2$/Si has been widely used due to its availability, reliability, price and the compatibility of silicon with current CMOS technology. In this work standard silicon wafers, with a thickness of ∼500 $\mu$m with (100) plane orientation, produced by the Czochralski process[142] were used. The top layer contains a native oxide and the silicon surface is usually further oxidised by rapid thermal oxidation to form a 300 nm oxide layer, as $SiO_2$ is insulating. This $SiO_2$ layer is amorphous, resulting in random orientation of materials grown on top. Growth of TMDs on $SiO_2$/Si is a mature process and there are ubiquitous examples of monolayer TMD growth present throughout the literature.

A disadvantage of the use of silicon as a substrate is that silicon is limited to temperatures of ∼500 °C in atmospheric conditions, and ∼650 °C under vacuum, as higher temperatures result in degradation of charge carrier lifetime as well as degradation of the oxide for certain growth methods.[254–256] Therefore reaction temperatures should optimally be kept below this temperature or the synthesized material should best be transferred to a different substrate for further processing.

Another commonly used growth substrate is sapphire. Sapphire ($Al_2O_3$) is a single-crystal material known for its chemical and thermal stability.[145] It is used as a substrate for the epitaxial growth of a wide range of materials, most notably on C-

and R-plane sapphire.[145,146] Besides the use of sapphire as a growth substrate, the material also has applications in optics[147] and chemical catalysis.[148] The stability of sapphire notably exceeds that of commonly used $SiO_2$/Si substrates, which have a more limited thermal range and provide an amorphous surface for growth, resulting in randomly-oriented material growth. Furthermore, there is less mismatch between the thermal expansion coefficient of $MoS_2$ and sapphire compared with $MoS_2$ and silicon dioxide, which should result in less strain between the substrate and the $MoS_2$.[257,258]

Epitaxial growth of $MoS_2$ on different sapphire planes has been explored to a degree in literature. Dumcenco *et al.* showed the epitaxial growth of $MoS_2$ flakes on C-plane sapphire, while Ma *et al.* showed aligned growth of $MoS_2$ domains on A-plane sapphire after annealing.[116,248] Studies on the directed CVD growth of $MoS_2$ on other sapphire planes have been limited. A paper on the influence of C- and R-plane substrates on the PL intensity for $MoS_2$ has been published by Zhang *et al.*[259] In this paper a strong increase in the PL signal for $MoS_2$ grown on R-plane sapphire was observed in comparison to the growth on C-plane sapphire. The increased PL signal for $MoS_2$ on R-plane in this publication is assumed to be due to increased molybdenum-oxygen bonding. This increase is similar to the increase of PL signal at grain boundaries.[260]

In contrast to amorphous surfaces, such as $SiO_2$, crystalline surfaces are naturally vicinal due to imperfect alignment with low index planes. The surfaces naturally feature steps, whose configurations depend on the planar orientation of the surface. While C-plane (0001) sapphire is the most commonly used of the low-index sapphire planes, others including R-plane $(1\bar{1}02)$, A-plane $(11\bar{2}0)$ and M-plane $(10\bar{1}0)$ have also been the subject of studies.[261] An illustration of the different sapphire planes on the crystal is shown in Figure 7.1.

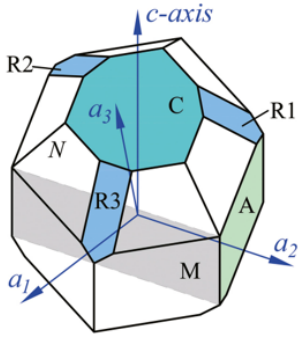


Figure 7.1: Illustration of the crystal geometry showing the crystal planes of sapphire. Image adapted from Wang *et al.*[261]

Each of the sapphire planes have distinct facet-dependent properties, resulting in different growth mechanisms occurring on the surface. For example R-plane sapphire is used in high-speed integrated circuits and as a substrate for the growth of III-V materials,[149,150] while A-plane sapphire has been used for the production of hybrid microcircuits.[145]

It is known that $Al_2O_3$ surface morphology is greatly affected by surface preparation, and in particular high-temperature annealing, which in turn impacts the nature of any film grown on the substrate.[262,263] To improve the ordering of the surface, the substrates can be annealed as the surface thermodynamically relaxes under annealing. This relaxation typically results into an improvement in the surface ordering. Here the different planes were also studied after annealing at 1200 °C, 1300 °C and 1400 °C for 24h in air, which is sufficient time for the surface to evolve to its equilibrium crystal state.[262,264,265]

The annealing temperature used defines the terrace width and step height of the surface.[262] Generally the terraces become more defined and wider with increasing annealing temperature until an equilibrium state where the energy of the surface is minimised is reached. The temperature dependency and resulting faceting of the system is related to the minimization of the surface free energy of the system.

## 7.2 Synthesis

The CVD growth of the $MoS_2$ was performed in a two-zone sulfur furnace, as described in subsection 5.1.3, based on the process described by Gatensby *et al.*[102] In the lower-temperature upstream heating zone sulfur powder (Sigma-Aldrich 99.98% purity) was placed in an alumina crucible. The growth substrates were placed downstream in the high-temperature, reactor, zone of the furnace. The samples were placed face-down on the molybdenum precursor. The molybdenum precursor was 40 $\mu$L of a 1 mg/L exfoliated molybdenum trioxide (Sigma-Aldrich) in HPLC IPA drop casted on an 8.5x8.5 mm $SiO_2$/Si sample. The growth substrates were 7.5x7.5 mm pieces of sapphire cut from wafers supplied by AdValue Technology. A distance of ∼25 cm was present between the sulfur crucible and the downstream crucible containing the growth substrates. To study the affect of annealing on the growth of $MoS_2$ on the different sapphire planes, part of the sapphire samples from all the studied planes were annealed at 1400 °C for 24 h in atmospheric conditions.

An Ar-flow of 150 sccm was maintained during growth. For the growth procedure, the primary heating zone was first ramped up to 750 °C and after the reaction temperature had stabilized sulfur vapor was produced by independently heating the secondary upstream furnace to 117 °C. The $SiO_2$ samples required longer sulfur exposure and a post-annealing step to form $MoS_2$ on the surface. For this reason the sulfur flow was maintained for 25 min. for the $SiO_2$/Si samples, though it was only maintained for 15 min. for the sapphire samples. After the sulfur heating was switched off the sample was post-annealed for respectively another 25 or 15 min. at 750 °C for $SiO_2$/Si or sapphire. Following this step, the system was cooled to room temperature.

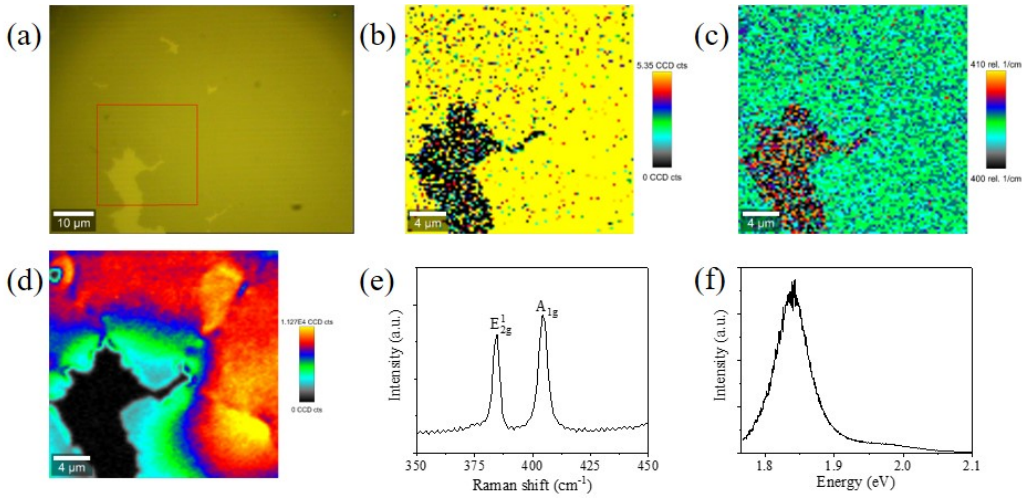


Figure 7.2: (a) Optical microscopy image of the $SiO_2$/Si sample covered in CVD grown $MoS_2$. The red square depicts the area of the Raman sum map of the $E^1_{2g}$ peak ∼385 $cm^{-1}$ shown in (b), (c) shows the peak position map of the $A_{1g}$ peak which is at ∼405 $cm^{-1}$ and in (d) the PL sum map of the A-exciton peak at ∼1.85 eV. In (e) the individual spectrum for monolayer $MoS_2$ on $SiO_2$/Si is given and in (f) the PL spectrum for monolayer $MoS_2$ is shown.

### 7.2.1 Silicon

The CVD growth of $MoS_2$ on $SiO_2$/Si results in large areas of $MoS_2$ on the surface, as is shown in the optical microscopy image in Figure 7.2(a). The optical microscopy image indicates that the complete $MoS_2$ area shown is monolayer, with grain sizes in the order of 10 $\mu$m. These observations are confirmed by Raman and PL spectroscopy measurements.

The Raman and PL maps, Figure 7.2(b)-(d) show a large even area of $MoS_2$ on the surface with overall a quite constant intensity, as is clearly visible in the $E^1_{2g}$ intensity map and $A_{1g}$ positon map, Figure 7.2(b) and (c). Even though the $MoS_2$ film appears uniform the PL map, see Figure 7.2(d), shows the grain boundaries between the $MoS_2$ domains present on the surface. In the Raman spectrum the $E^1_{2g}$ (E′ for monolayer) and $A_{1g}$ ($A'_1$ for monolayer) peaks are located at respectively ∼384.68 $cm^{-1}$ and ∼404.26 $cm^{-1}$, which corresponds with the values for monolayer $MoS_2$.[31,175] For the FWHM the following widths were obtained: ∼4.18 $cm^{-1}$ for $E^1_{2g}$ and ∼6.63 $cm^{-1}$ for $A_{1g}$, indicating good crystallinity of the $MoS_2$ area.[166,266]

PL measurements show that the A1-exciton peak, which reflects the direct bandgap of monolayer $MoS_2$, is clearly present at ∼1.843 eV, while the B1-exciton peak is almost invisible at ∼1.966 eV with the A1-exciton peak being almost 20x more intense compared with the B1-exciton peak, see Figure 7.2(f). The FWHM of the A1-peak is only ∼0.05 eV, indicating that there is a little scattering due to grains and defects on the surface.

### 7.2.2 C-plane sapphire

The C-plane (0001) is the basal plane of sapphire and the naturally most commonly occurring form of sapphire The C-plane samples used have a small miscut angle of approximately 0.2 °, which is in theory low enough to result in homogeneous crystalline growth on the sapphire surface.[267] Non-annealed C-plane surfaces have a step height of c/6=0.22 nm, where c is the length of the unit cell along the {0001} direction. Annealing of C-plane results in step clusters. Increasing the annealing temperature results in larger terraces.

AFM images for the different annealing temperatures are shown in Figure 7.3. With increasing temperature the terraces start to form and become more pronounced. Barely any terrace was distinguishable on the non-annealed C-plane sapphire surface, as the terraces in part may be obscured by surface adsorbents. Annealing the sapphire substrate results in visible terraces. For annealing at 1200 °C both the terrace width and step height can be identified after annealing at 1200 °C and the width and step height increases with increased annealing temperatures.

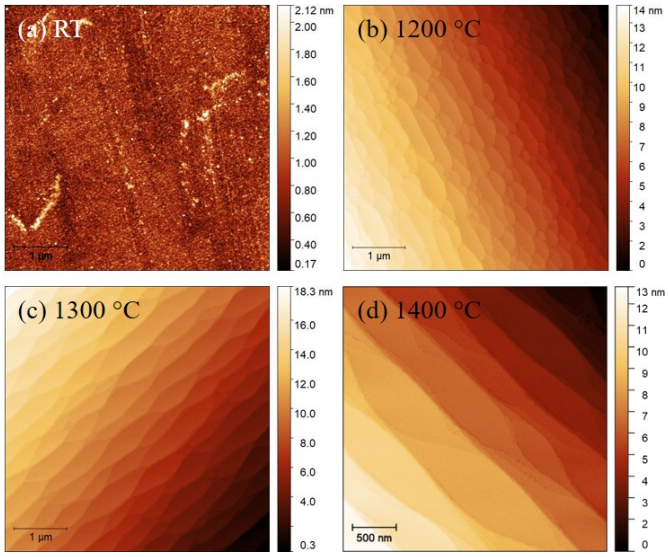


Figure 7.3: AFM images of C-plane sapphire before annealing and after various annealing temperatures. (a) C-plane before annealing, (b) annealing at 1200 °C, (c) annealing at 1300 °C and (d) annealing at 1400 °C

For the C-plane sapphire substrates annealed at 1400 °C several crossing steps are visible, which have a minimum height ∼0.2 nm, but a typical step height of ∼0.45 nm was observed by AFM. This value is in agreement with other studies as steps increase in multiples of 2c/6 for annealing at temperatures over ∼1100 °C.[262,265,268] Other sapphire planes which are studied here are R-, A- and M-plane, which have step heights of 0.25 – 0.8 nm as shown in Table 7.1.

For the CVD growth of $MoS_2$ firstly the results on the non-annealed C-plane sapphire will be discussed. The CVD growth of $MoS_2$ on non-annealed C-plane sapphire results in growth of large $MoS_2$ areas on the surface, as shown in Figure 7.4(a). Parts of these films are monolayer, ∼ 43%, though most of the surface is covered

| Sapphire plane | Step height | Terrace size | Offcut |
|---|---|---|---|
| C-plane | 0.22-1.5 nm | 310 nm | 0.22 ° |
| R-plane | 0.36 nm | 410 nm | 0.05 ° |
| A-plane | 0.25x nm | Variable | 0.03 ° |
| M-plane | 40.8 nm | 123 nm | 2.2 ° |

Table 7.1: Step height, terrace size and offcut of the different annealed (1400 °C) sapphire planes obtained by AFM.

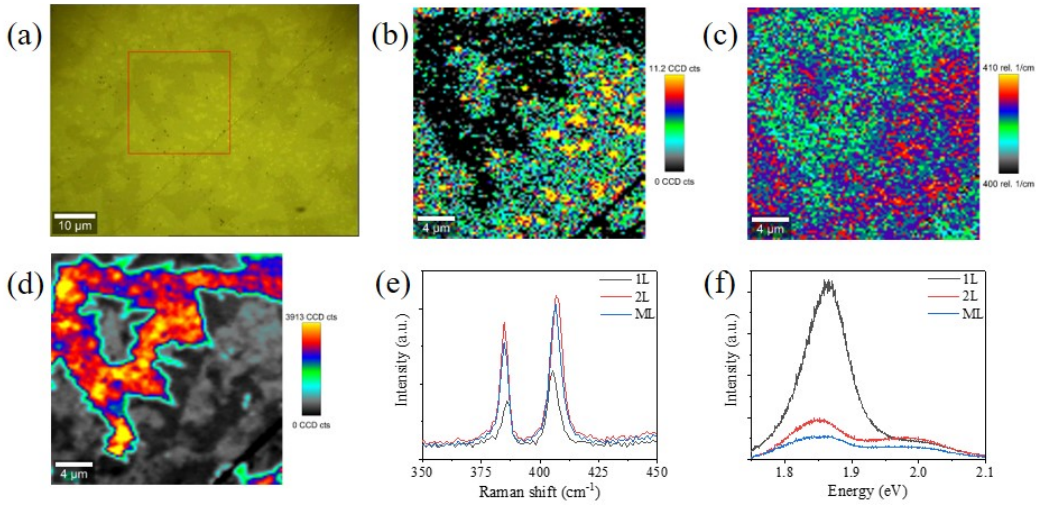


Figure 7.4: (a) Optical microscopy image of the non-annealed C-plane substrate covered in $MoS_2$. The red square depicts the area of the Raman sum map of the $E^1_{2g}$ peak ~385 $cm^{-1}$ shown in (b), (c) shows the peak position map of the $A_{1g}$ peak which is at ~405 $cm^{-1}$ and in (d) the PL sum map of the A-exciton peak at ~1.85 eV. In (e) the individual spectra for the single, bi- and multi-layer $MoS_2$ on C-plane sapphire are given, the same is shown in (f) for the PL spectra.

with large areas of bi- and multilayer $MoS_2$. The surface coverage on this substrate is higher than the coverage on $SiO_2$/Si and also in contrary to growth on $SiO_2$/Si a certain degree of epitaxial alignment of the $MoS_2$ flakes appears to be present on the surface.

The Raman maps, see Figure 7.4(b) for the $E^1_{2g}$ intensity map and Figure 7.4(c) for the $A_{1g}$ position map, clearly display the $MoS_2$ bilayer flakes on the monolayer $MoS_2$ surface pointing towards the same direction, see Figure 7.4(b) and (c). The $A_{1g}$ position map indicates that the complete underlying area visible in the optical microscopy image is covered by monolayer, ~405 $cm^{-1}$ $MoS_2$. The presence of monolayer $MoS_2$ is confirmed in the PL map in Figure 7.4(d).

Contrary to the non-annealed surface, the annealed surface shows clearly defined terraces in the AFM height image of the substrate. Clearly defined terraces could be an indication that the annealed substrate would be a better growth substrate for aligned growth. The large well-defined uniform areas present on the substrate result in unhindered growth of the $MoS_2$. The terrace steps are expected to have a catalytic function for the formation of nuclei on the substrate. However, this does not appear to be the case for the growth of $MoS_2$ on C-plane sapphire. Less

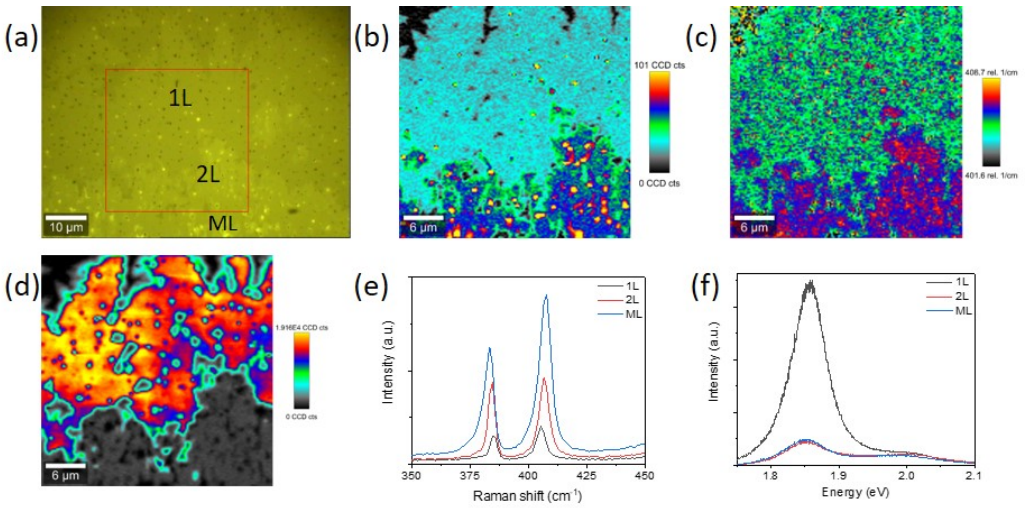


Figure 7.5: (a) Optical microscopy image of the C-plane substrate covered in $MoS_2$. The red square depicts the area of the Raman sum map of the $E^1_{2g}$ peak ∼385 $cm^{-1}$ shown in (b), (c) shows the peak position map of the $A_{1g}$ peak which is at ∼405 $cm^{-1}$ and in (d) the PL sum map of the A-exciton peak at ∼1.85 eV. In (e) the individual spectra for the single, bi- and multi-layer $MoS_2$ on C-plane sapphire are given, the same is shown in (f) for the PL spectra.

alignment appears to be present on the surface according to the optical microscopy image in Figure 7.5(a). While growth on 1400 °C annealed C-plane sapphire yields relatively large triangular $MoS_2$ flakes, with lateral dimensions in the order of tens of microns, there is little apparent orientation of the flake direction. Thus, despite the use of a crystalline substrate, and the presence of steps, the orientation of the flakes is ostensibly random and not aligned.

The lack of observed flake alignment is in contrast to results from some other publications.[116,269] Alignment of CVD-grown $MoS_2$ has been described for growth on C-plane sapphire by Suenaga *et al.*[269] Suenage *et al.* indicated the crucial role of the sulfur concentration for alignment. This could possibly explain the lack of observed alignment on C-plane sapphire here as an excess of sulfur was used to ensure a complete reaction and maximum coverage. Another critical factor is that their reaction temperature used is much higher than what is employed here. As the desorption of oxygen from sapphire occurs above 823 °C, there is stronger interaction with the surface and thus better alignment can be expected.[270] A final factor that could influence the formation of aligned $MoS_2$ domains on the surface is the presence of forming gas, $H_2$/Ar 1/9, during annealing. Alignment of $MoS_2$ is aided by an Al-terminated sapphire surface. The $H_2$-gas gas reduces the oxygen termination on the surface, resulting in an Al-terminated surface.[154,271]

Even though there is a lack of alignment of $MoS_2$ on the annealed surface, the surface is largely covered by $MoS_2$. The surface is reaching a total coverage of ∼90% with ∼47% of the surface being covered by monolayer $MoS_2$. See Figure 7.21 and Table 7.3 for the $MoS_2$ surface coverages for the different annealed sapphire planes.

The AFM images show both the step and terrace structure of the sapphire sub-

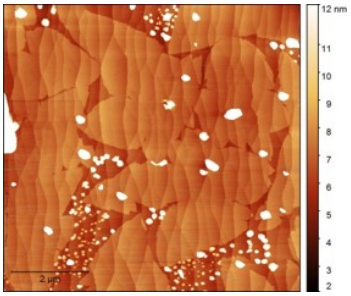


Figure 7.6: AFM height images for the growth of $MoS_2$ on C-plane sapphire. (a) Non-annealed C-plane sapphire and (b) 1400 °C annealed C-plane sapphire

strates and the $MoS_2$ flakes on the surfaces, thereby giving convincing evidence as to whether the $MoS_2$ grows according to the underlying crystallographic directions. In Figure 7.6 the $MoS_2$ grown on C-plane sapphire, for growth on both the annealed and non-annealed substrates, is shown. The $MoS_2$ flakes on the non-annealed C-plane sapphire are all oriented in the same direction, while the flakes on the annealed C-plane are oriented in various directions. When comparing the shapes of the flakes, the flakes on the non-annealed substrate are very triangular, while the flakes are more rounded on the annealed substrate.

In addition to the $MoS_2$, high peaks are visible on the surface. The heights and shapes of these peaks are similar to that of molybdenum oxides.[272,273] The oxides are formed when the molybdenum oxide precursor evaporates and is deposited on the surface. There appears to be less of an excess of Mo for the growth on the non-annealed substrate as that surface has significantly less oxide peaks on the surface. This is possibly due to the higher $MoS_2$ coverage of the non-annealed sample, resulting in less Mo and $MoO_x$ on the surface. Though the AFM suggests that these features are oxides this cannot be clearly identified by Raman spectroscopy.

### 7.2.3 R-plane sapphire

For R-plane sapphire $(1\bar{1}02)$ steps are resolvable by AFM on the surface before annealing (See Figure 7.7(a)) The step and terrace structure becomes more pronounced with increased annealing temperature. For annealing at 1200 °C the terraces have a width of ∼300 nm, while this increases to ∼400 nm for the substrates annealed at 1300 and 1400 °C. The high temperature annealed substrates show terraces similar to those on C-plane, though the terraces on R-plane are wider and more uniform, with an average width of 410 nm for R-plane compared to 310 nm for C-plane (See Table 7.1). Annealing results in a more stable equilibrium surface as the surface reorganises to an ordering where the surface energy strives towards a minimum.

Growth on non-annealed R-plane sapphire results in a continuous polycrystalline film of $MoS_2$. The optical microscopy image of the growth on R-plane is shown in Figure 7.8(a). The quality of the material does not appear to be very high as the Raman and PL maps, Figure 7.8(b) and (c), show a very grainy continuous layer of $MoS_2$ on the substrate. In the Raman spectrum the $E^1_{2g}$ and $A_{1g}$-peaks are at

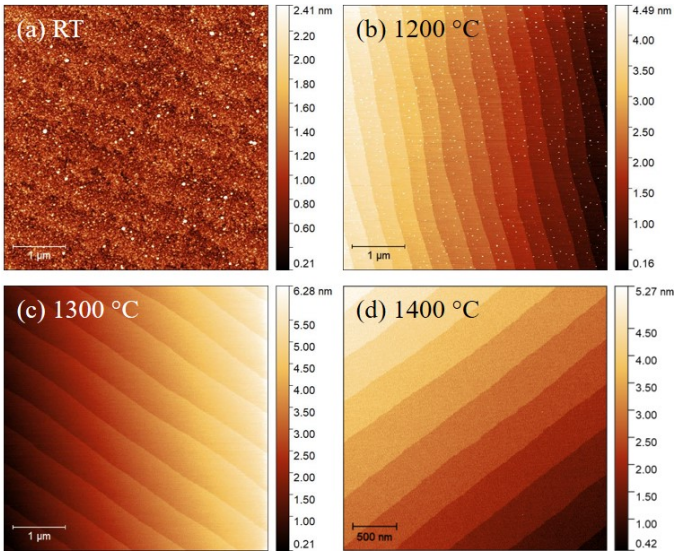


Figure 7.7: AFM images of R-plane sapphire before annealing and after various annealing temperatures. (a) C-plane before annealing, (b) annealing at 1200 °C, (c) annealing at 1300 °C and (d) annealing at 1400 °C

the expected position for monolayer $MoS_2$, but the $E^1_{2g}/A_{1g}$ ratio is very low 0.55, which is usually the case for few layer $MoS_2$. As the $MoS_2$ is monolayer this is a possible indication for low crystallinity or the presence of many defects. A LA(M) disorder peak is observed in the Raman spectrum around ∼227 $cm^{-1}$, not shown in the spectrum, indicating a low inter-defect distance.[165] The grainy features on the optical microscopy image and Raman maps imply that this is due to the low crystallinity. The FWHM of the Raman peaks are 10.01 $cm^{-1}$ for $E^1_{2g}$ and 6.53 $cm^{-2}$ for $A_{1g}$, which is extremely broad for the $E^1_{2g}$ peak.[166]

Further information given by the PL spectra shows the A1 exciton peak is located at 1.90 eV, while the B1 exciton peak is located at 2.03 eV. This is a strong red shift for both peaks compared to the $MoS_2$ grown on C-plane, most likely caused by the poor crystallinity, and thereby scattering, of the $MoS_2$ on the surface. This is further confirmed by the FWHM of the A1 peak, 0.10 eV, which is much higher compared to the A1 FWHM of the other substrates. Growth of $MoS_2$ on non-annealed R-plane sapphire substrate therefore leads to large area growth of $MoS_2$. The $MoS_2$ is polycrystalline and there is no apparent ordering of the $MoS_2$ on the surface.

Growth on 1400 °C annealed R-plane sapphire does result in qualitatively better growth, in contrast to annealed C-plane. An optical microscopy image, Figure 7.9(a), clearly shows crystalline triangular shapes. Although the shapes are triangular they are somewhat dendritic. The feature sizes of the $MoS_2$ domains are of a reasonable size, ∼20 $\mu$m and the crystal shapes indicate a crystalline structure.

The Raman $E^1_{2g}$ intensity map and $A_{1g}$ position map, Figure 7.9(b) and (c) show that a large area of the surface is covered with $MoS_2$, with quite a significant part being monolayer $MoS_2$. This is also confirmed in the PL A1 exciton intensity map, Figure 7.9(d). For monolayer $MoS_2$ the $E^1_{2g}$-peak is situated at ∼385.96 $cm^{-2}$ and a FWHM of ∼3.89 $cm^{-1}$, while the $A_{1g}$-peak is located at ∼405.53 and has a FWHM

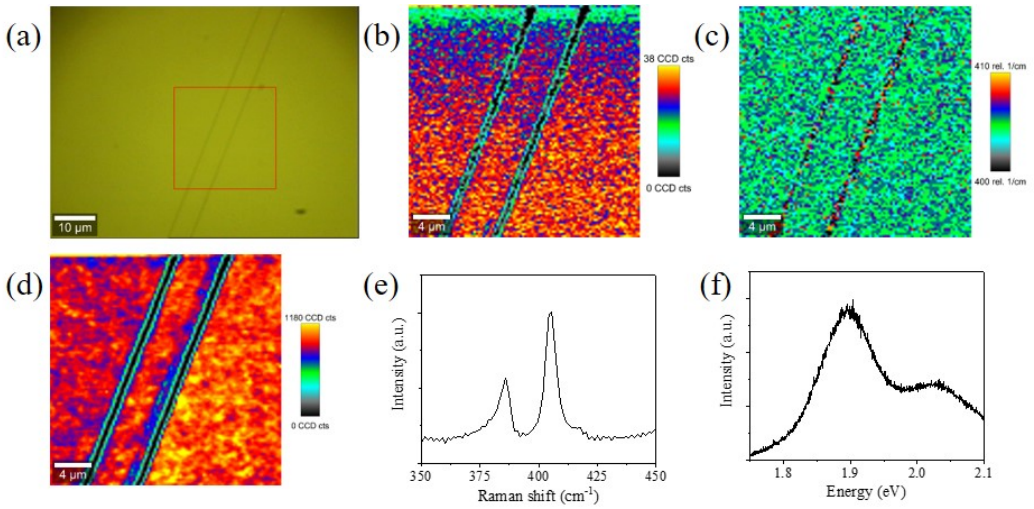


Figure 7.8: (a) Optical microscopy image of the non-annealed R-plane substrate covered in $MoS_2$. The red square depicts the area of the Raman sum map of the $E^1_{2g}$ peak ~385 $cm^{-1}$ shown in (b), (c) shows the peak position map of the $A_{1g}$ peak which is at ~405 $cm^{-1}$ and in (d) the PL sum map of the A-exciton peak at ~1.85 eV. In (e) the spectrum for single layer $MoS_2$ on R-plane sapphire are given, the same is shown in (f) for the PL spectrum.

of 6.92 $cm^{-1}$. (See Figure 7.9(e).) The values obtained are in correspondence with those of monolayer growth as are the results from the PL spectrum. (Shown in Figure 7.9(f))

The growth mechanism of $MoS_2$ on the annealed R-plane surface appears to be Stranski-Krastanov, layer plus island growth.[122] Most of the underlying surface is covered with monolayer $MoS_2$ and regions, or islands, of bi- and multilayer $MoS_2$ are found on top of the monolayer $MoS_2$. Alignment of flakes is also visible as the flakes grow in the same direction.

In Figure 7.10 an AFM height image for $MoS_2$ growth on 1400 °C annealed R-plane sapphire is shown. The AFM image clearly shows the $MoS_2$ on the R-plane surface. The $MoS_2$ is aligned as it grows in a parallel direction along the terraces on the surface. Clearly distinguishable in the AFM image are the long dendritic shapes of the flakes following the terrace direction, indicating an interaction with the substrate. This alignment appears to merge the flakes on the surface as there are barely any boundaries visible on the AFM image though different flake tips, indicating the initial nucleation and growth of multiple flakes, are observed.

### 7.2.4 A-plane

The A-plane $(11\bar{2}0)$ of sapphire is often used in applications requiring a uniform dielectric constant and highly insulating characteristics.[145] Prior to annealing there is no structure discernible by AFM for A-plane sapphire as shown in Figure 7.11(a). Post-annealing the surface of the A-plane $(11\bar{2}0)$ sapphire shows shows clearer evidence of the vicinal nature of the surface and it is notable that the step edge is rough and corrugated. Higher temperature annealing leads to further roughening of

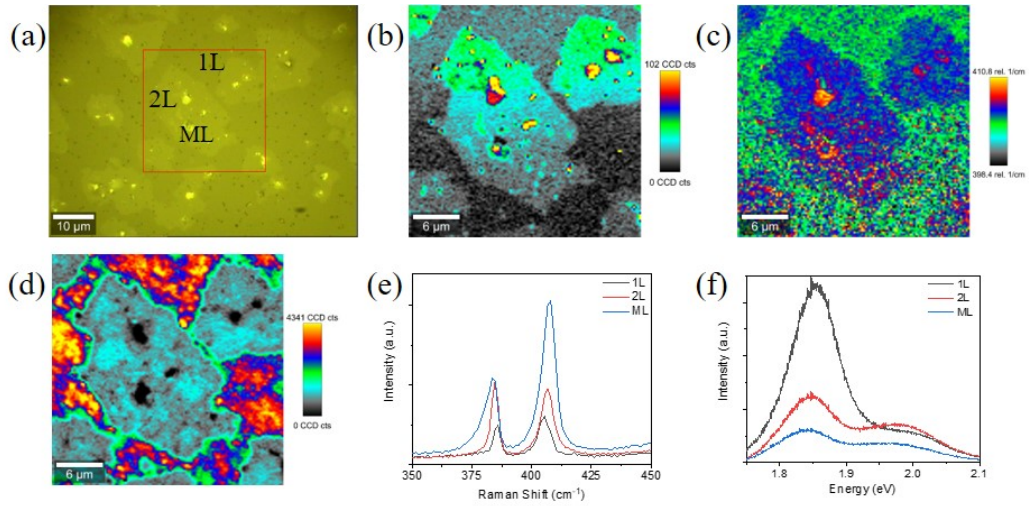


Figure 7.9: (a) Optical microscopy image of the annealed (1400 °C) R-plane substrate covered in $MoS_2$. The red square depicts the area of the Raman sum map of the $E^1_{2g}$ peak ∼385 $cm^{-1}$ shown in (b), (c) shows the peak position map of the $A_{1g}$ peak which is at ∼405 $cm^{-1}$ and in (d) the PL sum map of the A-exciton peak at ∼1.85 eV. In (e) the individual spectra for the single, bi- and multi-layer $MoS_2$ on C-plane sapphire are given, the same is shown in (f) for the PL spectra.

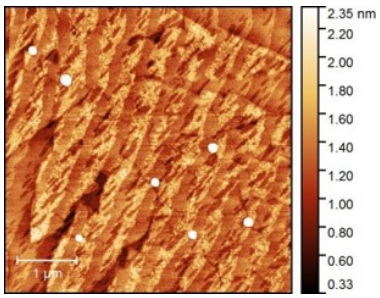


Figure 7.10: AFM height image for the growth of $MoS_2$ on 1400 °C annealed R-plane sapphire

the step edges, to the extent where the terraces are interrupted.

AFM analysis (See Figure 7.11(b-d)) of the annealed A-plane surfaces reveals comb-like structures along the $[10\bar{1}0]$ and [0001] directions, the intersection between the R- and A-planes, which is in agreement with findings by Curiotto *et al.*[265] These ragged shapes result in a combination of a large amount of small terraces as well as some large terraces. The sizes of the terraces range from ∼150-500 nm. A higher surface roughness is also present on A-plane sapphire. The faceted steps, the comb-like structures, and high terrace steps all lower the surface energy, thereby stabilising the surface structure.[274]

CVD growth on non-annealed A-plane sapphire results in the growth of $MoS_2$ with a large variation of layer numbers as shown in Figure 7.12(a). The feature sizes of the $MoS_2$ are very limited and localised areas with bi- and multilayer growth are distinct on the surface. There is no apparent ordering of the $MoS_2$ domains on the surface. The Raman maps, Figure 7.12(b) and (c) confirm this observation.

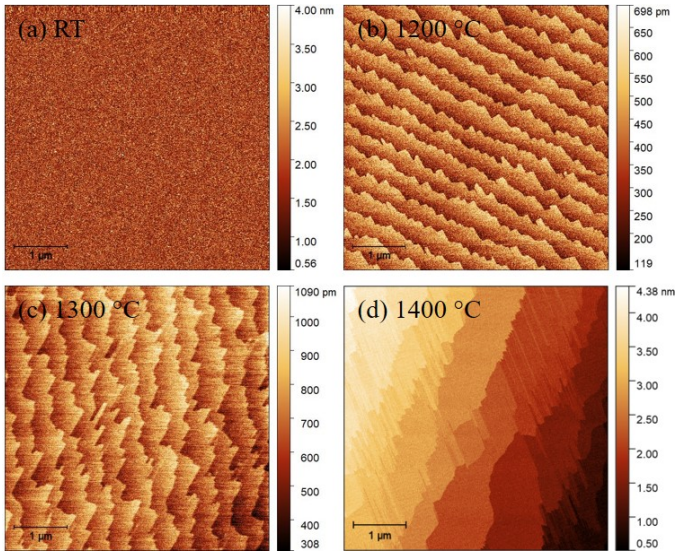


Figure 7.11: AFM images of A-plane sapphire before annealing and after various annealing temperatures. (a) C-plane before annealing, (b) annealing at 1200 °C, (c) annealing at 1300 °C and (d) annealing at 1400 °C

The Raman peaks in the spectrum in Figure 7.12(e) for the monolayer area are positioned at ∼386 $cm^{-1}$ for the $E^1_{2g}$-peak and 406 $cm^{-1}$ for the $A_{1g}$-peak, while the $E^1_{2g}/A_{1g}$ ratio is ∼0.70. The peaks are at the expected position for monolayer $MoS_2$ but the ratio is much lower than normal for monolayer $MoS_2$, which is ∼1 for perfect monolayer $MoS_2$, though generally is ≥0.80 for CVD grown samples on sapphire.[266] The ratio nominally decreases with increasing layer number as well as the presence of defects and grain boundaries.[228] The low crystalline quality of the material is also shown in the high FWHM of both peaks, respectively 7.25 $cm^{-1}$ and 8.92 $cm^{-1}$ for the $E^1_{2g}$ and $A_{1g}$ peaks as well as in the $A_{1g}$ position map. In the $A_{1g}$ position map no discernible features are present due to the polycrystalline nature of the film.

The PL map, shown in Figure 7.12(d), clearly indicates the presence of both monolayer and multilayer $MoS_2$ on the substrate. The intensity of the A1 exciton peak at ∼1.85 eV is almost 6x the intensity of the B1 exciton peak for monolayer $MoS_2$. Meaning that the luminescence of the A1-exciton is not very intense, causing the B1 exciton to show as relatively more pronounced in the spectrum as shown in Figure 7.12f). This indicates either a strong interaction with the substrate or the presence of defects on the surface. Monolayer $MoS_2$ on annealed A-plane shows a FWHM of 0.10, which is quite broad for monolayer $MoS_2$ PL, compared to the FWHM values obtained for $MoS_2$ on the C- and R-plane sapphire.

Growth on the annealed A-plane substrate results in larger structures, as shown in Figure 7.13(a) though on the annealed substrate there are also large variations in the layer thickness present with localised bulk growth on the substrate. Similar to the growth on non-annealed A-plane sapphire there is also an apparent lack of orientation or alignment of the $MoS_2$ structures formed on the surface. This is in contrast with the findings of Ma *et al.* where aligned $MoS_2$ structures where found

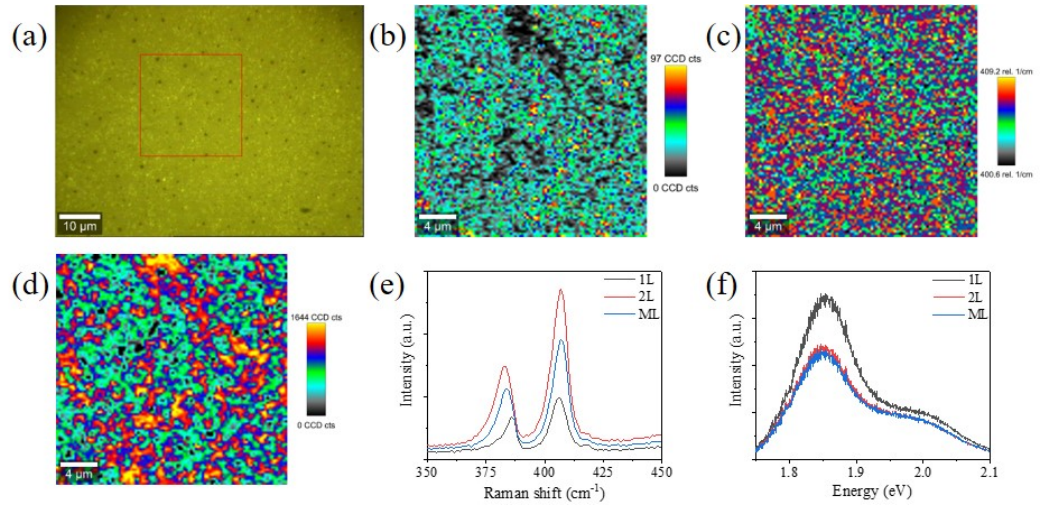


Figure 7.12: (a) Optical microscopy image of the non-annealed A-plane substrate covered in $MoS_2$. The red square depicts the area of the Raman sum map of the $E^1_{2g}$ peak ∼385 $cm^{-1}$ shown in (b), (c) shows the peak position map of the $A_{1g}$ peak which is at ∼405 $cm^{-1}$ and in (d) the PL sum map of the A-exciton peak at ∼1.85 eV. In (e) the spectrum for the single layer $MoS_2$ on A-plane sapphire are given, the same is shown in (f) for the single layer PL spectrum.

on 1100 °C annealed A-plane sapphire.[248] This could possibly be due to the lower temperature used in this particular study.

The Raman and PL maps, Figure 7.13(b-d), showing small flakes with a large presence of mono- and bi-layer $MoS_2$ on the surface. Both the $E^1_{2g}/A_{1g}$ ratio, 0.63, and the FWHM of the Raman peaks, 3.93 $cm^{-1}$ for $E^1_{2g}$ and 6.25 $cm^{-1}$ for $A_{1g}$, indicate a lower crystalline quality of the monolayer $MoS_2$ domains compared to the monolayer $MoS_2$ on non-annealed A-plane. (See Figure 7.13(e) for the Raman spectrum.) The PL spectrum shows an intense A1 exciton peak for the monolayer $MoS_2$, see Figure 7.13(f). The peak has a FWHM of ∼0.08 eV which is smaller than the ∼0.10 eV for the monolayer $MoS_2$ on non-annealed A-plane sapphire. Though this could fall within the error of the measurement.

In Figure 7.14 an AFM height image of the growth of $MoS_2$ on A-plane sapphire is shown. The AFM image clearly shows flakes which have sharp edges and disordered growth, as well as a large distribution of flake sizes and thicknesses present due to the underlying terraces with ragged edges. The flakes are all limited in size, around 1-7 $\mu$m. The step edges show a lot of decoration after growth, pointing towards these regions being highly reactive. The ragged edges of the A-plane will hinder diffusion of the atoms over the surface, trapping the precursors, thereby causing more restricted local growth. In combination with the high reactivity of the steps, this results in multilayer growth as the precursors used here limit the ability of precursors to diffuse over the surface.

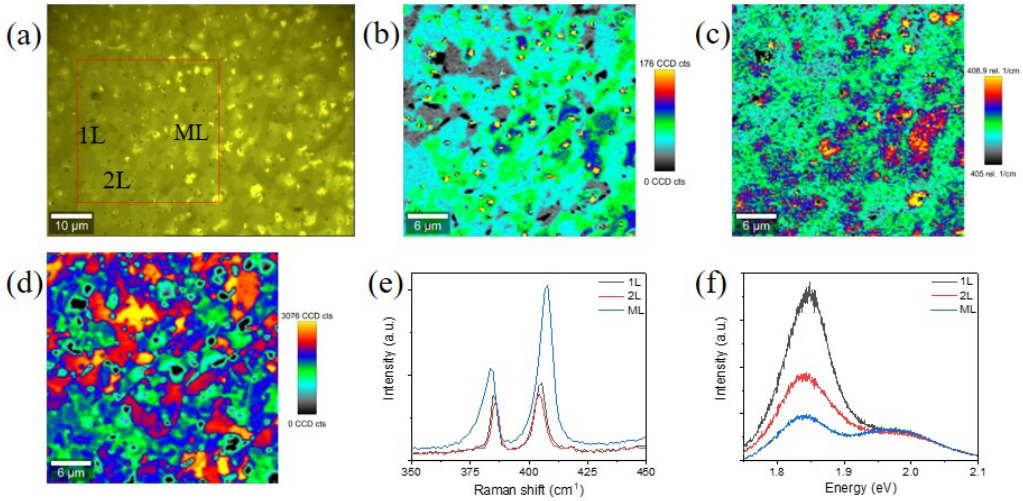


Figure 7.13: (a) Optical microscopy image of the annealed (1400 °C) A-plane substrate covered in $MoS_2$. The red square depicts the area of the Raman sum map of the $E^1_{2g}$ peak ∼385 $cm^{-1}$ shown in (b), (c) shows the peak position map of the $A_{1g}$ peak which is at ∼405 $cm^{-1}$ and in (d) the PL sum map of the A-exciton peak at ∼1.85 eV. In (e) the individual spectra for the single, bi- and multi-layer $MoS_2$ on C-plane sapphire are given, the same is shown in (f) for the PL spectra.

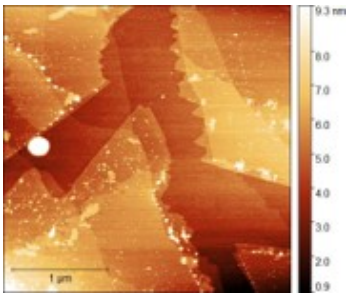


Figure 7.14: AFM height image for the growth of $MoS_2$ on 1400 °C annealed R-plane sapphire

### 7.2.5 M-plane

The M-plane ($10\bar{1}0$) does not show any apparent terraces before annealing, see Figure 7.15a). M-plane sapphire is thermodynamically unstable at high temperature, and transforms into developing facets of both the S-plane ($10\bar{1}1$) and R-plane ($1\bar{1}02$) under suitable annealing.[275–277] The decomposition of the M-plane sapphire surface into R- and S-facets results in a higher surface area, though the surface energy decreases as the surface becomes more thermodynamically stable.[276,277]

Annealing at 1200 °C results in a small degree of relief on the surface which shows the outline of terraces on the AFM height image shown in Figure 7.15(b). Higher temperature annealing at 1300 °C, shown in Figure 7.15(c), shows partially formed terraces in the AFM image with an average length of ∼1.5 $\mu$m. These terraces are formed along the S-facet of the M-plane. The width of the terraces is 100-200 nm, while the height of the step is ∼0.5 nm.

In the AFM image for M-plane sapphire annealed at 1400 °C, Figure 7.15(d), pronounced terraces along the S-facet are visible. Less visible are the smaller terraces in the R-facets though this can be observed at a ∼30 °angle from the terraces in the S-direction. The width of the terraces along the S-facet is ∼123 nm, while the step height is very high at 40.8 nm which is more pronounced than the steps of any of the other sapphire planes before or after annealing.

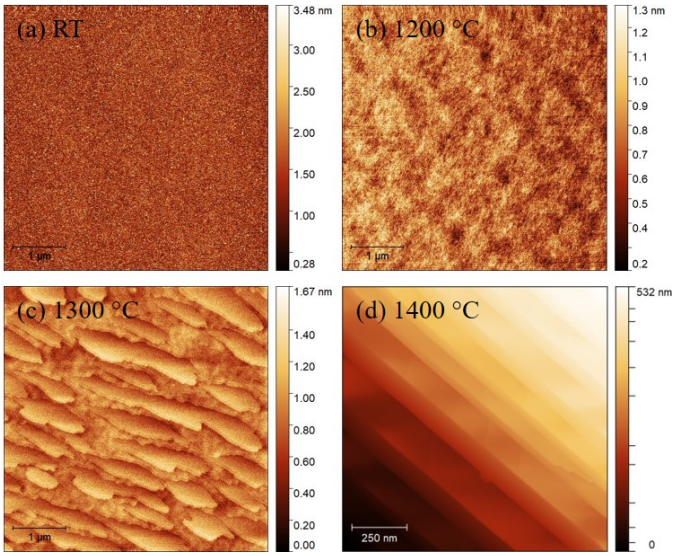


Figure 7.15: AFM images of M-plane sapphire before annealing and after various annealing temperatures. (a) C-plane before annealing, (b) annealing at 1200 °C, (c) annealing at 1300 °C and (d) annealing at 1400 °C

Growth of $MoS_2$ on non-annealed M-plane sapphire results in a continuous layer of $MoS_2$ nuclei, similar as observed for both non-annealed R- and A-plane sapphire. In Figure 7.16 the corresponding optical microscopy, Raman and PL data for the CVD growth is shown. The optical microscopy image, Figure 7.16(a) shows a grainy continuous area only interrupted by the scratches made on the surface to provide more contrast.

The Raman and PL maps also clearly show large $MoS_2$ regions, while the Raman $MoS_2$ $E^1_{2g}$-peak is located at 383.5 $cm^{-1}$ and the $A_{1g}$-peak at 408 $cm^{-1}$. These peaks are both shifted towards the position of multilayer $MoS_2$, which can also correspond to a polycrystalline nature of the $MoS_2$-film. The FWHM values for the $E^1_{2g}$ and $A_{1g}$ peaks are ∼6.44 $cm^{-1}$ and ∼6.00 $cm^{-1}$, which are much broader than would be expected for high-quality monolayer $MoS_2$. The PL spectrum shows both the A1 and B1 exciton peaks. The A1 exciton peak is ∼2x the intensity of the B1 exciton peak and has a FWHM of 0.11 $cm^{-1}$, thereby also confirming the polycrystalline nature of the grown film.

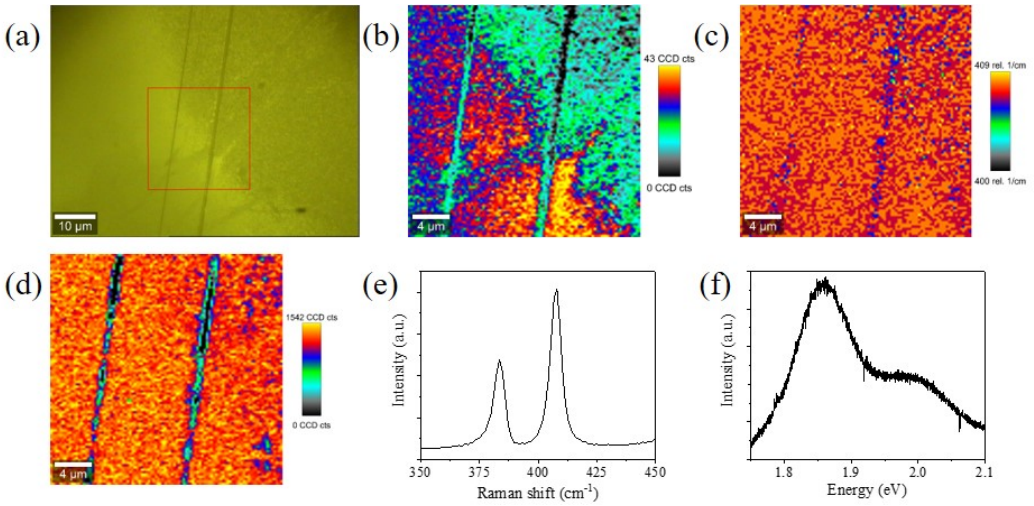


Figure 7.16: (a) Optical microscopy image of the non-annealed M-plane substrate covered in $MoS_2$. The red square depicts the area of the Raman sum map of the $E^1_{2g}$ peak ∼385 $cm^{-1}$ shown in (b), (c) shows the peak position map of the $A_{1g}$ peak which is at ∼405 $cm^{-1}$ and in (d) the PL sum map of the A-exciton peak at ∼1.85 eV. In (e) the individual spectrum for single layer $MoS_2$ on M-plane sapphire is given, the same is shown in (f) for the PL spectrum.

Annealing of the substrate at 1400 °C results in the formation of straight terraces with clear steps on the surface. The substrate shows similarities to that of the annealed R-plane sapphire, as discussed in subsection 7.2.3, where alignment of $MoS_2$ was shown. CVD growth of $MoS_2$ on 1400 °C annealed M-plane sapphire resulted in slim elongated flakes with lengths of ∼10 $\mu$m and widths of ∼1-3 $\mu$m. (See Figure 7.17(a).) The structures appear to follow the terrace direction, giving pronounced growth in the direction of the facets. As the flakes are not triangular but more dendritic, this indicates a stronger interaction with the substrate.[35,278] A stronger interaction with the surfaces increases the likelihood of oriented growth.

The surface coverage of $MoS_2$ on the M-plane surface is high, about 88%. The coverage varies from areas consisting mainly of monolayer coverage, 47.64%, to areas where bi- and multilayer $MoS_2$ are predominantly prevalent. Only a small area of the surface is covered in multilayer growth, <10%.

The Raman maps Figure 7.17(b) and (c) also clearly show the elongated $MoS_2$ structures, which are all orientated in the same direction. The peaks for monolayer

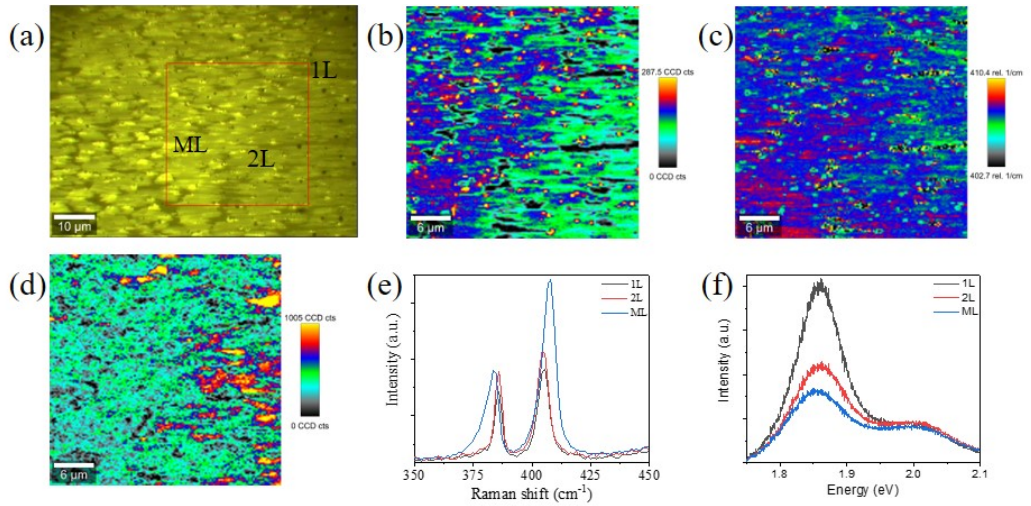


Figure 7.17: (a) Optical microscopy image of the annealed (1400 °C) M-plane substrate covered in $MoS_2$ which is grown with the gas flow parallel to the terraces. The red square depicts the area of the Raman sum map of the $E^1_{2g}$ peak ∼385 $cm^{-1}$ shown in (b), (c) shows the peak position map of the $A_{1g}$ peak which is at ∼405 $cm^{-1}$ and in (d) the PL sum map of the A-exciton peak at ∼1.85 eV. In (e) the monolayer $MoS_2$ on M-plane sapphire is given, in (f) the PL spectrum for monolayer $MoS_2$ is shown.

$MoS_2$ are 385.95 $cm^{-1}$ ($E^1_{2g}$) and 405.53 $cm^{-1}$ ($A_{1g}$) and have a $E^1_{2g}/A_{1g}$ ratio of 0.78. (See Figure 7.17(e) for the Raman spectra) This Raman data corresponds to the growth of monolayer $MoS_2$, though the FWHM of the $E^1_{2g}$-peak is 4.185 $cm^{-1}$ which is much lower compared to that of $MoS_2$ grown on the non-annealed M-plane sapphire. However, the FWHM is much higher than the other annealed sapphire planes.[222] This indicates that the growth on annealed M-plane sapphire results in better quality than on the non-annealed M-plane, but it produces a lower crystallinity than $MoS_2$ grown on other sapphire planes.

Monolayer $MoS_2$ grown on 1400 °C annealed M-plane sapphire shows an A1 exciton peak at ∼1.86 eV and has a FWHM of 0.76 eV, see Figure 7.17(e) for the PL spectrum. this is a blue-shift of ∼ 0.1 eV, from the normal position of the monolayer A1-exciton peak.[31] Generally shifts in the energy of the A1-exciton peak for monolayer $MoS_2$ are attributed to defects, contaminants or strain.[180] The blue shift here can be attributed to a low strain between the $MoS_2$ and the substrate, since the substrate does not hinder the growth of $MoS_2$ in any direction.

It is important to note that the data of the growth of $MoS_2$ on annealed M-plane sapphire described up to this point was from growth with the terraces on the substrate aligned parallel to the gas flow in the furnace. A different growth morphology is observed when the substrates terraces are perpendicular to the gas flow. In Figure 7.18 the growth of $MoS_2$ on annealed M-plane sapphire substrates where the terraces were perpendicular to the gas flow is shown. In the optical microscopy image, Figure 7.17(a), small long dendritic $MoS_2$ flakes are visible. These flakes follow the direction of the terraces on the substrate. The flakes have a different

aspect ratio, the size of the flakes is very limited, with a width of ∼2 $\mu$m and the flakes are ∼3-4$\mu$m long.

The Raman and PL maps, see Figure 7.18(b-d), clearly show the small triangular, though quite dendritic $MoS_2$ flakes on the annealed M-plane substrate. The PL map clearly shows the monolayer nature of all the flakes present on the surface. On the surface mainly monolayer flakes are discerned, for this reason only monolayer Raman and PL spectra are included, see Figure 7.18(e) and (f). A small peak is present ∼420 cm$^{-1}$, corresponding to the sapphire Raman peak. Due to the lower $MoS_2$ coverage this peak appears on the spectrum.

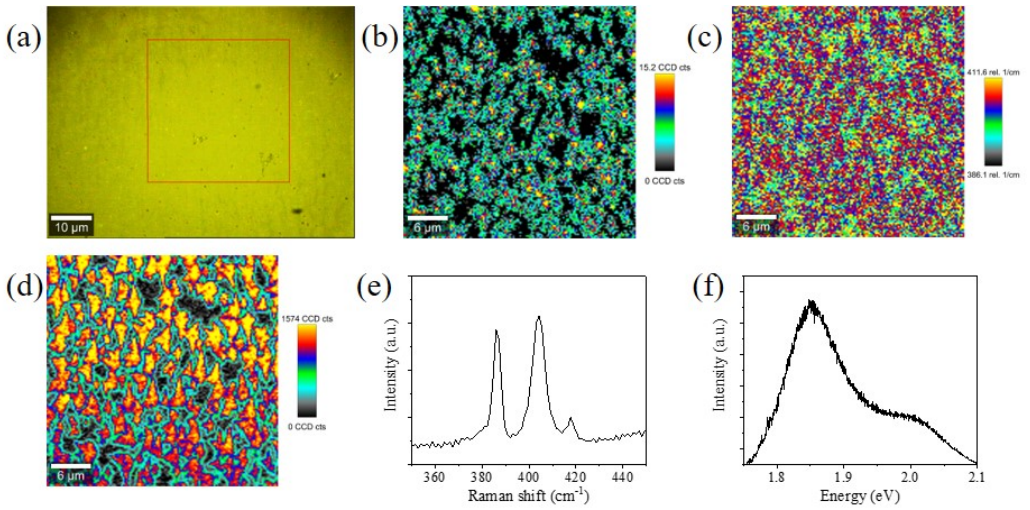


Figure 7.18: (a) Optical microscopy image of the annealed (1400 °C) M-plane substrate covered in $MoS_2$, which is grown with the gas flow perpendicular to the terraces. The red square depicts the area of the Raman sum map of the $E^1_{2g}$ peak ∼385 cm$^{-1}$ shown in (b), (c) shows the peak position map of the $A_{1g}$ peak which is at ∼405 cm$^{-1}$ and in (d) the PL sum map of the A-exciton peak at ∼1.85 eV. In (e) the individual spectra for the single, bi- and multi-layer $MoS_2$ on C-plane sapphire are given, the same is shown in (f) for the PL spectra.

When comparing the growth parallel and perpendicular to the terrace direction, see Figure 7.19, the length of the grown $MoS_2$ flakes is strongly limited for the perpendicular growth. Though the width of the flakes in both scenarios is comparable. A reasonable explanation for the limitation when growing perpendicular to the flow is that the surface morphology limits the diffusion of the precursors in both the gaseous phase as well as surface diffusion. For the perpendicular growth, the opposite is valid as the precursors can easily diffuse along the even terrace, without being interrupted by the steps on the substrate. The presence of terrace steps might also cause a turbulent flow for the perpendicular growth, resulting in a decrease in nucleation.[279]

The Raman spectra of the growth on the orthogonally oriented substrates show a more intense signal for the $MoS_2$ growth on the parallel directed terraces. Whilst this results in a lower $E^1_{2g}/A_{1g}$ ratio,∼0.78 cm$^{-1}$, compared to the growth on the perpendicular directed terraces, ∼0.91 cm$^{-1}$. Indicating that growing $MoS_2$ on

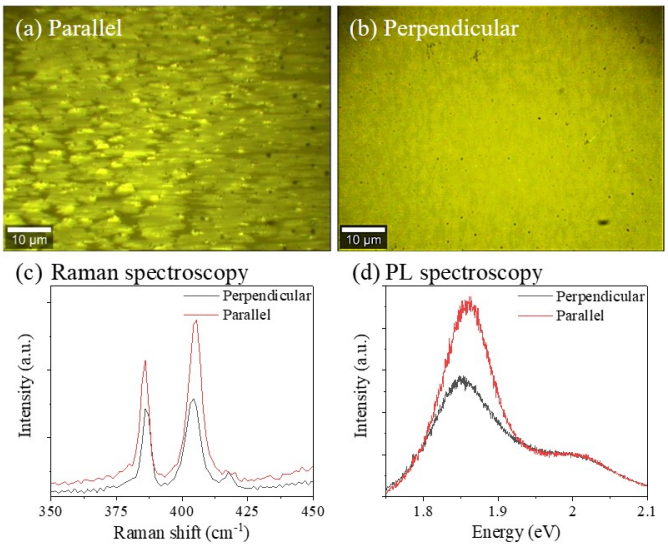


Figure 7.19: Comparison of $MoS_2$ growth with terraces aligned parallel and perpendicular to the gas flow direction on 1400 °C annealed M-plane sapphire. (a) Optical microscopy image of parallel $MoS_2$ growth, (b) Optical microscopy image of perpendicular growth, (c) Raman spectra of both parallel and perpendicular growth of $MoS_2$ on annealed M-plane sapphire and (d) the corresponding PL spectra.

annealed M-plane results in a higher crystallinity and better quality $MoS_2$ when the terraces are aligned perpendicular to the gas flow.

In the PL spectrum a strong PL intensity is observed for the $MoS_2$ grown on the samples aligned with terraces parallel to the gas flow, which is ∼1.6x the intensity of the PL peak for the perpendicular directed terraces, 2.88 eV. The A1 exciton peak position also varies slightly, ∼1.848 eV for perpendicular and ∼1.861 eV for parallel. The PL intensity, peak position and FWHM all indicate that the crystalline quality of the $MoS_2$ grown on annealed M-plane sapphire with terraces aligned parallel to the gas flow was better compared to that of the perpendicular configuration.

It is so demonstrated that CVD growth is very sensitive to growth condition, even for substrates that have been subjected to the same treatments and reaction condition. Differences in the growth mechanisms can occur due to the alignment of the terraces when placing the growth substrate in the furnace, as clearly shown here for the $MoS_2$ grown on the 1400 °C annealed M-plane sapphire. Where the terraces are parallel towards the gas flow in the furnace, a higher coverage with large feature sizes is obtained. There are varying layer numbers present, with monolayer being dominant though bi- and multilayer $MoS_2$ are also present. For the substrate where the terraces were perpendicular towards the gas flow, a growth of smaller, mainly monolayer $MoS_2$ flakes occurred. These flakes were of higher quality as indicated by Raman and PL.

Due to the large steps on the annealed M-plane sapphire (40-200 nm), it is not easy to discern the monolayer $MoS_2$ height difference on this substrate. For the AFM height image, shown in Figure 7.20(a) only the terraces are visible on the surface. By use of the PF-TUNA c-AFM mode it was possible to identify the $MoS_2$

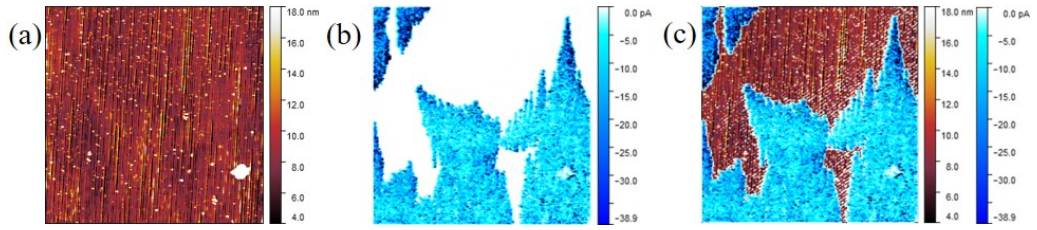


Figure 7.20: AFM height images for the growth of $MoS_2$ on 1400 °C annealed M-plane sapphire. (a) Height image of surface, (b) PF-TUNA contact current image at -0.5 V and (c) Combined height and PF-TUNA image

due to the contrast in conductivity between the $MoS_2$ layer and the substrate. The PF-TUNA contact current image is shown in Figure 7.20(b).

A comparison between the terraces on the height image and the $MoS_2$ on the c-AFM image is possible by overlaying the images as shown in Figure 7.20(c). This shows that the growth of the $MoS_2$ flakes is indeed aligned with the terraces on the surface as the flakes follow the length of the terraces. It is notable that no grain boundaries were identified in the c-AFM images. According to Giannazzo *et al.* this suggests aligned growth, as the electrical effect of the grain boundaries of CVD-grown $MoS_2$ is typically resolvable by c-AFM,[280] though the observation of grain boundaries can also be limited by practical constraints.

## 7.3 Summary & Discussion

Water contact angle measurements of the sapphire substrates, before and after annealing of sapphire planes, show a strong decrease in the contact angle as the substrates become more hydrophilic after annealing. This is shown in Table 7.2. After annealing, M-plane sapphire shows the lowest contact angle of the different substrates, 8.75 °. As freshly exfoliated or non-contaminated $MoS_2$ is intrinsically mildly hydrophilic, increased hydrophilicity can be beneficial for the growth of $MoS_2$.[281] $SiO_2$ has a contact angle which is 57.4 °, a value in between the contact angles of the non-annealed and annealed sapphire substrates.

Table 7.2 also shows the varying surface energies of the different substrates. The surface energy of few-layer $MoS_2$ is 46.5 $mJ/m^2$, which is close to the surface energies of the annealed A-plane and M-plane sapphire, respectively 46.3 $mJ/m^2$ and 45.23 $mJ/m^2$.[282,283] Both the surface energy for A- and M-plane sapphire increases by annealing as shown in Table 7.2. $SiO_2$ shows a surface energy which is higher compared to the other substrates with a energy of 48.8 $mJ/m^2$. The C-plane sapphire surface energy decreases under annealing from 40.9 $mJ/m^2$ to 38.9 $mJ/m^2$. Finally the surface energy of the R-plane differs most from the $MoS_2$ value, both on the non-annealed, 32.5 $mJ/m^2$, and annealed, 35.8 $mJ/m^2$, surface.

$SiO_2/Si$ is known to result in qualitative CVD growth of $MoS_2$, though the growth results in random orientation of the flakes. The results obtained in this work confirm these findings, though $SiO_2$ results in large crystalline monolayer flakes, the

| Substrate | | Contact angle | | Surface energy | |
|---|---|---|---|---|---|
| | | $T_{RT}$ | $T_{1400C}$ | $T_{RT}$ | $T_{1400C}$ |
| Sapphire | C-plane | 76.5 | 14.9 | 40.9 | 38.9 |
| | R-plane | 91.1 | 15.8 | 32.5 | 35.8 |
| | A-plane | 77.9 | 21.7 | 39.9 | 46.3 |
| | M-plane | 78.3 | 8.75 | 41.0 | 45.2 |
| $SiO_2$ | | 57.4 | N.A. | 48.8 | N.A. |

Table 7.2: Table containing the water contact angles and surface energy for $SiO_2$ and the different sapphire planes, non-annealed and annealed at 1400 °C

material does not show ordering or alignment of the grown domains on the surface. $SiO_2$/Si will be considered as a comparison material for the quality of the material in this discussion of the substrates, though it will be excluded in the discussion of directed growth of $MoS_2$.

For the annealing of sapphire planes, improvement of the results was visible for all but one substrate. Where the crystal/flake size, quality and alignment of the formed material improved for R-, A- and M-plane, it is worth noting that $MoS_2$ grown on annealed C-plane sapphire does not show any alignment. In contrast to the annealed C-plane a degree of alignment is present for the non-annealed sample, as shown in Figure 7.4, though the quality of the flakes appears to decrease as the $E^1_{2g}/A_{1g}$-ratio decreases for annealed sapphire as well as the FWHM of the $E^1_{2g}$-peak, while the peak positions remain constant.(See Table 7.4)

The degree of alignment of $MoS_2$ shown on non-annealed C-plane sapphire can possibly be explained by the surface energy. The surface energy was calculated from the contact angles of water, diimide and glycerol. As the surface energy of C-plane sapphire decreases with annealing, the surface energy differs more with that of $MoS_2$, 45.23 mJ/m$^2$, after annealing.[282] The surface energies for the different planes before and after annealing are summarized in Table 7.2. The surface energy appears to be more important in this case than the surface morphology or the surface interaction. Though the surface energy appears to play a small role in the alignment of the flakes, the surface energy does not appear to be a limiting factor. It is not a limiting factor for R-plane as the surface energy from R-plane, both non-annealed and 1400 °C annealed, varies widely from that of $MoS_2$, but growth on annealed R-plane sapphire results in aligned growth. Therefore it can be concluded that the presence of straight and long terraces, and thus the influence of the surface morphology, has a higher importance.

From this point on only the annealed sapphire planes will be discussed as these lead to the most directed growth. The differently annealed sapphire substrates resulted in different growth mechanisms of $MoS_2$ on the surface as shown in the optical microscopy images in Figure 7.21a-d). Growth of $MoS_2$ was observed on all the tested growth substrates, showing mainly a Stranski-Krastanov like growth mode.[122] The surface coverage was quite high for all sapphire surfaces, resulting in an average coverage of ∼87%. (See Figure 7.21e).) The surface coverage was

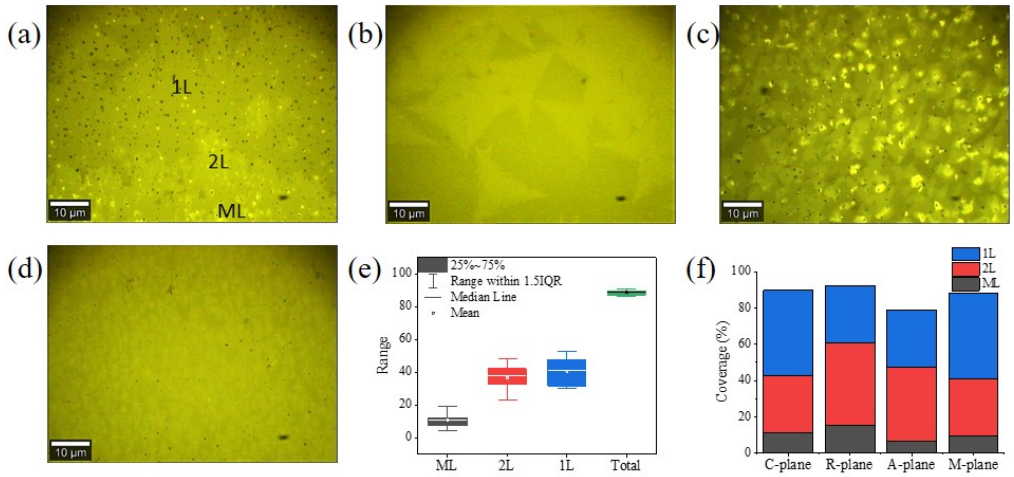


Figure 7.21: Optical microscopy images and surface coverage data for the growth of $MoS_2$ on 1400 °C annealed sapphire planes. Optical microscopy image of CVD grown $MoS_2$ on (a) C-plane, (b) R-plane, (c) A-plane and (d) M-plane. (e) Shows the average mono-, bi- and multilayer coverage on sapphire in general, while (f) shows the surface coverage for the different planes

taken by measuring the whole surface of various samples and averaging these out. In Figure 7.21f) a graph depicting the mono-, bi-, multilayer and total coverage per plane is shown, the exact numbers for this are shown in Table 7.3.

Mono- and bilayer $MoS_2$, identified from the contrast on the optical microscopy images as well as AFM, dominated on all the annealed sapphire substrates, contributing to over 80% of the total surface coverage, though it should be mentioned that all substrates also displayed areas of multilayer growth. It is also interesting to note that AFM was performed multiple times over the course of a year and no reduction in the $MoS_2$ crystal quality was observed for any of the samples.

Differences in coverage on the samples appear to be largely due to the growth substrate topography, which leads to different surface coverages as the terraces and steps can improve or hinder the growth of $MoS_2$ on the different growth substrates. The large faceted steps on M-plane appear to hinder the growth from stretching over a multitude of terrace steps. This interrupted growth would also explain the relatively small size of the flakes on A-plane.

| Sapphire plane | Monolayer (%) | Bilayer (%) | Multilayer (%) | Coverage (%) |
|---|---|---|---|---|
| C-plane | 46.96 | 31.60 | 11.12 | 89.68 |
| R-plane | 31.86 | 45.10 | 15.39 | 92.35 |
| A-plane | 31.51 | 40.61 | 6.62 | 78.74 |
| M-plane | 47.64 | 31.01 | 9.62 | 88.27 |

Table 7.3: Overview of mono-, bi & multilayer coverages of $MoS_2$ on the different annealed (1400 °C) sapphire planes.

In Figure 7.22(a) the Raman spectra for monolayer $MoS_2$ on the different annealed sapphire substrates is shown. For all monolayer areas the $E^1_{2g}$ peak is situated at ~386 $cm^{-1}$, for growth on all substrates but A-plane sapphire (384.72

$cm^{-1}$), while the $A_{1g}$ peak is situated at 405.5 $cm^{-1}$ for all the substrates.[37,175] This is also shown in Table 7.4 The broadness of the peaks, characterized by the FWHM for the $MoS_2$ peaks on each of the growth substrates, varies as the different growth substrates result in different degrees of crystallinity.[284] Broader peaks are a result of scattering and therefore indicate lower crystallinity. The FWHM of the $E^1_{2g}$ peak is smallest for $MoS_2$ grown on C-plane sapphire (3.841 $cm^{-1}$) and increases slightly for $MoS_2$ on R-plane sapphire (3.883 $cm^{-1}$). It remains unclear whether this is a actual difference or within the error margin. There is a strong increase in the FWHM for the $MoS_2$ grown on A- and M-plane sapphire (respectively 3.926 $cm^{-1}$ and 4.185 $cm^{-1}$). This, in addition to the $E^1_{2g}/A_{1g}$ ratios of 0.8 and 0.82 (See Table 7.4), indicates that the $MoS_2$ grown on C-plane and R-plane have the best crystallinity.[222]

The PL signal for monolayer $MoS_2$ is very strong due to the direct band gap, decreased interlayer interaction and quantum confinement effects.[32] All the samples show a peak around 1.85 eV corresponding to the A1 exciton in $MoS_2$. See Figure 7.22(b) for the different PL spectra. In monolayer $MoS_2$ this is the main expected peak, though the B1 exciton peak ∼2.0 eV is also present due to spin-orbit coupling. On C-plane sapphire the A1 exciton peak is at least 4x more intense compared to monolayer $MoS_2$ grown on the other sapphire planes, which is attributed to the relative strength of interaction of the $MoS_2$ with the substrate. In the case of epitaxial growth, or aligned growth, there should be a larger interaction between the interfaces, resulting in a stronger or tighter bond with the surface. This interaction leads to a decreased PL signal.[248,285]

An Al-terminated surface, obtained for example by growth at higher temperature or in the presence of $H_2$, also increases the interaction of the $MoS_2$ with the sapphire surface.[271] Another factor which influences the intensity of the PL is strain. The growth on the C-plane surface will experience homogenous in-plane strain as opposed to the other substrates where the mismatch in the expansion coefficients will lead to uniaxial strain upon cooling. The other planes result in $MoS_2$ with comparable

| Substrate | Position $E^1_{2g}$ ($cm^{-1}$) | FWHM $E^1_{2g}$ ($cm^{-1}$) | Position $A_{1g}$ ($cm^{-1}$) | FWHM $A_{1g}$ ($cm^{-1}$) | $E^1_{2g}/A_{1g}$ ratio |
|---|---|---|---|---|---|
| C-plane | 385.96 | 6.00 | 405.53 | 6.41 | 0.64 |
| C-plane annealed | 385.95 | 3.84 | 405.53 | 5.88 | 0.80 |
| R-plane | 385.96 | 10.01 | 405.53 | 6.53 | 0.55 |
| R-plane annealed | 385.96 | 3.89 | 405.53 | 6.92 | 0.82 |
| A-plane | 385.96 | 7.25 | 406.75 | 8.92 | 0.70 |
| A-plane annealed | 384.73 | 3.93 | 405.53 | 6.25 | 0.85 |
| M-plane | 383.50 | 6.44 | 407.97 | 6.00 | 0.58 |
| M-plane annealed | 385.96 | 4.19 | 405.53 | 6.57 | 0.78 |
| $SiO_2$ | 384.68 | 4.18 | 404.26 | 6.63 | 0.86 |

Table 7.4: Overview of the $E^1_{2g}$ and $A_{1g}$ peak positions and FWHM as well as the $E^1_{2g}/A_{1g}$ intensity ratio for all substrates

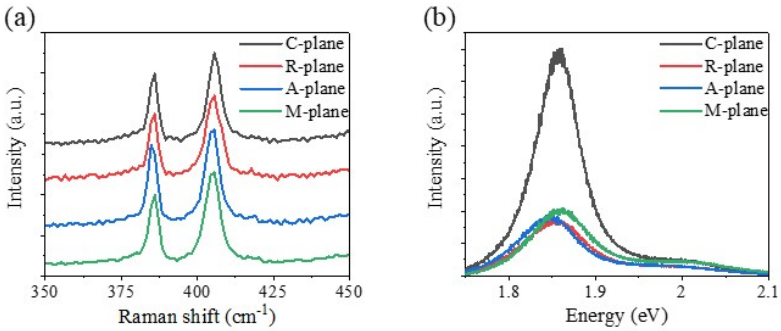


Figure 7.22: (a) Raman spectra for monolayer $MoS_2$ grown on the different annealed sapphire planes and (b) the corresponding photoluminescence spectra for monolayer $MoS_2$.

PL intensities though the peak for 1L $MoS_2$ on A-plane sapphire is at slightly lower energies, ∼1.85 eV, compared to 1.86 eV for the other planes. This shift can possibly be attributed to low crystallinity caused by the formation of small mismatched flakes on the surface, though this seems unlikely as the PL intensity is comparable to that of $MoS_2$ on M- and R-plane sapphire.

The highest degree of crystallinity for $MoS_2$ was found on the C- and R-plane sapphire, as evidenced by Raman and PL spectra. The $MoS_2$ on these substrates has flakes/grains with lateral sizes of 20-50 $\mu$m, while the $MoS_2$ flake-length scale on A-plane sapphire is 1-5 $\mu$m and the $MoS_2$ on M-plane sapphire is about 10 $\mu$m in length along the direction of the facets. This could in part be explained by the terrace sizes of C- and R-plane sapphire, as these are larger than the terrace sizes of M- and A-plane sapphire. When looking at the flake-sizes, as well as the PL-intensity, C-plane sapphire results in the largest flakes and most intense PL-intensity, though there is a lack of alignment of the $MoS_2$ flakes on this plane.

Aligned growth is observed for $MoS_2$ on R-plane and M-plane sapphire. On both planes the flakes grow preferentially in the direction of the terraces. R-plane can be considered as a better growth substrate for directing the morphology compared to M-plane sapphire as there is more growth in the direction perpendicular to the terraces, whereas this is hindered for M-plane. Furthermore, growth of $MoS_2$ on R-plane sapphire results in larger flake sizes, though growth on M-plane sapphire could be preferable if long flakes with narrow widths were desired.

The alignment of $MoS_2$ on R-plane sapphire can be attributed in part to the large terrace size and small straight steps, which allow unimpeded growth. Both R- and M-plane sapphire show straight and well-defined terraces, which allows for unimpeded diffusion of precursors along these directions, which is beneficial for aligned growth. This contrasts with the growth on C-plane sapphire, whose terraces have more curved edges and are less homogeneous. The ragged terraces on A-plane sapphire would sterically hinder the growth of large aligned flakes as the diffusion of nuclei would be strongly inhibited. These differences in morphology explain the apparent lack of alignment observed on the latter two substrates.

Another possible explanation for the observed alignment is the lower symmetries of the R-, M- and A-plane, which results in anisotropic strain on the surface. This strain can result in anisotropic growth of TMDs; the anisotropic strain can cause the newly formed nuclei to diffuse over the surface to minimize the surface energy, thereby resulting in alignment of the flakes.[286] Such growth leads to highly-crystalline aligned flakes without antiphase boundaries, separating two domains of the same ordered phase. As discussed before, the surface morphology of the A-plane would hinder diffusion, which would explain the lack of alignment observed on this plane. This argument is supported by the lack of grain boundaries observed for $MoS_2$ on M-plane when characterized by c-AFM.

The shape of the flakes is less triangular and more dendritic for $MoS_2$ growth on M- and R-plane sapphire, compared with the $MoS_2$ growth on C-plane sapphire. This shape and the lower PL intensity indicate a stronger interaction between the substrate and the grown material for M- and R-plane sapphire. The stronger interaction between the substrate and material can lead to epitaxial growth, or in this case aligned growth, as the increased interaction results in substrate directed growth.

Finally, the A-plane sapphire substrate is very reactive at the terrace steps as observed by AFM, making it a suitable substrate for high-density nucleation of $MoS_2$. Due to the ragged edges of the terraces, the growth is limited in the lateral direction and therefore results in limited flake size as well as growth in the vertical direction. This causes flakes to preferentially nucleate near the steps though the orientation of the flakes appears to be random. Such small flakes with varying thicknesses can also provide advantages and potential applications as the material has a large surface area, these applications include catalysis and batteries.[50,287,288]

The research performed here shows that the growth mode of $MoS_2$ is strongly influenced by the surface morphology as well as the surface interaction. Aligned growth of $MoS_2$ is possible on M- and R-plane under the growth parameters used here. The alignment of the CVD-grown $MoS_2$ can be improved by selecting an appropriate growth substrate as well as optimizing the growth conditions of the material. This is largely dictated by the surface morphology as well as the enhanced surface interaction.

An approach which could be used to further improve the growth, or result in alignment, would be to use an Al-terminated sapphire substrate, as this causes a higher interaction with the material. This could be achieved by increasing the reaction temperature or by using hydrogen as carrier gas. Other parameters that could improve the growth are the duration and temperature of the annealing. As C-plane results in better $MoS_2$ for non-annealed substrates, while Ma *et al.* reported annealed A-plane sapphire at a lower temperature. CVD of $MoS_2$ on M-plane could possibly result in broader more crystalline flakes when the terrace stepsizes are well-defined but lower in size.

# 8 Direct Growth of TMD Heterostructures

As noted in section 3.6 when TMDs are combined as heterostructures, they offer the potential for devices with atomically sharp, bond-free interfaces without the need for lattice matching considerations for vertical heterostructures, where lateral heterostructures can lead to seamless transitions between the different materials.[289] When combining semiconductors which support different carrier types, a wide range of possibilities for fabrication of devices completely made from 2D materials is opened.

The strong light–matter interaction and direct band gap properties of monolayer TMDs, such as $MoS_2$, $MoSe_2$ and $WSe_2$, suggest that TMD heterostructures are promising candidates for applications in photodiodes,[290] light-emitting,[131] light-harvesting,[291] and p-n junctions or FETs.[130,292] Vertical heterostructures, where different TMD monolayers are stacked vertically in a layer-by-layer fashion, are interesting for applications in flexible opto-electronics.[293–295] Lateral heterojunctions provide scope to devise new devices with optimised performance.[290,296] The properties of the lateral heterojunctions are diverse and depend on the nature and quality of the interface.[297,298] Therefore it is important to synthesize lateral heterojunctions with atomically sharp interfaces to be able to optimise the properties.

Direct CVD growth of 2D heterostructures is the formation of heterostructures *in-situ*, during the synthesis of the material, without the need to transfer or manipulate the flakes post synthesis. This growth method allows the formation of atomically sharp interfaces. A benefit of this approach is the possibility of sequential growth, which can be repeated multiple times for the selective combination of materials. This chapter describes in detail the development of methodologies for direct synthesis of TMD heterostructures by both single- and double-step CVD growth. In the single-step CVD both TMDs are synthesized in a single furnace run by varying reaction parameters such as the temperature or precursors in the furnace thus activating the sequential growth of the different materials. While in a double-step process two separate consecutive CVD processes are required. At each stage of the process a different TMD is synthesised.

The advantage of the single-step synthesis is the minimization of oxidation and defects at the interface as the system vacuum remains intact during the whole process, though the control over the growth is more limited.[80] In double-step growth

there is more control over the growth parameters in the individual furnace runs. This growth method also allows for a larger variety of combinations of constituent materials and allows for patterning of the initially grown material, therefore allowing directed growth of the second material. The double step growth method is a more flexible process but this is achieved at the expense of interface quality.

In the process for double-step synthesis the standard CVD process for the desired TMD is used. After this initial growth a second CVD run is executed to add the second TMD, to form the heterostructure. This process relies on the thermal stability of the first material to allow the growth of the second material, while the initially grown material stays intact. Furthermore, it may also rely on the relative stability of the second precursor during the growth of the first TMD. More details on the reaction parameters in general are discussed in subsection 5.1.3 and the optimisation of reaction parameters for CVD growth is discussed in detail for $WSe_2$ in chapter 6.

For single-step synthesis the grown heterostructures were limited to a combination of different sulfide TMDs or selenide TMDs due to tool limitations. For the furnace systems used in this study the chalcogen source cannot be changed during reaction. As this work focuses on Mo and W TMDs, the resultant heterostructures were $MoS_2/WS_2$ and $MoSe_2/WSe_2$ heterostructures. The growth recipes needed to be optimised for the single-step processes. This is needed to prevent the growth of multilayer structures. The precursors are also already present in chamber before the growth of the second TMD which can prevent interaction of the second metal precursor with the chalcogenide precursor. When growing Se TMDs, Se can also interact with $H_2$ to form $H_2Se$ which can etch away the flakes on the surface and prevent the growth of multilayer structures.

In both the double and single-step synthesis a microreactor approach has been used, resulting in the use of less metal precursor compared to other common CVD synthesis methods for heterostructures. The use of a microreactor improves the reactivity due to the close proximity between the metal precursor and the growth substrate and this approach has yielded good results for the synthesis of individual TMDs.[208] Therefore it appears to be a logical step to expand this synthesis method for heterostructures as depending on the application heterostructures can have optimised properties compared to individual TMDs.

## 8.1 Double-step synthesis

Double-step synthesis is the most straightforward manner to fabricate 2D heterostructures directly by CVD as this process gives better control over the reaction parameters which leads to an optimised reaction. The reaction parameters, such as precursors, temperatures and pressures, can be controlled independently for both TMD furnace runs, while the single-step synthesis requires an overlap of certain parameters.[296] Double-step growth can also lead to the growth of larger fea-

ture sizes.[299] Another advantage of this method is the possibility to characterise the growth at each synthesis step before subsequent modifications, thereby resulting in a more convenient identification of the different TMDs after the second CVD run. This characterisation also allows for patterning of the first TMD flakes, to direct the growth of the subsequent TMD. Finally with the double-step synthesis approach many different heterostructure combinations of TMDs can be synthesized with fewer limitations from the precursors or from tool constraints.[136,299] This approach can also lead to the formation of both lateral and vertical heterostructures depending on the quality of the materials and the reaction parameters.[296,299,300]

The most significant disadvantage of this synthesis approach is the disruption caused by the different reaction steps. After the first run, the sample is exposed to atmospheric conditions directly resulting in partial oxidation of the TMD at edges, grain boundaries and defects.[301,302] This oxidation can lead to diminished material quality, though it can also be a starting point for the etching of the initially synthesized TMD during the second furnace step, thereby removing the first TMD and only leaving the subsequently grown TMD behind. This could in theory be interesting for selective single layer templated growth.

### 8.1.1 $MoS_2$ +$WS_2$

When $MoS_2$ is initially grown followed by the synthesis of $WS_2$ in the furnace setup described in this work there appears to be etching of the initial material during the second synthesis step as shown in the optical microscopy images before and after $WS_2$ synthesis in Figure 8.1. For the $MoS_2$ growth a standard growth recipe with a growth time of 30 min and a 30 min annealing, both at 750 °C, was used to synthesize $MoS_2$. Optical microscopy images of the resulting flakes are shown in Figure 8.1(a) and (b). The subsequent CVD process step to form $WS_2$ also was according to a standard growth recipe, similar to that for $MoS_2$, though the reaction temperature, 850 °C, was higher. In Figure 8.1(c) and (d) optical microscopy images corresponding to the locations in Figure 8.1(a) and (b) are shown. Everything but the thicker multilayer $MoS_2$ appears to have etched away in these images and thick $WS_2$ structures have replaced the $MoS_2$ flakes.

Further inspection by Raman, performed after $MoS_2$ and $WS_2$ synthesis, shows that the $MoS_2$ has almost completely disappears from the surface after the $WSe_2$ growth step, as shown in the Raman $MoS_2$ $E^1_{2g}$ intensity maps in Figure 8.1(e) and (f). Where there are clear $MoS_2$ flakes present in Figure 8.1(e) these flakes appear to have been lost, possibly etched, after the second furnace run, see Figure 8.1(f). Figure 8.1(g) shows the $WS_2$ $E^1_{2g}$ Raman intensity map after the synthesis of $WS_2$. This map shows the presence of $WS_2$, though the Raman and PL spectra, Figure 8.1(h) and (i) indicate that these $WS_2$ areas are not monolayer $WS_2$. The Raman spectrum of $WS_2$ shows a broad combined peak for the 2LA(M)+$E^1_{2g}$ modes, with a FWHM of 12.46 $cm^{-1}$, and the $E^1_{2g}/A_{1g}$ ratio is 0.89 indicating few layer $WS_2$.[303] The $MoS_2$ map of the sample after both furnace growth runs shows some very low intensity

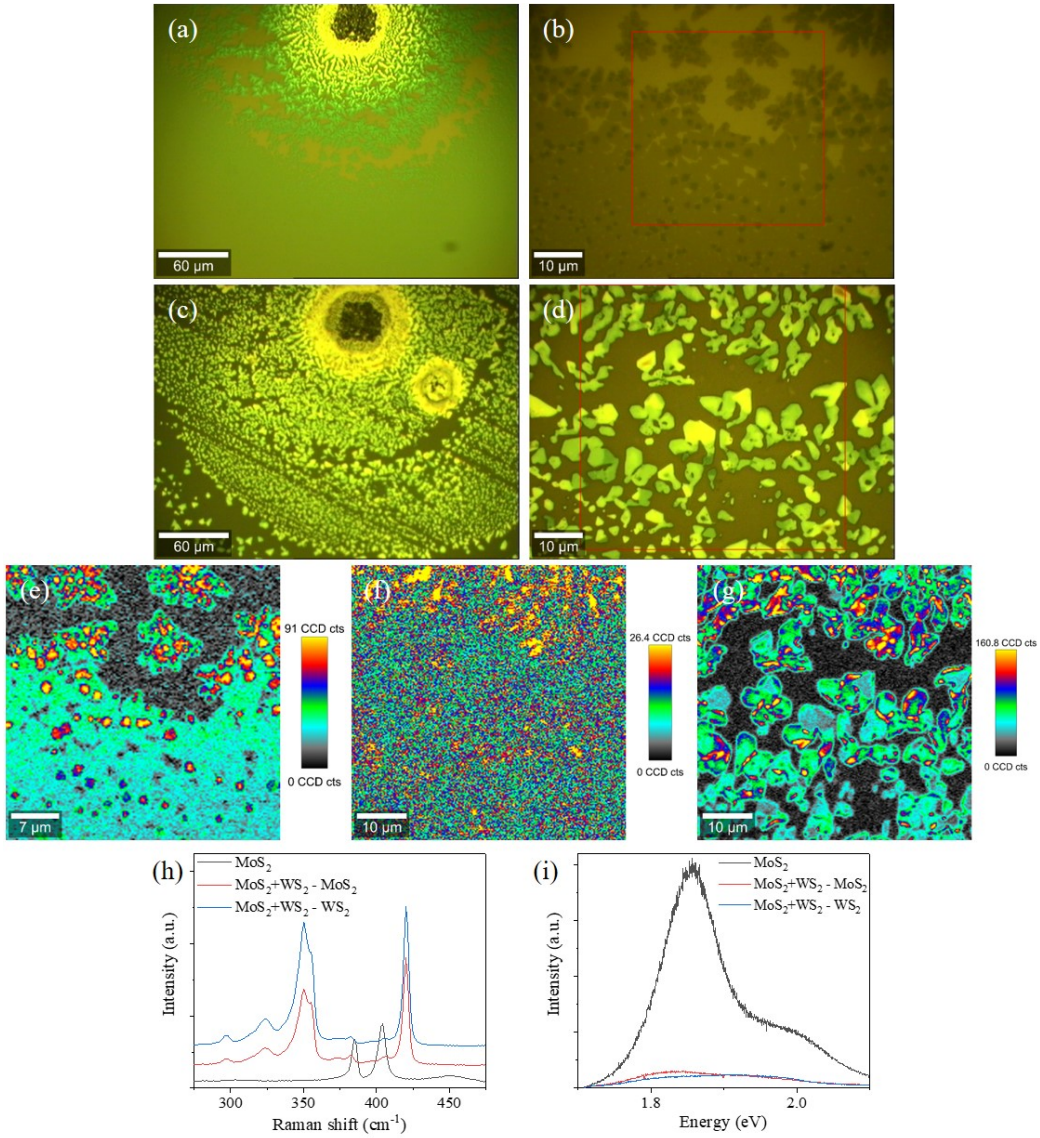


Figure 8.1: Optical microscopy, Raman and PL data of double step synthesized $MoS_2/WS_2$ after the first $MoS_2$ and subsequent $WS_2$ furnace run. (a) 20x magnification optical microscopy image of $MoS_2$, (b) 100x magnification image of $MoS_2$, with (c) and (d) the corresponding optical microscopy images at the same location after $WS_2$ growth. Raman intensity maps of $MoS_2$ $E^1_{2g}$-peak after the first furnace run (e) and after the second furnace run (f) from the areas outlined in red in (b) and (d). (g) shows the $WS_2$ $E^1_{2g}$ Raman intensity map. The Raman spectra and PL spectra of $MoS_2$ before and after the $WS_2$ run as well as that of $WS_2$ are shown in (h) and (i)

$MoS_2$ peaks, where the $WS_2$ map shows a more pronounced presence of $WS_2$. Thus indicating that though most $MoS_2$ is removed during the second furnace run, traces still remain on the substrate.

The A1-exciton peak in the PL spectrum of $MoS_2$ after the $MoS_2$ furnace run is more intense prior to the $WS_2$ growth. The B1-exciton becomes more pronounced in the $MoS_2$ spectrum after the second furnace run. Indicating the presence of multilayer $MoS_2$ or the B1-exciton is pronounced due to electron scattering. Not only the peaks of the $MoS_2$ spectrum, but also overall the intensity of the peaks of the $WS_2$ spectrum have a lower intensity compared to individual $WS_2$ flakes on the same sample. The $WS_2$ spectrum is shifted to lower energies, 1.857 eV, compared to the standard ∼1.98 eV.[175] This shift is possibly due to interaction with $MoS_2$, which has a PL peak at a lower wavelength.

### 8.1.2 $WS_2$+$MoS_2$

When $WS_2$ was initially synthesized followed by the synthesis of $MoS_2$ this did not lead to a significant etching of the initially formed $WS_2$ flakes. The $WS_2$ is synthesized at a higher temperature and is more stable than $MoS_2$, therefore the growth of $MoS_2$ did not etch away the $WS_2$. The optical microscopy images of the $WS_2$ growth, see Figure 8.2(a) and (b), show triangular monolayer flakes of $WS_2$, which are quite clustered together. The flakes are ∼10-20 $\mu$m in size. Small multilayer flakes, ∼5 $\mu$m, surround the monolayer flakes.

The $WS_2$ monolayer flakes are also observed in the 2LA(M)+$E^1_{2g}$ Raman map in Figure 8.2(b) and the A1-exciton PL sum map in Figure 8.2(e). The edges of the flake contain some small bilayer regions. The Raman spectrum of the $WS_2$ area shows the 2LA(M)+$E^1_{2g}$ peak at ∼350 cm$^{-1}$ and the $A_{1g}$ peak at ∼ 418 cm$^{-1}$. The FWHM of the 2LA(M)+$E^1_{2g}$ peak is 17.77 cm$^{-1}$, where the FWHM of the $A_{1g}$ is ∼8.17 cm$^{-1}$, both values are broader than the FWHM of monolayer $WS_2$, though the values are not significantly broader. The 2LA(M)+$E^1_{2g}$ peak is ∼ 2.6x the intensity of the $A_{1g}$ peak, indicating that the $WS_2$ is indeed monolayer. Several weak peaks are also visible in the spectrum, ∼232 cm$^{-1}$, ∼296 cm$^{-1}$ and ∼322 cm$^{-1}$, these peaks correspond to $WS_2$ as well.[304]

In the $WS_2$ A1 exciton intensity map, from the PL spectrum, the edges have a more intense signal compared to the body of the flake. The A1 exciton peak is located at ∼ 1.94 eV, which corresponds to literature values for monolayer $WS_2$.[260]. The peak shifts to higher energies for thicker $WS_2$ layers, therefore the flakes appear to be mainly monolayer.

Figure 8.3(a) and (b) shows the sites depicting the optical images shown in Figure 8.2(a) and (b) after $MoS_2$ growth. The $WS_2$ area appears to be removed on the optical microscopy image, though the $WS_2$ 2LA(M)+$E^1_{2g}$ Raman map of the area, see Figure 8.3(c) shows that $WS_2$ is still present on the surface. The grain boundaries, which were already present after the first synthesis step, have become more pronounced after the second CVD process, thus indicating a degree of etching

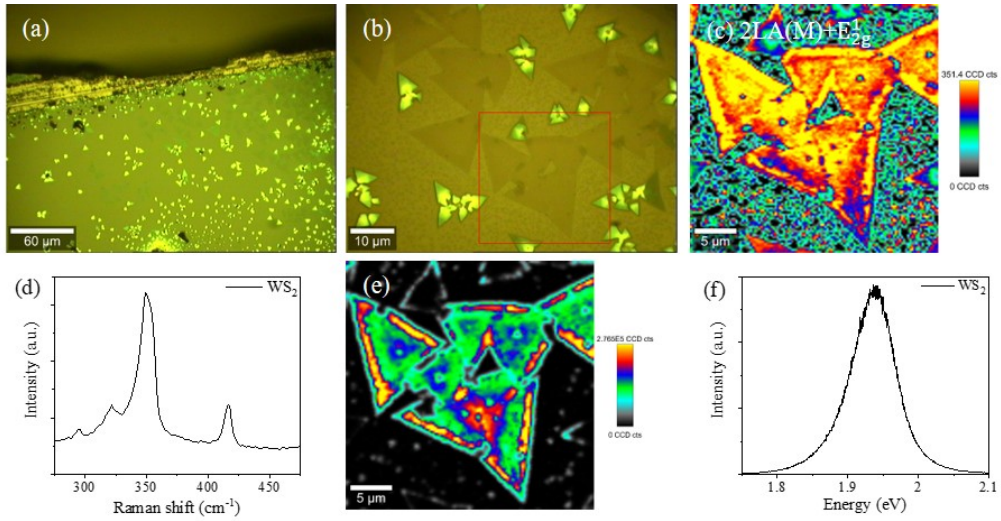


Figure 8.2: Optical microscopy, Raman and PL data of CVD grown $WS_2$ (a) 20x magnification optical microscopy image of $WS_2$, (b) 100x magnification image of $WS_2$, with (c) the Raman intensity maps of $WS_2$ 2LA(M)+$E^1_{2g}$-peak and (d) the Raman spectrum of the $WS_2$ area. (e) shows the PL intensity map of the A1 exciton at ∼1.94 eV and (f) the PL spectrum of the $WS_2$ area

at these boundaries.

Figure 8.3(d) shows a $MoS_2$ $E^1_{2g}$ Raman map, where the presence of $MoS_2$ is visible at the edges and grain boundaries of the $WS_2$ flakes. In the optical microscopy image these areas can be identified due to their darker contrast on the surface. The $MoS_2$ appears to grow mostly laterally in the plane around the multilayer $WS_2$ areas.

The Raman spectra for the $WS_2$ and $MoS_2$ areas are shown in Figure 8.3(e). The $WS_2$ spectrum for the heterostructure growth is similar to that of the individual growth of $WS_2$, though the ratio between the 2LA(M)+$E^1_{2g}$ and $A_{1g}$ peaks is smaller.[303] The FWHM of the peaks remains constant in both the $WS_2$ spectra, thus suggesting the quality of the $WS_2$ is not adversely affected. However, the grain boundaries appear more pronounced on the surface. The $MoS_2$ $E^1_{2g}$ and $A_{1g}$ peaks are located at ∼381 $cm^{-1}$ and ∼404 $cm^{-1}$, corresponding to monolayer $MoS_2$. The ratio of the $E^1_{2g}/A_{1g}$ peaks is ∼ 0.68, the low ratio indicates the poor crystallinity of the $MoS_2$ after the $WS_2$ growth.

In Figure 8.4 the PL data for the $WS_2$+$MoS_2$ heterostructure growth is shown. The $WS_2$ A1 exciton intensity map, see Figure 8.4(b), shows a strong PL signal at some of the $WS_2$ flakes, the flakes where there are no traces of $MoS_2$ according to the $MoS_2$ $E^1_{2g}$ Raman map, Figure 8.3(d). In contrast to the $WS_2$ PL map, the $MoS_2$ A1 exciton intensity map does not show any sharp $MoS_2$ peak, see Figure 8.4(c). This can be explained by the PL spectra of the $WS_2$ and the $MoS_2$ regions, as shown in Figure 8.4(d), where the $MoS_2$ spectrum clearly shows both the A1 and B1 exciton peaks. Both peaks are about the same intensity, the pronounced presence of the B1 exciton peak indicates either a strong interaction with the substrate or a defective $MoS_2$ growth.[32] As $SiO_2$/Si does not have a strong interaction with $MoS_2$, the presence of defects on the surface is more probable. The $WS_2$ PL signal is also

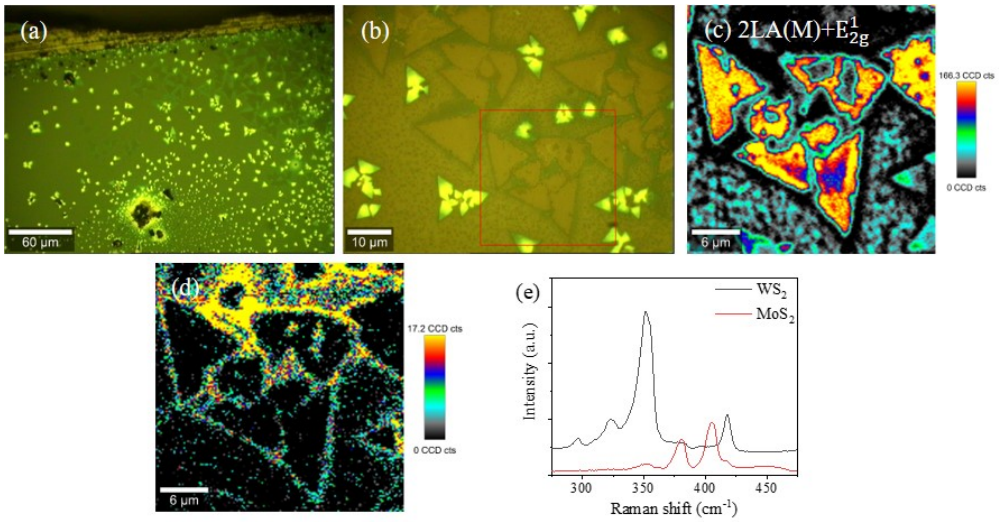


Figure 8.3: Optical microscopy and Raman data of the sample shown in Figure 8.2 after $MoS_2$ growth. (a) 20x magnification optical microscopy image, (b) 100x magnification image, with (c) the Raman intensity maps of $WS_2$ 2LA(M)+$E^1_{2g}$-peak and (d) the Raman intensity map of the $MoS_2$ $E^1_{2g}$ peak. (e) shows the Raman spectra of the $WS_2$ and $MoS_2$ areas

very pronounced, more than 30x as intense as the $MoS_2$ signal. This is in part due to the stronger resonance of $WS_2$, though there is a dramatic decrease of the photoluminescence efficiency with increasing layer number.[31,303]

An AFM height image of the surface after both of the CVD steps is shown in Figure 8.5. In the AFM image the $WS_2$ flakes are lower than the surrounding area. This height difference can indicate the etching of $SiO_2$ or the deposition of material on the $SiO_2$/Si, most likely $MoS_2$. Especially in smaller areas between the flakes the surface is higher. This corresponds with the presence of $MoS_2$ as indicated by Raman spectroscopy in Figure 8.3.

Thus, it appears that the direct growth of heterostructures by a double-step approach can lead to etching of the initially grown material if this material is less stable as is the case for the synthesis of $MoS_2$ followed by $WS_2$. Moreover, when the more stable TMD is synthesised first, the subsequently grown TMD appears to have poorer crystallinity. The chance of a TMD nucleating on a defective site, compared to nucleation on a pristine TMD surface, is higher as this can be energetically more favourable. Therefore, to produce TMD heterostructures suitable for electronic device applications a more stable synthesis approach would be desirable, such as the single-step synthesis described hereafter.

## 8.2 Single-step synthesis

The single-step growth of heterostructures has been shown in numerous publications, such as the work by Shi *et al.* where a change in the temperature regime was adopted for selective growth of materials to form heterostructures.[79] For the reaction process used in this work, the temperature was also increased throughout

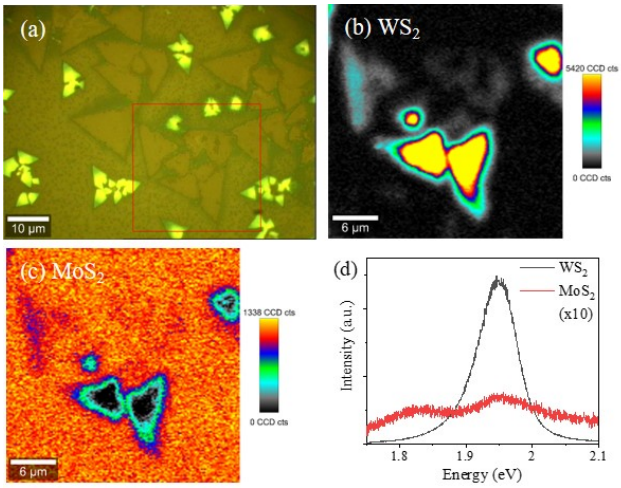


Figure 8.4: Optical microscopy and PL data of the sample shown in Figure 8.2 after $MoS_2$ growth. (a) 100x magnification optical microscopy image, (b) the PL A1 exciton intensity map of $WS_2$, (c) the PL intensity map of the $MoS_2$ A1 exciton peak. (d) shows the PL spectra of the $WS_2$ and $MoS_2$ areas

the process, to first form the TMD with the lower synthesis temperature, and then the reaction temperature was increased to synthesize the second TMD at its specific growth temperature. The growth temperatures were set to the standard reaction temperature for the individual CVD growths of the corresponding TMDs, 750 °C for $MoS_2$ and $MoSe_2$ and 850 °C for $WS_2$ and $WSe_2$. An example of the time dependent reaction parameters for combined $MoSe_2$+$WSe_2$ growth is shown in Figure 8.6. As separate furnaces were used to grow the sulfide and selenide TMDs, only $MoS_2/WS_2$ and $MoSe_2/WSe_2$ junctions were pursued in this study. This is due to the tendency of S to displace Se in TMDs, as sulfide TMDs are typically more stable than selenide TMDs resulting in uncontrolled cross-contamination,[305]

In this single-step process both metal precursors were placed consecutively on the seed substrate. The precursor which reacts at the higher temperature regime was placed first, while the metal which reacts at lower temperature was then placed on top of the seed substrate. This ordering was to ensure that precursor required for the first TMD was exposed at the surface to chalcogen flux. Other reaction parameters, such as the gas flow, were kept constant throughout the process as this resulted in the formation of heterostructures. For the exact growth parameters used

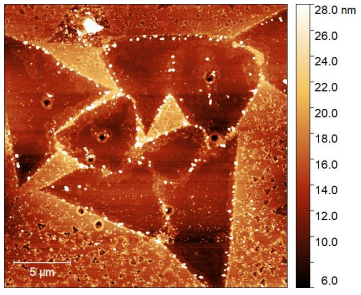


Figure 8.5: AFM height image of the $WS_2/MoS_2$ heterostructure sample.

see section A.2, where the process sheets for both the growth of $MoS_2/WS_2$ and $MoSe_2/WSe_2$ are given.

The advantage of the single-step synthesis is the uninterrupted consecutive CVD growth of the different TMDs in the furnace. Due to the vacuum and flow of carrier gases in the system, most of the oxygen is removed from the system, thereby minimising unwanted oxidation reactions as well as keeping contamination of the material interface from external sources to a minimum. However, control over the specific reactions in the furnace and the reaction mechanisms is limited in the single-step synthesis. In literature, control over the lateral and vertical growth of heterostructures is exercised by controlling the reaction temperature,[80,306] a cooling and purge step between the two TMD growths, to cause clean terminated growths[307] or precursor sequence.[308] Besides control over the growth direction a temperature-mediated synthesis method can also control the stacking order of the TMDs.[79]

Proposed here is single-step growth, where the temperature is varied for selective TMD synthesis. The method differs from other synthesis methods due to the use of a microreactor, resulting in better control over the concentration of metal precursors, therefore requiring less precursor. This method also gives more localised control over the synthesis.

### 8.2.1 Selenide heterostructures

As shown in Figure 8.6 first the temperature was ramped up to 750 °C to initiate the growth of $MoSe_2$ after which it was ramped up further to 850 °C for the synthesis of $WSe_2$. When the temperature was kept at 750 °C, it was insufficiency for $WSe_2$ growth so only $MoSe_2$ was formed, whereas keeping the temperature at 850 °C lead to polycrystalline alloy formation. For the seed layer a 20 nm W layer was sputtered, which was subsequently oxidised for 1h at 500 °C in atmospheric conditions, as this leads to the formation of a $WO_3$ layer.[309] On top of the tungsten oxide layer a solution of 40 $\mu$L of 2.5 g/L $MoO_3$ exfoliated in IPA was drop casted to form a $MoO_2$ layer. See Figure 8.7 for a schematic overview of the work-flow process to

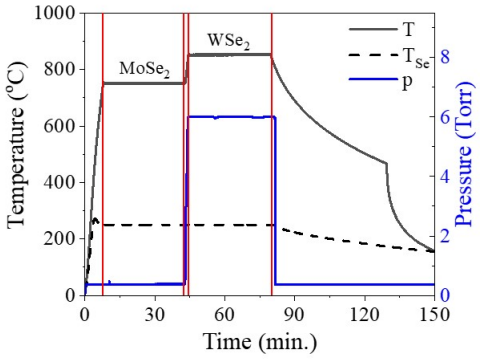


Figure 8.6: Graph showing the reaction temperatures, dwell times and pressures used to form $MoSe_2/WSe_2$ heterostructures

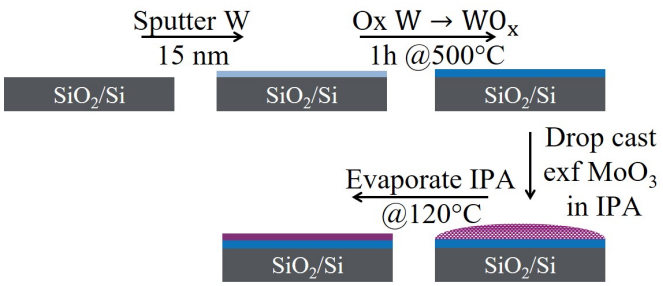


Figure 8.7: Schematic overview of formation of the seed layer by first depositing 15 nm W metal by sputtering, subsequently oxidising the metal at 500 °C for 1h, followed by deposition of the $MoO_3$ precursor, which is LPE exfoliated $MoO_3$ dissolved in IPA which is drop casted on the substrate at 120 °C

form the seed layer. Reaction parameters such as reaction time and pressure were optimised first for heterostructure growth by a parametric study, before the following results were obtained. During the reaction $MoSe_2$ was first synthesized at 750 °C for 35 min after which the temperature was ramped up to 850 °C and $WSe_2$ was grown for 40 min. For a detailed overview of the reaction parameters see the process sheet in section A.2.

This synthesis method is differs from other reports due to the use of a microreactor for the heterostructure synthesis, therefore requiring less metal precursor. The method is also better than other heterostructure synthesis where a microreactor is used as this is a single step approach, where only the temperature is modulated. Since it is a single step process there is no contamination and oxidation of the sample between the different TMD growths.

It was found during an attempt to synthesize $MoSe_2/WSe_2$ heterostructures, the nucleation and growth of $WSe_2$ occurred at the edges, defects and grain boundaries of $MoSe_2$, as shown in Figure 8.8. This was also observed by Robinson *et al.*[218] This synthesis method resulted in both lateral and vertical growth at the edge interface. It was notable that lateral growth of $WSe_2$ was associated with growth from the edges of dendritic $MoSe_2$, as can be seen in Figure 8.8. A pronounced herringbone structure can be observed, suggesting there was a molydenum deficiency during the growth of the $MoSe_2$.[310] It is possible that due to this molybdenum deficiency, tungsten was able to incorporate in the existing lattice and grow further in the lateral direction to form $WSe_2$. The initial growth direction of the $WSe_2$ flakes appears to be random due to the presence of a large availability of nucleation sites at the edges of the $MoSe_2$ flakes. This results in the formation of an edge at the material interface between the different TMDs. Further growth does result in lateral growth as this appears to be more energetically favorable than vertical growth.[80]

Increasing the molybdenum precursor concentration, until an excess of the Mo precursor is reached, results in CVD growth where the $MoSe_2$ flakes have a more triangular shape, as the ratio is closer to 1:2 Mo:Se, the stoichiometric ratio.[310,311] For the formation of $MoSe_2$, initially metallic Mo nuclei are formed from which the

growth of $MoSe_2$ expands.[127] An excess of Se results in Mo deficiencies in the crystal lattice and a herringbone structure, while a higher Mo:Se stoichiometry results in triangular flakes. These triangular flakes have fewer reactive dangling bonds at the edge interface. Similarly, the $WSe_2$ found on these structures tended to grow from the edges of the $MoSe_2$ but these flakes also grow further out as a bilayer on top of the $MoSe_2$ towards the center of the flake, rather than increasing the total coverage. The formation of these vertical heterostructures, in contrast to lateral heterostructures in the case of molybdenum deficient flakes, is due to the reduced availability of reactive sites or possibly the smoother $MoSe_2$ offers a preferential growth substrate to $SiO_2$. As the perfect triangular $MoSe_2$ flakes have fewer dangling bonds or reactive sites at the edges, the $WSe_2$ is unable to nucleate from these sites.

### Vertical growth

For the flakes with vertical growth of $WSe_2$ the lateral dimensions of the $MoSe_2$ is $\sim$10-50 $\mu$m, while in the $WSe_2$ areas the growth is strongly limited to dimensions in the order of $\sim$1-7 $\mu$m. In Figure 8.8 optical microscopy images for a lateral heterostructure are shown. The optical contrast between the different TMDs is very limited making characterisation difficult. A slightly darker area is observed at the edge, while the more central part of the flake is lighter. This difference in contrast indicates the presence of monolayer material in the lighter area, while bilayers are present at the darker areas near the edges of the flakes. This visual representation of the surface does not give any reliable information on whether different TMDs are present on the surface. To determine if the flakes are heterostructures, area selective characterisation by methods such as Raman, PL spectroscopy and AFM is required.

Raman and PL maps of the area outlined in red on the optical microscopy image, Figure 8.8, make it possible to identify the different TMDs on the surface. The Raman maps for both the $MoSe_2$ $A_{1g}$-peak intensity and $WSe_2$ $E^1_{2g}$+$A_{1g}$-peak intensity are provided in Figure 8.8(b) and (c) and the PL intensity map for the $MoSe_2$ A-exciton peak is shown in Figure 8.8(e). The individual Raman maps show where $MoSe_2$ and $WSe_2$ are present on the surface. When comparing the maps it becomes clear that both $MoSe_2$ and $WSe_2$ are present on the surface, while there is some mixing of the materials present at the interface. This mixing can be explained by stacking of the TMDs or by the incorporation of W at the Mo deficient edge sites, thereby creating an alloy region at the $MoSe_2/WSe_2$ interface. Alloy formation is expected as the formation of alloys are thermodynamically preferred to the formation of segregated heterostructures.[312] Decreasing the amount of defects, by reducing the Mo deficiency at the interface, reduces the formation of alloys at the interface.

The Raman spectra of the $MoSe_2$ and $WSe_2$ areas are extracted from the Raman maps and are shown in Figure 8.8(d). The peak positions of the Raman peaks, $\sim$240 cm$^{-1}$ for the $MoSe_2$ $A_{1g}$-peak and $\sim$249 cm$^{-1}$ for the $WSe_2$ $E^1_{2g}$+$A_{1g}$-peak, are located at the same positions as those of the corresponding monolayer values.[175] As all spectra are obtained from the same Raman map it can be concluded that the

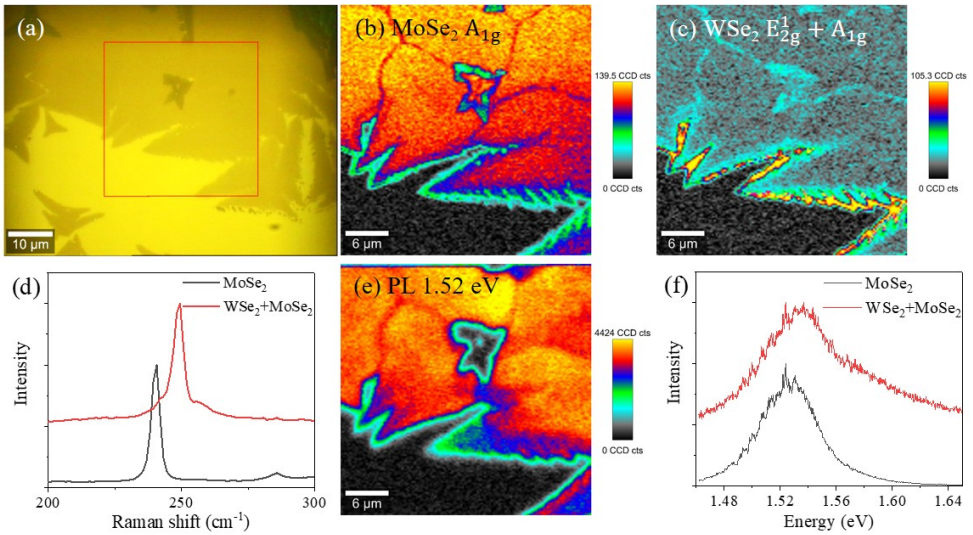


Figure 8.8: Optical microscopy, Raman & PL data for direct vertical $MoSe_2/WSe_2$ heterostructure growth. (a) Optical microscopy image of surface, (b) Raman intensity map at 240 $cm^{-1}$, showing the $A_{1g}$ peak of $MoSe_2$. (c) shows the Raman intensity map at 250 $cm^{-1}$ at which the $E^1_{2g}$+$A_{1g}$-peak of $WSe_2$ is located. (d) The Raman spectra for the $MoSe_2$ and $WSe_2$ areas on the surface. (e) The PL map at 1.52 eV and (f) The PL spectra for the $MoSe_2$ and $WSe_2$ areas on the surface.

intensity of the $WSe_2$ $E^1_{2g}$+$A_{1g}$-peak is similar to that of the $MoSe_2$ $A_{1g}$-peak. As the quantum yield of $WSe_2$ is much higher than the yield of $MoSe_2$, especially when probed with a laser at 532 nm, this should normally result in a higher intensity of the $WSe_2$ peaks compared to that of the $MoSe_2$ peaks for the growth of individual structures.[260] The increased $WSe_2$ Raman intensity is not observed for the vertical heterostructures formed here, the partial quenching of the $WSe_2$ Raman signal could be due to a lower crystallinity of the $WSe_2$, interaction with $MoSe_2$ or the presence of defects on the surface.

The $WSe_2$+$MoSe_2$ bilayer Raman spectrum shows a slight shoulder peak at ~240 $cm^{-1}$, which is the $MoSe_2$ $A_{1g}$-peak position, confirming that $MoSe_2$ is present in that area as well as $WSe_2$, while the $E^1_{2g}$+$A_{1g}$-peak of $WSe_2$, at ~249 $cm^{-1}$, appears dominantly in the spectrum. The lower intensity of the $MoSe_2$ $A_{1g}$ peak can be explained by both the lower quantum yield and by quenching of the signal by the $WSe_2$ layer on top. Another feature of importance is the slight shoulder peak at higher wavenumbers for the $E^1_{2g}$+$A_{1g}$-peak in the $WSe_2$ Raman spectrum, which is the 2LA(M) phonon mode of $WSe_2$. This mode is more intense for bi- and multilayers.[228] As the $WSe_2$ nucleates from a limited number of sites on the surface it would be expected that there would be growth of a few large crystalline $WSe_2$ flakes on the surface, which can possibly merge, if oriented correctly, when coming into contact. The $MoSe_2$ can function as a template for the growth of $WSe_2$ on top of the $MoS_2$, therefore is is likely that the $WSe_2$ growth will follow the same crystalline orientation. As the 2LA(M) phonon mode is somewhat visible on the surface this seems to indicate that the surface is not perfectly crystalline as the

different domains do not merge perfectly. Most likely the domains do not merge as they do not align, causing the formation of grain boundaries on the surface.

The PL spectra, Figure 8.8(f), show a main peak around ∼1.53 eV for the $MoSe_2$ spectrum and ∼1.54 eV for the $WSe_2$+$MoSe_2$ spectrum and a FWHM of 0.051 eV and 0.058 eV for respectively $MoSe_2$ and $WSe_2$+$MoSe_2$. The $WSe_2$+$MoSe_2$ PL spectrum also shows a second peak at around ∼1.58 eV with a FWHM of 0.03 eV and this is about half the intensity, 0.54x, of the main peak at ∼1.54 eV. The literature values for the monolayer A-exciton peak are 1.55 eV for $MoSe_2$ and 1.62 eV for $WSe_2$.[175,313] According to these values, the PL spectra in Figure 8.8 both show the A-exciton peak for $MoSe_2$. Though the signal has slightly red-shifted to lower energies in both spectra, possibly due to strain or surface roughness.[314,315] The second peak at 1.58 eV in the $WSe_2$+$MoSe_2$-spectrum can be attributed to the A-exciton of $WSe_2$. This signal has strongly red-shifted, by 0.4 eV in regards to the theoretical value, due to interaction of the $WSe_2$ with the $MoSe_2$, the peak is located in between the energy values for the peaks of $MoSe_2$ and $WSe_2$.[316,317] The PL signal for the $WSe_2$ A-exciton is also strongly quenched, possibly due to the interaction with the $MoSe_2$ layer, defects on the surface or due to the bi-layer nature of the vertical heterostack, as the intensity of the $WSe_2$ A-exciton decreases exponentially when the layer thickness increases from mono- to bilayer.[318]

AFM height images of these areas show a continuous surface with a small height difference between $MoSe_2$ and $WSe_2$. An AFM height image is shown in Figure 8.9(a). The AFM height image shows the height difference of the edges of the flakes as well as the bilayer area on the surface. The vertical TMD structure can be distinguished in the height image as the $MoSe_2$/$WSe_2$ areas, this area is ∼0.5-1 nm higher in comparison to the $MoSe_2$ area, corresponding with the height of monolayer $WSe_2$, ∼0.7 nm.

Other nano-mechanical AFM modes are also shown in Figure 8.9. The peak force error, shown in Figure 8.9(b), indicating the deflection error mainly highlights the outline of the complete heterostructure flake as well as the $MoSe_2$+$WSe_2$ heterostructure channels growing towards the center of the flake. The adhesion and deformation of the grown material, as shown in Figure 8.9(c) and (d), stays constant over the whole flake, lacking any difference between the $MoSe_2$ and heterostructure region of the flake, thus indicating that both are very similar for the different TMDs. In the deformation image the outline of the flake is the most apparent feature, where the adhesion image also shows the grain boundaries on the surface as the adhesion with the substrate is weaker compared to the adhesion with the TMDs. As the adhesion can be used to calculate the strength and orientation of the layer interaction, this would suggest that there is interlayer coupling present between the TMD layers[319], which is confirmed in the deformation image.

Other AFM modes such as peak force tunneling AFM (PF-TUNA), a conductive AFM mode, can probe the difference in conductivity between the different TMDs as well as the substrate. The $MoSe_2$/$WSe_2$ flakes were large and were mainly located

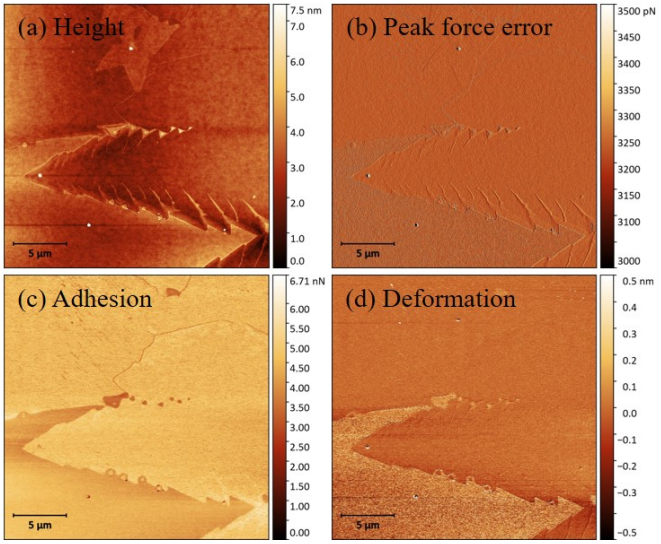


Figure 8.9: Different nanomechanical AFM mode images of the vertical $MoSe_2/WSe_2$ heterostructure area. (a) Height image, (b) Peak force error image, (c) Adhesion image and (d) Deformation image.

near the edge of the substrates, therefore a simple side-contact made by conductive silver paint sufficed to contact the grown heterostructure. A forward bias was applied to the sample. The structure was probed at different voltages (-2.5 V to +1.6 V) to study the differences in conductivity. See Figure 8.10 for the corresponding images. At negative voltages (-2.5 V) there is no signal of any current going through the surface. The current is quite uniform over the surface, ranging from -0.4 – 0.2 pA When increasing the voltage to +0.5 V there is a partial current on the surface, which is located on the vertical heterostructure area. The $MoSe_2$ area meanwhile there is no conduction between the $MoSe_2$ and the tip visible, as the current is ∼0 pA. The same value is found for the $SiO_2$ surface, while the $WSe_2$ shows a current of ∼100 pA. Further increase of the voltage results in complete current of the TMD area.

The current only flowing through the $WSe_2$ area at 0.5 V can be caused by different conductivity or the different bandgap of the $WSe_2$. Though $WSe_2$ is supposed to be less conductive than $MoSe_2$, the observations here are in contradiction to this.[320] This could be due to the voltage bias being applied from the substrate to the tip. According to Son *et al.* $WSe_2$ is less conductive than $MoSe_2$ when applying a bias from the tip to the substrate.[321] However the behaviour at negative bias would suggest the conductive behaviour of both $MoSe_2$ and $WSe_2$ are asymmetric. For $WSe_2$ in particular the conductivity decreases with increasing layer number.[154]

### Lateral growth

Whereas vertical growth occurs when Mo is in excess, lateral growth requires a deficiency of Mo. An advantage of the microreactor approach is that it is much easier to adjust the Mo concentration compared to the use of metal powders. To

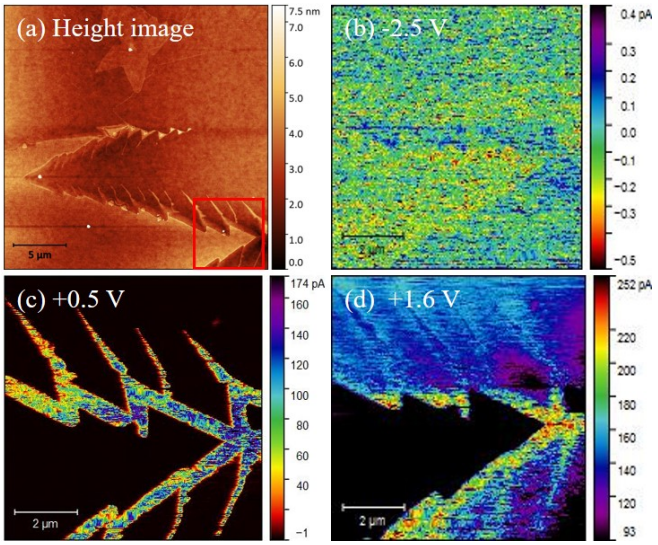


Figure 8.10: AFM images of vertical $MoSe_2$+$WSe_2$ heterostructures. (a) shows the AFM height image, with the red outline showing the area measured with PF-TUNA. The different PF-TUNA AFM mode images of $MoSe_2$/$WSe_2$ area are shown in (b)-(d). (b) Contact current at -2.5 V (c) Contact current at 0.5 V, (d) Contact current at 1.6 V

obtain a Mo deficiency the amount of Mo precursor was decreased while the substrate area was kept constant, from the initial 40 $\mu$L, until a optimal of 35 $\mu$L of 2.5 g/L was reached, as this amount resulted in the growth of lateral heterostructures. The amounts of the other precursors remained constant. Lateral grown $MoSe_2$/$WSe_2$ structures result in a 2D surface where the molybdenum deficient edges of the $MoSe_2$ flake result in Mo vacancies where the W atoms incorporate into the crystal lattice. From the W areas the $WSe_2$ continues to grow in an outwards lateral direction. In Figure 8.11(a) an optical microscopy image of a lateral $MoSe_2$/$WSe_2$ heterostructure is shown. Due to the 2D nature of the structure, there is no visible contrast between the different materials. As a consequence no material boundary can be identified from only optical microscopy images of the lateral heterostructures.

Raman maps and spectra, see Figure 8.11(b)-(d), show the presence of both $MoSe_2$ and $WSe_2$. When examining at the spectra clear individual $MoSe_2$ and $WSe_2$ spectra are visible. At the interface region a single Raman peak is located between ~246 $cm^{-1}$, which indicates that the peak is shifted in between the $A_{1g}$-peak of $MoSe_2$ at ~240 $cm^{-1}$ and the $E^1_{2g}$+$A_{1g}$-peak of $WSe_2$ at ~250 $cm^{-1}$. This single shifted peak corresponds to an alloy region.[322] From this spectrum it can be concluded that the interface region between the $MoSe_2$ and $WSe_2$ is an alloy region since the lateral size of this area, ~1-1.5 $\mu$m, is larger than spot size of the Raman laser, ~300 nm, therefore identification of both TMD peaks should be possible. The intensity of the peak at 246 $cm^{-1}$ is about the average of the intensity of the two other peaks, providing further confirmation of alloy formation as the mixed lattice results in a signal, which is a mixture of $MoSe_2$ and $WSe_2$.

As the $WSe_2$ nucleates from various edge sites this leads to many grains which can

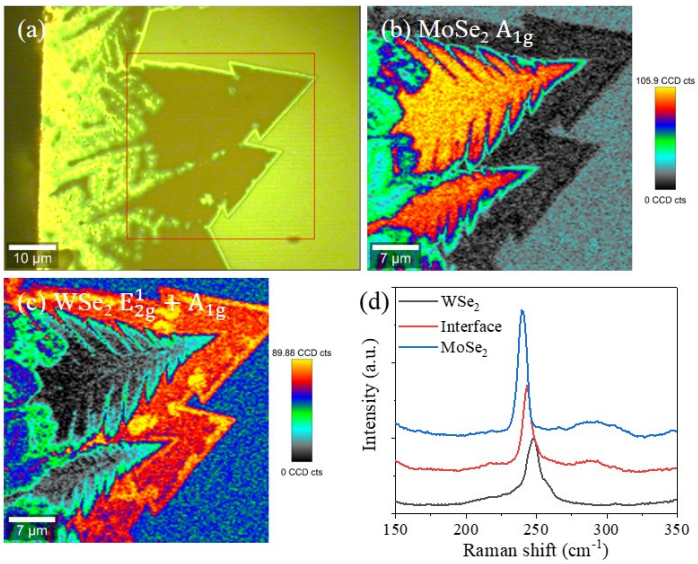


Figure 8.11: Optical microscopy, Raman & PL data for direct growth of lateral $MoSe_2/WSe_2$ heterostructures. (a) Optical microscopy image of surface, (b) Raman peak intensity map at 240 $cm^{-1}$, showing the $A_{1g}$ peak of $MoSe_2$. (c) shows the Raman peak intensity map at 250 $cm^{-1}$ at which wavelength the $E^1_{2g}$+$A_{1g}$-peak of $WSe_2$ is located. (d) The Raman spectra for the $MoSe_2$, $WSe_2$ and $MoSe_2/WSe_2$ interface areas on the surface.

merge together when they come into contact. This will lead to the formation of grain boundaries because the grains need to have the same orientation to merge seamlessly. Any misalignment results in grain boundaries, therefore it is practically impossible to form a single crystalline $WSe_2$ area. The presence of the 2LA(M) phonon mode in the $WSe_2$ spectrum, as well as the low intensity of the $E^1_{2g}$+$A_{1g}$-peak, shows that the $WSe_2$, though continuous, does not form a large mono-crystalline surface. Instead multiple crystalline domains are present. The domains form in a direction which is most energetically favorable for the whole surface, thereby forming an overall shape which is a triangular flake with low surface energy.[286]

The AFM height map does not show a clear contrast between the different TMDs, see Figure 8.12(a), as the $MoSe_2$ and $WSe_2$ are in the same plane and have practically the same height, this demonstrates that lateral heterostructures have formed. There is some indication that the $WSe_2$ is defective as the $WSe_2$ layer does not appear to be as uniform as the $MoSe_2$ layer. The height difference between the two TMDs in the same plane is in the order of ∼1 Å, where the thickness of $WSe_2$ is around ∼0.7 nm. PF-TUNA gives more information about the surface through current mapping. When probing the surface at a low voltage there is a partial conductivity of the $WSe_2$ area as a number of sites in that area becomes conductive. Meanwhile the $MoSe_2$ region does not show a current, making the region appear non-conductive at this voltage. Increasing the voltage further increases the number of sites on the $WSe_2$ through which conduction was possible. Even with increased voltage there is no conductivity in the $MoSe_2$ areas. Since the materials have a similar height the difference in conductivity can be traced back to the material properties. However,

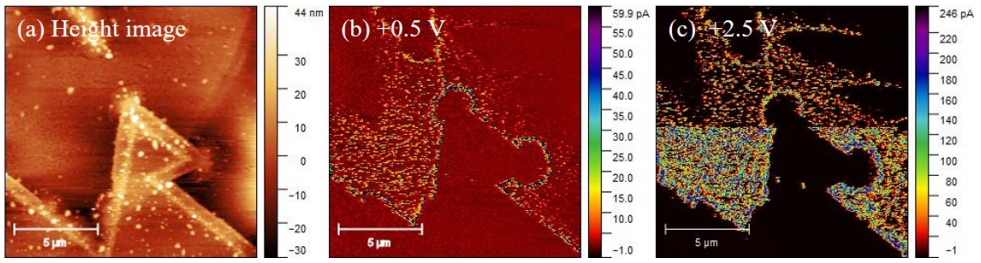


Figure 8.12: AFM and PF-TUNA images of Lateral $MoSe_2/WSe_2$ heterostructure. (a) Height image, (b) contact current at 0.5 V, (c) Contact current at 2.5 V.

the apparent resistance is also influenced by the nature of the probe. The series resistance will increase with wear as this leads to demetalisation of the tip. A possible example of this can be seen in Figure 8.12 where there is a reduction in apparent conductivity in the top half of the image. Due to this, high voltages were required to get a signal from the $WSe_2$. Furthermore, due to tool limitations voltages above 5.0 V were not attempted. It is assumed that further increase of the voltage would eventually lead to conductivity through the $MoSe_2$ region as well if a stable tip that could provide a reliable contact with the surface is used.

To obtain information on the stoichiometry of the heterostructure and the amount of defects contaminants present on the surface, XPS-measurements were performed by Dr. Conor Cullen in a monochromated $\mu$-XPS system. $\mu$-XPS has the advantage over normal XPS that it has a smaller minimum spotsize, $\sim$10 $\mu$m instead of mm scale size, making it possible to measure more localised areas of the surface. The $\mu$m scale spot-size is too large to identify individual $MoSe_2$, $WSe_2$ and heterostructure areas but it is sufficient to identify the different TMDs in a single heterostructure area. The XPS-spectrum measured is shown in Figure 8.13. The spectrum is that of the flake shown in Figure 8.11(a).

The spectrum shows the presence of both $MoSe_2$ and $WSe_2$. For the Mo 3d core-level spectrum the Mo peaks are visible at 229.3 eV and 232.4 eV and there is some overlap from the Se 3s core-level at 230.2 eV, while in the W 4f core-level spectrum the main contributions stem from the $WSe_2$ 4f levels at 32.76 and 36.64 eV. Other contributions include the $WSe_2$ 5p (38.26 eV), $WO_x$ (35.99 eV and 38.17 eV) and $WSe_x$ (32.28 eV and 34.47 eV). The Mo 4p core-level (36.03) is also seen in this spectral region. The $WO_x$ binding energies are located at 35.99 eV and 38.17 eV, where the $WSe_x$ peaks are at 32.28 eV and 34.47 eV The Mo 4p core-levels are also slightly visible in this spectrum at 36.03 eV. The Se 3d core-level is deconvoluted into overlapping contributions from $MoSe_2$ (55.02 eV and 55.88 eV) and $WSe_2$ (54.86 eV and 55.72 eV).

The ratio of the different components is 11% Mo, 26% W and 63% Se, indicating that there is about $\sim$1.7 times the amount of Se compared to that of Mo and W combined which is close to the optimal stoichiometric value of 2, though the experimental values from literature have a large range between 1 and 3.[323] A high M:X ratio can indicate the presence of excess metal and is generally associated with

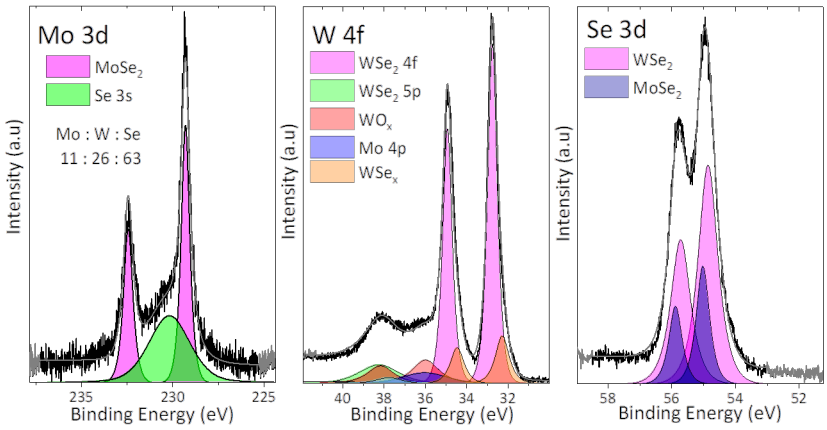


Figure 8.13: $\mu$-XPS spectra of vertical $MoSe_2/WSe_2$ flake. The spectra for the Mo 3d, W 4f and Se 3d regions are shown.

the formation of initial nuclei which are rich in metal.[324] From the peak areas in the XPS-spectrum it can be concluded that there is 2.4x as much W compared to Mo, which seems high as from optical spectroscopy it appears that the total $WSe_2$ area is roughly the same size as that of the $MoSe_2$ area. This is most likely due to to exact area of the flake which was measured by the XPS tool.

When comparing the lateral and vertical heterostructures, see Figure 8.14, the area covered with $WSe_2$ growth is much larger for the lateral growth. Though this is not visible in the optical microscopy images, see Figure 8.14(a) and (d), the Raman $E^1_{2g}$-peak intensity maps do show the different materials. For lateral growth, shown in Figure 8.14(b) the length of the $WSe_2$ is ∼5-10 $\mu$m from the $MoSe_2$ boundary, while the area for $WSe_2$ for vertical growth, see Figure 8.14(e) lags at ∼1–5 $\mu$m. In practice this would mean that the lateral growth structures would be much more convenient to contact and be more suitable for devices, not taking into account the required properties of the device. Besides the size of the $WSe_2$ area the crystallinity of the lateral growth appears to be higher than that of the vertical growth as the $WSe_2$ in the vertical growth mainly consists of separate crystals, where these crystals fuse together in case of the lateral growth.

### 8.2.2 Sulfide heterostructures

For the direct synthesis of $MoS_2/WS_2$ heterostructures a similar approach compared to the direct synthesis of $MoSe_2/WSe_2$ heterostructures was adopted. Initial attempts involved the standard reaction parameters for the CVD growth of both individual TMDs. The growth recipe was optimised from that point. The initial seed layer was a 20 nm sputtered W layer, which was subsequently oxidised for 1h at 500 °C, with a drop casted layer of 40 $\mu$L of 2.5 g/L $MoO_3$ exfoliated in IPA on top, as applied for the heterostructure growth for $MoSe_2$+$WSe_2$. This seed layer did not result in the formation of heterostructures since this growth method only yielded in the formation of $MoS_2$ triangles on the surface. Replacing the tungsten precursor

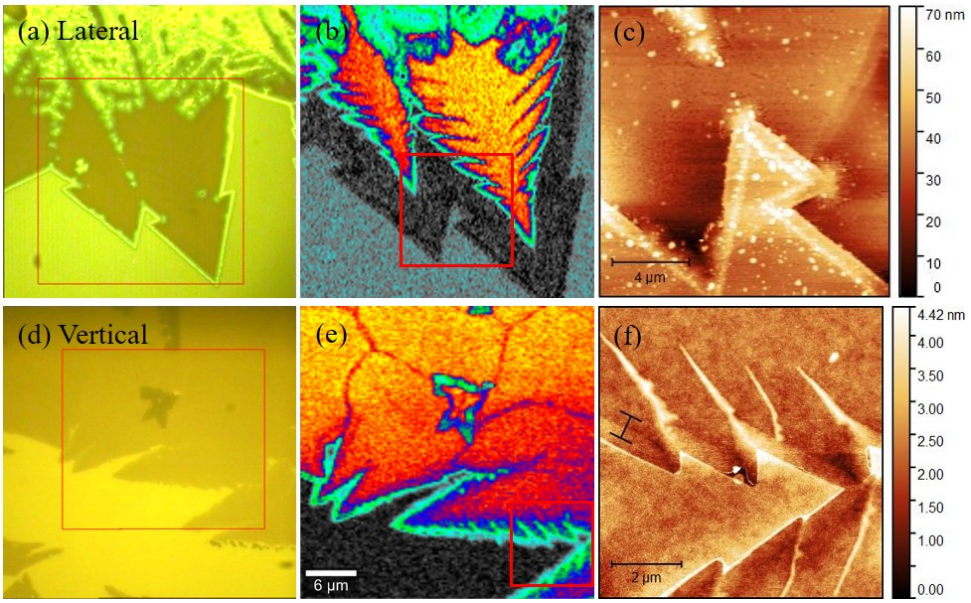


Figure 8.14: Comparison of lateral and vertical $MoSe_2/WSe_2$ heterostructures by optical microscopy images, Raman & AFM data. (a), (b) and (c) show the data for the lateral structures, where (d), (e) and (f) show the vertical heterostructure data. (a) and (d) show the optical microscopy images with the red outlines showing the area measured by Raman as shown in the $MoSe_2$ peak intensity Raman maps in (b) and (e). The red outlines on the Raman maps show the area scanned by AFM. In (c) and (f) the AFM height images of these areas are depicted.

with LPE $WO_3$ in IPA lead to the formation of small $WS_2$ domains, though it did not result in $WS_2$ flakes.

The failure to grow $WS_2$ flakes suggested that the $WS_2$ could not nucleate on the surface. According to Li *et al.* the use of halides can be beneficial for the nucleation of TMDs.[213] The anion forms an oxyhalide species with the metal oxide precursor. The possible oxyhalide species formed are $MO_2X_2$ and $MOX_4$, with X being the anion $I^-$, $Br^-$ or $Cl^-$ as shown in Equation 8.1 and Equation 8.2.[325] These components have strongly reduced melting temperatures enabling $WS_2$ to form at temperatures as low as 700 °C.[213] The addition of NaCl has also led to the successful formation of in-plane heterostructures by Wang *et al.*[326]

$$2MO_3(s) + 2X^-(g) \rightarrow 2MO_2X_2 + O_2 \tag{8.1}$$

$$MO_3(s) + 4X^-(g) \rightarrow MOX_4 + O_2 \tag{8.2}$$

To improve the growth of $WS_2$, low concentrations of NaCl, 25 g/L, dissolved in DI-water, were drop casted on the seed layers in an attempt to stimulate the nucleation of $WS_2$ as shown in Figure 8.15. The addition of these small quantities helped the nucleation of both $MoS_2$ and $WS_2$, especially when the NaCl solution was drop casted between the tungsten and molybdenum precursor layers. When NaCl was drop casted on the Mo precursor the NaCl helped nucleation of the $MoS_2$ growth but did not have any effect on the growth of $WS_2$, whereas deposition in

between the layers helped the nucleation of $WS_2$ as the NaCl only becomes available when the Mo precursor is (partially) evaporated.

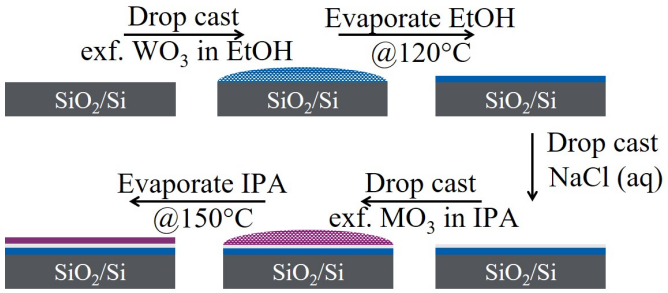


Figure 8.15: Schematic overview of formation of the seed layer by first drop casting $WO_3$ dissolved in EtOH at 120 °C, subsequently drop casting a NaCl solution at 120 °C, followed by deposition of the $MoO_3$ precursor, which is LPE exfoliated $MoO_3$ dissolved in IPA which is drop casted on the substrate at 120 °C

A downside of this approach was the formation of concentric salt circles as the salt crystallised out on the surface in a lateral direction, as shown in Figure 8.16, which cannot be removed by rinsing the sample after the synthesis. The formation of these salt circles was partially resolved by decreasing the NaCl concentration to a tenth of the concentration, 2.5 g/L. The addition of NaCl did increase the nucleation of TMDs on the surface, though this also led to an increase in multilayer formation as the nucleation rate increased. Control over the concentration and proportions of both the halides and metal precursors is essential to the formation of monolayer TMDs.

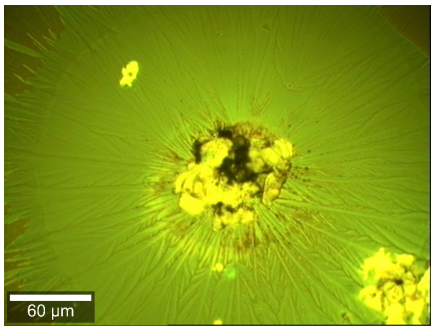


Figure 8.16: Optical microscopy image of concentric circular shape formed by the NaCl on the surface

The synthesis resulted in the formation of vertical heterostructures, where $WS_2$ formed triangular domains from the edge of the $MoS_2$ flakes towards the centre of the underlying $MoS_2$ flake as shown in Figure 8.17(a). The $MoS_2$ flakes had lateral dimensions of ∼30-100 $\mu$m, while the $WS_2$ flakes grown on top were more restricted in size to ∼5-10 $\mu$m. A large number of these heterostructures were present dispersed across the surface. The high density of these flakes makes it convenient to characterise the structures by Raman and AFM.

In Figure 8.17(a) and (b) optical microscopy images are shown of the surface.

Large monolayer triangles are clearly distinguishable, which are expected to be $MoS_2$ as the $MoS_2$ is grown first and has therefore more time to nucleate and grow out further. Some of these flakes have even merged on the $SiO_2$ surface. On the monolayer flakes visible in the optical microscopy images bilayer growth in triangular shapes are visible at the edges of the 1L flakes, while central more hexagonal bilayer areas are also present. The hexagonal bilayer areas appear to form from the initial nuclei as the triangular bilayer flakes seem to nucleate from the edges. For $MoSe_2/WSe_2$ heterostructures the $WSe_2$ nucleated from the edge of the $MoSe_2$ flake as the crystal lattices and growth mechanisms are similar, therefore it is reasonable to assume that this is also the case for the sulfur counterpart.

To confirm the presence of $WS_2$ on $MoS_2$ Raman spectroscopy was performed. The Raman maps and spectra are shown in Figure 8.17(c-e). Figure 8.17(c) shows the Raman map for the $MoS_2$ $E^1_{2g}$-peak at $\sim$380 $cm^{-1}$. This shows a clear large $MoS_2$ triangle on the surface. When comparing this with the Raman map for the $WS_2$ $A_{1g}$-peak the small triangular $WS_2$ regions present are concentrated around the edges of the $MoS_2$ growth. There is also a hexagonally shaped feature in the center grown around a small $MoS_2$ bilayer flake, resulting in a kind of lateral bilayer growth.

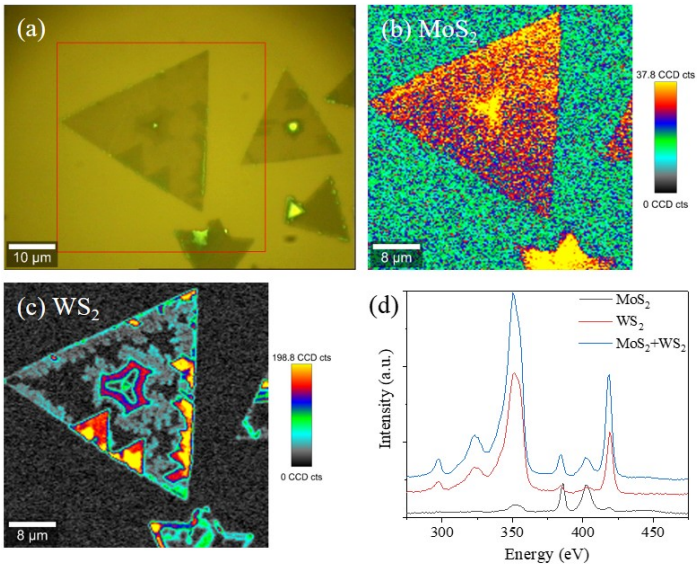


Figure 8.17: Optical microscopy & Raman data for direct $MoS_2/WS_2$ heterostructure growth. (a) shows the optical microscopy image of the surface with the red outline indicating the area from which Raman spectra were taken. In (b) the sum map for the $MoS_2$ $E^1_{2g}$ peak is shown, where (c) shows the corresponding $WS_2$ $A_{1g}$ sum map and (d) shows the Raman spectra for the $MoS_2$, $WS_2$ and the $MoS_2$+$WS_2$ heterostructure area.

Since the $WS_2$ preferentially grows on top of the $MoS_2$, it appears that the $MoS_2$ has a templating effect on the growth of $WS_2$. The lattices of $WS_2$ and $MoS_2$ are very similar with a lattice mismatch of $<0.01\%$.[242] This is an almost negligible mismatch, in comparison the mismatch between $WSe_2$ and $MoSe_2$ is $0.1\%$.[327] Thus the growth of $MoS_2/WS_2$ heterostructures in both lateral and vertical direction should result in

a low level of lattice mismatch defects. Analogous lattices can also lead to epitaxial or templated growth of materials.[328,329] The $MoS_2$ seems to catalyse the growth of $WS_2$ on the surface as $WS_2$ is exclusively found on $MoS_2$, while $WS_2$ is not observed to form separately on the $SiO_2$ surface. The $WS_2$ Raman map also shows some signal at grain boundaries in the flake, nucleating at edges and defects in the $MoS_2$. This might be a result of damage to the $MoS_2$ during the higher temperatures regime required for the growth of $WS_2$ as the higher synthesis temperature of $WS_2$ can lead to a partial breakdown of the $MoS_2$.

The Raman spectra of $MoS_2$ and $MoS_2$+$WS_2$, obtained from the corresponding regions in the Raman maps, both show peaks for $MoS_2$, $E^1_{2g}$-peak at ∼380 $cm^{-1}$ and $A_{1g}$ at ∼405 $cm^{-1}$ as expected. The Raman spectrum for $MoS_2$+$WS_2$ also shows clear and intense peaks for $WS_2$, 2LA(M)+$E^1_{2g}$-peak at ∼350 $cm^{-1}$ and $A_{1g}$ at ∼417 $cm^{-1}$. The peaks for $WS_2$ are more intense than the $MoS_2$ peaks, about ∼3.5x. This is expected as $WS_2$ is resonantly excited by the laser used and therefore resulting in relatively higher intensity Raman signals.[260] The $E^1_{2g}/A_{1g}$ ratio of $MoS_2$ for the monolayer is ∼0.84, while the ratio for $MoS_2$ peaks in the heterostructure is increased to almost 1 (∼0.99). For $MoS_2$ this ratio usually decreases for increasing layer number, though the heterostructure area is a bilayer the ratio still exceeds that of the monolayer $MoS_2$. The increase in the ratio for the $MoS_2/WS_2$ bilayer area can be explained by the interaction between the $WS_2$ and $MoS_2$ as interlayer coupling influences the properties of the structure.

The $MoS_2$ spectrum also shows some peaks of relatively low intensity at the $WS_2$ regions. As the crystalline quality of $MoS_2$ is not perfect and there are many areas where the $WS_2$ can incorporate in the film, at defects and grain boundaries, these peaks are probably from these $WS_2$ traces. Due to this incorporation of $WS_2$ in the $MoS_2$ film, the $WS_2$ appears all over the $MoS_2$ surface and therefore it is almost impossible to filter these out, leading to the presence of $WS_2$ in the spectrum. It remains unclear whether the defects originate from the initial growth of the $MoS_2$ or whether the $MoS_2$ film is damaged during the $WS_2$ growth step.

To better understand the observed structures low-frequency Raman spectra were obtained. Information on the shear modes (SM) and layer breathing modes (LBM) of the material can be obtained by low-frequency (LF) Raman spectroscopy. Low frequency Raman can be used for determining the layer thickness as the SM and LBM are more sensitive to changes in layer thickness than the $E^1_{2g}/A_{1g}$ modes. It can also be used to identify the polytype. For the $MoS_2$ and $WS_2$ the following polytypes can be formed: 1T, 2H or 3R, of these polytypes 2H and 3R are the most commonly formed.[330,331] Both 2H and 3R have the same arrangement of S around Mo, though they have different stacking sequences. LF Raman can distinguish these different sequences whereas normal Raman cannot. The 1T phase has an octahedral crystal structure and a completely different Raman signal in the normal (high frequency) range. In Figure 8.18 the low-frequency Raman spectroscopy data of a heterostructure is provided. Figure 8.18(a) shows an optical microscopy image,

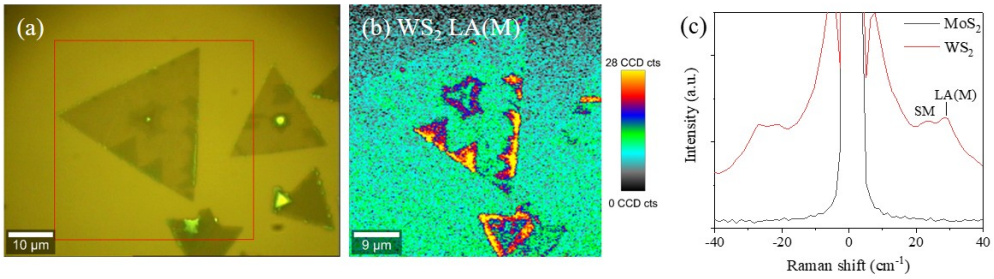


Figure 8.18: low-frequency Raman spectroscopy of a $MoS_2$+$WS_2$ heterostructure area. (a) Optical microscopy image with the measured area outlined in red. (b) Raman map at ∼27.8 $cm^{-1}$ which corresponds to the LA(M) related mode of $WS_2$ and (c) low-frequency Raman spectra of both the $MoS_2$ and $WS_2$ areas.

with a red rectangular outline indicating the measured area. When measuring this area a broad peak is observed at ∼27.8 $cm^{-1}$ on the $WS_2$ areas shown in the Raman map in Figure 8.18(b). This peak corresponds to the LA(M) related mode in $WS_2$. This mode is always visible for thin $WS_2$ layers.[175]

In vertical $MoS_2$/$WS_2$ heterostructures an interlayer SM signal is expected at ∼22 $cm^{-1}$ as described by Saito *et al*, which lies between the expected peaks for 2L $MoS_2$ and 2L $WS_2$.[332,333] The Raman spectrum of the $MoS_2$+$WS_2$ region, as shown in Figure 8.18, shows a broad LA(M) peak which is slightly shifted to higher energy than expected at 28.2 $cm^{-1}$. It appears that a peak is present at ∼23.1 $cm^{-1}$ which is largely obscured by the LA(M) related peak. This peak is assumed to be the SM peak originating from the $MoS_2$/$WS_2$ vertical heterostructure, this indicates that a strong interlayer interaction is present.

The $MoS_2$ spectrum does not show any peak at low-frequency features, see Figure 8.18. This appears to correspond with monolayer $MoS_2$. Monolayer $MoS_2$ does not to have a Raman signal in the low-frequency range as there are no shearing and layer breathing for a single layer.[175,176] This observation confirms the monolayer nature of the $MoS_2$ area.

The PL maps and spectra of the $MoS_2$/$WS_2$ heterostructure are shown in Figure 8.19. The findings are largely in agreement with the data from the Raman spectra. In Figure 8.19(a) an optical microscopy image of a heterostructure is shown, in this image the red outline in the figure indicates the area where the PL maps were taken. The large flake area corresponds to $MoS_2$, see Figure 8.19(b), while the smaller flakes growing from the edges on top of the monolayer $MoS_2$ are $WS_2$, as shown in Figure 8.19(c).

In the PL spectrum, Figure 8.19(d), there is a peak present at ∼ 1.97 eV in the $MoS_2$ area. This peak could either originate from the $MoS_2$ B1-exciton, 1.98 eV, or from the $WS_2$ bilayer A1-exciton peak, ∼1.96 eV.[260] According to the Raman spectra of $MoS_2$ in Figure 8.17(e), the crystallinity of the monolayer $MoS_2$ appears compromised as the Raman signal over the $MoS_2$ area is non-uniform, though $WS_2$ peaks were observed in the spectra of $MoS_2$ areas as well. Most likely these $WS_2$

peaks are present because of damaged $MoS_2$ areas, with $WS_2$ nucleating in defective areas, as well as the presence of $WS_2$ on top of the $MoS_2$ flake.

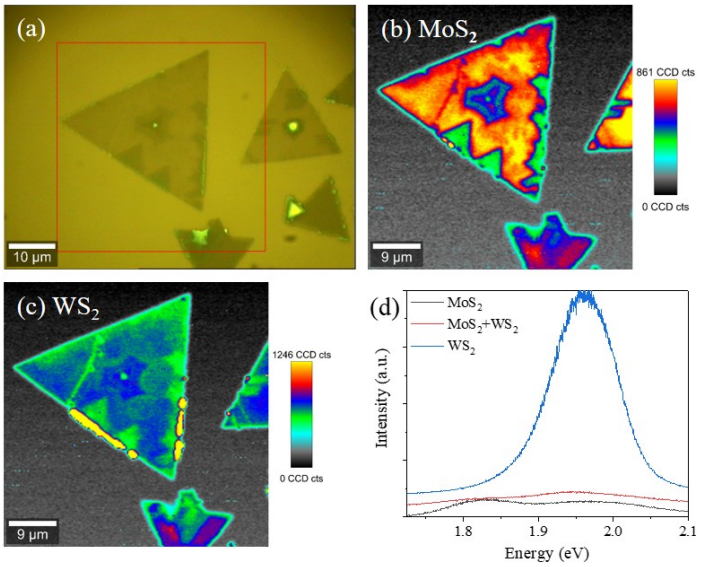


Figure 8.19: PL maps and spectra for $MoS_2/WS_2$ vertical heterostructures. (a) shows optical microscopy image with the scanned area outlined in red, (b) PL map of $MoS_2$ A1-exciton at ∼1.82 eV, (c) PL map of $WS_2$ A1-exciton at ∼1.96 eV. (d) graph showing the spectra for the $MoS_2$, heterostructure and $WS_2$ areas on the surface.

The heterostructure area has strongly quenched PL signals of both $MoS_2$ and $WS_2$. This quenching is caused by the interlayer coupling between the two different TMDs, due to the type II band structure.[80] The electron–hole separation in a type II junction complicates the direct exciton transitions in each TMD monolayer, resulting in exciton relaxation in the heterostructure area.[133,334] The $WS_2$ peak is more prominently present in the heterostructure area, with almost 2x the intensity of the $MoS_2$ peak, due to the stronger resonance.[303]

In contrast to the Raman map of $WS_2$, the PL map, shown in Figure 8.19(c), shows the presence of monolayer $WS_2$ at the outer edge of the $MoS_2/WS_2$ flakes of about 1-2 $\mu$m. These flakes form a small lateral area at the outside of the $MoS_2$ edge. This is confirmed in the PL spectrum, Figure 8.19(d) where there is no presence of $MoS_2$ peaks in these $WS_2$ areas. This thin ribbon of $WS_2$ at the edge of the $MoS_2$ flake supports the theory that the $WS_2$ nucleates from the edge sites. The $WS_2$ outside the $MoS_2$ is not triangular in contrast to the $WS_2$ inside the larger $MoS_2$ flake, which could be an indication that the $MoS_2$ has a templating effect for the growth of $WS_2$. The $WS_2$ outside the $MoS_2$ flake is a monolayer, the minimal surface energy, the most energetically favourable condition, is obtained when the nucleation and growth occurs alongside the edge of the flake instead of growing out laterally.

In an attempt to increase the lateral size of the $WS_2$ extending onto the $SiO_2$ surface, the amount of tungsten precursor on the seed layer was increased. Increasing the tungsten concentration did improve the lateral size of the $WS_2$ growing outside of

the $MoS_2$ flake. The lateral size of the $WS_2$ flakes outside of the $MoS_2$ flake doubled by increasing the volume of exfoliated $WO_3$ dissolved in EtOH a factor of 1.5x from 40 $\mu$L 5mg/L $WO_3$ to 60 $\mu$L 5 mg/L $WO_3$ on the 7.5x7.5 mm seed substrate. In Figure 8.20(a) an optical microscopy image of the improved structure is displayed, showing the large $MoS_2$ flakes with smaller $WS_2$ flakes nucleating from the edge of the $MoS_2$ flakes in both inwards and outwards directions. The $WS_2$ flakes are up to 5 $\mu$m long and the area extends $\sim$2 $\mu$m beyond the edge of the $MoS_2$ flakes.

In contrast to the earlier results, where less W precursor was used, the outlying $WS_2$ is a continuous part of the $WS_2$ flake growth, this can be concluded as the flake outline remains uninterrupted and the angle formed by the edge of the flake does not change when crossing the edge of the $MoS_2$ flake. The center of the $WS_2$ flakes are all located close to the $MoS_2$ edge, further indication that the $WS_2$ nucleates from the $MoS_2$ edge sites and grow over the $MoS_2$ flakes. The location of the apparent centre of the flakes would also suggest the growth rates are different on $MoS_2$ and $SiO_2$.

Figure 8.20(b) and (c) show Raman peak sum maps for respectively the $MoS_2$ $E^1_{2g}$ peak, $\sim$385 cm$^{-1}$, and the $WS_2$ $E^1_{2g}$ peak, $\sim$350 cm$^{-1}$. The $MoS_2$ $E^1_{2g}$ map shows the outline of the $MoS_2$ flake. For $WS_2$ the $WS_2$ $E^1_{2g}$+2LA(M) map clearly shows the 1L $WS_2$ flakes, where the signal for the $WS_2$ on $MoS_2$ is strongly decreased in intensity. Figure 8.20(d) shows the Raman spectra for the $MoS_2$, $MoS_2$+$WS_2$ and $WS_2$ areas on the surface. The $MoS_2$+$WS_2$ heterostructure area shows a less intense $E^1_{2g}$ peak compared to the peak in the $WS_2$ spectrum, though the $A_{1g}$ peak has a higher intensity. These observations are due to increased out-of-plane character, since the $WS_2$ layer is on top of the monolayer $MoS_2$ this can be considered a bilayer. The $MoS_2$ peaks slightly increase in intensity. For the heterostructure area and the $E^1_{2g}/A_{1g}$ peak ratios remain practically constant. There does not appear to be any quenching of the $MoS_2$ signal caused by the interaction with the $WS_2$ layer.

A PL intensity map for the A1-exciton of $WS_2$ is shown in Figure 8.20(e). The PL map only clearly shows the monolayer $WS_2$, while the $WS_2$ PL signal is strongly quenched for the heterostructure area. Figure 8.20(f) shows the PL spectra for the different areas on the surface. The PL signal of the $WS_2$ area is divided by a factor of 20x to fit it in the image. The PL signal for the $WS_2$ A1-exciton peak is quenched 24.1x in the heterostructure spectrum. The peak position is practically constant with only a negligible 0.003 eV difference towards higher energies. The quenching of the PL signal is much stronger than for the samples with less W precursor shown in Figure 8.19, where the quenching of the peak intensity is only $\sim$14.3x. Most likely the strong quenching is an indication for the higher quality of the $WS_2$ in this area or due to a strong interlayer coupling between the $MoS_2$ and the $WS_2$.

The low-frequency Raman data, shown in Figure 8.21, clearly shows the $WS_2$ LA(M) related mode, $\sim$27.8 cm$^{-1}$, in both the $WS_2$ and $MoS_2$+$WS_2$ areas. The heterostructure area also shows a peak at $\sim$23.1 cm$^{-1}$ which corresponds to the SM mode in $MoS_2/WS_2$ heterostructures.[332,333] The interlayer coupling strength of

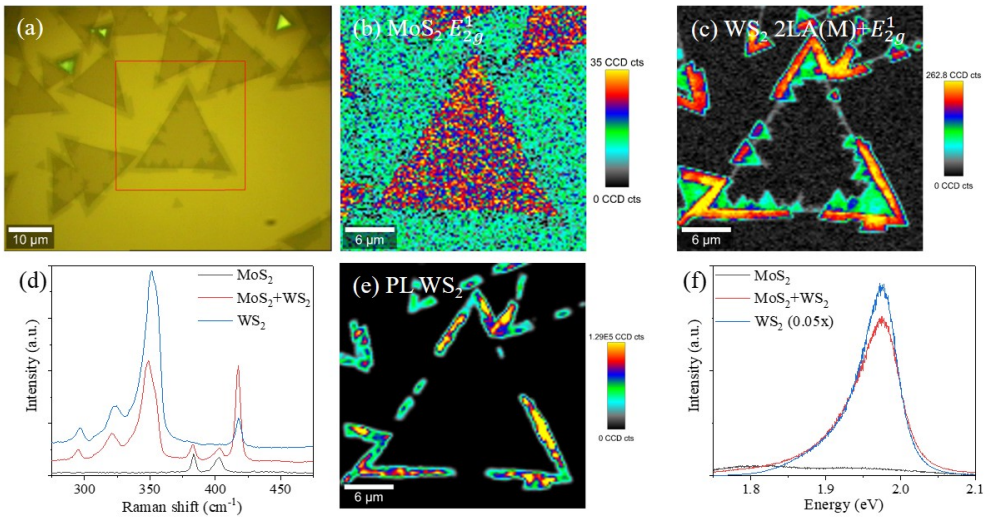


Figure 8.20: Growth of $MoS_2$+$WS_2$ heterostructures with increased concentration of W precursor. In (a) an optical microscopy image of heterostructure flakes, the red outline on the image shows the area measured for Raman and PL, (b) shows the Raman intensity map for $MoS_2$ $E^1_{2g}$ peak, where (c) shows the Raman intensity map of $WS_2$ $E^1_{2g}$ peak. The Raman spectra of $MoS_2$, $MoS_2$+$WS_2$ and $WS_2$ areas on the surface can be found in (d). In (e) the PL intensity map of the A1- exciton of $WS_2$, at ∼1.96 eV, is shown, where (f) shows the PL spectra of $MoS_2$, $MoS_2$+$WS_2$ and $WS_2$ areas on the surface.

$MoS_2$ and $WS_2$ can be derived from the intensity of the SM mode peak in relation to other Raman modes.[333] As the SM mode is visible in the LF spectrum, the conclusion can be drawn that interlayer coupling is present. There is no $MoS_2$ peak visible in the LF region of the $MoS_2$ spectrum which corresponds to the expected spectrum of monolayer $MoS_2$.[175].

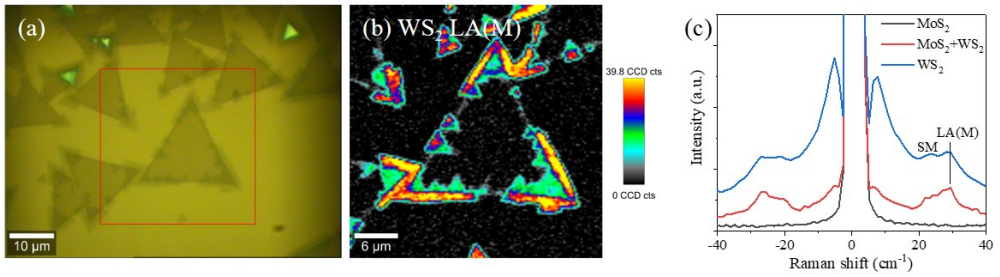


Figure 8.21: Low-frequency Raman of $MoS_2$+$WS_2$ heterostructures growth with $WS_2$ decorating the edges of the $MoS_2$ flake. In (a) an optical microscopy image of heterostructure flakes, the red outlined area is the area measured for Raman, (b) shows the Raman map for $WS_2$ LA(M) peak, where (c) shows the low-frequency Raman spectra of $MoS_2$, $MoS_2$+$WS_2$ and $WS_2$ areas on the surface.

Further information on the surface was obtained by AFM measurements. In Figure 8.22 AFM images of the height, Figure 8.22(a), and of PF-TUNA contact currents, Figure 8.22(b) and (c), are shown. The height image shows large $MoS_2$ flakes, recessed below the surrounding $SiO_2$ surface possibly due to etching by the

salt. Small $WS_2$ triangles are present on the edges of the $MoS_2$ flakes visible as lighter triangles on the $MoS_2$ flakes. These $WS_2$ triangles have a thickness of ∼0.8 nm, see the height profile in Figure 8.22(a), which roughly corresponds to the thickness of monolayer $WS_2$ on top of the monolayer $MoS_2$, thus confirming the bilayer nature of the heterostructure. On the PF-TUNA images at 0 V the only notable signal on the surface is from AC electrical noise. At 0 V the conductivity is that of an off state.

Increasing the voltage to +0.5 V results in a current signal for the whole TMD area. For +0.5 V there is less current for the heterostructure area, 0.5 nA, compared to the $MoS_2$ monolayer area, which shows a conductivity of 1.6 nA. The $SiO_2$ surface shows no conductivity. This is in contrast to the selenide heterostructures where the $WSe_2$ and heterostructure areas showed a higher current in comparison to the $MoSe_2$ area. This indicates that the vertical heterostructures have different conductivities due to intrinsic material properties as well as interactions between the different layers. The electronic properties will depend on the constituent TMDs.

To further understand the heterostructures elemental mapping of the sulfide heterostructures was done with TOF-SIMS by Rita Tilmann from UniBW München. For a more detailed explanation of TOF-SIMS see subsection 5.2.6. A heterostructure area was measured by this technique and maps and spectra for the positive ion polartiy and negative ion polarity were obtained.

Maps of the expected concentration for positive ion polarity are shown in Figure 8.23. The sum of all Mo ion isotopes collected in the positive ion mode is shown in Figure 8.23(a), this image shows the local concentration of Mo ions in the center of the flake. This the area of exposed $MoS_2$, in agreement with finding of Raman and PL measurements.

Figure 8.23(b) shows the total sum of the W ions. This map identifies areas which contain W.[335] The outline of the shape of the W in the map is triangular, while more inwards individual triangle peaks are visible, however the inside of the triangular shape is clear of W. The W areas appear as an outline of the Mo rich area, see Figure 8.23(d). This coincides with the $WS_2$ areas on the $MoS_2$ areas as observed before with the other characterisation techniques. $MoS_2$ is present as both

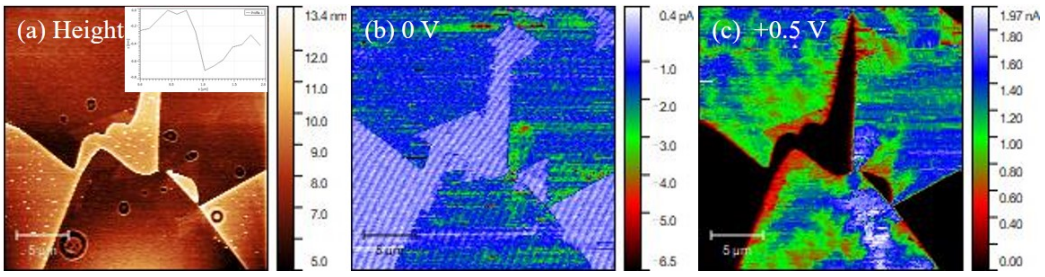


Figure 8.22: AFM images of the $MoS_2/WS_2$ heterostructure. In (a) the height image is shown with the height profile between the $MoS_2$ and $WS_2$ shown in the inset where (b) and (c) show the PF-TUNA images at different voltages. The images obtained correspond to the following applied voltages: (b) 0 V and (c) +0.5 V

a freestanding monolayer and as a single layer under the $WS_2$ flakes, though this underlying $MoS_2$ cannot be easily observed in the overlay TOF-SIMS map. Due to the sensitive nature of TOF-SIMS the penetration dept of the method is only 1 nm, showing only a significant contribution from the top layer on the substrate.

Another positive ion found on the surface is Si, see Figure 8.23(c), originating from the $SiO_2$/Si growth substrate. As would be expected Si ions are mainly found in areas where there is no $WS_2$ or $MoS_2$ coverage. The spatial separation of the Mo, W and Si is especially noticeable on the overlay image of the different TOF-SIMS maps, Figure 8.23(d). The areas where Mo, W and Si are present in the top layer are clearly distinguishable and overlap of the ions is almost completely absent, thereby confirming the growth of $WS_2$ on top of $MoS_2$.

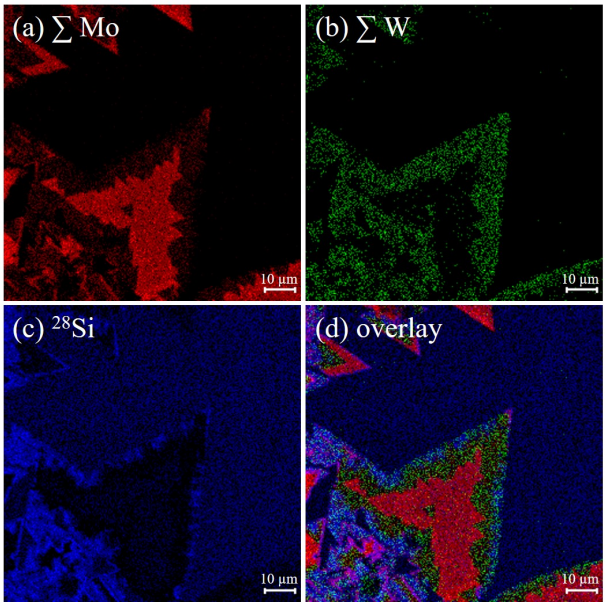


Figure 8.23: TOF-SIMS spectra of the positive ion polarity. (a) Shows the sum of all different Mo isotopes, (b) the sum of the different W isotopes, (c) shows the $^{28}$Si atoms on the surface and (d) shows an overlay map of the Mo, W and $^{28}$Si maps.

Other positive ions found to be in notable concentrations on the surface are carbon and carbohydrate compounds, such as PDMS, as well as sodium. The TOF-SIMS maps of these compounds are shown in Figure 8.24. C on the surface, as shown in Figure 8.24(a), is most likely due to carbon contamination in the furnace and the laboratory environment, which is probably also the cause of the carbohydrate contamination. PDMS related ions were also found on the surface, see Figure 8.24(c). PDMS was not used while synthesizing these heterostructures, as no transfer step was required, and the characterizations also did not require PDMS. Ostensibly PDMS should not have been present, it is likely that the PDMS contamination has been introduced during storage in the $N_2$-flow cabinets, as sample storage boxes can contain PDMS.

The significant presence of Na on the surface, as observed in Figure 8.24(d), can be explained by the use of NaCl (aq) solution on the seed layers, which was applied

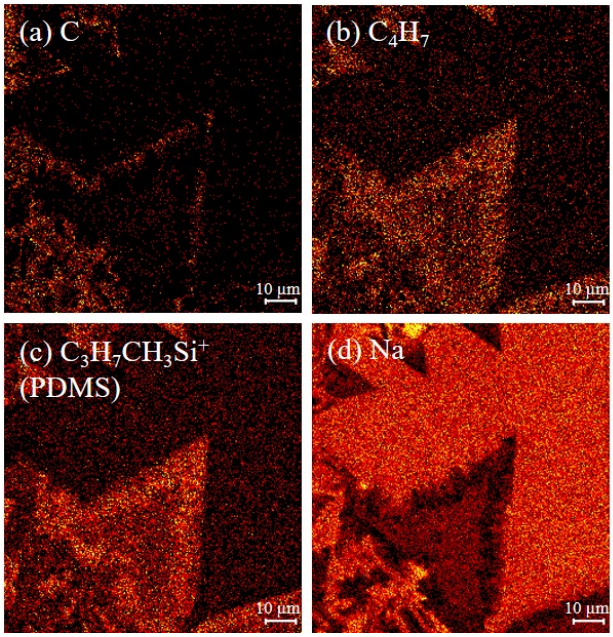


Figure 8.24: TOF-SIMS maps of the positive ion polarity ions. (a) Shows the sum of all C isotopes, (b) shows the map of $C_4H_7$, (c) shows the presence of PDMS related ions on the surface and (d) shows where Na is present on the surface.

to improve the nucleation of $WS_2$ on the surface. The Na is present over the whole surface which can influence the properties of the TMDs. Ionic contamination can lead to an increase in leakage current in devices.[336] Since it is apparent that a large excess of Na is present during growth, the NaCl concentration should be decreased to the minimum required for $WS_2$ nucleation to prevent a negative impact on the material quality. These ions can be washed away after synthesis in water, though as TMDs delaminate in water therefore this is not possible with these samples. Other rinsing solutions such as acetone and IPA are used to remove contaminants from the surface, but prolonged exposure to these solvents can do damage to the TMD films as well.

The negative ion polarity measurements, see Figure 8.25 for the corresponding maps, mainly show the presence of sulfur in various isotope states. The sulfur isotopes $^{32}S$, $^{33}S$ and $^{34}S$ are all present and distributed throughout the total $MoS_2/WS_2$ flake area, as shown in Figure 8.25a-c), indicating that Mo and W are indeed present with sulfur as $MoS_2$ and $WS_2$ in those areas.

In addition to the oxygen signal from the $SiO_2$, a strong oxygen signal, see Figure 8.25(d), is present on the edge of the flake and a very intense signal is present in the multilayer region. This indicates that these regions are adsorption sites for oxygen or a higher amount of oxidation of the sample has occurred in these regions. This oxidation was not visible on the Raman spectra of the areas, shown in Figure 8.17, suggesting there is not a significant proportion of metal oxides on the surface. Though considering that edge sites of CVD-synthesized TMDs have more defects and dangling bonds, it is not unreasonable to assume that a higher level of oxidation occurs at these sites.

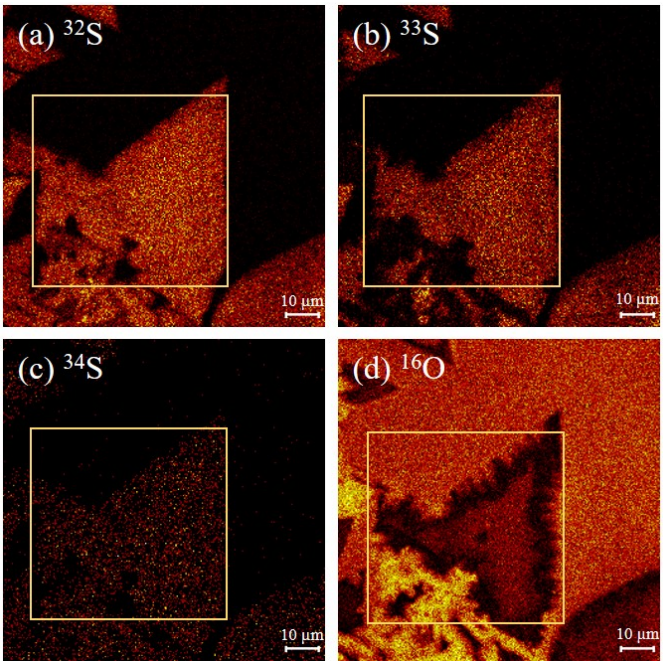


Figure 8.25: TOF-SIMS spectra of the negative ion polarity. (a) Shows the map of the $^{32}$S isotope, (b) the $^{33}$S isotope map, (c) shows the $^{34}$S isotopes on the surface and (d) shows the map of the $^{18}$O isotope.

$\mu$-XPS measurements can be used to further investigate the state of the oxides present and the amount of oxidation on the surface. The $\mu$-XPS spectrum was taken from a heterostructure flake see the area outlined in red in Figure 8.26(a). This area resulted in the $\mu$-XPS map shown in Figure 8.26(b). The following elements were identified on the surface: Mo, S, W and Si as well as $MoS_x$ and $WS_x$ compounds.

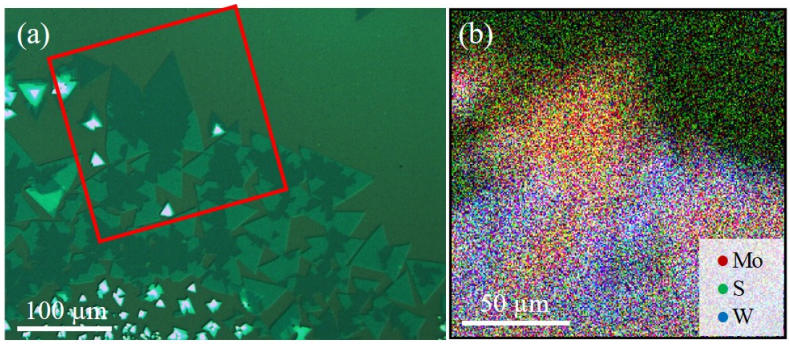


Figure 8.26: (a) Optical microscopy image with the red outline indicating the area characterised by $\mu$-XPS and (b) $\mu$-XPS map of different components present on the surface.

The $\mu$-XPS spectra, see Figure 8.27, shows the presence of both $MoS_2$ and $WS_2$. For the Mo 3d core level spectrum the $MoS_2$ peaks are visible at 229.3 eV and 232.4 eV and there is some overlap from the S 2s core level at 226.8 eV. There are also small amounts of molybdenum oxide present as there are peaks at 233 eV and 236.2 eV corresponding to $MoO_3$. In the W 4f core level spectrum the main contributions stem from the $WS_2$ 4f levels at 33.24 and 35.39 eV. Other contributions include the

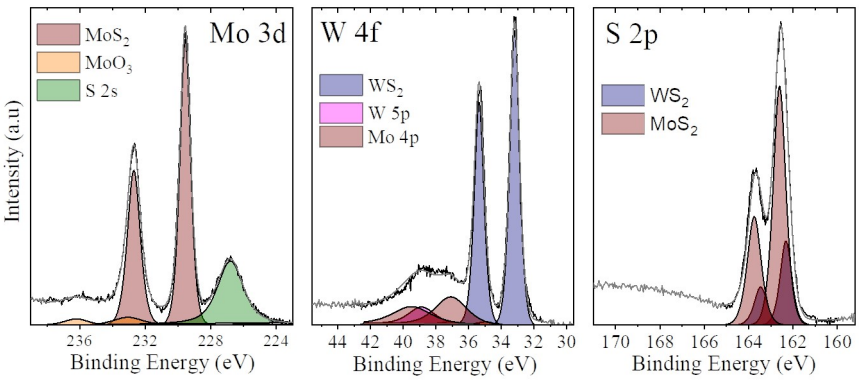


Figure 8.27: $\mu$-XPS spectra of $MoS_2/WS_2$ heterostructure flake. The spectra for the Mo 3d, W 4f and S 2p regions are shown.

Mo 4p core level at 37.11 eV and 39.5 eV and $WSe_2$ 5p at 38.87 eV. The S 2p core level is deconvoluted into overlapping contributions from $MoS_2$ (162.6 eV and 163.75 eV) and $WS_2$ (162.33 eV and 163.46 eV).

There does not seem to be any W oxides, but W oxides appear in very similar positions to the Mo 4p, therefore a very small amount of oxide would be extremely hard to identify inside overlapping components. Since the size of the Mo 4p peak is proportional to the Mo 3d peak, it can be concluded that the components from that peak are mostly Mo 4p and therefore there are negligible amounts of W-oxide present. Thus indicating the chemical stability of the $WS_2$ compound. Due to the overlapping sulfur contributions it is difficult to get an exact $MoS_2$:$WS_2$ ratio, though it appears to be around 60:40 $MoS_2$:$WS_2$ as the amounts can be calculated from the W 4f and Mo 3d regions. A small peak attributed to the Na 1s core level was found at 1071.0 eV, this peak corresponded to ~27.6 % of the Mo peak, indicating that NaCl was present on the surface, so while it does indicate that NaCl was present on the surface its contributions are smaller than those of the $MoS_2$ and $WS_2$.

In contrast to the Se-heterostructures there was no growth of pure lateral heterostructures observed for the sulfur TMDs. The lateral size of the vertical grown $WS_2$ on top of the $MoS_2$ was quite large reaching up to 10 $\mu$m, which is greater than the dimensions for the selenide heterostructures, for these growth conditions. may be due to the more stoichiometric Mo:S ratio of $MoS_2$, as indicated by the regular triangular growth of the $MoS_2$ flakes. Due to this ratio of the precursors such $MoS_2$ would have fewer defects and would be less Mo deficiencies. Because of the high quality of the $MoS_2$-flake, the $MoS_2$ flake would act as a template for the growth of $WS_2$. As seen before for the formation of the $MoSe_2/WSe_2$ heterostructures the presence of edge defects benefits the formation of lateral heterostructures, as this leads to low energy nucleation sites.[218] In contrast a low concentration of defects, such as is the case here, this results in the growth of vertical heterostructures.

Zhang *et al.* used a similar approach for the growth of their growth of heterostructures, though they used metal oxide powder between the seed substrate and growth substrate to create a close proximity precursor, requiring a larger amount of

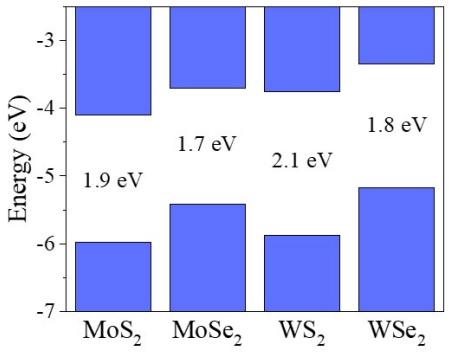


Figure 8.28: Band alignment diagram of $MoS_2$, $MoSe_2$, $WS_2$ and $WSe_2$. The value of the electrical band gap is shown in the center. Data obtained from Guo *et al.*[338]

metal precursors.[337] In their work the hydrogen flow of the carrier gas was used to control the nucleation. In contrast to Zhang's work the reaction process described here used forming gas throughout the growth of both $MoS_2$ and $WS_2$. In an attempt to recreate the conditions to control nucleation the synthesis process was adapted. Ar-gas was used as carrier gas and the gas flow was switched to the forming gas at the point where the temperature was increased for the $WS_2$ growth, though this did not yield any appreciable improvement in nucleation.

### 8.2.3 $MoS_2$-$WS_2$ Devices

Continuing from the synthesis of $MoS_2/WS_2$ heterostructures, as described above, these materials were contacted to probe their electrical properties. This combination of TMD materials forms a type II, staggered gap, heterojunctions as shown in the band alignment diagram in Figure 8.28.[289,338] To illustrate such a type II staggered gap heterojunction, consider a $MoS_2/WS_2$ heterostructure. From Figure 8.28, it is clear that the conduction band minimum, which is energetically favourable for electrons, is on the $MoS_2$ side of the interface at -4.10 eV, while the energetically favourable valence band edge, -5.88 eV, is on the $WS_2$ side. Thus this type II aligned heterostructure leads to charge separation at the interface improving device performance in for example a solar cell where the charge is photoinduced.[73]

The $MoS_2/WS_2$ device architecture discussed here is an asymmetric junction, where one contact is placed on the vertical heterostructure stack and the other contact is placed on the monolayer $MoS_2$ as shown in Figure 8.29. As the device is a partial vertical stack it is an indirect band gap semiconductor and a type-II junction as the calculated CB and VB of $WS_2$ are higher in energy than those of $MoS_2$ as defined previously. This means that while both $MoS_2$ and $WS_2$ are n-type materials, due to the small band offset between $MoS_2$ and $WS_2$ the TMD combination has been shown to function as a rectifying heterojunction.[82]

Other studies using STM measurements put the indirect band gap of the $MoS_2/WS_2$ heterostack at 1.45 eV $\pm$0.06 eV.[339] The valence band maximum consists of the d-


Figure 8.29: Schematic overview of the $MoS_2/WS_2$ heterostructure device with asymmetric contacts on the monolayer $MoS_2$ and heterostack $MoS_2/WS_2$

orbitals of W and Mo and the p-orbitals of S, while the conduction band minimum is predominantly formed by the d-orbitals of Mo.[340]

As described in subsection 3.6.1 type II junctions have many applications in photonics. Indeed devices utilising $MoS_2$-$WS_2$ heterostructures have been shown in literature for photonic applications.[81–83,132,137] These devices have been realised with chemically exfoliated,[132] TAC[82] and CVD[83,137] synthesized materials. The heterostructure of $MoS_2$ and $WS_2$ results in fast charge separation and recombination.[341] This makes $MoS_2/WS_2$ heterostructures perfect for applications in photovoltaics, photodetectors and catalysis.

As a proof of concept a 2-probe heterostructure device was fabricated. From the $MoS_2/WS_2$ heterostructures, growth process described in subsection 8.2.2, the devices were made by use of maskless UV lithography, as detailed in subsection A.3.2. Ti/Au Contacts (5/100 nm) were placed on both the $WS_2$ and $MoS_2$ to produce a heterostructure device. After the deposition of the contact metals, the samples were annealed to decrease the contact resistance between the semiconductor and the metal, since measurements performed before annealing did not yield any reliable results.[18]

In Figure 8.30 an optical microscopy image of such a device is shown. The left probe as visualised in Figure 8.30(b) is contacted to the freestanding $WS_2$, where the other probe is located on the center of the $MoS_2$ flake. The channel length is $\sim$ 6.5 $\mu$m and the channel width is $\sim$ 3.7 $\mu$m. In this device the $MoS_2$-$WS_2$ heterostack was used as the source, while the $MoS_2$ functioned as the drain.

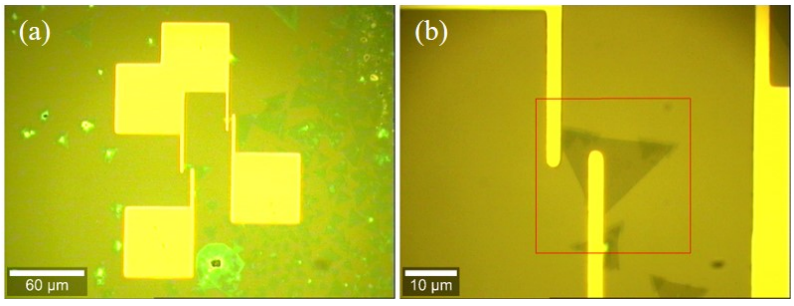


Figure 8.30: Optical microscopy images of initial 2-probe device (a) 20x magnification image (b) 100x magnification image.

To verify to contacts were correctly positioned on the separate TMDs Raman spectroscopy was performed. In Figure 8.31 the Raman intensity map of the $E^1_{2g}$ $MoS_2$ peak, Figure 8.31(a), and the Raman intensity map of the 2LA(M)+$E^1_{2g}$ $WS_2$ peak, Figure 8.31(b) are shown. On the images a clear cut-off of the Raman signal is

visible where the metal contacts are located, which are recognisable as straight ∼3 $\mu$m low intensity lines on the maps. $MoS_2$ is visible between the 2 contacts. The left contact appears to be located on mainly on the freestanding $WS_2$ with a small part located on the $MoS_2/WS_2$ area, as such it should not be in direct contact with the underlying $MoS_2$, whereas the right contact is placed on top of the $MoS_2$, making the device indeed a heterojunction.

A simple IV-curve with a gate - source voltage ($V_{gs}$) of 100 mV and a $V_{ds}$ ranging from -1.0 to 1.0 V. was measured first in atmospheric conditions, as shown in the graph in Figure 8.32 where the current was flown from the heterostructure area to the $MoS_2$. The IV-curve shows a high hysteresis, while the conductivity is limited to ∼19.8 nA. The $MoS_2/WS_2$ device was expected to show photoconductivity behaviour, meaning that the device will show higher electric conductivity with increased light exposure. The photo response of the devices was checked by performing simple measurements under increased light, ambient brightness and dark conditions. The increase in light intensity did increase the photoconductivity of the sample, increasing the conductivity from ∼19.8 nA to ∼55.4 nA, thus increasing the conductivity by a factor of ∼2.8. When switching off all external light sources, a dark measurement was performed. In this measurement the conductivity decreased 26.8% to a current of 14.5 nA at a $V_{ds}$ of 1 V.

There is a large hysteresis present in the IV-curves, during the up ramp in the voltage sweep there is a high rise in the current during the ramp up but linear behaviour during the back sweep. Hysteresis of the IV curve appeared to slightly decrease with increasing light intensity. The hysteresis is likely due to source trapped charges caused by absorbates on the surface or defects at the $MoS_2/WS_2$ interface. The device hysteresis could perhaps be improved by repeated cycling of the device, annealing, measurement in vacuum or longer acquisition time allowing relaxation. Other research shows that electrons have been trapped in the material, Lee *et al.* showed the presence of large hysteresis in the IV curve of a $MoS_2$/h-BN/graphene stack, which was due to trapped electrons in the graphene layers.[342] If the hysteresis is attributed to charge transfer between the $MoS_2$ and $WS_2$ layer it could be beneficial for applications in memory devices.[343] The stacked layers can trap electrons

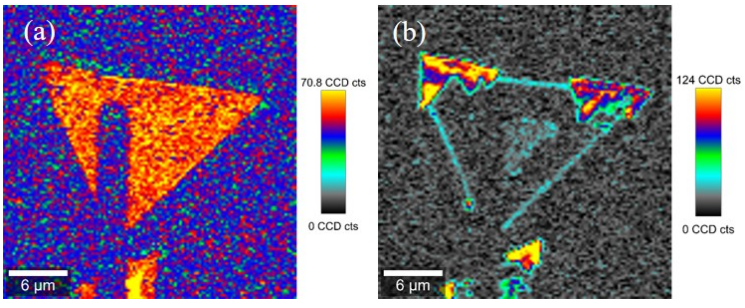


Figure 8.31: Raman maps of $MoS_2/WS_2$ flake after contact deposition. In (a) the Raman intensity map of the $E^1_{2g}$ peak of $MoS_2$ is shown where (b) shows the Raman intensity map of the $E^1_{2g}$ peak of $WS_2$.

and function as a memristor, resistive memory. Other factors which can possibly influence the hysteresis are temperature and doping.

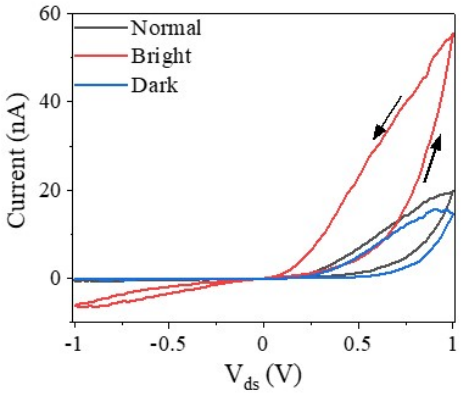


Figure 8.32: Graph showing the IV-curve of the 2-probe $MoS_2/WS_2$ device in normal, bright and dark environments.

The delicate finger architecture of the devices resulted in a high failure rate for the devices, as the small contact area often did not result in a good contact between the semiconductor and the metal. The contacts were also sensitive to scratches on the surface as well as defects. To minimise these issues another more robust contact configuration was used for further measurements. Large contact pads were placed overlapping over the $MoS_2$ and $MoS_2/WS_2$ area ensuring large contact areas, as shown in Figure 8.33.

Vertical heterostructures were again produced by maskless lithography with 5/100 nm Ti/Au contacts. Optical images in Figure 8.33 show both the semiconductor material as well as the contacts thus indicating that there is a larger surface area of the semiconductor covered by the contact pad, thereby resulting in a better contact between the semiconductor material and the contact metal. The use of maskless lithography allowed to design of custom contacts for an optimal fit with the specific areas of heterostructure and $MoS_2$ growth.

For these devices Raman measurements were also performed to confirm the integrity of the heterojunction. In Figure 8.34 the obtained Raman maps are shown.

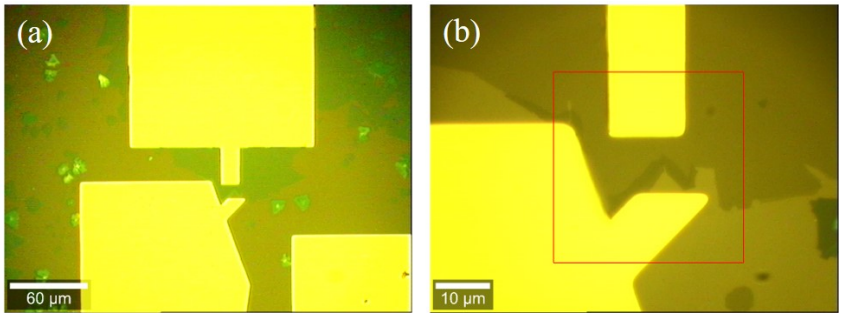


Figure 8.33: Optical microscopy images of heterostructure devices with increased contact areas. (a) 20x magnification image and (b) 100x magnification image.

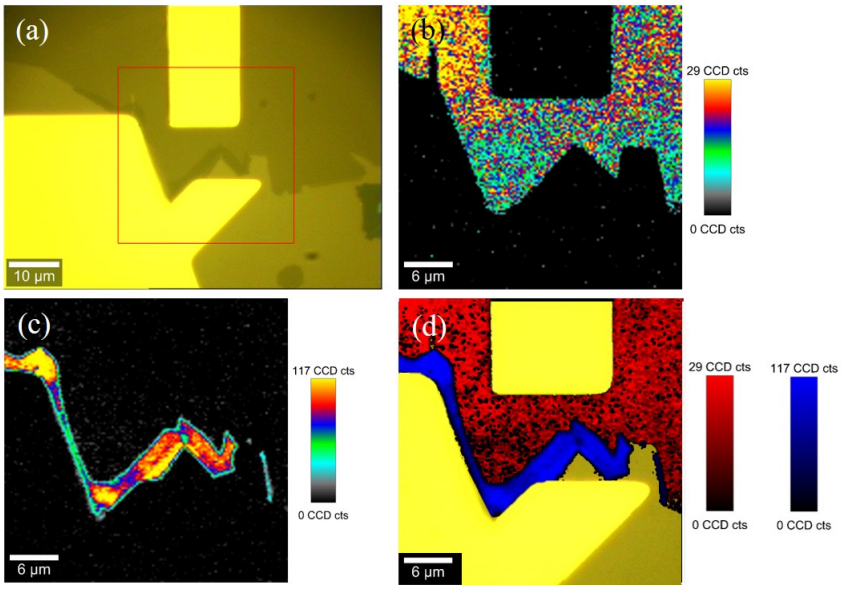


Figure 8.34: Optical microscopy image and Raman maps of contacted area. (a) 100x magnification optical microscopy image, (b) Raman map of the $MoS_2$ $E^1_{2g}$ Raman peak, (c) $WS_2$ 2LA(M)+$E^1_{2g}$ Raman map and (d) overlapping Raman map of the $MoS_2$ and $WS_2$ Raman maps with the $MoS_2$ area shown in blue and $WS_2$ in red and on top of the optical microscopy image

Figure 8.34(b) shows the $MoS_2$ $E^1_{2g}$ Raman map, which shows a large $MoS_2$ area spanning most of the area between the contacts. Some scattering is present in the spectrum, possibly due to defects on the surface, but it is clearly a continuous crystalline $MoS_2$ film. In Figure 8.34(c) the $WS_2$ 2LA(M)+$E^1_{2g}$ Raman map is shown, indicating the presence of a $WS_2$ area surrounding the contact at the bottom of the image. To distinctly show the heterostructure area an overlapping Raman map is shown in Figure 8.34(d). In red the $MoS_2$ area is shown, whereas the area in blue corresponds to the $WS_2$ area. In the image the Raman maps are placed on top of the optical microscopy picture, thereby showing the location of the $MoS_2$ and $MoS_2/WS_2$ areas in relation to the metal contacts. This image shows that the device is a vertical heterojunction where one contact is located on the $MoS_2$ and the other contact is placed on the vertical $MoS_2/WS_2$ stack.

Initial measurements were performed in the off-state, without an applied back gate voltage, under vacuum conditions. The monolayer $MoS_2$ functioned as the source contact, while the $MoS_2/WS_2$ stack was used as the drain. The IV-curve of this measurement is shown in Figure 8.35. The device shows asymmetric behaviour. Different explanations are possible for the non-linearity in the IV-curve, it could be due to a Schottky barrier (SB) at the contacts, due to the band offset between $MoS_2$ and $WS_2$, or the device contact asymmetry or due to a combination of either. If the asymmetric IV-curve is caused by the SB, the device acts like a back-to-back diode. The asymmetric behaviour could also be explained by image force band lowering due to the band offset of the staggered band gap junction.[344]

Diode behaviour is expected from a staggered band gap junction and has been

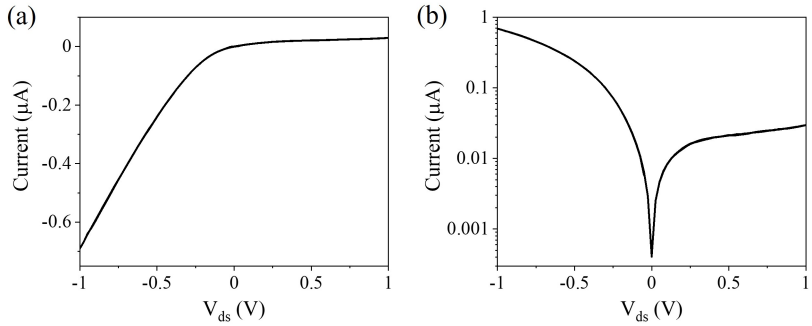


Figure 8.35: IV-curve of the 2-probe $MoS_2/WS_2$ device under vacuum without gate modulation. The graphs show the IV-characteristics at a (a) linear and (b) semi-logarithmic scale.

observed in literature.[54,82,296] This device is a vertical heterostructure, therefore there is also the potential depletion of the entire monolayer area due to slight band bending at interface. An applied bias results in band bending causing the valence band of the more p-type material to align with the conduction band of the more n-type material. For the $MoS_2/WS_2$ heterostructure $MoS_2$ has a lower valence and conduction band compared to $WS_2$, therefore the $WS_2$ is more p-type and the valence band of $WS_2$ will bend towards the conduction band of $MoS_2$.

The turn-on voltage, calculated by linear extrapolation, is around -0.22 V as the Ohmic region is located at voltages below -0.22 V. The cut-off region starts around 0 V and reaches its limit at 0.1 $\mu$A. The behaviour appears to be like that of n-channel depletion. The current shown in these conductivity measurements is 3 orders of magnitudes larger compared to the heterostructure devices measured in atmospheric conditions, $\mu$A instead of nA. It is unclear if this is due to the measurements being performed in vacuum or the larger contacts, creating a wider channel and improved contact. Conducting the measurements in vacuum allowed the desorption of contaminants from the surface, which could lead to a change in conductivity or a shift in the doping of the material, where the larger contact area is assumed to increase the current as well. Other parameters which could be of influence on the devices are the crystallinity of materials, channel dimensions and the contact resistance.

IV-curves of monolayer $MoS_2$ and mono- to bi-layer $MoS_2$ devices on the same chip were obtained for comparison with the heterostructure device. These IV-curves are shown in Figure 8.36. The IV behaviour of the monolayer $MoS_2$ device seems to be inverted in comparison to both the heterostructure and the mono-bilayer $MoS_2$ device. Though the monolayer $MoS_2$ is more conductive compared to the heterostructure, the monolayer bilayer junction of $MoS_2$ conducts more than either of the other devices. In addition to the inherent electronic differences between the layers, this difference is probably in part due to the a better interface between the $MoS_2$ layers, whereas there is a small lattice mismatch between $MoS_2$ and $WS_2$.

Gate modulation can be used to obtain the transfer characteristics of the devices.

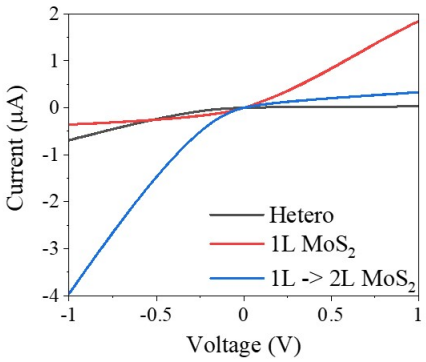


Figure 8.36: IV-curves of the 2-probe devices under vacuum without gate modulation. The graphs shown are the graphs for the $MoS_2/WS_2$ heterostructure, monolayer $MoS_2$ and mono to bi-layer $MoS_2$.

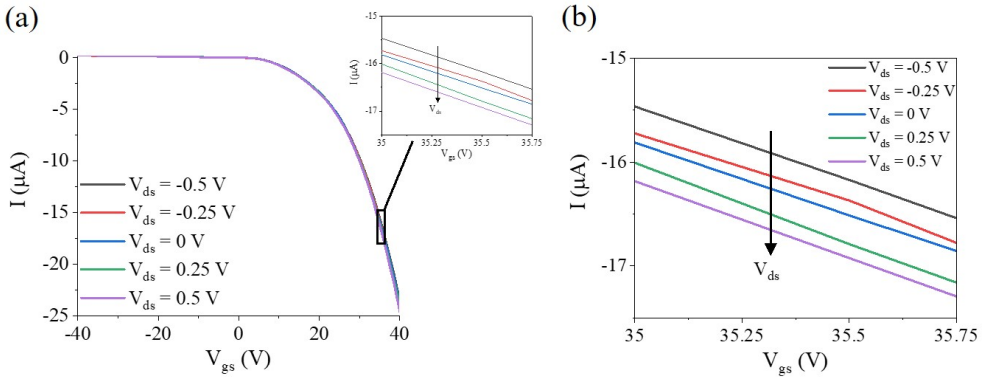


Figure 8.37: Transfer characteristics curves for the $MoS_2/WS_2$ heterostructure at 140 K. The applied $V_{ds}$ ranged from -0.5 – 0.5 V, with a decrease in conductivity for increased $V_{ds}$

To gate the devices a back gate voltage was applied. The transfer curves for varying $V_{ds}$ at 140 K is shown in Figure 8.37. The $V_{ds}$ was varied between -0.5 V and 0.5 V and the graph shows an decrease in the slope for increased applied voltage. The Ohmic region of this device is $\sim$ 20 V, where the cut-off voltage is around 10 V. As the device switches off with increasing $V_{gs}$, the device shows p-type behaviour, which is most likely caused by flowing the current from the monolayer $MoS_2$ (source) to the $MoS_2/WS_2$ bilayer (drain). While the devices here indicate p-type behaviour, most lateral $MoS_2/WS_2$ devices show n-type behaviour as well.[342,345,346]

The currents of the heterostructure device, range from $3x10^{-7}$ to $9x10^{-10}$ and the on/off ratio is therefore in the order of $\sim$2.4. The on/off ratio found here is in line with other values found in literature.[345–347] From plotting the slopes of the linear part of the transfer characteristic curves the field-effect mobility can be calculated as the intercept of the linear fitted slope is $\frac{\partial I_{ds}}{\partial V_{gs}}$. The intercept value is $-1.89x10^{-6}$. For a bias voltage of -0.5 to 0.5 V, the field effect mobility was estimated to be around 4.34 $cm^2/(Vs)$

The mobility was calculated below room temperature, 140 K, at which the mobil-

ity should be higher compared to the mobility at room temperature. This is because at room-temperature field effect mobility is limited by phonon scattering events.[348] Performing electrical measurements at lower temperatures minimises the phonon scattering, thereby resulting in higher mobilities. Decreasing the temperature does however result in a reduced number of carriers, thereby hindering the conductivity of devices.

Finally the devices were measured at different temperatures. The IV-curves for the temperature-dependent measurements are shown in Figure 8.38. The temperature was varied between 100 – 200 K. When the temperature is increased the resistance decreases as expected for semiconductors, resulting in a higher current through the device in the IV-curve, as shown in Figure 8.38. The transfer characteristics show that the device switches at a lower voltage when the temperature is increased, thus confirming the semiconductor nature of the device.

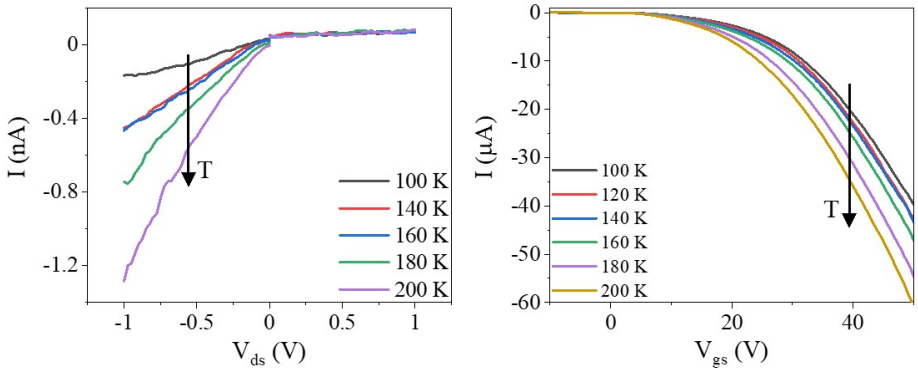


Figure 8.38: Temperature-dependent measurements of $MoS_2/WS_2$ heterostructure. (a) IV-curves for the different temperatures and (b) transfer characteristic curves with $V_{ds}$ = -0.5 V. With a increase in conductivity for increased temperature

To better understand the behaviour of the device and the obtained electrical data, density functional theory (DFT) calculations were performed by Dr. Lida Ansari and Dr. Farzan Gity from Tyndall National Institute. The band structures for the individual $MoS_2$ and $WS_2$ layers have been calculated initially and are shown in Figure 8.39(a) and (b). The calculated band gap is around 1.96 eV for the monolayer $WS_2$, where the calculated band gap for $MoS_2$ is ∼1.77 eV. In Figure 8.39(c) the calculated band structure for the vertical $MoS_2/WS_2$ stack is shown. The interaction between the TMD layers reduces the band gap to 1.35 eV. The reduction of the band gap in the bilayer region is due to an increase in the indirect band gap of the system.[294]

In this stacking there should be a higher contribution of $MoS_2$ in the conduction band, whereas the contribution of $WS_2$ is higher in the valence band which can be expected due to the higher conduction and valence band of $WS_2$ monolayer compared to the $MoS_2$ monolayer. The current in the device goes from monolayer $MoS_2$ to a bilayer heterostack, therefore a band offset is present. DFT calculations of the valence band offset between the materials give quite a large offset of ∼0.45

eV between the single and bilayer area.

It is interesting to note that the type of heterostructure synthesised in this work where the $WS_2$ flake grows on top of the $MoS_2$ in small triangles from the edges of the $MoS_2$ and the corresponding simulations, appear to be novel as no similar papers were found in literature from simulation point of view.

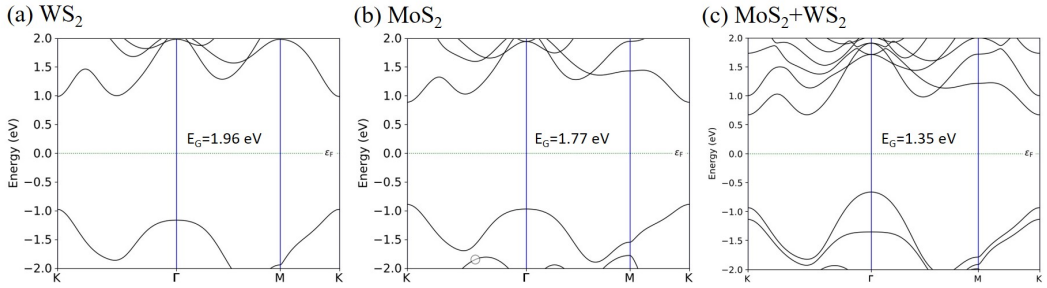


Figure 8.39: DFT calculated band structures and band gaps of (a) $WS_2$, (b) $MoS_2$ and (c) the $MoS_2/WS_2$ hetero stack

To conclude, the heterostructure devices show semiconductor behaviour and light sensitivity, like a photo conductor, the conductivity of the devices increased when exposed to a light source. Hysteresis was present in the IV curves, which was most likely caused by trapped charge carriers between the TMD layers. The charge carrier type appears to display p-type behaviour as the current drops when the $V_{gs}$ is increased. This behaviour was observed when the source was located on the single layer $MoS_2$, while the drain was placed on the vertical $MoS_2/WS_2$ stack. The $V_{ds}$ went from the more n-type material to the more p-type material.

## 8.3 Summary

It was demonstrated that both the double-step and single-step growth approaches can result in the formation of heterostructures. The double-step approach is more versatile for the choice of TMDs, however the material quality of the initially synthesised TMD degrades during the second CVD run. For some TMD combinations the first TMD is completely etched by the growth of the second material, for the furnace setup and growth procedures used. When the more stable TMD is synthesised first, the growth of the second TMD does not lead to crystalline growth on the surface as the interruption caused by this stepped growth results in poor crystallinity. The chance of a TMD nucleating on a defective site, compared to nucleation on a pristine TMD surface, is higher as this is energetically more favourable. Therefore, to produce TMD heterostructures suitable for electronic device applications a more stable synthesis approach is desirable.

The single-step approach resulted in more crystalline flakes, for both the selenide and the TMD heterostructures. Spectroscopic characterisation by Raman and PL spectroscopy as well as AFM showed that there was growth of either lateral or vertical heterostructures depending on the presence of defects and vacancies on the

edge of the initially grown TMD. When these defects or vacancies were present the nucleation of the CVD growth of the second TMD started at the edges of the initial TMD flake and grew out in a horizontal direction, leading to lateral heterostructures. For growth with stoichiometry closer to the ideal ratio, where the metal/chalcogen ratio corresponds to the growth of $MX_2$, the secondary TMD material tended to grow on top of the initial TMD forming a vertical heterostructure.

For the selenide heterostructures, $MoSe_2$+$WSe_2$, both lateral and vertical heterostructures were formed during the synthesis process depending on the metal precursor concentration. The formation of the heterostructures was confirmed by Raman spectroscopy, PL spectroscopy and XPS. The rate of $WSe_2$ growth is largely dependent on the surface on which it is growing. For lateral growth the length of the $WSe_2$ is ∼5-10 $\mu$m starting from the $MoSe_2$ boundary, while the area for $WSe_2$ for vertical growth is only ∼1–5 $\mu$m. The crystallinity of the lateral growth is higher compared to that of the vertical structure as the $WSe_2$ in the vertical growth mainly consists of separate crystals, where these crystals fuse together in case of the lateral growth. The hetero interface area shows alloying of both $MoSe_2$ and $WSe_2$ as the $WSe_2$ fills the $MoSe_2$ vacancies on the edge, which can be seen in the Raman spectrum where the main peak in the interface area is located between the $MoSe_2$ $A_{1g}$-peak and the $WSe_2$ $E^1_{2g}$+$A_{1g}$-peak. When inspected with PF-TUNA the $MoSe_2$/$WSe_2$ heterostructures show that $WSe_2$ conducts at a lower voltage, though the surface becomes completely conductive when a threshold voltage for the $MoSe_2$ is reached.

In contrast to the Se-heterostructures there was no growth of pure lateral heterostructures observed for the sulfur TMD heterostructures. The lateral size of the $WS_2$ on top of the $MoS_2$ flake was quite large reaching up to 10 $\mu$m, which is larger than the dimensions of the selenide heterostructures. Spectroscopic characterisation confirmed the presence of both $MoS_2$ and $WS_2$ and the presence of the bilayer heterostack. Since the $MoS_2$ was highly crystalline, the $MoS_2$ surface leads as a template for the growth of $WS_2$, resulting in the growth of the $WS_2$ flakes from the edges along the $MoS_2$ crystal direction.

The growth of $WS_2$ on top of the $MoS_2$ flakes made them convenient to contact for the production of heterostructure devices. 2-probe, back-gated devices were produced to study to behaviour of the heterostructure. The devices are clearly semiconducting with p-type behaviour and function as a photoconductor as predicted by DFT calculations. The characterisation of the photoconductor behaviour was only elemental as there was no appropriate measurement setup, but shows promising results. The reported devices show proof of concept and there is further scope for optimisation through improved device architecture.

# Part V

# Conclusions and Outlook

# 9 Conclusion & Outlook

In this thesis the CVD synthesis of TMDs and TMD heterostructures has been developed and thoroughly examined. The effects of reaction parameters on the nucleation and growth as well as how the growth substrate directs the morphology of the synthesised TMD have been studied. Heterostructures were synthesised using the growth parameters obtained by the optimisation studies and were comprehensively characterised and studied for their properties and possible applications.

In chapter 6 a parametric study on the growth of $WSe_2$ was explored. Different reaction parameters such as the metal precursor, reaction temperature, pressure, gas flow and reaction time were studied to optimise the growth of large, highly crystalline $WSe_2$ flakes. The effects of the parameters were intensively studied by optical microscopy, Raman spectroscopy and AFM. The reaction parameters have a large impact on the formation of $WSe_2$, growth mechanism, crystallinity and the lateral flake size.

The $WSe_2$ flakes obtained by the optimised growth process were used to produce proof-of-concept FET devices to study the electrical properties and possible applications. In-house measurements showed p-type charge carrier type and a mobility of $\sim$25 - 27 $cm^2/(Vs)$. Collaborations with CNR-SPIN in Salerno showed the influence of environmental effects on the behaviour of the device and $WSe_2$ flakes were used as the channel material in the first ever vertical field emission transistor.

Where chapter 6 discussed the reaction parameters and their influence on the CVD growth of $WSe_2$, chapter 7 delved deeper into the influence of the growth substrate on the growth, alignment and morphology of CVD $MoS_2$. The growth mode of $MoS_2$ is strongly influenced by the surface morphology as well as the surface interaction. Sapphire substrates were investigated by AFM to obtain more information on the surface morphology and how the surface might influence the $MoS_2$ growth.

Aligned growth of $MoS_2$ was possible on M- and R-plane sapphire for the growth parameters used in this work as was confirmed by Raman spectroscopic analysis as well as PL and AFM. Growth on A-plane sapphire resulted in high-density nucleation of $MoS_2$ as the substrate is provides a large number sites for nucleation at the terrace steps. The alignment of the CVD-grown $MoS_2$ can be improved by selecting an appropriate growth substrate as well as optimizing the growth conditions of the material. This is largely dictated by the surface morphology as well as the enhanced surface interaction. The growth mechanism is not only influenced by the surface morphology, but also the alignment of terraces parallel or perpendicular to the gas

flow in the reaction furnace as was observed on M-plane sapphire.

For further improvement of the $MoS_2$ growth, or better alignment, one approach would be to use an Al-terminated sapphire substrate, as this causes a higher interaction with the material. This could be achieved by increasing the reaction temperature or by using hydrogen as carrier gas before reaction to remove the hydroxyl groups on the sapphire surface. Other parameters that could improve the growth are the duration and temperature of the annealing. C-plane sapphire results in better $MoS_2$ for non-annealed substrates, while annealed A-plane sapphire has been reported to result in aligned TMD growth at a lower temperature. CVD of $MoS_2$ on M-plane could possibly result in broader more crystalline flakes when the terrace step sizes are well-defined but lower in width.

To better understand the growth mechanism of the $MoS_2$ on the various sapphire planes extended characterisation would be useful with techniques such as TEM or angle resolved optical techniques such as reflection anisotropy spectroscopy. It would be optimal to study the growth and nucleation mechanism in-situ with electron microscopy and Raman spectroscopy during the synthesis process. Another interesting thing to study further would be the growth of $MoS_2$ on other substrates such as h-BN in the microreactor CVD growth proposed here as well as the study of different TMDs and TMD heterostructures on sapphire.

Chapter 8 discussed the direct growth of heterostructures using the double-step synthesis approach as well as the single-step synthesis approach. Both the double-step and single-step growth approach can result into the formation of heterostructures. The double-step approach is more versatile for the choice of TMDs, however the material quality of the initially synthesised TMD degrades during the second CVD run. For some TMD combinations the first TMD even gets etched away completely with the used furnace setup and growth procedures. Though, when the more stable TMD is synthesised first, the growth of the second TMD does not lead to crystalline growth on the surface. The chance of a TMD nucleating on a defective site, compared to nucleation on a pristine TMD surface, is higher as this is energetically more favourable. Therefore, to produce TMD heterostructures suitable for electronic device applications a more stable synthesis approach would be desirable

The single-step approach resulted in more crystalline flakes, for both the selenide and the sulfide heterostructures. Spectroscopic characterisation by Raman and PL spectroscopy as well as AFM showed that there was growth of either lateral or vertical heterostructures depending on the presence of defects and vacancies on the edge of the initially grown TMD. When these defects or vacancies were present the nucleation of the second TMD started at the edges of the initial TMD flake and grew out in a horizontal direction, leading to lateral heterostructures. On initial flakes with less edge defects the secondary TMD material tended to grow on top of the initial TMD forming a vertical heterostructure.

For the selenide heterostructures, $MoSe_2$+$WSe_2$, both lateral and vertical heterostructures were formed during the synthesis process depending on the metal pre-

cursor concentration. The formation of the heterostructures was confirmed by Raman spectroscopy, PL spectroscopy and XPS. The area of the formed $WSe_2$ varies strongly between lateral and vertical growth. For lateral growth the length of the $WSe_2$ is ∼5-10 $\mu$m starting from the $MoSe_2$ boundary, while the length of $WSe_2$ for vertical growth is only ∼1–5 $\mu$m. The crystallinity of the lateral growth is higher compared to that of the vertical structure as the $WSe_2$ in the vertical growth mainly consists of separate crystals, where these crystals fuse together in case of the lateral growth. The hetero interface area shows alloying of both $MoSe_2$ and $WSe_2$ as the $WSe_2$ starts filling up the $MoSe_2$ vacancies on the edge, which can be seen in the Raman spectrum where the main peak in the interface area is located between the $MoSe_2$ $A_{1g}$-peak and the $WSe_2$ $E^1_{2g}$+$A_{1g}$-peak. When inspected with PF-TUNA the $MoSe_2$/$WSe_2$ heterostructures show that $WSe_2$ conducts at a lower voltage, though the surface becomes completely conductive when the threshold voltage for the $MoSe_2$ is reached.

To obtain more information on the electrical properties of the $MoSe_2$/$WSe_2$ heterojunction it would be informative to create electrical devices from these heterostructures and to perform point IV measurements via conductive AFM. For better control over the hetero growth a more in-depth study on the surface reaction is needed. This would require an in-situ study of the growth.

In contrast to the Se-heterostructures there was no growth of pure lateral heterostructures observed for the sulfur TMD heterostructures. The lateral size of the $WS_2$ on top of the $MoS_2$ flake was quite large reaching up to 10 $\mu$m, which is larger than the dimensions of the selenide heterostructures. Spectroscopic characterisation confirmed the presence of both $MoS_2$ and $WS_2$ and the presence of a bilayer heterostack. Since the $MoS_2$ flake was highly crystalline, the flake acted as a template for the growth of $WS_2$, resulting in the growth of the $WS_2$ flakes from the edges along the $MoS_2$ crystal direction.

The growth of $WS_2$ on top of the $MoS_2$ flakes made them convenient to contact for the production of heterostructure devices. 2-probe, back-gated devices were produced to study to behaviour of the heterostructure. The devices clearly are semiconducting with p-type behaviour and function as a photoconductor as predicted by DFT calculations. The characterisation of the photoconductor behaviour was only preliminary as there was no appropriate measurement setup. The reported devices are proof-of-concept and there is further scope for optimisation through improved device architecture as well as optimisation of the lithography process. Measurements under better controlled environments as well as photoconductive measurements would give more information on the properties of the heterostack.

To conclude, in this thesis optimisation of TMD and TMD heterostructure growth processes have been investigated and the effect of the growth substrate on the growth morphology and growth mechanism has been studied. The properties of both individual TMDs and TMD heterostructures have been thoroughly examined by spectroscopic techniques and surface microscopy. Electronic devices were created

which showed the electrical properties and possible applications of the materials. However, there is further scope for more in-depth study and characterisation of the materials as well as opportunities to further improve the synthesis parameters.

# Part VI

# Bibliography

# Bibliography


[1] G. Moore, *Electronics*, 1965, **38**, 33–35.

[2] R. P. Feynman, R. B. Leighton and M. L. Sands, *The Feynman Lectures on Physics*, Caltech.Edu, 1963, vol. 2, p. 1376.

[3] K. S. Novoselov, D. Jiang, F. Schedin, T. J. Booth, V. V. Khotkevich, S. V. Morozov and A. K. Geim, *Proc. Natl. Acad. Sci. U. S. A.*, 2005, **102**, 10451–10453.

[4] P. R. Wallace, *Phys. Rev.*, 1947, **71**, 622–634.

[5] K. S. Novoselov, A. K. Geim, S. V. Morozov, D. Jiang, Y. Zhang, S. V. Dubonos, I. V. Grigorieva and A. A. Firsov, *Science (80-. ).*, 2004, **306**, 666–669.

[6] S. Fujii and T. Enoki, *Acc. Chem. Res.*, 2012, **46**, 2202–2210.

[7] K. S. Kim, Y. Zhao, H. Jang, S. Y. Lee, J. M. Kim, K. S. Kim, J.-H. Ahn, P. Kim, J.-Y. Choi and B. H. Hong, *Nature*, 2009, **457**, 706–710.

[8] C. Lee, X. Wei, J. W. Kysar and J. Hone, *Science (80-. ).*, 2008, **321**, 385–388.

[9] A. a. Balandin, S. Ghosh, W. Bao, I. Calizo, D. Teweldebrhan, F. Miao and C. N. Lau, *Nano Lett.*, 2008, **8**, 902–907.

[10] K. Bolotin, K. Sikes, Z. Jiang, M. Klima, G. Fudenberg, J. Hone, P. Kim and H. Stormer, *Solid State Commun.*, 2008, **146**, 351–355.

[11] L. Banszerus, M. Schmitz, S. Engels, J. Dauber, M. Oellers, F. Haupt, K. Watanabe, T. Taniguchi, B. Beschoten and C. Stampfer, *Sci. Adv.*, 2015, **1**, e1500222–e1500222.

[12] A. H. Woomer, T. W. Farnsworth, J. Hu, R. A. Wells, C. L. Donley and S. C. Warren, *ACS Nano*, 2015, **9**, 8869–8884.

[13] V. Tran, R. Soklaski, Y. Liang and L. Yang, *Phys. Rev. B*, 2014, **89**, 235319.

[14] B. Li, C. Lai, G. Zeng, D. Huang, L. Qin, M. Zhang, M. Cheng, X. Liu, H. Yi, C. Zhou, F. Huang, S. Liu and Y. Fu, *Small*, 2019, **15**, 1804565.

[15] M. Pumera and Z. Sofer, *Adv. Mater.*, 2017, **29**, 1605299.

[16] M. Chhowalla, H. S. Shin, G. Eda, L.-j. Li, K. P. Loh and H. Zhang, *Nat. Chem.*, 2013, **5**, 263–275.

[17] Q. H. Wang, K. Kalantar-Zadeh, A. Kis, J. N. Coleman and M. S. Strano, *Nat. Nanotechnol.*, 2012, **7**, 699–712.

[18] B. Radisavljevic, A. Radenovic, J. Brivio, V. Giacometti and A. Kis, *Nat. Nanotechnol.*, 2011, **6**, 147–150.

[19] D. a. C. Brownson, D. K. Kampouris and C. E. Banks, *Chem. Soc. Rev.*, 2012, **41**, 6944–6976.

[20] X. Sang, X. Li, W. Zhao, J. Dong, C. M. Rouleau, D. B. Geohegan, F. Ding, K. Xiao and R. R. Unocic, *Nat. Commun.*, 2018, **9**, 2051.

[21] L. Lin, P. Sherrell, Y. Liu, W. Lei, S. Zhang, H. Zhang, G. G. Wallace and J. Chen, *Adv. Energy Mater.*, 2020, **10**, 1903870.

[22] M. Ye, D. Winslow, D. Zhang, R. Pandey and Y. Yap, *Photonics*, 2015, **2**, 288–307.

[23] C. Ataca, H. {\c S}ahin, E. Aktürk and S. Ciraci, *J. Phys. Chem. C*, 2011, **115**, 3934–3941.

[24] K. Kobayashi and J. Yamauchi, *Phys. Rev. B*, 1995, **51**, 17085–17095.

[25] V. Varshney, S. S. Patnaik, C. Muratore, A. K. Roy, A. A. Voevodin and B. L. Farmer, *Comput. Mater. Sci.*, 2010, **48**, 101–108.

[26] A. Castellanos-Gomez, M. Poot, G. A. Steele, H. S. J. van der Zant, N. Agraït and G. Rubio-Bollinger, *Adv. Mater.*, 2012, **24**, 772–775.

[27] A. C. Loheac, J. Braun, J. E. Drut and D. Roscher, *Phys. Rev. A*, 2015, **92**, 063609.

[28] S. Das, M. Kim, J.-w. Lee and W. Choi, *Crit. Rev. Solid State Mater. Sci.*, 2014, **39**, 231–252.

[29] Y. Wang, L. Li, W. Yao, S. Song, J. T. Sun, J. Pan, X. Ren, C. Li, E. Okunishi, Y. Q. Wang, E. Wang, Y. Shao, Y. Y. Zhang, H. T. Yang, E. F. Schwier, H. Iwasawa, K. Shimada, M. Taniguchi, Z. Cheng, S. Zhou, S. Du, S. J. Pennycook, S. T. Pantelides and H. J. Gao, *Nano Lett.*, 2015, **15**, 4013–4018.

[30] X. Ling, H. Wang, S. Huang, F. Xia and M. S. Dresselhaus, *Proc. Natl. Acad. Sci.*, 2015, **112**, 4523–4530.

[31] A. Splendiani, L. Sun, Y. Zhang, T. Li, J. Kim, C.-Y. Chim, G. Galli and F. Wang, *Nano Lett.*, 2010, **10**, 1271–1275.

[32] K. F. Mak, C. Lee, J. Hone, J. Shan and T. F. Heinz, *Phys. Rev. Lett.*, 2010, **105**, 136805.

[33] S. Balendhran, S. Walia, H. Nili, J. Z. Ou, S. Zhuiykov, R. B. Kaner, S. Sriram, M. Bhaskaran and K. Kalantar-zadeh, *Adv. Funct. Mater.*, 2013, **23**, 3952–3970.

[34] A. Castellanos-Gomez, M. Buscema, R. Molenaar, V. Singh, L. Janssen, H. S. J. van der Zant and G. A. Steele, *2D Mater.*, 2014, **1**, 011002.

[35] Y. Zhang, Q. Ji, G.-F. Han, J. Ju, J. Shi, D. Ma, J. Sun, Y. Zhang, M. Li, X.-Y. Lang, Y. Zhang and Z. Liu, *ACS Nano*, 2014, **8**, 8617–8624.

[36] J. Huang, L. Yang, D. Liu, J. Chen, Q. Fu, Y. Xiong, F. Lin and B. Xiang, *Nanoscale*, 2015, **7**, 4193–4198.

[37] C. Lee, H. Yan, L. Brus, T. Heinz, J. Hone and S. Ryu, *ACS Nano*, 2010, **4**, 2695–2700.

[38] M. S. Fuhrer and J. Hone, *Nat. Nanotechnol.*, 2013, **8**, 146–147.

[39] B. Radisavljevic and A. Kis, *Nat. Mater.*, 2013, **12**, 815–820.

[40] V. Podzorov, M. E. Gershenson, C. Kloc, R. Zeis and E. Bucher, *Appl. Phys. Lett.*, 2004, **84**, 3301–3303.

[41] T. Georgiou, R. Jalil, B. D. Belle, L. Britnell, R. V. Gorbachev, S. V. Morozov, Y.-J. Kim, A. Gholinia, S. J. Haigh, O. Makarovsky, L. Eaves, L. a. Ponomarenko, A. K. Geim, K. S. Novoselov and A. Mishchenko, *Nat. Nanotechnol.*, 2013, **8**, 100–103.

[42] M. H. Tahersima and V. J. Sorger, *Nanotechnology*, 2015, **26**, 344005.

[43] N. Perea-López, A. L. Elías, A. Berkdemir, A. Castro-Beltran, H. R. Gutiérrez, S. Feng, R. Lv, T. Hayashi, F. López-Urías, S. Ghosh, B. Muchharla, S. Talapatra, H. Terrones and M. Terrones, *Adv. Funct. Mater.*, 2013, **23**, 5511–5517.

[44] W. Zhang, J.-k. Huang, C.-h. Chen, Y.-h. Chang, Y.-J. Cheng and L.-J. Li, *Adv. Mater.*, 2013, **25**, 3456–3461.

[45] B. W. H. Baugher, H. O. H. Churchill, Y. Yang and P. Jarillo-Herrero, *Nat. Nanotechnol.*, 2014, **9**, 262–267.

[46] L. Britnell, R. M. Ribeiro, A. Eckmann, R. Jalil, B. D. Belle, A. Mishchenko, Y.-J. Kim, R. V. Gorbachev, T. Georgiou, S. V. Morozov, A. N. Grigorenko, A. K. Geim, C. Casiraghi, A. H. C. Neto and K. S. Novoselov, *Science (80-. ).*, 2013, **340**, 1311–1314.

[47] S. Wi, H. Kim, M. Chen, H. Nam, L. J. Guo, E. Meyhofer and X. Liang, *ACS Nano*, 2014, **8**, 5270–5281.

[48] R. Ge, X. Wu, M. Kim, J. Shi, S. Sonde, L. Tao, Y. Zhang, J. C. Lee and D. Akinwande, *Nano Lett.*, 2018, **18**, 434–441.

[49] K. Lee, R. Gatensby, N. McEvoy, T. Hallam and G. S. Duesberg, *Adv. Mater.*, 2013, **25**, 6699–6702.

[50] M. A. Lukowski, A. S. Daniel, F. Meng, A. Forticaux, L. Li and S. Jin, *J. Am. Chem. Soc.*, 2013, **135**, 10274–10277.

[51] J. P. B. Silva, C. Almeida Marques, J. A. Moreira and O. Conde, *J. Mater. Chem. C*, 2017, **5**, 10353–10359.

[52] R. Ge, X. Wu, L. Liang, S. M. Hus, Y. Gu, E. Okogbue, H. Chou, J. Shi, Y. Zhang, S. K. Banerjee, Y. Jung, J. C. Lee and D. Akinwande, *Adv. Mater.*, 2021, **33**, 2007792.

[53] H. Li, L. Tao and J.-B. Xu, *J. Appl. Phys.*, 2021, **129**, 050902.

[54] N. Choudhary, J. Park, J. Y. Hwang, H.-S. Chung, K. H. Dumas, S. I. Khondaker, W. Choi and Y. Jung, *Sci. Rep.*, 2016, **6**, 25456.

[55] E. G. da Silveira Firmiano, A. C. Rabelo, C. J. Dalmaschio, A. N. Pinheiro, E. C. Pereira, W. H. Schreiner and E. R. Leite, *Adv. Energy Mater.*, 2014, **4**, 1301380.

[56] P. T. K. Loan, W. Zhang, C.-t. Lin, K.-h. Wei, L.-j. Li and C.-h. Chen, *Adv. Mater.*, 2014, **26**, 4838–4844.

[57] P. Bollella, G. Fusco, C. Tortolini, G. Sanzò, G. Favero, L. Gorton and R. Antiochia, *Biosens. Bioelectron.*, 2017, **89**, 152–166.

[58] C. Yim, K. Lee, N. McEvoy, M. O'Brien, S. Riazimehr, N. C. Berner, C. P. Cullen, J. Kotakoski, J. C. Meyer, M. C. Lemme and G. S. Duesberg, *ACS Nano*, 2016, **10**, 9550–9558.

[59] H. Medina, J.-G. Li, T.-Y. Su, Y.-W. Lan, S.-H. Lee, C.-W. Chen, Y.-Z. Chen, A. Manikandan, S.-H. Tsai, A. Navabi, X. Zhu, Y.-C. Shih, W.-S. Lin, J.-H. Yang, S. R. Thomas, B.-W. Wu, C.-H. Shen, J.-M. Shieh, H.-N. Lin, A. Javey, K. L. Wang and Y.-L. Chueh, *Chem. Mater.*, 2017, **29**, 1587–1598.

[60] K. Yang, X. Wang, H. Li, B. Chen, X. Zhang, S. Li, N. Wang, H. Zhang, X. Huang and W. Huang, *Nanoscale*, 2017, **9**, 5102–5109.

[61] J. B. Mc Manus, D. V. Horvath, M. P. Browne, C. P. Cullen, G. Cunningham, T. Hallam, K. Zhussupbekov, D. Mullarkey, C. Ó. Coileáin, I. V. Shvets, M. Pumera, G. S. Duesberg and N. McEvoy, *Nanotechnology*, 2020, **31**, 375601.

[62] W. Shockley, *Proc. IRE*, 1952, **40**, 1365–1376.

[63] K. Dawon, *Electric field controlled semiconductor device*, 1963.

[64] R. Dong and I. Kuljanishvili, *J. Vac. Sci. Technol. B, Nanotechnol. Microelectron. Mater. Process. Meas. Phenom.*, 2017, **35**, 030803.

[65] M. Van de Put, Eurocon 2013, 2013, pp. 2134–2139.

[66] M. Ek, B. M. Borg, A. W. Dey, B. Ganjipour, C. Thelander, L.-E. Wernersson and K. A. Dick, *Cryst. Growth Des.*, 2011, **11**, 4588–4593.

[67] D. Ercolani, F. Rossi, A. Li, S. Roddaro, V. Grillo, G. Salviati, F. Beltram and L. Sorba, *Nanotechnology*, 2009, **20**, 505605.

[68] J. Campbell, A. Dentai, C. Burrus and J. Ferguson, *Electron. Lett.*, 1980, **16**, 713.

[69] C. R. Dean, A. F. Young, I. Meric, C. Lee, L. Wang, S. Sorgenfrei, K. Watanabe, T. Taniguchi, P. Kim, K. L. Shepard and J. Hone, *Nat. Nanotechnol.*, 2010, **5**, 722–726.

[70] B. You, X. Wang, Z. Zheng and W. Mi, *Phys. Chem. Chem. Phys.*, 2016, **18**, 7381–7388.

[71] M. Yagmurcukardes, E. Torun, R. T. Senger, F. M. Peeters and H. Sahin, *Phys. Rev. B*, 2016, **94**, 195403.

[72] D. D. Vo, T. V. Vu, N. V. Hieu, N. N. Hieu, H. V. Phuc, N. T. T. Binh, L. T. T. Phuong, M. Idrees, B. Amin and C. V. Nguyen, *Phys. Chem. Chem. Phys.*, 2019, **21**, 25849–25858.

[73] W. Hu and J. Yang, *J. Mater. Chem. C*, 2017, **5**, 12289–12297.

[74] R. Yan, S. Fathipour, Y. Han, B. Song, S. Xiao, M. Li, N. Ma, V. Protasenko, D. a. Muller, D. Jena and H. G. Xing, *Nano Lett.*, 2015, **15**, 5791–5798.

[75] F. Chen, H. Ilatikhameneh, Y. Tan, D. Valencia, G. Klimeck and R. Rahman, *J. Phys. Conf. Ser.*, 2017, **864**, 012053.

[76] J. Lee, N. T. Duong, S. Bang, C. Park, D. A. Nguyen, H. Jeon, J. Jang, H. M. Oh and M. S. Jeong, *Nano Lett.*, 2020, **20**, 2370–2377.

[77] H. Fang, C. Battaglia, C. Carraro, S. Nemsak, B. Ozdol, J. S. Kang, H. A. Bechtel, S. B. Desai, F. Kronast, A. A. Unal, G. Conti, C. Conlon, G. K. Palsson, M. C. Martin, A. M. Minor, C. S. Fadley, E. Yablonovitch, R. Maboudian and A. Javey, *Proc. Natl. Acad. Sci.*, 2014, **111**, 6198–6202.

[78] E. Pomerantseva and Y. Gogotsi, *Nat. Energy*, 2017, **2**, 17089.

[79] J. Shi, R. Tong, X. Zhou, Y. Gong, Z. Zhang, Q. Ji, Y. Zhang, Q. Fang, L. Gu, X. Wang, Z. Liu and Y. Zhang, *Adv. Mater.*, 2016, **28**, 10664–10672.

[80] Y. Gong, J. Lin, X. Wang, G. Shi, S. Lei, Z. Lin, X. Zou, G. Ye, R. Vajtai, B. I. Yakobson, H. Terrones, M. Terrones, B. K. Tay, J. Lou, S. T. Pantelides, Z. Liu, W. Zhou and P. M. Ajayan, *Nat. Mater.*, 2014, **13**, 1135–1142.

[81] N. Huo, J. Kang, Z. Wei, S.-S. Li, J. Li and S.-H. Wei, *Adv. Funct. Mater.*, 2014, **24**, 7025–7031.

[82] Y. Xue, Y. Zhang, Y. Liu, H. Liu, J. Song, J. Sophia, J. Liu, Z. Xu, Q. Xu, Z. Wang, J. Zheng, Y. Liu, S. Li and Q. Bao, *ACS Nano*, 2016, **10**, 573–580.

[83] L. Wang, M. Tahir, H. Chen and J. B. Sambur, *Nano Lett.*, 2019, **19**, 9084–9094.

[84] C. Huang, S. Wu, A. M. Sanchez, J. J. P. Peters, R. Beanland, J. S. Ross, P. Rivera, W. Yao, D. H. Cobden and X. Xu, *Nat. Mater.*, 2014, **13**, 1096–1101.

[85] X. Huang, Z. Zeng and H. Zhang, *Chem. Soc. Rev.*, 2013, **42**, 1934.

[86] M. Velický, G. E. Donnelly, W. R. Hendren, S. McFarland, D. Scullion, W. J. I. DeBenedetti, G. C. Correa, Y. Han, A. J. Wain, M. A. Hines, D. A. Muller, K. S. Novoselov, H. D. Abruña, R. M. Bowman, E. J. G. Santos and F. Huang, *ACS Nano*, 2018, **12**, 10463–10472.

[87] J. N. Coleman, M. Lotya, A. O'Neill, S. D. Bergin, P. J. King, U. Khan, K. Young, A. Gaucher, S. De, R. J. Smith, I. V. Shvets, S. K. Arora, G. Stanton, H.-Y. Kim, K. Lee, G. T. Kim, G. S. Duesberg, T. Hallam, J. J. Boland, J. J. Wang, J. F. Donegan, J. C. Grunlan, G. Moriarty, A. Shmeliov, R. J. Nicholls, J. M. Perkins, E. M. Grieveson, K. Theuwissen, D. W. McComb, P. D. Nellist and V. Nicolosi, *Science (80-. ).*, 2011, **331**, 568–571.

[88] S. D. Bergin, V. Nicolosi, P. V. Streich, S. Giordani, Z. Sun, A. H. Windle, P. Ryan, N. P. P. Niraj, Z. T. T. Wang, L. Carpenter, W. J. Blau, J. J. Boland, J. P. Hamilton and J. N. Coleman, *Adv. Mater.*, 2008, **20**, 1876–1881.

[89] P. Kumar Srivastava and S. Ghosh, *Appl. Phys. Lett.*, 2013, **102**, 043102.

[90] A. G. Cano-Márquez, F. J. Rodríguez-Macías, J. Campos-Delgado, C. G. Espinosa-González, F. Tristán-López, D. Ramírez-González, D. A. Cullen, D. J. Smith, M. Terrones and Y. I. Vega-Cantú, *Nano Lett.*, 2009, **9**, 1527–1533.

[91] W.-S. Kuo, N.-H. Tai and T.-W. Chang, *Compos. Part A Appl. Sci. Manuf.*, 2013, **51**, 56–61.

[92] C. Backes, T. M. Higgins, A. Kelly, C. Boland, A. Harvey, D. Hanlon and J. N. Coleman, *Chem. Mater.*, 2017, **29**, 243–255.

[93] M. B. Dines, *Mater. Res. Bull.*, 1975, **10**, 287–291.

[94] P. Joensen, R. Frindt and S. Morrison, *Mater. Res. Bull.*, 1986, **21**, 457–461.

[95] T. Suntola, *Mater. Sci. Reports*, 1989, **4**, 261–312.

[96] R. Huang and A. H. Kitai, *J. Electron. Mater.*, 1993, **22**, 215–220.

[97] J. Aarik, A. Aidla, A.-A. Kiisler, T. Uustare and V. Sammelselg, *Thin Solid Films*, 1999, **340**, 110–116.

[98] D. Triyoso, R. Liu, D. Roan, M. Ramon, N. V. Edwards, R. Gregory, D. Werho, J. Kulik, G. Tam, E. Irwin, X.-D. Wang, L. B. La, C. Hobbs, R. Garcia, J. Baker, B. E. White and P. Tobin, *J. Electrochem. Soc.*, 2004, **151**, F220.

[99] A. Delabie, M. Caymax, B. Groven, M. Heyne, K. Haesevoets, J. Meersschaut, T. Nuytten, H. Bender, T. Conard, P. Verdonck, S. Van Elshocht, S. De Gendt, M. Heyns, K. Barla, I. Radu and A. Thean, *Chem. Commun.*, 2015, **51**, 15692–15695.

[100] K. Haesevoets, B. Groven, M. Heyne and A. Delabie, *Master's dissertation*, KULeuven, 2015.

[101] R. Browning, P. Padigi, R. Solanki, D. J. Tweet, P. Schuele and D. Evans, *Mater. Res. Express*, 2015, **2**, 35006.

[102] R. Gatensby, N. McEvoy, K. Lee, T. Hallam, N. C. Berner, E. Rezvani, S. Winters, M. O'Brien and G. S. Duesberg, *Appl. Surf. Sci.*, 2014, **297**, 139–146.

[103] D. Chiappe, I. Asselberghs, S. Sutar, S. Iacovo, V. Afanas'ev, A. Stesmans, Y. Balaji, L. Peters, M. Heyne, M. Mannarino, W. Vandervorst, S. Sayan, C. Huyghebaert, M. Caymax, M. Heyns, S. De Gendt, I. Radu and A. Thean, *Adv. Mater. Interfaces*, 2016, **3**, 1500635.

[104] Y. Yu, C. Li, Y. Liu, L. Su, Y. Zhang and L. Cao, *Sci. Rep.*, 2013, **3**, 1866.

[105] Y. Zhan, Z. Liu, S. Najmaei, P. M. Ajayan and J. Lou, *Small*, 2012, **8**, 966–971.

[106] Y. H. Lee, X. Q. Zhang, W. Zhang, M. T. Chang, C. T. Lin, K. D. Chang, Y. C. Yu, J. T. W. Wang, C. S. Chang, L. J. Li and T. W. Lin, *Adv. Mater.*, 2012, **24**, 2320–2325.

[107] J.-K. Huang, J. Pu, C.-L. Hsu, M.-H. Chiu, Z.-Y. Juang, Y.-H. Chang, W.-H. Chang, Y. Iwasa, T. Takenobu and L.-J. Li, *ACS Nano*, 2014, **8**, 923–930.

[108] K. N. Kang, K. Godin and E.-h. Yang, *Sci. Rep.*, 2015, **5**, 13205.

[109] T. Tsirlina, Y. Feldman, M. Homyonfer, J. Sloan, J. L. Hutchison and R. Tenne, *Fuller. Sci. Technol.*, 1998, **6**, 157–165.

[110] M. Kim, J. Seo, J. Kim, J. S. Moon, J. Lee, J.-H. Kim, J. Kang and H. Park, *ACS Nano*, 2021, **15**, 3038–3046.

[111] S. Wagner, C. Yim, N. McEvoy, S. Kataria, V. Yokaribas, A. Kuc, S. Pindl, C.-P. Fritzen, T. Heine, G. S. Duesberg and M. C. Lemme, *Nano Lett.*, 2018, **18**, 3738–3745.

[112] X.-T. Yan and Y. Xu, *Chemical Vapour Deposition: An Integrated Engineering Design for Advanced Materials*, Springer Science & Business Media, 2010, p. 342.

[113] H. O. Pierson, *Handbook of Chemical Vapor Deposition, 2nd Edition: Principles, Technology and Applications*, William Andrew, 1999, 2nd edn., 1991, p. 506.

[114] *Springer Handbook of Crystal Growth*, ed. G. Dhanaraj, K. Byrappa, V. Prasad and M. Dudley, Springer Berlin Heidelberg, Berlin, Heidelberg, 2010.

[115] A. M. van der Zande, P. Y. Huang, D. A. Chenet, T. C. Berkelbach, Y. You, G.-H. Lee, T. F. Heinz, D. R. Reichman, D. A. Muller and J. C. Hone, *Nat. Mater.*, 2013, **12**, 554–561.

[116] D. Dumcenco, D. Ovchinnikov, K. Marinov, P. Lazić, M. Gibertini, N. Marzari, O. L. Sanchez, Y.-c. Kung, D. Krasnozhon, M.-w. Chen, S. Bertolazzi, P. Gillet, A. Fontcuberta i Morral, A. Radenovic and A. Kis, *ACS Nano*, 2015, **9**, 4611–4620.

[117] L. Peters, C. Ó Coileáin, P. Dluzynski, R. Siris, G. S. Duesberg and N. McEvoy, *Phys. status solidi*, 2020, **217**, 2000073.

[118] J. Lin, S. Monaghan, N. Sakhuja, F. Gity, R. K. Jha, E. M. Coleman, J. Connolly, C. P. Cullen, L. A. Walsh, T. Mannarino, M. Schmidt, B. Sheehan, G. S. Duesberg, N. McEvoy, N. Bhat, P. K. Hurley, I. M. Povey and S. Bhattacharjee, *2D Mater.*, 2020, **8**, 025008.

[119] J. Wilson and A. Yoffe, *Adv. Phys.*, 1969, **18**, 193–335.

[120] M. Volmer and A. Weber, *Zeitschrift Fur Phys. Chemie*, 1926, 277–301.

[121] F. C. Frank and J. H. van der Merwe, *Proc. R. Soc. London A Math. Phys. Eng. Sci.*, 1949, **198**, 216–225.

[122] I. N. Stranski and L. Krastanov, *Abhandlungen der Math. Klasse IIb. Akad. der Wissenschaften Wien.*, 1938, **148**, 797–810.

[123] S. A. Kukushkin and A. V. Osipov, in *Encycl. Nanosci. Nanotechnol.*, American Scientific Publishers, 2004, vol. 8, pp. 113–136.

[124] J. Jeon, S. K. Jang, S. M. Jeon, G. Yoo, Y. H. Jang, J.-H. Park and S. Lee, *Nanoscale*, 2015, **7**, 1688–1695.

[125] L. Liang, W. Hu, Z. Xue and J.-W. Shen, *FlatChem*, 2017, **2**, 8–14.

[126] S. Najmaei, Z. Liu, W. Zhou, X. Zou, G. Shi, S. Lei, B. I. Yakobson, J.-C. Idrobo, P. M. Ajayan and J. Lou, *Nat. Mater.*, 2013, **12**, 754–759.

[127] J. D. Cain, F. Shi, J. Wu and V. P. Dravid, *ACS Nano*, 2016, **10**, 5440–5445.

[128] R. Addou, S. McDonnell, D. Barrera, Z. Guo, A. Azcatl, J. Wang, H. Zhu, C. L. Hinkle, M. Quevedo-Lopez, H. N. Alshareef, L. Colombo, J. W. P. Hsu and R. M. Wallace, *ACS Nano*, 2015, **9**, 9124–9133.

[129] H. Kim, D. Ovchinnikov, D. Deiana, D. Unuchek and A. Kis, *Nano Lett.*, 2017, **17**, 5056–5063.

[130] T. Roy, M. Tosun, X. Cao, H. Fang, D.-H. Lien, P. Zhao, Y.-Z. Chen, Y.-L. Chueh, J. Guo and A. Javey, *ACS Nano*, 2015, **9**, 2071–2079.

[131] F. Withers, O. Del Pozo-Zamudio, A. Mishchenko, A. P. Rooney, A. Gholinia, K. Watanabe, T. Taniguchi, S. J. Haigh, A. K. Geim, A. I. Tartakovskii and K. S. Novoselov, *Nat. Mater.*, 2015, **14**, 301–306.

[132] F. M. Pesci, M. S. Sokolikova, C. Grotta, P. C. Sherrell, F. Reale, K. Sharda, N. Ni, P. Palczynski and C. Mattevi, *ACS Catal.*, 2017, **7**, 4990–4998.

[133] X. Hong, J. Kim, S.-F. Shi, Y. Zhang, C. Jin, Y. Sun, S. Tongay, J. Wu, Y. Zhang and F. Wang, *Nat. Nanotechnol.*, 2014, **9**, 682–686.

[134] A. Jain, P. Bharadwaj, S. Heeg, M. Parzefall, T. Taniguchi, K. Watanabe and L. Novotny, *Nanotechnology*, 2018, **29**, 265203.

[135] Y. Yoo, Z. P. Degregorio and J. E. Johns, *J. Am. Chem. Soc.*, 2015, **137**, 14281–14287.

[136] Y. Zhang, L. Yin, J. Chu, T. A. Shifa, J. Xia, F. Wang, Y. Wen, X. Zhan, Z. Wang and J. He, *Adv. Mater.*, 2018, **30**, 1803665.

[137] Y. Yu, S. Hu, L. Su, L. Huang, Y. Liu, Z. Jin, A. A. Purezky, D. B. Geohegan, K. W. Kim, Y. Zhang and L. Cao, *Nano Lett.*, 2015, **15**, 486–491.

[138] A. Sharma, R. Mahlouji, L. Wu, M. A. Verheijen, V. Vandalon, S. Balasubramanyam, J. P. Hofmann, W. M. M. (Erwin) Kessels and A. A. Bol, *Nanotechnology*, 2020, **31**, 255603.

[139] J. Zhu, W. Li, R. Huang, L. Ma, H. Sun, J.-H. Choi, L. Zhang, Y. Cui and G. Zou, *J. Am. Chem. Soc.*, 2020, **142**, 16276–16284.

[140] J. Deng, K. Dong, P. Yang, Y. Peng, G. Ju, J. Hu, G. M. Chow and J. Chen, *J. Magn. Magn. Mater.*, 2018, **446**, 125–134.

[141] M. M. Benameur, B. Radisavljevic, J. S. Héron, S. Sahoo, H. Berger and a. Kis, *Nanotechnology*, 2011, **22**, 125706.

[142] J. Czochralski, *Zeitschrift für Phys. Chemie*, 1918, **92**, 219–221.

[143] S. Hao, B. Yang and Y. Gao, *J. Chem. Phys.*, 2016, **145**, 084704.

[144] J. Cheng, T. Jiang, Q. Ji, Y. Zhang, Z. Li, Y. Shan, Y. Zhang, X. Gong, W. Liu and S. Wu, *Adv. Mater.*, 2015, **27**, 4069–4074.

[145] E. R. Dobrovinskaya, L. A. Lytvynov and V. Pishchik, *Sapphire*, Springer US, Boston, MA, 2009.

[146] I. Akasaki, H. Amano, Y. Koide, K. Hiramatsu and N. Sawaki, *J. Cryst. Growth*, 1989, **98**, 209–219.

[147] P. E. Dyer, S. R. Jackson, P. H. Key, W. J. Metheringham and M. J. Schmidt, *Appl. Surf. Sci.*, 1996, **96-98**, 849–854.

[148] I. Stará, V. Nehasil and V. Matolin, *Surf. Sci.*, 1996, **365**, 69–77.

[149] M. D. Craven, S. H. Lim, F. Wu, J. S. Speck and S. P. DenBaars, *Appl. Phys. Lett.*, 2002, **81**, 469–471.

[150] J.-C. Villegirr, N. Hadacek, S. Monso, B. Delnet, A. Roussy, P. Febvre, G. Lamura and J.-Y. Laval, *IEEE Trans. Appiled Supercond.*, 2001, **11**, 68–71.

[151] X. Zhang, Z. Y. Al Balushi, F. Zhang, T. H. Choudhury, S. M. Eichfeld, N. Alem, T. N. Jackson, J. A. Robinson and J. M. Redwing, *J. Electron. Mater.*, 2016, **45**, 6273–6279.

[152] J. Park, W. Lee, T. Choi, S.-H. Hwang, J. M. Myoung, J.-H. Jung, S.-H. Kim and H. Kim, *Nanoscale*, 2015, **7**, 1308–1313.

[153] T. T. Kodas and M. J. Hampden-Smith, *The Chemistry of Metal CVD*, John Wiley & Sons, 2008, p. 562.

[154] S. M. Eichfeld, L. Hossain, Y.-C. Lin, A. F. Piasecki, B. Kupp, A. G. Birdwell, R. A. Burke, N. Lu, X. Peng, J. Li, A. Azcatl, S. McDonnell, R. M. Wallace, M. J. Kim, T. S. Mayer, J. M. Redwing and J. A. Robinson, *ACS Nano*, 2015, **9**, 2080–2087.

[155] C. J. Carmalt, I. P. Parkin and E. S. Peters, *Polyhedron*, 2003, **22**, 1263–1269.

[156] F. Bozheyev, D. Friedrich, M. Nie, M. Rengachari and K. Ellmer, *Phys. status solidi*, 2014, **211**, 2013–2019.

[157] M. Leewenhoeck and R. de Graaf, *Philos. Trans. R. Soc. London*, 1673, **8**, 6037–6038.

[158] J. R. Ferraro, K. Nakamoto and C. W. Brown, *Introductory Raman Spectroscopy*, Elsevier, 2003, pp. 1–434.

[159] T. Dieing, O. Hollricher and J. Toporski, *Confocal Raman Spectroscopy*, 2010.

[160] L. Boltzmann, *Über die Beziehung zwischen dem zweiten Hauptsatze des mechanischen Wärmetheorie und der Wahrscheinlichkeitsrechnung, respective den Sätzen über das Wärmegleichgewicht*, Kk Hof-und Staatsdruckerei, 1877.

[161] A. Molina-Sánchez and L. Wirtz, *Phys. Rev. B*, 2011, **84**, 155413.

[162] Y. Li, Y. Rao, K. F. Mak, Y. You, S. Wang, C. R. Dean and T. F. Heinz, *Nano Lett.*, 2013, **13**, 3329–3333.

[163] P. Tonndorf, R. Schmidt, P. Böttger, X. Zhang, J. Börner, A. Liebig, M. Albrecht, C. Kloc, O. Gordan, D. R. T. Zahn, S. Michaelis de Vasconcellos and R. Bratschitsch, *Opt. Express*, 2013, **21**, 4908.

[164] H. Li, Q. Zhang, C. C. R. Yap, B. K. Tay, T. H. T. Edwin, A. Olivier and D. Baillargeat, *Adv. Funct. Mater.*, 2012, **22**, 1385–1390.

[165] S. Mignuzzi, A. J. Pollard, N. Bonini, B. Brennan, I. S. Gilmore, M. A. Pimenta, D. Richards and D. Roy, *Phys. Rev. B*, 2015, **91**, 195411.

[166] B. Chakraborty, A. Bera, D. V. S. Muthu, S. Bhowmick, U. V. Waghmare and A. K. Sood, *Phys. Rev. B*, 2012, **85**, 161403.

[167] C. Rice, R. J. Young, R. Zan, U. Bangert, D. Wolverson, T. Georgiou, R. Jalil and K. S. Novoselov, *Phys. Rev. B*, 2013, **87**, 081307.

[168] C. R. Zhu, G. Wang, B. L. Liu, X. Marie, X. F. Qiao, X. Zhang, X. X. Wu, H. Fan, P. H. Tan, T. Amand and B. Urbaszek, *Phys. Rev. B*, 2013, **88**, 121301.

[169] P. Maguire, D. S. Fox, Y. Zhou, Q. Wang, M. O'Brien, J. Jadwiszczak, C. P. Cullen, J. McManus, S. Bateman, N. McEvoy, G. S. Duesberg and H. Zhang, *Phys. Rev. B*, 2018, **98**, 134109.

[170] M. Buscema, G. A. Steele, H. S. J. van der Zant and A. Castellanos-Gomez, *Nano Res.*, 2014, **7**, 561–571.

[171] J. Tang, Z. Wei, Q. Wang, Y. Wang, B. Han, X. Li, B. Huang, M. Liao, J. Liu, N. Li, Y. Zhao, C. Shen, Y. Guo, X. Bai, P. Gao, W. Yang, L. Chen, K. Wu, R. Yang, D. Shi and G. Zhang, *Small*, 2020, **16**, 2004276.

[172] Y. Y. Hui, X. Liu, W. Jie, N. Y. Chan, J. Hao, Y.-T. Hsu, L.-J. Li, W. Guo and S. P. Lau, *ACS Nano*, 2013, **7**, 7126–7131.

[173] A. Castellanos-Gomez, R. Roldán, E. Cappelluti, M. Buscema, F. Guinea, H. S. J. van der Zant and G. A. Steele, *Nano Lett.*, 2013, **13**, 5361–5366.

[174] S. Luo, C. P. Cullen, G. Guo, J. Zhong and G. S. Duesberg, *Appl. Surf. Sci.*, 2020, **508**, 145126.

[175] M. O'Brien, N. McEvoy, D. Hanlon, T. Hallam, J. N. Coleman and G. S. Duesberg, *Sci. Rep.*, 2016, **6**, 19476.

[176] H. Zeng, B. Zhu, K. Liu, J. Fan, X. Cui and Q. M. Zhang, *Phys. Rev. B*, 2012, **86**, 241301.

[177] V. Senthilkumar, L. C. Tam, Y. S. Kim, Y. Sim, M.-J. Seong and J. I. Jang, *Nano Res.*, 2014, **7**, 1759–1768.

[178] T. Korn, S. Heydrich, M. Hirmer, J. Schmutzler and C. Schüller, *Appl. Phys. Lett.*, 2011, **99**, 102109.

[179] F. Cadiz, E. Courtade, C. Robert, G. Wang, Y. Shen, H. Cai, T. Taniguchi, K. Watanabe, H. Carrere, D. Lagarde, M. Manca, T. Amand, P. Renucci, S. Tongay, X. Marie and B. Urbaszek, *Phys. Rev. X*, 2017, **7**, 021026.

[180] H. J. Conley, B. Wang, J. I. Ziegler, R. F. Haglund, S. T. Pantelides and K. I. Bolotin, *Nano Lett.*, 2013, **13**, 3626–3630.

[181] Y. Hu, F. Zhang, M. Titze, B. Deng, H. Li and G. J. Cheng, *Nanoscale*, 2018, **10**, 5717–5724.

[182] S. Tongay, J. Suh, C. Ataca, W. Fan, A. Luce, J. S. Kang, J. Liu, C. Ko, R. Raghunathanan, J. Zhou, F. Ogletree, J. Li, J. C. Grossman and J. Wu, *Sci. Rep.*, 2013, **3**, 2657.

[183] Z. Lin, B. R. Carvalho, E. Kahn, R. Lv, R. Rao, H. Terrones, M. A. Pimenta and M. Terrones, *2D Mater.*, 2016, **3**, 022002.

[184] M. Amani, P. Taheri, R. Addou, G. H. Ahn, D. Kiriya, D.-H. Lien, J. W. Ager, R. M. Wallace and A. Javey, *Nano Lett.*, 2016, **16**, 2786–2791.

[185] H. Hertz, *Ann. der Phys. und Chemie*, 1887, **267**, 983–1000.

[186] A. Einstein, *Ann. Phys.*, 1905, **322**, 132–148.

[187] G. Binnig, C. F. Quate and C. Gerber, *Phys. Rev. Lett.*, 1986, **56**, 930–933.

[188] J. Lennard-Jones, *Proc. R. Soc. London. Ser. A, Contain. Pap. a Math. Phys. Character*, 1924, **106**, 441–462.

[189] K. Xu, W. Sun, Y. Shao, F. Wei, X. Zhang, W. Wang and P. Li, *Nanotechnol. Rev.*, 2018, **7**, 605–621.

[190] N. Lockyer and J. Vickerman, in *Ref. Modul. Mater. Sci. Mater. Eng.*, Elsevier, 2016, ch. SIMS, Time, pp. 8624–8628.

[191] T. Young, *Philos. Trans. R. Soc. London*, 1805, **95**, 65–87.

[192] C. J. Van Oss, M. K. Chaudhury and R. J. Good, *Chem. Rev.*, 1988, **88**, 927–941.

[193] E. Lifshitz, *Sov. Phys. JETP*, 1956, **2**, 73.

[194] 2011 Intelligent Micro Patterning, *SF-100 Platform Manual*, Intelligent Micro Patterning, LLC, 2012, p. 251.

[195] M. Politou, I. Asselberghs, B. Soree, C. S. Lee, S. Sayan, D. Lin, P. Pashaei, C. Huyghebaert, P. Raghavan, I. Radu, Z. Tokei, S. De Gendt and M. Heyns, *Microelectron. Eng.*, 2016, **156**, 131–135.

[196] S. Adam, E. H. Hwang, V. M. Galitski and S. Das Sarma, *Proc. Natl. Acad. Sci. U. S. A.*, 2007, **104**, 18392–7.

[197] C. M. Smyth, R. Addou, S. McDonnell, C. L. Hinkle and R. M. Wallace, *2D Mater.*, 2017, **4**, 025084.

[198] W. Liu, J. Kang, D. Sarkar, Y. Khatami, D. Jena and K. Banerjee, *Nano Lett.*, 2013, **13**, 1983–1990.

[199] Z. Jin, X. Li, J. T. Mullen and K. W. Kim, *Phys. Rev. B*, 2014, **90**, 045422.

[200] H. Fang, S. Chuang, T. C. Chang, K. Takei, T. Takahashi and A. Javey, *Nano Lett.*, 2012, **12**, 3788–3792.

[201] H.-J. Chuang, X. Tan, N. J. Ghimire, M. M. Perera, B. Chamlagain, M. M.-C. Cheng, J. Yan, D. Mandrus, D. Tománek and Z. Zhou, *Nano Lett.*, 2014, **14**, 3594–3601.

[202] A. N. Zelikman, Y. U. O. Kolchin and Y. U. M. Golutvin, *Russ. J. Phys. Chem*, 1983, **57**, 519–521.

[203] J. Zhou, J. Lin, X. Huang, Y. Zhou, Y. Chen, J. Xia, H. Wang, Y. Xie, H. Yu, J. Lei, D. Wu, F. Liu, Q. Fu, Q. Zeng, C.-H. Hsu, C. Yang, L. Lu, T. Yu, Z. Shen, H. Lin, B. I. Yakobson, Q. Liu, K. Suenaga, G. Liu and Z. Liu, *Nature*, 2018, **556**, 355–359.

[204] B. Liu, M. Fathi, L. Chen, A. Abbas, Y. Ma and C. Zhou, *ACS Nano*, 2015, **9**, 6119–6127.

[205] K. Park, Y. Kim, J.-g. Song, S. J. Kim, C. W. Lee and G. H. Ryu, *2D Mater.*, 2016, **3**, 014004.

[206] H. Zhou, C. Wang, J. C. Shaw, R. Cheng, Y. Chen, X. Huang, Y. Liu, N. O. Weiss, Z. Lin, Y. Huang and X. Duan, *Nano Lett.*, 2015, **15**, 709–713.

[207] H.-W. Cao, H.-M. Zhao, X. Xin, P.-Z. Shao, H.-Y. Qi, M.-Q. Jian, Y.-Y. Zhang, Y. Yang and T.-L. Ren, *Mod. Phys. Lett. B*, 2016, **30**, 1650267.

[208] M. O'Brien, N. McEvoy, T. Hallam, H.-Y. Kim, N. C. Berner, D. Hanlon, K. Lee, J. N. Coleman and G. S. Duesberg, *Sci. Rep.*, 2015, **4**, 7374.

[209] Y. Rong, Y. Fan, A. Leen Koh, A. W. Robertson, K. He, S. Wang, H. Tan, R. Sinclair and J. H. Warner, *Nanoscale*, 2014, **6**, 12096–12103.

[210] A. Thangaraja, S. M. Shinde, G. Kalita and M. Tanemura, *Appl. Phys. Lett.*, 2016, **108**, 053104.

[211] J. Haigh, G. Burkhardt and K. Blake, *J. Cryst. Growth*, 1995, **155**, 266–271.

[212] S. Dhar, V. Kranthi Kumar, T. H. Choudhury, S. A. Shivashankar and S. Raghavan, *Phys. Chem. Chem. Phys.*, 2016, **18**, 14918–14926.

[213] S. Li, S. Wang, D.-M. Tang, W. Zhao, H. Xu, L. Chu, Y. Bando, D. Golberg and G. Eda, *Appl. Mater. Today*, 2015, **1**, 60–66.

[214] Z. Wang, Q. Huang, P. Chen, J. Wang, Y. Lu, S. Zhang, X. Liang and L. Wang, *Jpn. J. Appl. Phys.*, 2017, **56**, 080303.

[215] V. Khodzhemirov, V. Yevdokimova and V. Cherednichenko, *Polym. Sci. U.S.S.R.*, 1976, **18**, 581–588.

[216] S. A. Wood, *Geochim. Cosmochim. Acta*, 1992, **56**, 1827–1836.

[217] Luxel, *VAPOR PRESSURE CHART*, 2013, `https://luxel.com/wp-content/uploads/2013/04/Luxel-Vapor-Pressure-Chart.pdf`.

[218] J. A. Robinson, S. Eichfeld, Y.-C. Lin, N. Lu and M. Kim, *Microsc. Microanal.*, 2015, **21**, 101–102.

[219] D. G. Kim, H. C. Lee and J. Y. Lee, *J. Mater. Sci.*, 1993, **28**, 6704–6708.

[220] W. Zhao, Z. Ghorannevis, L. Chu, M. Toh, C. Kloc, P.-H. Tan and G. Eda, *ACS Nano*, 2013, **7**, 791–797.

[221] S.-Y. Chen, C. Zheng, M. S. Fuhrer and J. Yan, *Nano Lett.*, 2015, **15**, 2526–2532.

[222] H. Sahin, S. Tongay, S. Horzum, W. Fan, J. Zhou, J. Li, J. Wu and F. M. Peeters, *Phys. Rev. B*, 2013, **87**, 165409.

[223] N. Onofrio, D. Guzman and A. Strachan, *J. Appl. Phys.*, 2017, **122**, 185102.

[224] F. Giannazzo, G. Greco, E. Schilirò, S. Di Franco, I. Deretzis, G. Nicotra, A. La Magna and F. Roccaforte, *AIP Conf. Proc.*, 2018, **1990**, 020008.

[225] S. Das and J. Appenzeller, *Appl. Phys. Lett.*, 2013, **103**, 103501.

[226] D. Li, X. Wang, Y. Chen, S. Zhu, F. Gong, G. Wu, C. Meng, L. Liu, L. Wang, T. Lin, S. Sun, H. Shen, X. Wang, W. Hu, J. Wang, J. Sun, X. Meng and J. Chu, *Nanotechnology*, 2018, **29**, 105202.

[227] S. T. Lee, I. T. Cho, W. M. Kang, B. G. Park and J.-H. Lee, *Nano Converg.*, 2016, **3**, 31.

[228] W. Zhao, Z. Ghorannevis, K. K. Amara, J. R. Pang, M. Toh, X. Zhang, C. Kloc, P. H. Tan and G. Eda, *Nanoscale*, 2013, **5**, 9677–9683.

[229] N. R. Pradhan, D. Rhodes, S. Memaran, J. M. Poumirol, D. Smirnov, S. Talapatra, S. Feng, N. Perea-Lopez, A. L. Elias, M. Terrones, P. M. Ajayan and L. Balicas, *Sci. Rep.*, 2015, **5**, 8979.

[230] A. Allain and A. Kis, *ACS Nano*, 2014, **8**, 7180–7185.

[231] P. R. Pudasaini, A. Oyedele, C. Zhang, M. G. Stanford, N. Cross, A. T. Wong, A. N. Hoffman, K. Xiao, G. Duscher, D. G. Mandrus, T. Z. Ward and P. D. Rack, *Nano Res.*, 2018, **11**, 722–730.

[232] L. Yu, A. Zubair, E. J. G. Santos, X. Zhang, Y. Lin, Y. Zhang and T. Palacios, *Nano Lett.*, 2015, **15**, 4928–4934.

[233] L. Kong, X. Zhang, Q. Tao, M. Zhang, W. Dang, Z. Li, L. Feng, L. Liao, X. Duan and Y. Liu, *Nat. Commun.*, 2020, **11**, 1866.

[234] F. Giubileo and A. Di Bartolomeo, *Prog. Surf. Sci.*, 2017, **92**, 143–175.

[235] P. M. Campbell, A. Tarasov, C. a. Joiner, M.-Y. Tsai, G. Pavlidis, S. Graham, W. J. Ready and E. M. Vogel, *Nanoscale*, 2016, **8**, 2268–2276.

[236] C. S. Boland, C. Ó. Coileáin, S. Wagner, J. B. McManus, C. P. Cullen, M. C. Lemme, G. S. Duesberg and N. McEvoy, *2D Mater.*, 2019, **6**, 045029.

[237] F. Urban, N. Martucciello, L. Peters, N. McEvoy and A. Di Bartolomeo, *Nanomaterials*, 2018, **8**, 901.

[238] A. Di Bartolomeo, F. Urban, M. Passacantando, N. McEvoy, L. Peters, L. Iemmo, G. Luongo, F. Romeo and F. Giubileo, *Nanoscale*, 2019, **11**, 1538–1548.

[239] W. Yang, G. Chen, Z. Shi, C.-C. Liu, L. Zhang, G. Xie, M. Cheng, D. Wang, R. Yang, D. Shi, K. Watanabe, T. Taniguchi, Y. Yao, Y. Zhang and G. Zhang, *Nat. Mater.*, 2013, **12**, 792–797.

[240] J. Xue, J. Sanchez-Yamagishi, D. Bulmash, P. Jacquod, A. Deshpande, K. Watanabe, T. Taniguchi, P. Jarillo-Herrero and B. J. LeRoy, *Nat. Mater.*, 2011, **10**, 282–285.

[241] M. Yankowitz, J. Xue, D. Cormode, J. D. Sanchez-Yamagishi, K. Watanabe, T. Taniguchi, P. Jarillo-Herrero, P. Jacquod and B. J. LeRoy, *Nat. Phys.*, 2012, **8**, 382–386.

[242] Q. Wang, P. Wu, G. Cao and M. Huang, *J. Phys. D. Appl. Phys.*, 2013, **46**, 505308.

[243] D. Dietzel, A. S. de Wijn, M. Vorholzer and A. Schirmeisen, *Nanotechnology*, 2018, **29**, 155702.

[244] M. T. Duffy, C. C. Wang, G. D. O'clock, S. H. McFarlane and P. J. Zanzucchi, *J. Electron. Mater.*, 1973, **2**, 359–372.

[245] R. D. Vispute, V. Talyansky, Z. Trajanovic, S. Choopun, M. Downes, R. P. Sharma, T. Venkatesan, M. C. Woods, R. T. Lareau, K. A. Jones and A. A. Iliadis, *Appl. Phys. Lett.*, 1997, **70**, 2735–2737.

[246] N. Kornblum, A. Katsman and B. Pokroy, *J. Phys. Chem. C*, 2019, **123**, 8770–8776.

[247] D. Ruzmetov, K. Zhang, G. Stan, B. Kalanyan, G. R. Bhimanapati, S. M. Eichfeld, R. A. Burke, P. B. Shah, T. P. O'Regan, F. J. Crowne, A. G. Birdwell, J. A. Robinson, A. V. Davydov and T. G. Ivanov, *ACS Nano*, 2016, **10**, 3580–3588.

[248] Z. Ma, S. Wang, Q. Deng, Z. Hou, X. Zhou, X. Li, F. Cui, H. Si, T. Zhai and H. Xu, *Small*, 2020, **16**, 2000596.

[249] K.-K. Liu, W. Zhang, Y.-H. Lee, Y.-C. Lin, M.-T. Chang, C.-Y. Su, C.-S. Chang, H. Li, Y. Shi, H. Zhang, C.-S. Lai and L.-J. Li, *Nano Lett.*, 2012, **12**, 1538–1544.

[250] Y. Shi, W. Zhou, A.-y. Lu, W. Fang, Y.-h. Lee, A. L. Hsu, S. M. Kim, K. K. Kim, H. Y. Yang, L.-J. Li, J.-C. Idrobo and J. Kong, *Nano Lett.*, 2012, **12**, 2784–2791.

[251] J. Shi, X. Zhang, D. Ma, J. Zhu, Y. Zhang, Z. Guo, Y. Yao, Q. Ji, X. Song, Y. Zhang, C. Li, Z. Liu, W. Zhu and Y. Zhang, *ACS Nano*, 2015, **9**, 4017–4025.

[252] X. Ling, *Nano Lett.*, 2014, **14**, 464–472.

[253] T. A. J. Loh and D. H. C. Chua, *ACS Appl. Mater. Interfaces*, 2014, **6**, 15966–15971.

[254] R. Varache, M. Darnon, M. Descazeaux, M. Martin, T. Baron and D. Muñoz, *Energy Procedia*, 2015, **77**, 493–499.

[255] A. Gudovskikh, K. Zelentsov, A. Baranov, D. Kudryashov, I. Morozov, E. Nikitina and J.-P. Kleider, *Energy Procedia*, 2016, **102**, 56–63.

[256] D. Kudryashov, A. Gudovskikh, A. Uvarov and E. Nikitina, *AIP Conf. Proc.*, 2018, **2012**, 040005.

[257] L. Zhang, Z. Lu, Y. Song, L. Zhao, B. Bhatia, K. R. Bagnall and E. N. Wang, *Nano Lett.*, 2019, **19**, 4745–4751.

[258] T. Soma and H. M. Kagaya, *EMIS Dataviews Ser.*, 1988, 33.

[259] K. Zhang, N. J. Borys, B. M. Bersch, G. R. Bhimanapati, K. Xu, B. Wang, K. Wang, M. Labella, T. A. Williams, M. A. Haque, E. S. Barnard, S. Fullerton-Shirey, P. J. Schuck and J. A. Robinson, *Sci. Rep.*, 2017, **7**, 16938.

[260] H. R. Gutiérrez, N. Perea-López, A. L. Elías, A. Berkdemir, B. Wang, R. Lv, F. López-Urías, V. H. Crespi, H. Terrones and M. Terrones, *Nano Lett.*, 2013, **13**, 3447–3454.

[261] J. Wang, B. Guo, Q. Zhao, C. Zhang, Q. Zhang and W. Zhai, *Ceram. Int.*, 2017, **43**, 10353–10360.

[262] F. Cuccureddu, S. Murphy, I. Shvets, M. Porcu, H. Zandbergen, N. Sidorov and S. Bozhko, *Surf. Sci.*, 2010, **604**, 1294–1299.

[263] M. Yoshimoto, T. Maeda, T. Ohnishi, H. Koinuma, O. Ishiyama, M. Shinohara, M. Kubo, R. Miura and A. Miyamoto, *Appl. Phys. Lett.*, 1995, **67**, 2615–2617.

[264] R. Verre, R. Sofin, V. Usov, K. Fleischer, D. Fox, G. Behan, H. Zhang and I. Shvets, *Surf. Sci.*, 2012, **606**, 1815–1820.

[265] S. Curiotto and D. Chatain, *Surf. Sci.*, 2009, **603**, 2688–2697.

[266] X. Zhang, X.-F. Qiao, W. Shi, J.-B. Wu, D.-S. Jiang and P.-H. Tan, *Chem. Soc. Rev.*, 2015, **44**, 2757–2785.

[267] G. Kusch, H. Li, P. R. Edwards, J. Bruckbauer, T. C. Sadler, P. J. Parbrook and R. W. Martin, *Appl. Phys. Lett.*, 2014, **104**, 092114.

[268] L. Pham Van, O. Kurnosikov and J. Cousty, *Surf. Sci.*, 1998, **411**, 263–271.

[269] K. Suenaga, H. G. Ji, Y.-C. Lin, T. Vincent, M. Maruyama, A. S. Aji, Y. Shiratsuchi, D. Ding, K. Kawahara, S. Okada, V. Panchal, O. Kazakova, H. Hibino, K. Suenaga and H. Ago, *ACS Nano*, 2018, **12**, 10032–10044.

[270] H. Ago, I. Tanaka, M. Tsuji, K.-i. Ikeda and S. Mizuno, *J. Phys. Chem. C*, 2008, **112**, 18350–18354.

[271] R. Pan, X.-L. Fan, H. Zhang and Y. Yang, *Comput. Mater. Sci.*, 2016, **122**, 118–125.

[272] S. Kim, M. S. Choi, D. Qu, C. H. Ra, X. Liu, M. Kim, Y. J. Song and W. J. Yoo, *2D Mater.*, 2016, **3**, 035002.

[273] X. Wang, H. Feng, Y. Wu and L. Jiao, *J. Am. Chem. Soc.*, 2013, **135**, 5304–5307.

[274] K. Simeonov and D. Lederman, *Surf. Sci.*, 2009, **603**, 232–236.

[275] M. Huth, K. Ritley, J. Oster, H. Dosch and H. Adrian, *Adv. Funct. Mater.*, 2002, **12**, 333.

[276] J. R. Heffelfinger, M. W. Bench and C. Carter, *Surf. Sci.*, 1995, **343**, L1161–L1166.

[277] J. R. Heffelfinger and C. Carter, *Surf. Sci.*, 1997, **389**, 188–200.

[278] T. Liang, S. Xie, Z. Huang, W. Fu, Y. Cai, X. Yang, H. Chen, X. Ma, H. Iwai, D. Fujita, N. Hanagata and M. Xu, *Adv. Mater. Interfaces*, 2017, **4**, 1600687.

[279] Q. Fu, W. Wang, L. Yang, J. Huang, J. Zhang and B. Xiang, *RSC Adv.*, 2015, **5**, 15795–15799.

[280] F. Giannazzo, M. Bosi, F. Fabbri, E. Schilirò, G. Greco and F. Roccaforte, *Phys. status solidi – Rapid Res. Lett.*, 2020, **14**, 1900393.

[281] A. Kozbial, X. Gong, H. Liu and L. Li, *Langmuir*, 2015, **31**, 8429–8435.

[282] A. P. S. Gaur, S. Sahoo, M. Ahmadi, S. P. Dash, M. J.-F. Guinel and R. S. Katiyar, *Nano Lett.*, 2014, **14**, 4314–4321.

[283] V. Nicolosi, M. Chhowalla, M. G. Kanatzidis, M. S. Strano and J. N. Coleman, *Science (80-. ).*, 2013, **340**, 1226419–1226419.

[284] N. McDevitt, J. Zabinski and M. Donley, *Thin Solid Films*, 1994, **240**, 76–81.

[285] T. Chowdhury, J. Kim, E. C. Sadler, C. Li, S. W. Lee, K. Jo, W. Xu, D. H. Gracias, N. V. Drichko, D. Jariwala, T. H. Brintlinger, T. Mueller, H.-G. Park and T. J. Kempa, *Nat. Nanotechnol.*, 2020, **15**, 29–34.

[286] L. Wu, W. Yang and G. Wang, *npj 2D Mater. Appl.*, 2019, **3**, 6.

[287] L. David, R. Bhandavat and G. Singh, *ACS Nano*, 2014, **8**, 1759–1770.

[288] C. Tsai, F. Abild-Pedersen and J. K. Nørskov, *Nano Lett.*, 2014, **14**, 1381–1387.

[289] C. Zhang, C. Gong, Y. Nie, K.-A. Min, C. Liang, Y. J. Oh, H. Zhang, W. Wang, S. Hong, L. Colombo, R. M. Wallace and K. Cho, *2D Mater.*, 2016, **4**, 015026.

[290] X. Duan, C. Wang, J. C. Shaw, R. Cheng, Y. Chen, H. Li, X. Wu, Y. Tang, Q. Zhang, A. Pan, J. Jiang, R. Yu, Y. Huang and X. Duan, *Nat. Nanotechnol.*, 2014, **9**, 1024–1030.

[291] M. M. Furchi, A. Pospischil, F. Libisch, J. Burgdörfer and T. Mueller, *Nano Lett.*, 2014, **14**, 4785–4791.

[292] T. Roy, M. Tosun, J. S. Kang, A. B. Sachid, S. B. Desai, M. Hettick, C. C. Hu and A. Javey, *ACS Nano*, 2014, **8**, 6259–6264.

[293] N. Huo, Y. Yang and J. Li, *J. Semicond.*, 2017, **38**, 031002.

[294] H. Terrones, F. López-Urías and M. Terrones, *Sci. Rep.*, 2013, **3**, 1549.

[295] S. Tongay, W. Fan, J. Kang, J. Park, U. Koldemir, J. Suh, D. S. Narang, K. Liu, J. Ji, J. Li, R. Sinclair and J. Wu, *Nano Lett.*, 2014, **14**, 3185–3190.

[296] K. Chen, X. Wan, J. Wen, W. Xie, Z. Kang, X. Zeng and C. E. T. Al, *ACS Nano*, 2015, **9**, 9868–9876.

[297] X. Li, R. Shen, S. Ma, X. Chen and J. Xie, *Appl. Surf. Sci.*, 2018, **430**, 53–107.

[298] Z. Song, T. Schultz, Z. Ding, B. Lei, C. Han, P. Amsalem, T. Lin, D. Chi, S. L. Wong, Y. J. Zheng, M.-Y. Li, L.-J. Li, W. Chen, N. Koch, Y. L. Huang and A. T. S. Wee, *ACS Nano*, 2017, **11**, 9128–9135.

[299] Y. Gong, S. Lei, G. Ye, B. Li, Y. He, K. Keyshar, X. Zhang, Q. Wang, J. Lou, Z. Liu, R. Vajtai, W. Zhou and P. M. Ajayan, *Nano Lett.*, 2015, **15**, 6135–6141.

[300] M. Zhao, M. Liu, Y. Dong, C. Zou, K. Yang, Y. Yang, L. Zhang and S. Huang, *J. Mater. Chem. C*, 2016, **4**, 10215–10222.

[301] J. Gao, B. Li, J. Tan, P. Chow, T. M. Lu and N. Koratkar, *ACS Nano*, 2016, **10**, 2628–2635.

[302] R. C. Longo, R. Addou, S. KC, J.-Y. Noh, C. M. Smyth, D. Barrera, C. Zhang, J. W. P. Hsu, R. M. Wallace and K. Cho, *2D Mater.*, 2017, **4**, 025050.

[303] A. Berkdemir, H. R. Gutiérrez, A. R. Botello-Méndez, N. Perea-López, A. L. Elías, C.-I. Chia, B. Wang, V. H. Crespi, F. López-Urías, J.-C. Charlier, H. Terrones and M. Terrones, *Sci. Rep.*, 2013, **3**, 1755.

[304] A. M. Hussain, G. A. T. Sevilla, K. R. Rader and M. M. Hussain, 2013 Saudi Int. Electron. Commun. Photonics Conf., 2013, pp. 1–5.

[305] G. Mirabelli, C. McGeough, M. Schmidt, E. K. McCarthy, S. Monaghan, I. M. Povey, M. McCarthy, F. Gity, R. Nagle, G. Hughes, A. Cafolla, P. K. Hurley and R. Duffy, *J. Appl. Phys.*, 2016, **120**, 125102.

[306] K. Bogaert, S. Liu, J. Chesin, D. Titow, S. Gradečak and S. Garaj, *Nano Lett.*, 2016, **16**, 5129–5134.

[307] Z. Zhang, P. Chen, X. Duan, K. Zang, J. Luo and X. Duan, *Science (80-. ).*, 2017, **357**, 788–792.

[308] R. Makino, S. Mizuno, H. Kageshima and H. Hibino, *Appl. Phys. Express*, 2020, **13**, 065007.

[309] A. Warren, A. Nylund and I. Olefjord, *Int. J. Refract. Met. Hard Mater.*, 1996, **14**, 345–353.

[310] W. Zhou, X. Zou, S. Najmaei, Z. Liu, Y. Shi, J. Kong, J. Lou, P. M. Ajayan, B. I. Yakobson and J.-C. Idrobo, *Nano Lett.*, 2013, **13**, 2615–2622.

[311] J. Hong, Y. Wang, A. Wang, D. Lv, C. Jin, Z. Xu, M. I. J. Probert, J. Yuan and Z. Zhang, *Nanoscale*, 2017, **9**, 10312–10320.

[312] S.-H. Su, Y.-T. Hsu, Y.-H. Chang, M.-H. Chiu, C.-L. Hsu, W.-T. Hsu, W.-H. Chang, J.-H. He and L.-J. Li, *Small*, 2014, **10**, 2589–2594.

[313] M. O'Brien, *Ph.D. thesis*, Trinity College Dublin, 2017.

[314] J. O. Island, A. Kuc, E. H. Diependaal, R. Bratschitsch, H. S. J. van der Zant, T. Heine and A. Castellanos-Gomez, *Nanoscale*, 2016, **8**, 2589–2593.

[315] J. Krustok, T. Raadik, R. Jaaniso, V. Kiisk, I. Sildos, M. Marandi, H.-P. Komsa, B. Li, X. Zhang, Y. Gong and P. M. Ajayan, *Appl. Phys. Lett.*, 2016, **109**, 253106.

[316] A. Arora, K. Nogajewski, M. Molas, M. Koperski and M. Potemski, *Nanoscale*, 2015, **7**, 20769–20775.

[317] Y. Liu, K. Tom, X. Zhang, S. Lou, Y. Liu and J. Yao, *New J. Phys.*, 2017, **19**, 073018.

[318] S. B. Desai, G. Seol, J. S. Kang, H. Fang, C. Battaglia, R. Kapadia, J. W. Ager, J. Guo and A. Javey, *Nano Lett.*, 2014, **14**, 4592–4597.

[319] P. Pimpang, A. S. Zoolfakar, D. Wongratanaphisan, A. Gardchareon, E. P. Nguyen, S. Zhuiykov, S. Choopun and K. Kalantar-zadeh, *J. Phys. Chem. C*, 2013, **117**, 19984–19990.

[320] S. H. El-Mahalawy and B. L. Evans, *Phys. Status Solidi*, 1977, **79**, 713–722.

[321] Y. Son, M.-Y. Li, C.-C. Cheng, K.-H. Wei, P. Liu, Q. H. Wang, L.-J. Li and M. S. Strano, *Nano Lett.*, 2016, **16**, 3571–3577.

[322] M. Zhang, J. Wu, Y. Zhu, D. O. Dumcenco, J. Hong, N. Mao, S. Deng, Y. Chen, Y. Yang, C. Jin, S. H. Chaki, Y.-S. Huang, J. Zhang and L. Xie, *ACS Nano*, 2014, **8**, 7130–7137.

[323] X. Chia, A. Ambrosi, P. Lazar, Z. Sofer and M. Pumera, *J. Mater. Chem. A*, 2016, **4**, 14241–14253.

[324] R. Yue, Y. Nie, L. A. Walsh, R. Addou, C. Liang, N. Lu, A. T. Barton, H. Zhu, Z. Che, D. Barrera, L. Cheng, P.-R. Cha, Y. J. Chabal, J. W. P. Hsu, J. Kim, M. J. Kim, L. Colombo, R. M. Wallace, K. Cho and C. L. Hinkle, *2D Mater.*, 2017, **4**, 045019.

[325] P. Schmidt, M. Binnewies, R. Glaum and M. Schmidt, in *Adv. Top. Cryst. Growth*, ed. S. Ferreira, InTech, 2013, ch. 9, pp. 227–305.

[326] Z. Wang, Y. Xie, H. Wang, R. Wu, T. Nan, Y. Zhan, J. Sun, T. Jiang, Y. Zhao, Y. Lei, M. Yang, W. Wang, Q. Zhu, X. Ma and Y. Hao, *Nanotechnology*, 2017, **28**, 325602.

[327] W.-T. Hsu, L.-S. Lu, P.-H. Wu, M.-H. Lee, P.-J. Chen, P.-Y. Wu, Y.-C. Chou, H.-T. Jeng, L.-J. Li, M.-W. Chu and W.-H. Chang, *Nat. Commun.*, 2018, **9**, 1356.

[328] A. Zur and T. C. McGill, *J. Appl. Phys.*, 1984, **55**, 378–386.

[329] A. Koma, *Thin Solid Films*, 1992, **216**, 72–76.

[330] H. Katzke, P. Tolédano and W. Depmeier, *Phys. Rev. B*, 2004, **69**, 134111.

[331] S. Presolski and M. Pumera, *Mater. Today*, 2016, **19**, 140–145.

[332] J. Zhang, J. Wang, P. Chen, Y. Sun, S. Wu, Z. Jia, X. Lu, H. Yu, W. Chen, J. Zhu, G. Xie, R. Yang, D. Shi, X. Xu, J. Xiang, K. Liu and G. Zhang, *Adv. Mater.*, 2016, **28**, 1950–1956.

[333] Y. Saito, T. Kondo, H. Ito, M. Okada, T. Shimizu, T. Kubo and R. Kitaura, *Jpn. J. Appl. Phys.*, 2020, **59**, 062004.

[334] W. Yang, H. Kawai, M. Bosman, B. Tang, J. Chai, W. L. Tay, J. Yang, H. L. Seng, H. Zhu, H. Gong, H. Liu, K. E. J. Goh, S. Wang and D. Chi, *Nanoscale*, 2018, **10**, 22927–22936.

[335] I. H. Abidi, L.-T. Weng, C. P. J. Wong, A. Tyagi, L. Gan, Y. Ding, M. Li, Z. Gao, R. Xue, M. D. Hossain, M. Zhuang, X. Ou and Z. Luo, *Chem. Mater.*, 2018, **30**, 1718–1728.

[336] V. Verdingovas, M. S. Jellesen and R. Ambat, *IEEE Trans. Device Mater. Reliab.*, 2014, **14**, 42–51.

[337] X. Zhang, L. Huangfu, Z. Gu, S. Xiao, J. Zhou, H. Nan, X. Gu and K. K. Ostrikov, *Small*, 2021, 2007312.

[338] Y. Guo and J. Robertson, *Appl. Phys. Lett.*, 2016, **108**, 233104.

[339] H. M. Hill, A. F. Rigosi, K. T. Rim, G. W. Flynn and T. F. Heinz, *Nano Lett.*, 2016, **16**, 4831–4837.

[340] C. Yelgel, Ö. C. Yelgel and O. Gülseren, *J. Appl. Phys.*, 2017, **122**, 065303.

[341] L. Li, R. Long and O. V. Prezhdo, *Chem. Mater.*, 2017, **29**, 2466–2473.

[342] G.-H. Lee, C.-H. Lee, A. M. van der Zande, M. Han, X. Cui, G. Arefe, C. Nuckolls, T. F. Heinz, J. Hone and P. Kim, *APL Mater.*, 2014, **2**, 92511.

[343] J. Yao, W. Guo, Y. Liu, X. Niu, M. Li, X. Wu, Y. Yu, T. Ou, J. Sha and Y. Wang, *J. Mater. Chem. C*, 2021, **9**, 8213–8219.

[344] C. Zhou, Y. Zhao, S. Raju, Y. Wang, Z. Lin, M. Chan and Y. Chai, *Adv. Funct. Mater.*, 2016, **26**, 4223–4230.

[345] J. H. Yu, H. R. Lee, S. S. Hong, D. Kong, H. W. Lee, H. Wang, F. Xiong, S. Wang and Y. Cui, *Nano Lett.*, 2015, **15**, 1031–1035.

[346] C. Chen, Y. Yang, X. Zhou, W. Xu, Q. Cui, J. Lu, H. Jing, D. Tian, C. Xu, T. Zhai and H. Xu, *ACS Appl. Nano Mater.*, 2021, acsanm.1c00890.

[347] Y. Chen and M. Sun, *Nanoscale*, 2021, **13**, 5594–5619.

[348] X. Liu, J. He, Q. Liu, D. Tang, J. Wen, W. Liu, W. Yu, J. Wu, Z. He, Y. Lu, D. Zhu, W. Liu, P. Cao, S. Han and K.-W. Ang, *J. Appl. Phys.*, 2015, **118**, 124506.

[349] R. Gatensby, *Ph.D. thesis*, Trinity College Dublin, 2018.

[350] D. Vikraman, S. Hussain, L. Truong, K. Karuppasamy, H.-J. Kim, T. Maiyalagan, S.-H. Chun, J. Jung and H.-S. Kim, *Appl. Surf. Sci.*, 2019, **480**, 611–620.

[351] C. H. Lui, Z. Ye, C. Ji, K.-C. Chiu, C.-T. Chou, T. I. Andersen, C. Means-Shively, H. Anderson, J.-M. Wu, T. Kidd, Y.-H. Lee and R. He, *Phys. Rev. B*, 2015, **91**, 165403.

[352] J. Xiao, Y. Zhang, H. Chen, N. Xu and S. Deng, *Nano-Micro Lett.*, 2018, **10**, 60.

# Part VII

# Appendix

# A Process Sheets

## A.1 TMD CVD process

### A.1.1 Tungsten Diselenide

| **Process Step** | **Description and details** |
|---|---|
| $MX_2$ deposition | 20 nm W sputtered on seed substrate<br>Oxidised on hotplate @500 °C, 30 min |
| Sample prep | 300nm/ 500$\mu$m $SiO_2$/Si<br>IPA clean<br>Place seed samples in boat<br>Cover with growth substrates (top down)<br>Load sample boatin Furnace tube |
| CVD | Heat furnace 1st step @850 °C, 5 min.<br>2nd step @850 °C, 45 min.<br>Heat Se-furnace @250 °C, 45 min<br>Gas flow: $H_2$/Ar-gas @50 sccm<br>Gas flow cooldown: Ar-gas @50 sccm<br>Pressure: 6.00±0.2 Torr<br>Open furnace @T<500 °C<br>Cooldown to T<90 °C<br>Remove samples |

### A.1.2 Molybdenum Disulfide

| **Process Step** | **Description and details** |
|---|---|
| $MX_2$ deposition | IPA clean samples<br>Drop casting 50 $\mu$L 20% $MoO_3$ in IPA<br>Hotplate @150 °C |
| Sample preparation | Dice substrates<br>IPA clean<br>Place seed substrates in boat<br>Cover with growth substrates (top down)<br>Load in tube |
| CVD | Heat main furnace @750 °C, 40 min.<br>Heat S-furnace @117 °C, 20 min<br>Cool down to T<90 °C<br>Remove samples |

## A.2 Heterostructures

### Single-step CVD Synthesis

$MoS_2$+$WS_2$

| **Process Step** | | **Description and details** |
|---|---|---|
| $MX_2$ deposition | | IPA clean samples |
| | W-precursor | Drop casting 50 µL 20% $WO_3$ in IPA<br>Hotplate @120 °C |
| | Mo-precursor | Drop casting 30 µL 20% $MoO_3$ in IPA<br>Hotplate @120 °C |
| Sample | | Dice substrates<br>IPA clean<br>Place seed substrates in boat<br>Cover with growth substrates (top down)<br>Load in tube |
| CVD | | Heat S-furnace @117 °C, |
| | $MoS_2$ | Heat main furnace @750 °C, 25 min. |
| | $WS_2$ | Heat main furnace @850 °C, 25 min. |
| | | Cool down to T <90 °C<br>Remove samples |

$MoSe_2$+$WSe_2$

| **Process Step** | | **Description and details** |
|---|---|---|
| $MX_2$ deposition | | IPA clean samples |
| | W-precursor | 20 nm W sputtered on seed substrate<br>Oxidised on hotplate @500 °C, 30 min |
| | Mo-precursor | Drop casting 30 µL 20% $MoO_3$ in IPA<br>Hotplate @120 °C |
| Sample | | Dice substrates<br>IPA clean<br>Place seed substrates in boat<br>Cover with growth substrates (top down)<br>Load in tube |
| CVD | | Heat S-furnace @117 °C, |
| | $MoS_2$ | Heat main furnace @750 °C, 25 min. |
| | $WS_2$ | Heat main furnace @850 °C, 25 min. |
| | | Cool down to T <90 °C<br>Remove samples |

## A.3 Devices

### A.3.1 $WSe_2$

| Process Step | | Description and details |
|---|---|---|
| $MX_2$ deposition | | 20 nm of W-dots sputtering on seed<br>Oxidised on hotplate @500 °C, 30 min |
| Sample | | Dice growth substrate 300 nm/500 mm $SiO_2$/Si sample<br>IPA clean<br>Place Seed samples in boat<br>Cover with growth substrate (top down)<br>Load in Tube |
| CVD | | Heat furnace 1st step @900 °C, 5 min.<br>2nd step @850 °C, 40 min.<br>Heat Se-furnace @250 °C, 40 min<br>Gas flow1: H2/Ar-gas @50 sccm<br>Gas flow2: Ar-gas @50 sccm<br>Pressure: 6.00±0.1 Torr<br>Open furnace @ T<500 °C<br>Cooldown to T<90 °C<br>Remove samples |
| EBL | Markers | PMMA A3 spinning 3000 rpm, 1 min.<br>Place markers<br>Develop TMAH:3IPA, 30 s<br>Deposition 5/50 nm Ni/Au<br>Dissolve PMMA in Acetone |
| | Contacts | PMMA A3 spinning 3000 rpm, 1 min.<br>Place contacts<br>Develop TMAH:3IPA, 30 s<br>Deposition 5/50 Ni/Au<br>Dissolve PMMA in Acetone |

### A.3.2 Optical lithography (IMP)

| Process Step | Description and details |
|---|---|
| Photoresist | Prebake 2 min., 120 °C<br>spin coating MICROPOSIT S1813 at 3000rpm, 1min.<br>Postbake 2 min., 120 °C |
| Optical litho (IMP) | Select mask and magnification (20x)<br>Align sample<br>Expose 0.8 s |
| Develop | Develop in MICROPOSIT MF-319, 60 s<br>Rinse in DI water |
| Metal deposition | Deposition 5/100 nm Ti/Au<br>Lift-off photoresist in Acetone |

# B TMD furnaces

Both TMD furnaces used in this work are two temperature zone furnaces, where the chalcogenide precursor is evaporated in a low temperature upstream heating zone, while the evaporation of the metal precursor and the reaction takes place in the downstream high temperature furnace zone. More detailed information and the differences between the furnace setups is given in the sections below.

## B.1 Sulfurisation TMD furnace

An image of the sulfurisation TMD furnace is shown in Figure B.1.

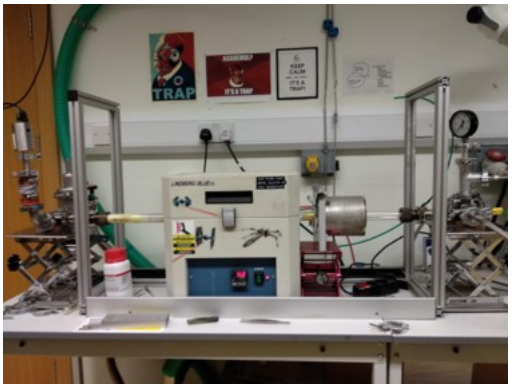


Figure B.1: Picture showing the sulfur TMD furnace

The furnace has two different heating zones of which the downstream high temperature heating zone is a Lindberg Blue hot wall horizontal quartz tube furnace. The second upstream low temperature zone utilising radiant heating from halogen bulbs to melt the sulfur precursor. A picture with both furnaces is shown in Figure B.2(a). The temperature resulting from the halogen bulbs is monitored by a thermocouple connected to the sulfur crucible and this output is send to a power supply box which controls the energy output, and thereby temperature, of the halogen light furnace. This power supply box is shown in Figure B.2(b).

The system is kept at a constant pressure with a vacuum system as detailed in Figure B.3. The base pressure of the system is about 0.03 Torr, where during the furnace run, when Ar or forming gas are running to the furnace, the pressure is about 0.68 Torr. In the system the pressure can be monitored up to ∼10 Torr can be measured in the system. Variations in the pressure can be due to the gas

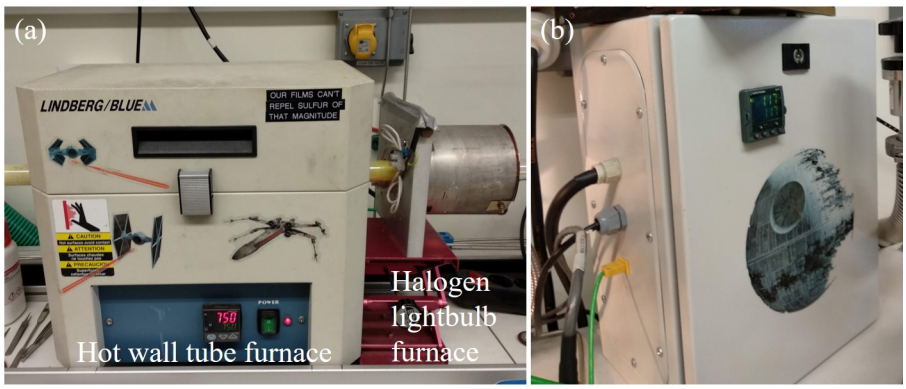


Figure B.2: (a) Image of the two different furnaces. the downstream high temperature hot wall furnace and the upstream low temperature halogen lightbulb furnace. (b) shows a picture of the power supply box coupled to the halogen lightbulb furnace to control the temperature.

flow, blockages in the cold trap or manual manipulation of the pressure by partially closing the valve to the vacuum pump.

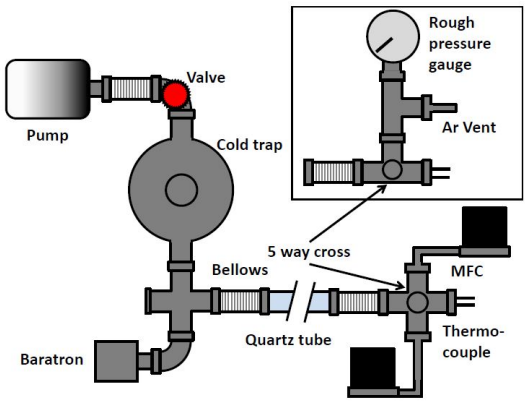


Figure B.3: Schematic of vacuum system for sulfurisation furnace. Reproduced from Gatensby *et al.*[349]

## B.2 Selenisation TMD furnace

An image of the selenisation TMD furnace is shown in Figure B.4. In contrast to the sulfurisation furnace two horizontal hot wall furnaces are used in this setup. The downstream high temperature zone tube is a horizontal split tube, Gero GmbH SR-A 40-250/11, where the upstream low temperature zone is a standard horizontal furnace, Gero GmbH SR 40-200/12.

The furnace setup is controlled by a LabView program, developed by Dr. Kangho Lee, which can automatically control and logs the temperatures, gas flow and pressure in the system. The vacuum system used here is similar to that described for the sulfurisation furnace. The pressure in this system can be measured below ~10 Torr as well. Due to the toxicity of Se-gas and $H_2Se$ the furnace is encapsulated and a custom build fumehood has been designed and produced by Dr. Riley Gatensby.[349]

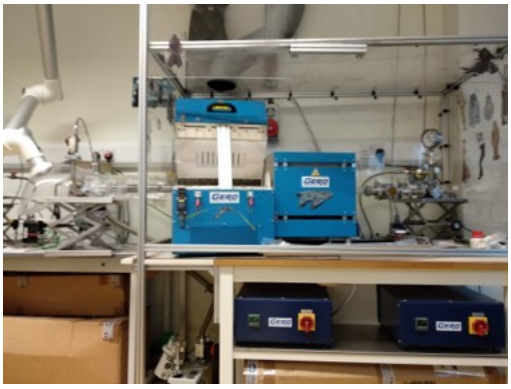

Figure B.4: Picture showing the selenium TMD furnace

# C Character tables

| $D_{6h}$ | E | $2C_6$ | ... | Linear rotations | Quadratic |
|---|---|---|---|---|---|
| $A_{1g}$ | 1 | 1 | ... | | $x^2+y^2+z^2$ |
| $A_{2g}$ | 1 | 1 | ... | $R_z$ | |
| $E_{1g}$ | 2 | 1 | ... | $(R_x,R_y)$ | (xy,yz) |
| $E_{2g}$ | 2 | -1 | ... | | $(x^2-y^2,xy)$ |
| $A_{1u}$ | 1 | 1 | ... | z | |
| $A_{2u}$ | 1 | 1 | ... | | |
| $E_{1u}$ | 2 | 1 | ... | (x,y) | |
| $E_{2u}$ | 2 | -1 | ... | | |

Table C.1: Character table for the $D_6h$ symmetry group. This is the symmetry group corresponding to bulk 2H $MoS_2$.

| $D_{3h}$ | E | $2C_3$ | $3C_2$ | $\sigma_h$ | $2S_3$ | $\sigma_v$ | Linear rotations | Quadratic |
|---|---|---|---|---|---|---|---|---|
| $A_1^{'}$ | 1 | 1 | 1 | 1 | 1 | 1 | $x^2+y^2+z^2$ | |
| $A_2^{'}$ | 1 | 1 | -1 | 1 | 1 | -1 | $R_z$ | |
| $E^{'}$ | 2 | -1 | 0 | 2 | -1 | 0 | (x,y) | $(x^2-y^2,xy)$ |
| $A_1^{''}$ | 1 | 1 | 1 | -1 | -1 | -1 | z | |
| $A_2^{''}$ | 1 | 1 | -1 | -1 | -1 | 1 | | |
| $E^{''}$ | 2 | -1 | 0 | -2 | 1 | 0 | $(R_x,R_y)$ | (xy,yz) |

Table C.2: Character table for the $D_3h$ symmetry group. This is the symmetry group for few odd layer 2H $MoS_2$ and monolayer $MoS_2$.

| $D_{3d}$ | E | $2C_3$ | $3C_2$ | $i$ | $2S_3$ | $\sigma_d$ | Linear rotations | Quadratic |
|---|---|---|---|---|---|---|---|---|
| $A_{1g}$ | 1 | 1 | 1 | 1 | 1 | 1 | $x^2+y^2+z^2$ | |
| $A_{2g}$ | 1 | 1 | -1 | 1 | 1 | -1 | $R_z$ | |
| $E_g$ | 2 | -1 | 0 | 2 | -1 | 0 | (x,y) | $(x^2-y^2,xy)$, (xy,yz) |
| $A_{1u}$ | 1 | 1 | 1 | -1 | -1 | -1 | z | |
| $A_{2u}$ | 1 | 1 | -1 | -1 | -1 | 1 | | |
| $E_u$ | 2 | -1 | 0 | -2 | 1 | 0 | $(R_x,R_y)$ | |

Table C.3: Character table for the $D_3h$ symmetry group. This is the symmetry group for few even layer 2H $MoS_2$.

# D PMMA thickness

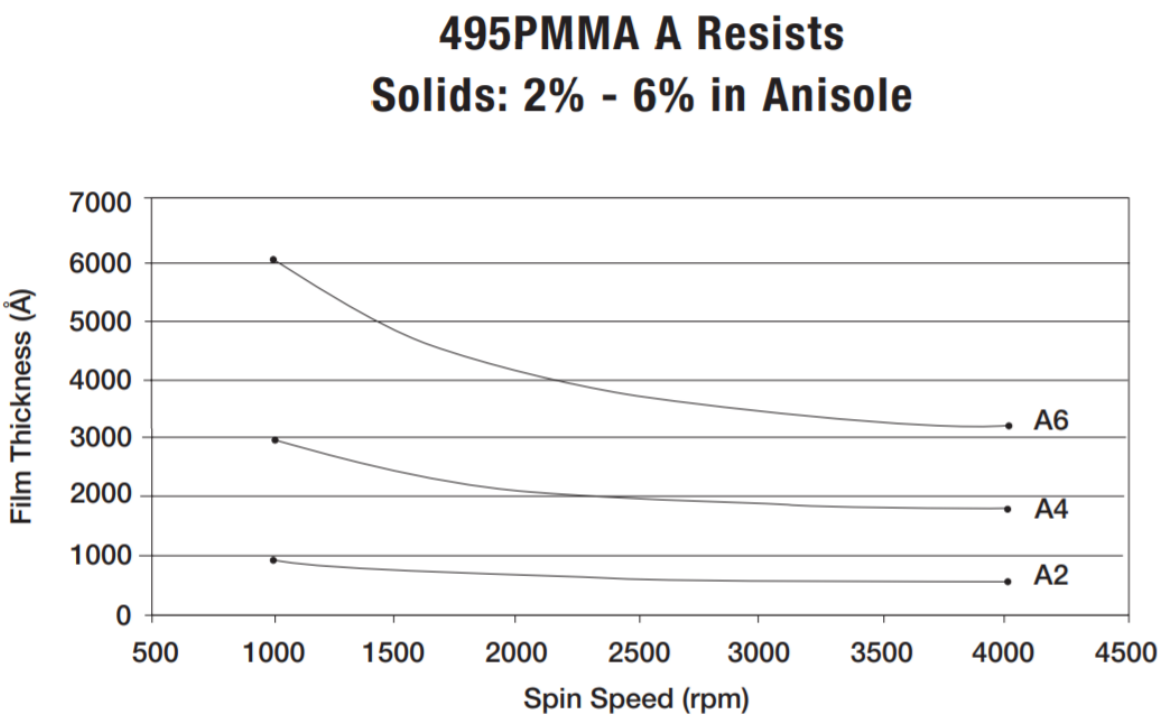


Figure D.1: Graph showing the thickness of PMMA in anisole for different spin rates

# E Indirect Synthesis of TMD Heterostructures

As mentioned in section 3.6 TMDs can, when combined as heterostructures, offer devices with atomically sharp, bond-free interfaces without the need for lattice matching considerations.[289] When combining semiconductors with complementary carrier types, considering the potential to dope TMDs to adjust the carrier levels, a wide range of possibilities for devices completely made from 2D materials opens up. Examples of such devices are p-n junctions or FETs.[130,292] In the production of heterostructures the distinction can be made between direct and indirect heterostructures. Indirect heterostructures are assembled manually, by combining TMDs obtained in separate growth runs and therefore require the need of a transfer step to stack the different materials, where in the direct synthesis the TMDs are immediately formed as heterostructures. In this chapter indirect synthesis of TMD heterostructures is described for various combinations of TMDs. The direct synthesis of heterostructures will be discussed separately in chapter 8. Due to distinctive individual material properties these various heterostructures should result in different material properties.

For the indirect synthesis of TMD heterostructures two separate CVD runs are performed to obtain the required TMD flakes. The CVD process proceeded as detailed in subsection 5.1.3. Growth of the TMDs was followed by a transfer step to create the heterostructure. The process for the transfer step shares similarities with mechanical exfoliation as described in subsection 4.1.1, though the target substrate for the heterostructure transfer is the other TMD substrate. Indirect synthesis of heterostructures leads exclusively to vertical heterostructures as there is no connecting interface between the different TMDs in the lateral direction. The experimental work described here contains guided project results generated by a fourth year undergraduate student, Mr. Alan Baldwin.

Post CVD synthesis, to produce the heterostructures, the flakes of one TMD were transferred on top of materials grown on a second target substrate. The TMD material intended to be the top layer, was lifted off from the growth substrate and transferred on top of the flakes of the other TMD sample to produce the heterostructure. The flakes were lifted off by the aid of a support layer, usually a polymer such as poly-methyl methacrylate (PMMA) or poly-dimethylsiloxane (PDMS) on the sample and during lift-off the TMD flakes adhere to this support layer. This support

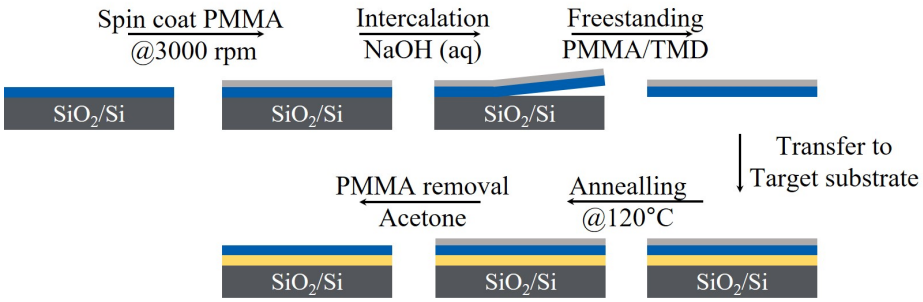


Figure E.1: Overview transfer process with PMMA as polymer carrier. In blue and yellow the different TMDs are shown which are transferred on top of each other by first spin coating PMMA on a TMD intended to be used as the top material of the hetrostructure. The PMMA/TMD stack is removed from the $SiO_2$/Si growth substrate by intercalation of $Na^+$ and $OH^-$ ions after which the stack is transferred to the target TMD layer, annealed and finally the PMMA layer is removed in acetone

layer with TMD flakes was then positioned on the other TMD sample and the flakes thereby transferred to that sample. The final step was to remove the support layer associated with the TMD overlayer.

Transfer methods can be broadly divided in two categories: wet transfer and dry transfer. In the wet transfer method there is solvent present at target interface, this contrasts with the dry transfer method, which is performed without such solvents. The purpose of the solvent is to act as a lubricant, which reduces physical damage during the transfer process. However, the use of a solvent can introduce contaminants to the surface and lead to pockets of trapped water beneath the TMD. In contrast dry transfers are more likely to cause physical damage, such as rips and tears, to the transferred film. In this work various transfer methods were tested for the transfer of the flakes which yielded a variety of results and success rates. All the methods bescribed here are wet transfers to minimise damage to the flakes.

One transfer method begins with spin coating a thin layer of PMMA, 50 $\mu$L of 2% PMMA in anisole at 3000 rpm for 1 min, onto the substrate with the TMD sample intended to be used as the top material of the hetrostructure. After spin coating the PMMA is baked at 180 °C for 2 min. to remove the remaining solvent and to relax the polymer. The thickness of the PMMA layer is ~60 $\mu$m see Appendix D. After the baking step the sample is placed in a 2 M NaOH solution. The $Na^+$ ions intercalate between the TMD flakes and the $SiO_2$, thereby lifting the flakes off from the substrate. This is schematically shown in Figure E.1. The PMMA layer with the TMD flakes are then fished from the NaOH solution on a dummy substrate and placed into a beaker of de-ionized water to rinse away the ions on the surface after which the film is placed on the target substrate. The substrate is placed overnight on the hotplate, 70 °C, to evaporate traces of water and to anneal the flakes to the substrate, after which the PMMA is dissolved in acetone.

The advantage of this transfer method is the relative ease and speed of the method. However, the freestanding thin PMMA layer can easily wrinkle in the

solution and there is little control as to how the flakes can be positioned on the target substrate. Therefore the formation of heterostructures is reliant of the statistical alignment of the upper and lower component TMDs. This method is preferably used when a high concentration of TMD flakes is present on both substrates and there is a probability of overlap between the different TMD flakes. Another complicating factor for this transfer method is the loss of TMD flakes, from the target substrate, while immersed in water. While transferring flakes to the target substrate, the target substrate is submerged in water for a short period which can lead to a degree of lift-off of the TMD flakes from the target substrate. Reducing the time in water, during this step decreases the amount of material lost from the surface due to it lifting of from the surface. While there are drawbacks with this method successful results can be achieved, as discussed further in this chapter.

Another method to transfer the flakes is to use a combination of a PMMA layer and a PDMS stamp, Gel-Pak A4, as a carrier layer. The Gel-Pak is a thicker, less flexible material compared to PMMA. After the lift-off of the flakes the polymer stack can be simply picked up with tweezers and it gives the possibility to align these flakes with the flakes on the target substrate by utilizing a micro-manipulator stage. This stage design was based on the transfer stage described by Castellanos-Gomez *et al.*[34] After transfer the sample was annealed overnight on the hotplate after which the Gel-Pak stamp was mechanically removed, followed by the dissolving of the PMMA layer in acetone.

This method allows alignment of the different TMD flakes, resulting in a higher probability of forming functioning heterostructures, in comparison with the PMMA transfer method. However, it should be appreciated this transfer process adds steps which can increase the likelihood of failure. Exact alignment of the flakes is not trivial due to relative movement of the flakes which occurs during the transfer and heating processes. The relative position of the individual flakes, or spacing between them, can be altered on the target substrate due to the presence of air pockets. To increase the chances of successful heterostructure formation, areas with high flake densities were selected and aligned. The technique is important when using this transfer method, to ensure success. The Gel-Pak stamp needs to be removed with a careful rolling motion, failure to do so can result in damage to the surface. Despite the difficulties and the associated risk of TMD damage, the use of the PDMS stamp resulted in a greater yield of viable aligned hetrostructures. To further improve the interaction between the different TMD flakes and to remove contaminants on the surface, annealing of the samples under vacuum for 2 h at 120 °C was performed after the transfer step.

## E.1 $WSe_2$+$MoS_2$

Indirect synthesis of $WSe_2/MoS_2$ heterostructures by the placement of CVD grown $MoS_2$ on the CVD grown of $WSe_2$ flakes results in vertically overlapping $WSe_2/MoS_2$

heterostructures. CVD of $MoS_2$ generally results in a high rate of nucleation spread over the surface. Due to this high nucleation a large number of flakes is present on the surface resulting in a statistically higher chance for the $MoS_2$ flakes to overlap with the target $WSe_2$ flakes. The $MoS_2$ flakes were transferred on top of the $WSe_2$ flakes by the Gelpack/PMMA transfer method. This transfer mainly led to the formation of vertical heterostructures as shown in the optical microscopy image in Figure E.2(a). In this image a large monolayer flake is present while smaller flakes, identifiable with the darker contrast, are scattered over the surface. Part of these flakes are overlapping with the large flake, creating a vertical heterostructure, where all $WSe_2$ flakes are located on the $SiO_2$.

The $WSe_2$ and $MoS_2$ Raman maps, shown in Figure E.2(b) and (c), indicate that the large flake on the surface is $WSe_2$, while the smaller flakes are $MoS_2$ flakes. The $MoS_2$ is not very clearly identifiable in the $MoS_2$ Raman map as the intensity of the $MoS_2$ peaks is low in comparison to that of $WSe_2$, which is expected as tungsten TMDs having a higher quantum yield than molybdenum TMDs. The intensity of the $WSe_2$ $E^1_{2g}/A_{1g}$ peak is over 10x the intensity of the $MoS_2$ $E^1_{2g}$ and $A_{1g}$ peaks, as is plotted in the Raman spectra of individual $WSe_2$ and $WSe_2$+$MoS_2$ heterostructure in Figure E.2(d).

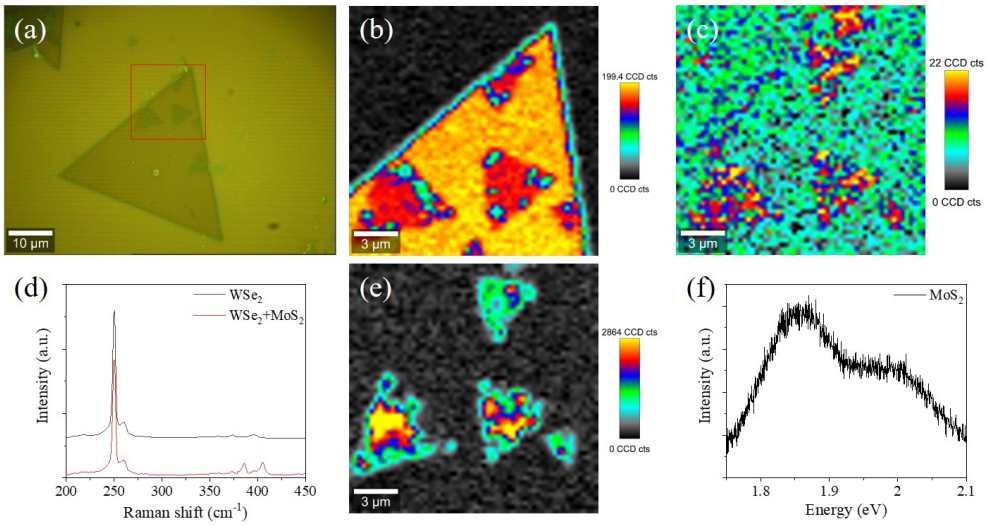


Figure E.2: Optical microscopy, Raman & PL data for direct $WSe_2/MoS_2$ heterostructure growth. (a) shows an optical microscopy image of a heterostructure area. (b) the $WSe_2$ $E^1_{2g}$+$A_{1g}$ Raman map of the red area outlined in the optical microscopy image, (c) the $MoS_2$ $A_{1g}$ Raman map and (d) shows the Raman spectra of the $WSe_2$ area and the $WSe_2/MoS_2$ heterostructure area. In (e) and (f) the PL data is shown. (e) shows the PL map for the $MoS_2$ A1 exciton peak, where (f) shows the PL spectrum for $MoS_2$

For $MoS_2$ in the heterostructure area the Raman peaks are located at ~385.94 $cm^{-1}$ and 405.53 $cm^{-1}$ for respectively the $E^1_{2g}$ an $A_{1g}$ peaks. with a FWHM of ~6.99 $cm^{-1}$ and ~7.60 $cm^{-1}$. The $WSe_2$ $E^1_{2g}$+$A_{1g}$ peaks for the monolayer and the heterostructure area are both located at ~250.79 $cm^{-1}$, with a FWHM of ~3.58 $cm^{-1}$ and ~3.71 $cm^{-1}$, where the 2LA(M) peaks are located at 259.57 $cm^{-1}$ and

260.82 $cm^{-1}$, with the FWHM at 8.33 $cm^{-1}$ 8.44 $cm^{-1}$. The broadening of the peak, increase of the FWHM, for $WSe_2$ at the heterostructure is due to the presence of the $MoS_2$ on the $WSe_2$. The $MoS_2$ peaks are quite broad, this is most likely due to damage sustained during the transfer process, as physical damage can result in in scattering of the Raman signal at defects and tears in the flakes, leading to the appearance of polycrystalline $MoS_2$ in the spectrum.

The PL map for the A1 exciton, see Figure E.2, clearly shows the $MoS_2$ areas on the surface, where the $WSe_2$ spectra show a small decrease in intensity on the heterostructure areas. This decrease in intensity is expected as the quantum efficiency decreases for thicker layers, though the intensity of the $WSe_2$ PL signal decreases exponentially when going from mono- to bilayer $WSe_2$, where the decrease for the heterostructure area is minimal.[31,175] As the intensity of the A1 exciton peak only decreases slightly it can be assumed that there is no strong interaction between the $MoS_2$ and the $WSe_2$.

The lack of interaction between the layers is also visible in the Raman peaks as there is no shift in the Raman peaks for both the $MoS_2$ and $WSe_2$ peaks in comparison to the freestanding monolayer peak positions. A shift in the peaks would indicate that there is a coupling of the TMD layers, which does not appear to be the case here. When a strong interlayer coupling between the different TMD layers is present this leads to a shift to higher wavenumbers.[132,350]

Coupling between the different TMD layers can be achieved by vacuum annealing of the sample. Annealing can remove the contaminants and increase the interactions between the layers. The Raman and PL spectra before and after annealing are shown in Figure E.3(a). When comparing the Raman spectra of the heterostructure area before and after annealing, with the peaks normalised on the $WSe_2$ $E^1_{2g}$+$A_{1g}$ peak, a clear increase in intensity for both the $MoS_2$ $E^1_{2g}$ peak and $MoS_2$ $A_{1g}$ peak is visible. After annealing it also appears that the $MoS_2$ $E^1_{2g}$ peak has red shifted, while the $A_{1g}$ has slightly blue shifted, thus indicating that the annealing was successful at increasing the interactions between the flakes, thereby creating a heterostructure. As the contaminants were removed, the flakes were able to become situated closer together and resulted in the atoms being able to be displaced less from their equilibrium positions.

The photoluminescence spectra for the $MoS_2$ and $WSe_2$ peaks are shown in Figure E.3(b) and (c) respectively with the energies for the different transitions displayed in table 4.2. The intensities of each of the transitions decreased after the annealing process. The $WSe_2$ PL map, see Figure E.3(b) shows that the $WSe_2$ PL intensity is quenched, to 0.6x the intensity for the heterostructure area after annealing. This decrease in intensity is also visible for the $MoS_2$ peaks after annealing, see Figure E.3(c), though this decrease is much stronger, the PL signal for the $MoS_2$ A1 exciton peak is quenched to half the intensity before annealing. The $WSe_2$ peak also shows a clear shift to higher energy. Before annealing the A1 exciton peak is located at 1.59 eV, where is shifts to 1.60 eV after annealing with the FWHM decreasing

from 0.07 eV to 0.06 eV, where the $MoS_2$ A1 exciton peak is located at 1.87 eV before and 1.86 eV after annealing, shifting to lower energies. The FWHM for the $MoS_2$ A1 peak decreases from 0.19 eV to 0.10 eV. The shift in the peak positions indicates interaction between the layers.

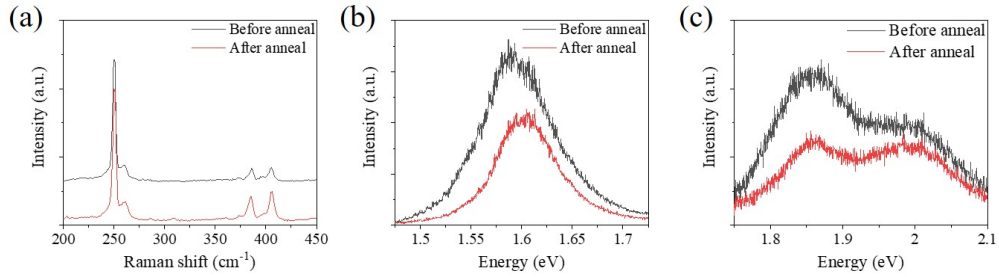


Figure E.3: Raman and PL spectra of the heterostructure areas before and after annealing. (a) shows the Raman spectra, the spectra are normalised on the $WSe_2$ $E^1_{2g}$+$A_{1g}$ peak, where (b) and (c) show the PL spectra for the $WSe_2$ A1 exciton peak in (b) and the $MoS_2$ PL peaks in (c). The PL spectra are normalised for the Si peak at ∼520 $cm^{-1}$.

The decrease in PL for the heterostructure area can be attributed to the formation of a type-II band alignment between $WSe_2$ and $MoS_2$. Type-II band alignment is when the top of the valence band of one of the materials is below the valence band of the other material while the valence band, for the material with the lower conduction band, is situated at an energy lower than the other materials valance band, as discussed in subsection 3.6.1. For $MoS_2$–$WSe_2$ heterostructures $MoS_2$ has lower valence band and conduction band energies. Type II of alignment allows holes present in the valence band of $MoS_2$ to go to lower energy positions by transferring to the $WSe_2$ with the electrons in $WSe_2$ being able to fill up the holes in the lower energy positions in the $MoS_2$.

The interlayer charge transfer creates an interlayer exciton as the two charges will still be bound as a result of the extremely small distances between the two layers. These are known to be highly stable excitons and resulting in a decreasing chance of recombination, they manifest themselves as a reduction in the PL intensity. The reductions here are around 0.5x the intensity before annealing. The reduction is expected due to the reduced number of recombinations that can occur however, the reduction of than the reductions of up to 2 orders reported in literature.[351,352]. Which could be due to defects present in the individual CVD grown materials, resulting in a lower initial PL signal. Still the reduction in the PL signal would indicate that a heterostructure has been created.

The indirect synthesis of heterostructures leads to successful formation of vertical TMD heterostructures, as shown in the results above. There is an interlayer coupling between the different TMDs, especially after post-annealment of the samples. The interlayer coupling indicates that a type II band alignment is formed between the $WSe_2$ and $MoS_2$. In this work $WSe_2/MoS_2$ heterostructures are formed, though also other TMD combinations can be made by this method. The indirect synthesis

method for TMD heterostructures gives good control over the alignment of the TMDs, though the method is time consuming and not suitable for up scaling. Hence this method is mainly suitable for proof of concept purposes and will the following chapter focus on direct synthesis of heterostructures, which is more scalable method.

# F List of Publications

1. S. A. O'Brien, E. Roy, N. Shelly, S. Meaney, L. Peters, G. Cunningham, C. Smith, C. P. Murray, N. McEvoy, D. McCloskey, *in preparation*

2. C. P. Cullen, O. Hartwig, C. Ó. Coileáin, J. B. McManus, L. Peters, C. Ilhan, G. S. Duesberg and N. McEvoy, *in preparation.*

3. R. Tilmann, C. Weiß, C. P. Cullen, L. Peters, O. Hartwig, L. Höltgen, T. Stimpel-Lindner, K. C. Knirsch, N. McEvoy, A. Hirsch and G. S. Duesberg, Adv. Electron. Mater., 2021, 2000564.

4. J. Lawless, C. Hrelescu, C. Elliott, L. Peters, N. McEvoy and A. L. Bradley, ACS Appl. Mater. Interfaces, 2020, **12**, 46406–46415.

5. J. B. Mc Manus, C. Ilhan, B. Balsamo, C. Downing, C. P. Cullen, T. Stimpel-Lindner, G. Cunningham, L. Peters, L. Jones, D. Mullarkey, I. V. Shvets, G. S. Duesberg and N. McEvoy, Tungsten, 2020, **2**, 321–334.

6. L. Peters, C. Ó Coileáin, P. Dluzynski, R. Siris, G. S. Duesberg and N. McEvoy, Phys. status solidi, 2020, **217**, 2000073.

7. A. Di Bartolomeo, F. Urban, M. Passacantando, N. McEvoy, L. Peters, L. Iemmo, G. Luongo, F. Romeo and F. Giubileo, Nanoscale, 2019, **11**, 1538–1548.

8. F. Urban, N. Martucciello, L. Peters, N. McEvoy and A. Di Bartolomeo, Nanomaterials, 2018, **8**, 901.

9. K. Verguts, K. Schouteden, C. H. Wu, L. Peters, N. Vrancken, X. Wu, Z. Li, M. Erkens, C. Porret, C. Huyghebaert, C. Van Haesendonck, S. De Gendt and S. Brems, ACS Appl. Mater. Interfaces, 2017, **9**, 37484–37492.

10. S. Brems, K. Verguts, N. Vrancken, B. Vermeulen, C. Porret, L. Peters, C. H. Wu, C. Huyghebaert, K. Schouteden, C. Van Haesendonck and S. De Gendt, ECS Trans., 2017, **77**, 3–13.

11. D. Chiappe, I. Asselberghs, S. Sutar, S. Iacovo, V. Afanas'ev, A. Stesmans, Y. Balaji, L. Peters, M. Heyne, M. Mannarino, W. Vandervorst, S. Sayan, C. Huyghebaert, M. Caymax, M. Heyns, S. De Gendt, I. Radu and A. Thean, Adv. Mater. Interfaces, 2016, 3, 1500635.